Universitat Autònoma de Barcelona

Preparation and characterization of biferroic nanostructures with magneto-electric coupling

Nico Dix

ADVERTIMENT. L'accés als continguts d'aquesta tesi queda condicionat a l'acceptació de les condicions d'ús establertes per la següent llicència Creative Commons: http://cat.creativecommons.org/?page_id=184

ADVERTENCIA. El acceso a los contenidos de esta tesis queda condicionado a la aceptación de las condiciones de uso establecidas por la siguiente licencia Creative Commons: http://es.creativecommons.org/blog/licencias/

WARNING. The access to the contents of this doctoral thesis it is limited to the acceptance of the use conditions set by the following Creative Commons license: https://creativecommons.org/licenses/?lang=en

Universitat Autònoma de Barcelona

Tesi Doctoral

Preparation and characterization of biferroic nanostructures with magneto-electric coupling

Autor:

Nico Dix

Directors:

Dr. Florencio Sánchez Barrera

Prof. Josep Fontcuberta i Griñó

Tutor:

Prof. Javier Rodríguez Viejo

Programa de Doctorat en Ciència de Materials.
Dept. de Física. Facultat de Ciències. Universitat Autònoma de Barcelona.
Institut de Ciència de Materials de Barcelona (ICMAB-CSIC).

2017

Memòria amb titul **Preparation and characterization of biferroic nanostructures with magneto-electric coupling** presentada per *Nico Dix* per aspirar al grau de doctor.

. . . . . .

Nico Dix
Autor

Dr. Florencio Sánchez Barrera i *Prof. Josep Fontcuberta i Griñó*, ambdós investigadors del Consejo Superior de Investigaciones Científicas (CSIC) a l'Institut de Ciència de Materials de Barcelona (ICMAB), i *Prof. Javier Rodríguez Viejo*, catedratic de la Universitat Autonoma de Barcelona (UAB),

CERTIFIQUEN:

Que *Nico Dix*, Diplom-Ingenieur für Technische Physik, Technische Universität Ilmenau (Alemanya), ha dut a terme aquesta tesis doctoral sota la seva dirreció amb títul **Preparation and characterization of biferroic nanostructures with magneto-electric coupling**. Aquesta tesis doctoral s'ha desenvolupat en el programa de Doctorat de Ciència de Materials del Departament de Física, Facultat de Ciència de l'Universitat Autònoma de Barcelona.

I perquè així consti, signen el present certificat:

. . . . . .

Dr. Florencio Sánchez Barrera
Director

. . . . . .

Prof. Josep Fontcuberta i Griñó
Co-Director

. . . . . .

Prof. Javier Rodríguez Viejo
Tutor

Bellaterra, febrer 2017.

Motivation

Complex oxide materials have a huge variety of functional properties, among them ferroelectric or ferromagnetic materials are widely used in everyday consumer electronics. The coexistence and coupling of the two ferroic properties would allow novel device architectures. Anyhow, single phase materials rarely unite these two properties above room temperature. An alternative route are composite materials combining two phases, one ferroelectric the other ferromagnetic.

The fabrication of high quality complex oxide single phase thin films as the ones used here can be difficult on its own. In the growth of ferrimagnetic $CoFe_2O_4$ spinel it is challenging to obtain flat (001) oriented epitaxial films, also the ferroelectric perovskite $BaTiO_3$ needs thorough optimization to grow flat, epitaxial with pure *c*-orientation and with a controlled strain. Different challenges are present for $BiFeO_3$ thin films as it has a strong tendency to grow in different phases (polymorphs) and in addition is affected by the volatility of bismuth (Bi).

Here we aim to study the growth conditions for single phase materials and combine them in more complex heterostructures. Challenges such as the growth of ferroelectric films on strongly dissimilar spinels in horizontal heterostructures or a trade off between optimal deposition conditions of each phase in vertical heterostructures may hamper the desired functionality. In vertical nanocomposites, the control of the vertical interfaces and simultaneously the film-substrate interface difficults engineering the strain of each phase, and the stoichiometry of nanocomposites.

We have studied in detail the growth of horizontal and vertical heterostructures, aiming to investigate the correlation between structure and functionality and where possible, to proof the capability of magneto-electric coupling.

Summary

Complex oxides present a broad spectrum of functional properties. In the last decade special attention was directed to materials with a possible coexistence of two or more ferroic orders (*i.e.* ferroelectric and ferromagnetic order). Such coexisting orders may be strongly coupled and thus lead to large magneto-electric responses. Appealing for application are materials that show these features well above room temperature, but single phase materials are scarce. Artificially combining materials with desired bulk properties is an alternative route to achieve coexistence of multiple ferroic orders above room temperature. In such systems magneto-electric coupling can arise via elastically coupled magnetostrictive and piezostrictive phases. In this work we have studied two promising model systems: *layered horizontal heterostructures* and *self-organized column-matrix heterostructures*. The ferroelectric perovskites $BaTiO_3$ (BTO) and $BiFeO_3$ (BFO) and ferrimagnetic spinel $CoFe_2O_4$ (CFO) were used, all have critical temperatures well above room temperature. First, we describe the growth of horizontal heterostructures by pulsed laser deposition, optimizing the deposition conditions of single ferroelectric (BTO) and ferromagnetic (CFO) films and then integrate them in bilayered structures studying the effect of stacking order on the structural and functional properties. It is found that in spite of the structural dissimilarity of CFO spinel and BTO perovskite, high quality $(00l)$-oriented epitaxial bilayered heterostructures can be grown, independent of the stacking order. We have used reflection high energy electron diffraction to monitor the lattice relaxation in real time. BTO slowly relaxes when grown on low-mismatched perovskite substrates while it instantaneously relaxes on highly mismatched CFO layer. The films are ferroelectric and ferromagnetic above room temperature, and the BTO layer undergoes structural transitions at temperatures close to bulk transition temperatures. At these transitions a large change in the dielectric permitivity is observed under magnetic field, indicating magneto-electric coupling.

Second, the growth of self-organized two-phase nanocomposite heterostructures will be described. Phase separation at the nanoscale can lead to materials with extremely large interface area, *i.e.* by forming columns with a few nanometers in diameter embedded in a continuous matrix. Thus it may be an alternative route to combine ferroelectric

and ferromagnetic phases and reduce the influence of the rigid substrate. Here, we have investigated $0.65BiFeO_3$-$0.35CoFe_2O_4$ columnar nanocomposites prepared by pulsed laser deposition on (001) and (111) $SrTiO_3$ (STO) and other (001) substrates. We determined a narrow window of growth conditions that permits stoichiometric growth of the nanocomposite at expense of limited size control of the columnar features. Exploring different mismatched (001) substrates showed that depending on the induced stress, *BFO* stabilized in the tetragonal *T-BFO* or rhombohedral *R-BFO* phase while *CFO* is growing as columns. The stabilization of different *BFO* phases allows to modify the ferroelectric polarization direction which can be rotated from [111] close to [001] substrate direction. The magnetization easy axis can be directed either out-of-plane or in-plane depending on the strain state of the magnetic columns. We confirmed magneto-electric coupling at the nanoscale by scanning probe techniques, measuring the local magnetic response before and after electric poling in *CFO–R-BFO* composites.
We also investigated a columnar nanocomposite system $0.65BaTiO_3$-$0.35CoFe_2O_4$ grown by rf-sputtering on $SrTiO_3$(001). Optimal growth conditions were found to produce epitaxial nanocomposite films with phase separation, (00l)-texture, column-matrix topology, as well as being ferromagnetic and ferroelectric at room temperature.

Resumen

Los óxidos complejos presentan tienen un amplio espectro de propiedades funcionales. En la última década se ha prestado atención a materiales que pueden mostrar simultáneamente varios ordenes ferróicos, en particular ferroelectricidad y ferromagnetismo. La coexistencia de los dos ordenes podría llevar a acoplamiento entre ambos y consecuentemente podría resultar en una gran respuesta magneto-eléctrica. Materiales que presenten este tipo de propiedades por encima de la temperatura ambiente serian interesantes para aplicaciones electrónicas, pero tales materiales son escasos. La combinación de materiales con las propiedades deseadas puede ser un camino alternativo para conseguir coexistencia de múltiple ordenes ferróicos por encima de temperatura ambiente. El acoplamiento en estos sistemas puede originarse de la interacción elástica de fases magnetostrictivas y piezostrictivas. En este trabajo hemos estudiado tipos de combinaciones prometedores: *heteroestructuras horizontales* y *heteroestructuras autoasemblados*. Hemos utilizado perovskitas ferroelectricas $BaTiO_3$ (BTO) y $BiFeO_3$ (BFO) y la espinela ferromagnética $CoFe_2O_4$ (CFO) todos con temperaturas críticas por encima de la temperatura ambiente.

Primero describiremos el crecimiento mediante depósito con láser pulsado (PLD) de heteroestructuras horizontales. Inicialmente se han optimizado las condiciones de crecimiento para capas finas ferroelectricas (BTO) y ferromagneticas (CFO), y seguidamente describimos su integración en heteroestructuras bilaminares estudiando el efecto del orden de apilamento en las propiedades estructurales y funcionales. A pesar de la diferencia estructural entre la spinela CFO y la perovskita BTO, se han conseguido capas finas epitaxiales de heteroestructuras bi-laminares, independiente del orden de apilamiento. Se ha monitorizado la relajación en tiempo real usando reflection high energy electron diffraction (RHEED). El BTO se relaja progresivamente si crece sobre perovskitas con desajuste moderado de malla, mientras que se relaja instantáneamente si crece sobre la espinela CFO, con la que el desajuste de malla es muy alto. Las capas finas obtenidas son ferroelectricas y ferromagneticas por encima de la temperatura ambiente, y en el BTO se observan transiciones estructurales a temperaturas similares a los del material macroscópico. En estas transiciones se ha observado variaciones de la permitividad dieléctrica aplicando campos magnéticos, indicando acoplamiento magneto-eléctrico.

En la segunda parte se describe el crecimiento de compuestos bifásicos autoasemblados. Una separación de fases a escala nanométrica, por ejemplo con una fase formando columnas de diámetro nanométrico en una matriz de la otra fase, daría lugar un area de interfase extremadamente grande. Esta topología constituye una alternativa para combinar fases ferroelectricas y ferromagneticas y podría reducir la influencia del sustrato rígido. Hemos investigado nanocompuestos columnares preparados por ablación laser de blancos de 0.65 $BiFeO_3$-0.35$CoFe_2O_4$ sobre sustratos de $SrTiO_3$ (STO) con orientación (001) and (111) y otros sustratos (001). El crecimiento estequiométrico sólo es posible en una ventana muy estrecha de parámetros de crecimiento, a coste de un control limitado del tamaño y la distribución de las nanocolumnas. Hemos usados sustratos (001) con diferente parámetro de malla y mostramos que en función de la tensión causada por el sustrato la matriz de BFO estabiliza la fase tetragonal T-BFO o rhombohédrica R-BFO, manteniendo el CFO su crecimiento en forma columnar.

La estabilización de diferentes fases de BFO permite modificar la dirección de la polarización ferroeléctrica, rotandola de la direccion [111] a una dirección próxima a la [001], la dirección perpendicular a la superficie del sustrato. El eje fácil de la magnetización se situa en el plano o perpendicular a él en función de la deformación de red de las columnas magnéticas. Utilizando microscopias de proximidad hemos confirmado el acoplamiento magneto-eléctrico en escala nanométrica, trás medir la respuesta magnética local antes y después de polarizar la matriz ferroélectrica en nanocompuestos de CFO–R-BFO.

Hemos investigado asimismo el crecimiento de nanocompuestos columnares de 0.65 $BaTiO_3$-0.35$CoFe_2O_4$ mediante pulverización catódica rf sobre sustratos de $SrTiO_3$(001). Se ha

determinado el rango de parámetros de crecimiento que permite la formación de un nanocompuesto epitaxial con separación de fases, textura $(00l)$, morfología de columna-matriz y respuesta ferroeléctrica y magnética a temperatura ambiental.

Resum

Els òxids complexos, particularment aquells que tenen estructura perovskita, presenten un ampli espectre de propietats funcionals. En l'ultima dècada s'ha posat molta atenció en materials que poden mostrar simultàniament diversos ordres ferroics, en particular: ferroelectricitat i ferromagnetisme. La coexistència de tots dos podria originar un acoblament entre ells i conseqüentment podria donar una gran resposta magneto-elèctrica. Materials que presentin aquest tipus de propietats, per sobre de la temperatura ambient, són interessants per a aplicacions electròniques, però aquests materials són escassos. La combinació de materials amb propietats desitjades pod ser un camí alternatiu per aconseguir coexistència de múltiples ordres ferroiques per sobre temperatura ambient. L'acoblament en aquests sistemes pot originar-se per la interactuació elàstica de fases magnetostrictives i piezostrictives. En aquest treball hem estudiat dos tipus de combinacions prometedores: *heteroestructures horitzontals* i *heteroestructures autoassemblades verticals*. Hem utilitzat perovskitas ferroelèctriques $BaTiO_3$ (BTO) i $BiFeO_3$ (BFO) i l'espinel·la ferromagnètica $CoFe_2O_4$ (CFO), les dues, amb temperatures crítiques per sobre temperatura ambient.
En primer lloc, descriurem el creixement mitjançant ablació láser (PLD) de heteroestructures horitzontals. Inicialment optimitzem les condicions de creixement per a capes primes ferroelèctriques (BTO) i ferromagnètiques (CFO) i després descriiurem com integra-les en heteroestructures bilaminars on estudiarem l'efecte de l'ordre de l'apilament en els propietats estructurals i funcionals. Tot i la disimilitud estructural de l'espinel·la CFO i la perovskita BTO, s'han aconseguit capes primes epitaxials d'heteroestructures bi-laminars, independentment de l'ordre d'apilament. S'ha monitoritzat la relaxació en temps real utilitzant la reflectió d'electrons d'alta energia (RHEED). S'ha observat que el BTO es relaxa progresivament si creix sobre de perovskitas amb un desajust de malla moderat, mentre es relaxa mòl rapidament si creix damunt l'espinel·la CFO amb qui te un desajust de malla molt gran. Les capes obtingudes són ferroelèctriques i ferromagnètiques per sobre de temperatura ambient, i s'observen transicions estructurals en el BTO a temperatures similars a les transicions pròpies del material massiu. En aquestes transicions s'han observat variacions de la permitivitat dielèctrica aplicant camps magnètics, indicant així acoblament magneto-elèctric.

A la segona part es descriu el creixement de compostos bifàsics autoassemblats. Amb una separació de fases a escala nanomètrica, per exemple una fase formant columnes amb un diàmetre nanomètric en una matriu de l'altre fase, s'aconsegueix un material amb un area interficial extremadament gran. Aquesta topologia és una alternativa per a combinar fases ferroelèctriques i ferromagnètiques i podria reduir la influencia del substrat rígid. Hem investigat nanocompostos columnars preparats per ablació làser de blancs $0.65BiFeO_3$-$0.35CoFe_2O_4$ sobre substrats de $SrTiO_3$ (STO) amb orientació (001) i (111) i altres substrats (001). El creixement estequiomètric dels nanocompostos només és possible en una finestra molt estreta dels paràmetres de creixement, a cost d'un control limitat de la mida i la distribució de les nanocolumnes. Hem fet servir substrats (001) amb diferent paràmetre de malla i mostrem que en funció de la tensió causat pel substrat, la matriu de *BFO* s'estabilitza en fase tetragonal *T-BFO* o romboèdrica *R-BFO*, mantenint el *CFO* el seu creixement columnar.
L'estabilització de diferents fases de *BFO* permet modificar la direcció de la polarització ferroelèctrica, girant-la de la direcció [111] a una direcció a prop de [001], la direcció perpendicular a la superfície del substrat. L'eix fàcil de la magnetització es situa en paral·lel o perpendicular al pla en funció de la deformació de la malla de les columnes magnètiques. Utilitzant microscòpias de proximitat hem confirmat l'acoblament magneto-eléctric a escala nanométrica, després de mesurar la resposta magnética local abans i després de polaritzar la matriu ferroeléctrica en nanocompostos de *CFO–R-BFO*.
Finalment, hem investigat el creixement de nanocompostos columnars de $0.65\ BaTiO_3$-$0.35CoFe_2O_4$ per pulverització catodica de radiofreqüència sobre substrats de $SrTiO_3$(001). S'ha determinat l'interval de paràmetres de creixement que permet la formació d'un nanocompost epitaxial amb separació de fases, texturat ($00l$), morfologia de columna-matriu i resposta ferroelèctrica i magnètica a temperatura ambient.

Zusammenfassung

Komplexe Oxide haben ein breites Spektrum an funktionellen Eigenschaften. In der letzten Dekade wurde besonderes Augenmerk auf Materialien mit einer möglichen Koexistenz von zwei oder mehr ferroischen Eigenschaften (zum Beispiel ferroelektrische und ferromagnetische Ordnung) gerichtet. Kopplung dieser Eigenschaften kann zu Materialen mit großen magneto-elektrischen Effekten führen. Interessant für elektronische Anwendungen sind Materialen, wenn sie diese Eigenschaften deutlich über Raumtemperatur zeigen. Allerdings

sind solche Materialien rar. Eine alternative Rute könnten künstlich kombinierte Materialien sein, um die Koexistenz und Kopplung von mehreren ferroischen Eigenschaften über Raumtemperatur zu erreichen. In solchen Systemen kann magneto-elektrische Kopplung indirekt über elastisch gekoppelte magnetostriktive und piezostriktive Phasen erreicht werden. Wir haben zwei vielversprechende Modellsysteme untersucht: *horizontale Heterostrukturen* und *selbstorganisierte Säulen-Matrix-Heterostrukturen.* Als aktive Phasen haben wir ferroelektrische Perovskite $BaTiO_3$ (BTO) und $BiFeO_3$ (BFO) und das ferrimagnetische Spinell $CoFe_2O_4$ (CFO) verwendet. Alle zeigen kritische Temperaturen deutlich über Raumtemperatur.

Wir beschreiben hier das Wachstum horizontaler Heterostrukturen mittels Pulsed Laser Depositon (PLD). Zuerst haben wir die Abscheidungsbedingungen der ferroelektrischen (BTO) und ferromagnetischen (CFO) Filme optimiert und danach zweischichtigen Heterostrukturen gewachsen, um die Wirkung der Schichtordnung auf die strukturellen und funktionellen Eigenschaften zu studieren. Trotz der stark unterschiedlichen Struktur von CFO (Spinell) und BTO (Perovskit) können qualitativ hochwertige (00l)-orientierte epitaktische Heterostrukturen abgeschieden werden, unabhängig von der Schichtfolge. Um die Relaxation der wachsenden Schichten in Echtzeit zu analysieren, haben wir Oberflächensensitives Reflection High Energy Electron Diffraction (RHEED) verwendet. BTO relaxiert langsam, wenn es auf Perovskit Substraten mit geringer Gitterfehlanpassung wächst, während es sich auf einer stark unterschiedlichen CFO Schicht augenblicklich entspannt. Die Filme sind ferroelektrisch und ferromagnetisch bei Raumtemperatur und darüber. BTO zeigt strukturelle Übergänge bei Temperaturen, ähnlich der Bulkübergangstemperaturen. An diesen Übergängen wurde eine Änderung in der dielektrischen Permittivität durch Einwirkung von externen Magnetfeldern beobachtet. Dies weist magneto-elektrische Kopplung nach.

Als Zweites Modellsystem beschreiben wir das Wachstum von selbstorganisierten zweiphasigen Nanokomposit-Heterostrukturen. Phasentrennung mit nanometrischer Größenordnung kann zu Materialien mit extrem großen Grenzflächen führen. Zum Beispiel könnten Säulen mit wenigen Nanometer Durchmesser eingebettet in eine Matrix wachsen. Dieser alternative Weg, um ferroelektrische und ferromagnetische Phasen zu kombinieren, könnte auch den Einfluß des starren Substrats verringern. Hier haben wir $0.65\%BiFeO_3$-$0.35\%CoFe_2O_4$ säulenförmige Nanokomposite mittels Pulsed Laser Deposition auf (001) und (111)$SrTiO_3$ (STO) und anderen (001)-Substraten abgeschieden. Stöchiometrisches Wachstum ist nur in einem kleinen Bereich von Wachstumsparamtern möglich, auf Kosten einer begrenzten Kontrolle über Größe und Verteilung der eingebetteten Säulen. (001)-Substrate mit unterschiedlicher Gitterfehlanpassung zeigten, dass in Funktion der induzierten Verspannung BFO in tetragonaler *T-BFO* oder rhomboedrischer *R-BFO* Phase stabilisert, während

CFO als Säulen wächst. Die Stabilisierung der verschiedenen *BFO* Phasen ermöglicht es, dass die ferroelektrische Polarisationsrichtung zwischen [111] und [001] gedreht werden kann. Die Magnetisierungsvorzugsachse kann parallel oder senkrecht zur Substratebene, in Abhängigkeit vom Spannungszustand der magnetischen Säulen, liegen. Mit Hilfe von Rastersondentechniken haben wir magneto-elektrische Kopplung im Nanometerbereich mittels Messung der lokalen Magnetisierungsrichtung vor und nach elektrischer Polarisierung der *CFO–R-BFO* Nanokomposite nachgewiesen.
Außerdem untersuchten wir das Wachstum von säulenförmige Nanokompositen $0.65BaTiO_3$-$0.35CoFe_2O_4$ durch radiofrequenz Kathodenzerstäubung auf $SrTiO_3$(001) Substraten. Optimierte Wachstumsbedingungen ermöglichen epitaktische Nanokompositfilme mit Phasentrennung, (00l)-Textur und Säulen-Matrix Morphologie. Die Kompositfilme sind ferromagnetisch und ferroelektrisch bei Raumtemperatur.

Outline

This thesis is structured in three parts. Part **I** is intended to briefly introduce the relevant materials (Chapter 1) and the experimental techniques used (Chapter 2).
Part **II** presents the main results of the investigated systems: Chapter 3 has the focus on horizontal heterostructures prepared by pulsed laser deposition. We present a study on the growth conditions of single $CoFe_2O_4$ (CFO) and single $BaTiO_3$ (BTO) thin films on $SrTiO_3$(001) aiming grow films with flat surface topology and good functional properties. Then their integration in bilayered heterostructures with alternate stacking (CFO on BTO and BTO on CFO) and the resulting functional properties are discussed.
The preparation of vertical nanocomposites $BiFeO_3$-$CoFe_2O_4$ (BFO-CFO) and $BaTiO_3$-$CoFe_2O_4$ (BTO-CFO) is described in Chapters 4 and 5, respectively. (BFO-CFO) nanocomposites prepared by pulsed laser deposition (Chapter 4). First we revise the influence of growth parameters on the stoichiometry of the composites and discuss the effects of the BFO matrix on the strain state of the embedded CFO-columns. We show that BFO can be stabilized with different crystal structure maintaining the matrix-column topology using suitable substrates. Within this investigation we describe the formation of largely deformed tetragonal-like BFO in composites and single phase films. BTO-CFO nanocomposites prepared by rf-sputtering are described in Chapters 5. Finally, the principal conclusions are presented in Chapter 6.
Part **III** contains lists of abbreviations used, scientific contributions and the bibliography.

Contents

List of Figures

List of Tables

PART I
Introduction

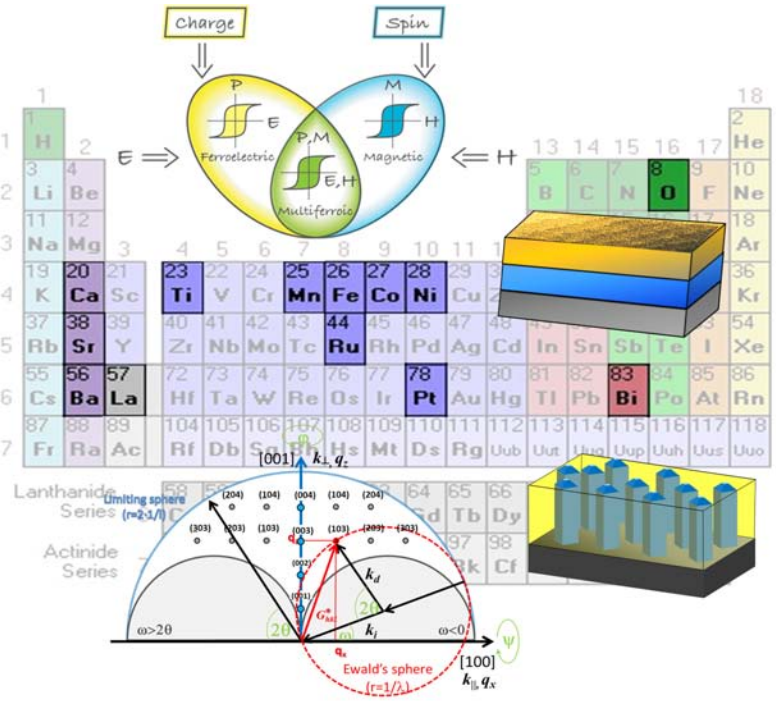

CHAPTER 1

Introduction

In the last decades investigation of electronic materials with novel features emerging at the nanometer scale advanced continuously. Complex functional oxides are an active playground, thus the physical properties range from strong electrical insulating behavior to high temperature superconductivity, as well as ferromagnetism, ferroelectricity or even multiferroicity [1]. In low dimensional oxide heterostructures interfaces and lattice strains are key to influence the physical properties of the material which are strongly correlated to metal-oxygen distances, bond tilt angles, defects or slight variation in stoichiometry [2]. Although, this makes the preparation of epitaxial oxide films challenging, it simultaneously opens a possible route to exploit epitaxial growth to modify functional properties, stabilize a particular structural polymorph, or even metastable phases not existing in bulk form.

Recently, multiferroic materials with a cross-coupled electric(magnetic) response provoked by an external magnetic(electric) field came back into the spotlight. The scarcity of single phase materials showing such functional response well above room temperature [3], directed the interest back to composite materials with indirect coupling via elastic interaction. Bulk composites combining FM and FE phases with indirect magnetoelectric (ME) coupling via elastic interaction, were investigated in the early 1970's [4]. The solidification of eutectic *Ba-Ti-Fe-Co-O* melts lead to $BaTiO_3$-$CoFe_2O_4$ (*BTO-CFO*) composites with ordered micro domains of pure *BTO* and *CFO*. Recently in 2004, nanocomposite thin films of *BTO-CFO* were grown by pulsed laser deposition (PLD) from a single target [5], forming well separated phases of self-organized epitaxial FM nanocolumns (*CFO*) embedded in a FE matrix (*BTO*). Also other material combinations showing similar self-organisation were reported, recently [6–9]. Nevertheless, the growth of layered heterostructures might be a simpler approach to allow accurate control of phase

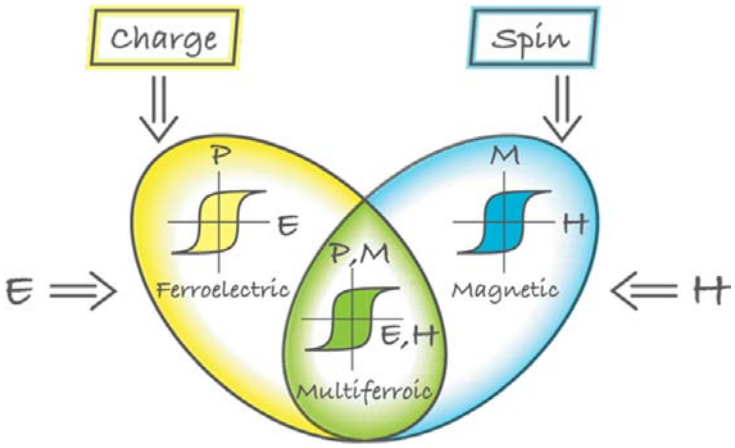

Figure 1.1: Multiferroic materials combine the presence of spontaneous magnetic and electric orders with hysteretic response to external fields. Which may allow for individually addressing its magnetisation(polarization) state, as well as, cross-coupled response of magnetic(electric) order to electric(magnetic) fields (adapted from Khomski [11]).

distribution by controlling the layer thickness and sharp interfaces between the layers [5, 10].

1.1 Multiferroic oxides

Multiferroics (MF) are materials with simutaneous occurance of at least two ferroic orders that include appart of FE and FM: *ferroelasticity* (spontaneous strain), *(anti)ferromagnetism* (spontaneous order of magnetic moments), *(anti)ferroelectricity* (spontaneous order of electric dipoles), and *ferrotoroicity* (spontaneous long range order of toroidal moments)[11–15]. In figure 1.1 a simple sketch indicates materials with stable and individually reversable ferroelectric (FE) and ferromagnetic (FM) order. Furthermore, it shows an overlapped region with both orders existing at the same time. Addressing each parameter individually or exploiting coupled responses may allow multiple state memories [11] and novel devices exploring the sensibility of magnetization(electric polarization) to electric(magnetic) fields. Such coupling is also called magnetoelectric (ME) effect.

Among transition metal oxides with *perovskite* structure both FE and FM materials are known, but only a few are multiferroic. This scarcity was addressed by N. Spaldin (2000)[3] and she relates its origin to the different and usually incompatible physical requirements of each phenomenon. While FE materials are insulators and the transition metal ion is typically in d^0 state, like Ti^{4+} in $BaTiO_3$ where Ti $3d$ is hybridized with the closest O $2p$ electrons which helps to stabilze the slightly off-centered positions and results in an effective dipole. In magnetic perovskite oxides, the partially filled d-orbitals, lead to magnetism by superexchange interaction over the interstitial oxygen sites. Since then, a

huge effort from experimental and theoretical side, guided the way to novel mechanisms being both FE and FM order compatible. According to the origin of FE in single phase multiferroics, they can be classified in two groups [11]: Type I MFs: here ferroelectricity and magnetsim are of different physical origin. Usually large polarizations and high critical temperatures are found for the FE phase, the FM one is typically much lower and only weak coupling is observed (i.e. $BiFeO_3$ - FE is originated by lone pairs of Bi^{3+} ion, or $LuFe_2O_4$ where FE is due to charge ordering). Type II MFs: the magnetic ordering causes FE polarization (*spiral cycloidic type*, i.e. $TbMnO_3$ or of *collinear type*, i.e. $HoMnO_3$). Despite the small FE polarizations, their direct coupling to the magnetic order allows large ME effects [16].

1.2 Multiferroic composites

The lack of single phase MFs showing simultaneously robust FE and FM above RT, may be overcome by composite materials, where each phase is maintaining their properties above RT and a possible cross interaction is mediated by the interface (see figure 1.2(a)). Considering a two phase MF composite in which material A is piezostrive (FE) and

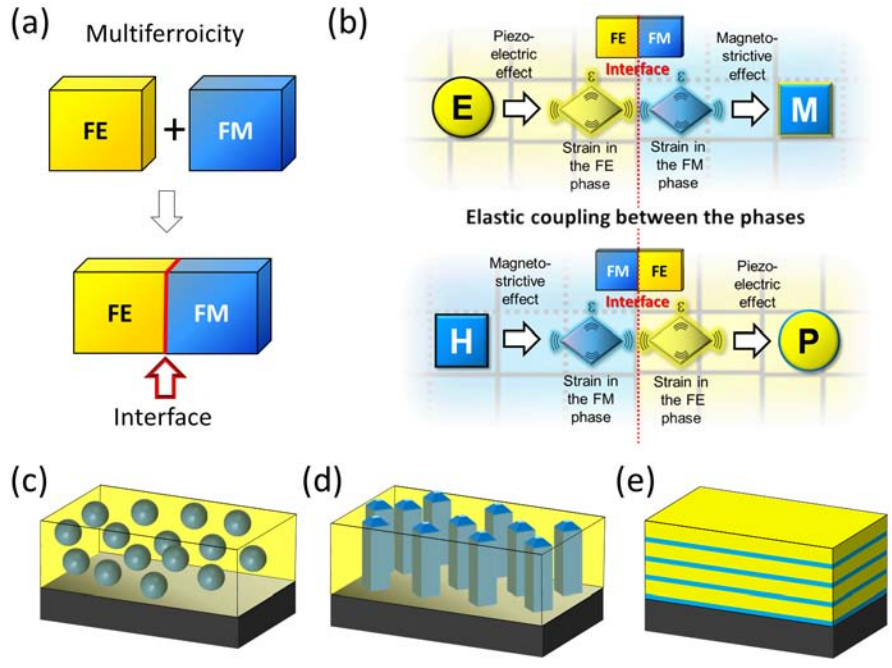

Figure 1.2: (a) MF can be achieved in a composite by combining two materials, one FE and the other FM. The strain can be mediated over the interfaces. (b) Diagram indicates the indirect coupling mechanism of E to M and H to P by interface mediated strain. Different types of two phase composites (c) [3-0], 3d matrix with particulated (0d) inclusions and [3-1] if (d) elongated or columnar structures (1d) are embedded. Horizontally layered structures where both phases are 2d, are labeled [2-2] (e). ((c)-(d) adapted from Ref. [10]).

material B is magnetostrictive (FM) and both are effectively connected by their interfaces,

then electric(magnetic) fields causes deformation of the piezostrictive (magnetostrictive) phase which in turn induces strain in the magnetostrictive(piezostrictive) secondary phase and thus indirectly alters the magnetization (electric polarization) of the latter. This is schematically depicted in figure 1.2(b). The overall ME response may be tailored by composition, particle size or connectivity schemes.

The simplest way to achieve bulk composites is mixing of ceramic powders and sinter compact ceramic pellets (see for example Ref. [17, 18]). But also bluk laminated heterostructures (clued or sintered together), were found to show significant ME coupling [19]. Another route was proposed by van Suchtelen [4] achieving a self organized composite of $BaTiO_3$ (ferroelectric) and $CoFe_2O_4$ (ferrimagnetic) by adequate cooling of euthectic $Ba\text{-}Ti\text{-}Co\text{-}Fe\text{-}O$ melts, but very high process temperatures (T$\geq$ 1200 °C) are required. In nanometric thin films one might envision similar heterostructures creating a very large interface area. Referring to the dimensionality of the involved phases one can indicate them as (**0**) for particulates/ nanodots, (**1**) for columns or wires, (**2**) for thin continuous layers and (**3**) continuous volume. For example a phase A forms a 3 dimensional matrix and phase B are particulate inclusions it is labeled **3-0** (figure 1.2(c)) and if phase B corresponds to columnar or wire-like structures it is consequently **3-1** (figure 1.2(d)). Layered heterostructures **2-2** have alternating layers of phase A and B (figure 1.2(e)).

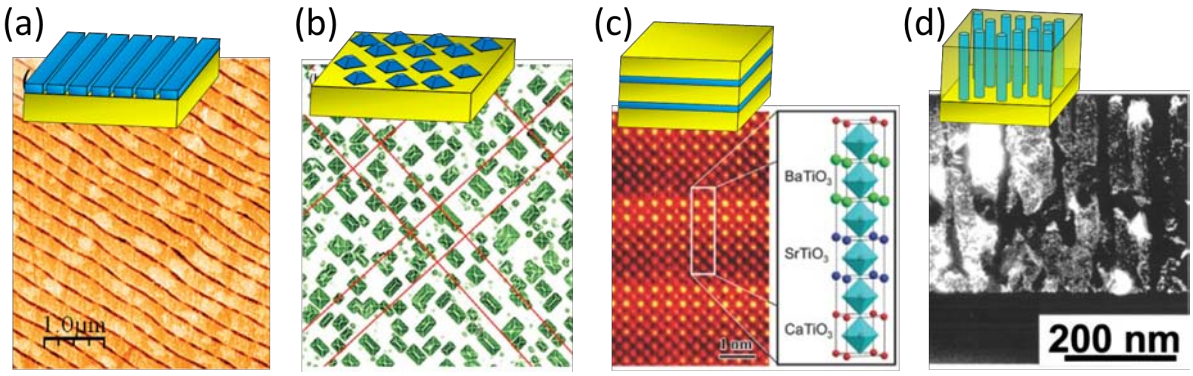

Figure 1.3: Fabrication of complex oxide nanostructures, can lead to self-organized formation of conducting nanowires (a) wires on treated substrates. (b) $CoCr_2O_4$ spinel islands on (001) oriented substrates with orientational ordering along [110] crystal direction and (111) faceting form. (c) Complex horizontal heterostructures containing 3 similar materials $BaTiO_3$, $SrTiO_3$ and $CaTiO_3$ grown with atomically sharp interfaces and unit cell control lead to increased polarization. Mixed phase self organized complex oxides (d) can form columnar structures ($CoFe_2O_4$) embedded in a 3d matrix material ($BaTiO_3$). (Images are adapted from (a) [20], (b) [21] and (c) [22] and (d) [5]).

Research on functional oxide films has been mostly focused on epitaxial layers, and two dimensional growth for many materials was achieved. Anyhow, recent studies suggest that self organization similar to previously studied semiconductors[23] can be a viable route to obtain complex oxide heterostructured, some examples are presented in figure 1.3.

As an example after suitable substrate treatment, nanowires of $SrRuO_3$ can be grown on $SrTiO_3$ substrates [20] (figure 1.3(b)). Spinel oxide nanoislands of $CoCr_2O_4$ were grown on (001) oriented substrates. The islands are (111) faceted (a sample atomic force image is shown in figure 1.3(b)), their morphological evolution is tunable by choosing adequate growth conditions and thus may be an interesting basis for the growth of more complex heterostructures [21]. Modern deposition techniques allow growth of atomically sharp interfaces with unit cell thickness control enabling the creation of complex layered heterostructures or superlattices. In figure 1.3(c) a transmission electron microscope (TEM) image of a complex superlattice, alternating 3 chemically different perovskites ($BaTiO_3$, $SrTiO_3$, $CaTiO_3$) each with 1-2 unit cell thickness. Zheng et. al [5] shows that spinel nanocolumns ($CoFe_2O_4$) inside a perovskite ($BaTiO_3$) matrix can form by self-organization in a single deposition process (see the cross sectional TEM image in figure 1.3(d)).

1.2.1 Horizontal heterostructures

Horizontal layered heterostructures appear to be in principle the most simple artificial multiferroic. Existing knowledge on complex oxide thin film epitaxy can be used as guide to grow bi- and multilayered heterostructures of FM and FE oxides, with accurate control of layer thickness, interface and composition. However, two main difficulties are known. First, the substrate clamping effect reduces the elastic response of an epitaxial thin film it would have as a free standing layer, and consequently deformation due to external fields or structural phase transitions might be hampered. Simplistically, it is a consequence of the $10^3..10^6$ times smaller film volume, atomically bonded to the large rigid substrate (depicted in figure 1.4(a), with typical thickness of substrate and film which are around $500\,\mu m$ and $1..500\,nm$, respectively). Second, convenient FM and FE oxides can be structurally dissimilar and consequently controlled epitaxial growth of one on top of the other can be challenging. The difference between film and substrate cell parameters (or a bottom layer) can be described by the mismatch:

$$F = \frac{a_{film\,bulk} - a_{substrate}}{a_{substrate}} \tag{1.1}$$

where $a_{film\,bulk}$ and $a_{substrate}$ correspond to the bulk film and substrate in-plane parameter. This difference in lattice parameters is causing bi-axial stress on the growing film and in the ideal case the film deforms elastically and grows perfectly matched on the substrate (fully coherent interface, see figure 1.4(b)). The strain resulting of the deformation of the

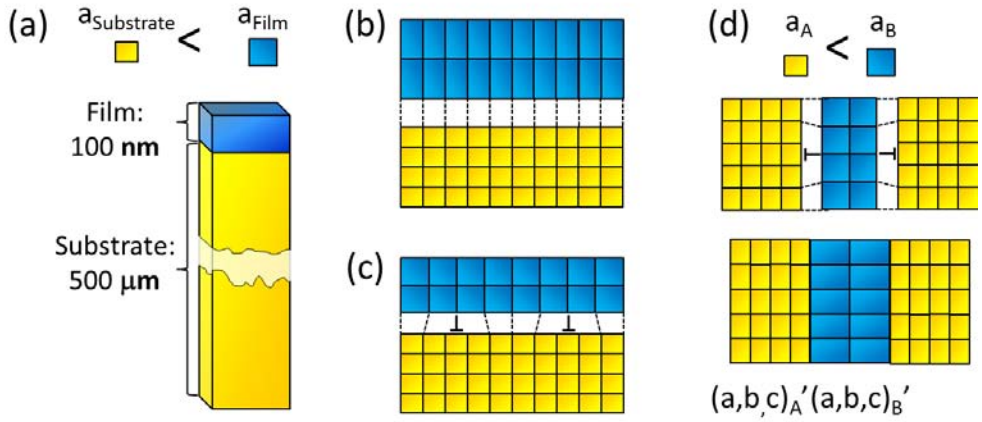

Figure 1.4: (a) The substrate is typically much thicker ($500\,\mu m$) than films ($\approx 100\,nm$) grown on top. Epitaxial layers can grow (b) fully coherent or (c) semicoherent forming dislocations. (d) in vertical composites [semi]coherent interfaces between phase A and B form and can be subject to elastic deformation and can result in modified lattice parameters ($a_A \rightarrow (a,b,c)'_A$, $a_B \rightarrow (a,b,c)'_B$) in the final structure.

film (a_{film}) compared to its bulk film parameter is:

$$\epsilon = \frac{a_{film} - a_{film\,bulk}}{a_{film\,bulk}} \tag{1.2}$$

The strain in the deformed film layer is correlated to the stored elastic energy. The system consequently tries to minimize energy and film material relaxes towards its bulk parameter, *i.e.* by formation of a dislocation network (plastic deformation) either directly at the interface (semicoherent, figure 1.4(c)) or after growing a certain number of fully coherent layers. The level of relaxation the film undergoes during growth is indicated by the relaxation factor R:

$$R(\%) = \left| \frac{a_{film} - a_{substrate}}{a_{film\ bulk} - a_{substrate}} \right| \times 100 \tag{1.3}$$

where it varies between two extremes: fully strained ($R = 0\%$ where $a_{film} = a_{substrate}$) and fully relaxed ($R = 100\%$ where $a_{film} = a_{film\ bulk}$).

In this thesis we investigate the growth mechanisms of FE $BaTiO_3$ perovskite and FM $CoFe_2O_4$ spinel aiming the fabrication of high quality epitaxial bilayers combining both oxides and determining if magnetoelectric coupling can arise in spite of the expected clamping effects.

1.2.2 Vertical heterostructures

Zheng *et. al.* [5] showed that using pulsed laser deposition (PLD) to ablate a mixed ceramic target containing a FM spinel (35% CFO) and a FE perovskite (65% BTO) oxide can result in the formation of well ordered FM columns in a FE matrix. At the deposition conditions

used (substrate temperature in the 700-950 °C range, oxygen pressure 0.133 *mbar*) the phases are immiscible and both grew epitaxially with cube-on-cube epitaxial relationship respect $STO(001)$ forming CFO columns (around 20 to 30 *nm* wide and 400 *nm* high) embedded in the BTO matrix, see example in figure 1.3(d). The system showed magnetic and ferroelectric response, as well as weak ME coupling (a drop of the magnetization of about 5% was observed at the transition temperature of the FE BTO). The advantages of this structure are a very high FM/FE interface area and that vertical interfaces are formed, so clamping by the substrate is reduced and larger ME effects may be expected. The column-matrix nanostructure has an intrinsically large interface between the two mixed phases and thus elastic deformation of either the column or matrix lattice parameter can occur even for largely mismatched phases A and B, see scheme in figure 1.4(d). Effectively, vertical deformations of 1-2% with respect to the bulk lattice in the direction normal to the film plane affected at least one of the composite phases [24, 25].

Nanocomposites with FM spinels (usually $CoFe_2O_4$ or $NiFe_2O_4$) and FE perovskites ($BaTiO_3$, $BiFeO_3$, $PbTiO_3$) were succesfully grown on a variety of substrates and substrate orientations [26], but also other complex oxides ((La,Sr)MnO_3-ZnO_2, $BiFeO_3$-Sm_2O_3) [25]. The topology of the spinel-perovskite nanocomposite system can be influenced by the relative composition of the two phases (FE:FM) and in combination with different substrate orientations [8, 27]. While a flat perovskite matrix (FE) and embedded columnar spinel (FM) nanostructures grow with a FE:FM ratio of 2/3:1/3 on a (001) oriented substrate. Column and matrix phase can be inverted choosing FE:FM ratio as 1/3:2/3 and (111) oriented substrates, where columns are formed by the perovskite (FE) and the flat matrix by the spinel (FM) [8, 28]. Composites grown on (110) cut substrates can result in maze or belt like shaped spinel (FM) objects embedded in the FE perovskite matrix [9, 27, 29].

In this thesis we investigate the growth and properties of vertical heteroestructures combining FM $CoFe_2O_4$ and either $BaTiO_3$ or $BiFeO_3$ as FE phase on (001) and (111)-oriented substrates. We determine the growth conditions to fabricate high-quality (secondary phases free) epitaxial nanocomposites and performed detailed structural and functional characterization.

1.3 Materials

1.3.1 Perovskite oxides

The perovskite structure is named after the mineral $CaTiO_3$ called *perovskite*. A cubic perovskite structure (see figure 1.5(a)) is described by the general formula of ABO_3. *A*-sites

are occupied by di- or trivalent cations (Sr, Ca, Ba, Bi, ...), and B is typically a tetra- or trivalent cation (Mn, Ti, Fe...). In the unit cell the A ions build the corners of the cube, the B ions occupy the body center surrounded by an octahedron of oxygen ions, thus the oxygen ions are at the face centers of the cube. Nevertheless, the ideal perovskite structure is not very common (*i.e.* $SrTiO_3$) and it is more likely the crystals are distorted with a lower symmetry. Various effects can play a role, *i.e.* geometric ratio of the A and B site ions can affect octahedron tilts, but also hybridization of bonding orbitals, ions with lone pairs (like $6s^2$ in Pb^{2+} or Bi^{3+}) or small ion displacements with respect to the oxygen sublattice can strongly influence the structure and thus electric and magnetic properties.

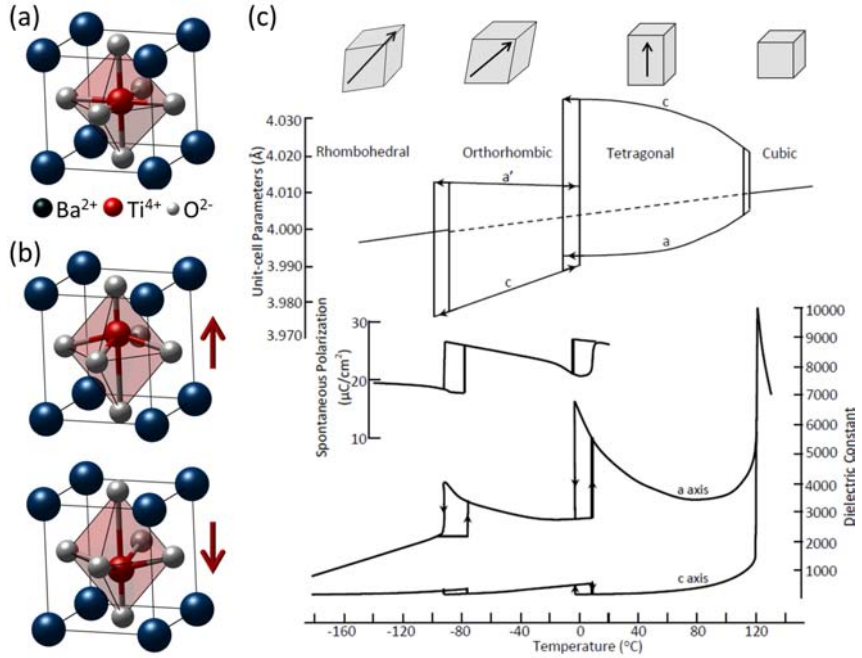

Figure 1.5: (a) $BaTiO_3$ in cubic structure, elements are labeled in legend. (b) Structure of tetragonal $BaTiO_3$ perovskite, for up and down polarization. The tetragonality and displacement are over-exaggerated for better visibility and indicated by red arrows. (c) Temperature phase diagram of BTO cell parameters, indicating the cubic to tetragonal (T_{ct} ≤120 °C) to orthorhombic (T_{to} ≤5 °C) to rhombohedral (T_{or} ≤-90 °C) phase transitions. The favored polarization direction changes from [001] in tetragonal, over [110] in orthorhombic to [111] in rhombohedral and is indicated by the insets. Additionally, the spontanious polarisation and dielectric constant are included in the plot ((c) adapted from [30]).

$BaTiO_3$

Barium titanate ($BaTiO_3$) is one of the most studied ferroelectrics of the perovskite class. As lead free ferroelectric it is widely used in applications due to a moderately high critical temperature ($T \approx 120 - 130\,°C$)[31], a spontaneous polarization ($26\,\mu C/cm^2$ [31, 32]), considerable piezoelectric coefficient ($d_{33} \approx 60..320\,pm/V$ [33]) and high dielectric constant (ε up to 15000 in bulk depending on temperature and crystal structure [34]). The A

site is occupied by the large Ba^{2+} ions and the tetravalent Ti^{4+} ions are sitting on the B sites of the perovskite structure (figure 1.5(a)). BTO has a cubic lattice constant of $a = 4.01\,\text{Å}$ above the critical temperature, while it undergoes several structural phase transitions on cooling down [31]. The first transition is from cubic to tetragonal, forming a slightly elongated c-axis ($a = 3.99\,\text{Å}$, $c = 4.04\,\text{Å}$), the Ti^{4+} ion does not remain in the center plane but is off-centered along the c-axis with two stable positions, this generates a spontaneous dipole moment. figure 1.5(b) indicates the two positions exaggerating the lateral dimensions (the ratio of c/a=1.01 in bulk) and displacement of the Ti^{4+} ion for better visualization. A further transition occurs at T_{to} ≤5 °C to orthorhombic and at T_{or} ≤-90 °C to rhombohedral phase. As consequence the BTO lattice parameters change notably at the transition temperatures, see figure 1.5(c). The structural changes also influence the physical properties of BTO; the favored polarization direction changes from $[001]_{PC}$ in tetragonal, over $[110]_{PC}$ in orthorhombic to $[111]_{PC}$ in rhombohedral, and also the dielectric constant show significant variations at the phase transitions as is shown by figure 1.5(c) [30]. Recently, in a work published by Choi et. al. [35] the authors reported enhanced FE properties of BTO by substrate induced strain. This lead to an increase of the remanent polarisation of a BTO thin film up to 50-70 $\mu C/cm^2$, significantly larger than bulk 26 $\mu C/cm^2$ and an increase of the transition temperature of tetragonal to cubic phase transition from 120 °C to nearly 400-540 °C, that may be of great technological relevance.

$BiFeO_3$

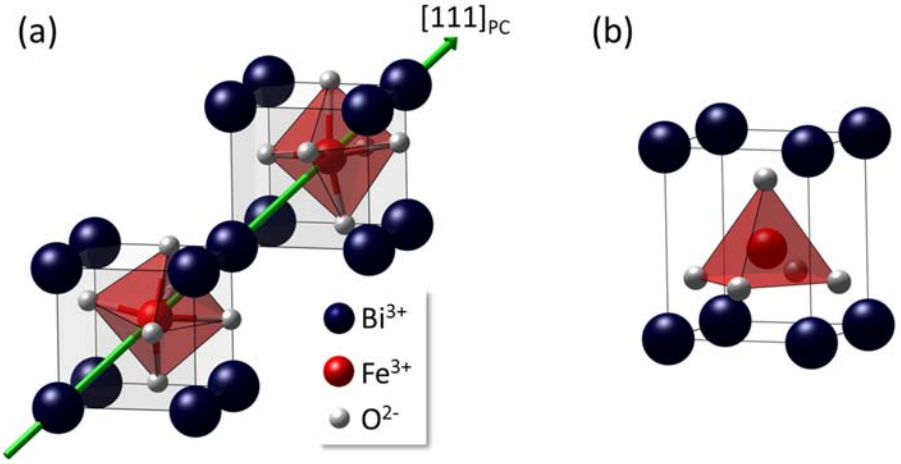

Figure 1.6: (a) Bulk $BiFeO_3$ has rhombohedral structure and can be represented by two pseudocubic cells along the [111] direction. The Fe ions are displaced and the oxygen octahedra are tilted. (b) There is also a metastable, strongly deformed $BiFeO_3$ with nearly tetragonal (P4mm) structure ($c > a$, $c/a \approx 1.2$, and also monoclinic phases with close pseudocubic parameters have been predicted [36]).

One of the few room temperature multiferroics is the ferroelectric/antiferromagnetic $BiFeO_3$. The structure of the bulk stable phase is a distorted perovskite with rhombohedral symmetry ($R3c$, with pseudocubic cell parameter $a_{PC} \approx 3.96$Å, the rhombohedral angle is about 89.4 °). The primitive unit cell (10 atoms) contains 2 formula units as shown in figure 1.6(a) and the spontaneous FE polarization develops along the $[111]_{PC}$ direction (indicated as green arrow). The *Fe-O-Fe* distances and bond angles are relevant for the orbital overlap and strongly influence the exchange coupling determining the magnetic ordering of *BFO*. Bulk *BFO* is ferroelectric with a Curie temperature (T_C) of about $\leq 870\,°$C, and posses a large saturation polarization of $P_S \approx 90..100 \mu\, C/cm^2$ in high quality bulk and thin film samples [37, 38], also moderate piezostrictive constants $d_{33} \approx 50..70\, pm/V$ where measured [38, 39]. The origin of the ferroelectric polarization in *BFO* is related to the *A*-site *Bi*-ions, and originates from lone pairs of the $6s^2$-Bi^{3+} orbitals (similar to $PbTiO_3$). *BFO* has a rich phase diagram [40], multiple phase transitions at high temperature and pressure are observed in bulk. Recently, the stabilization of metastable nearly tetragonal *BFO* phases (figure 1.6(b)) [41–43] by thin film techniques triggered further fundamental research [36, 44, 45]. The reports indicate that the absolute polarization varies only little with strain, but stabilization of different *BFO* phases depending on the substrate strain, can influence strongly the projection of the polarization direction with respect to the out of plane direction [46]. While the electric polarization is originated by the A site ions, the magnetic order is due to magnetic B site Fe^{3+}-ions, with magnetic moments coupled ferromagnetic within the pseudocubic (111) planes and antiferromagnetic between adjacent planes (G-type). Bulk *BFO* is antiferromagnetic with a Néel temperature $T_N \approx 643K$. Canting of the antiferromagnetic sublattices could result in a macroscopic magnetization, weak ferromagnetism, which is intensively studied in recent years.

1.3.2 Spinel oxides

The spinel oxides with common structure formula AB_2O_4, where A and B are typically transition metals, i.e. $MgAl_2O_4$ or $CoFe_2O_4$. The crystal structure is cubic; the unit cell contains 8 formula units (8x AB_2O_4). In figure 1.7(a) four green and four light shaded sub-cubes are shown. Each pair (one green plus one white sub-cube) contains two formula units. A total of 32 oxygen atoms are located in the unit cell, four in each octant. Their distribution can be described by a face-centered sub-lattice. In total 24 cations (8 A^{2+} and 16 B^{3+}) are distributed over the unit cell. See figure 1.7(b) and (c) were the distribution and the corresponding tetrahedral A and octahedral B sites are sketched.[1] Considering the distribution of the cations over the two possible sites, three different spinel types have

[1] Note that in figure 1.7(c) the oxygen polyhedron are allowed to protrude out of the unit cell to facilitate visualization.

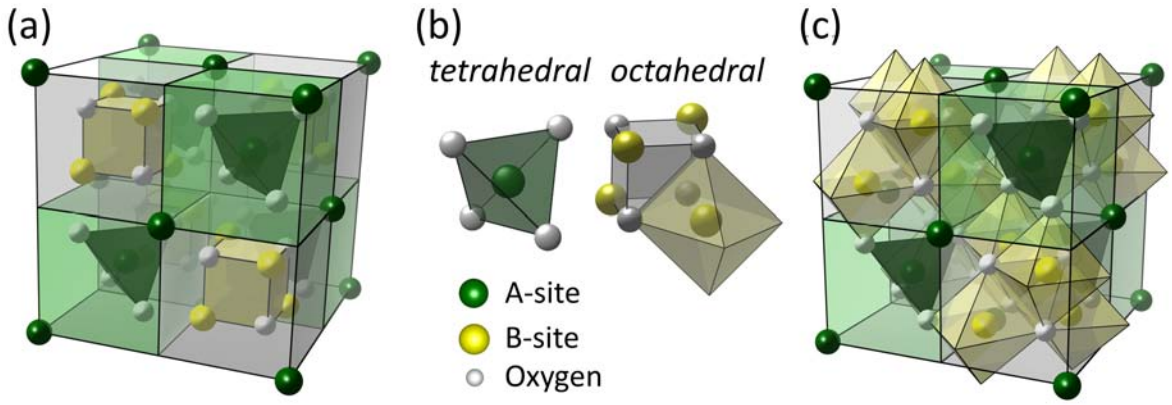

Figure 1.7: Schematic drawing of a spinel structure (a). Blue and light shaded boxes correspond to tetrahedral A-sites and octahedral B-sites, respectively. (b) Labels and close view of A and B sites. (c) Spinel structure with enabled octahedral polyhedrons.

to be distinguished. In the *normal* spinel structure the 8 divalent cations occupy the A-sites and the 16 trivalent cations are found only on the B-sites (e.g. $MgAl_2O_4$). On the other hand, if the 8 divalent ions occupy half of the B-sites and the trivalent ions are distributed equally over half of the B- and over the A-sites, it is called *inverse* spinel structure. In some cases where the inversion is not complete one often refers to *partially inversed* spinels. The spinel structure of $NiFe_2O_4$ is considered *fully inverse* whereas that of $CoFe_2O_4$ is partially inverted. The spinel ferrites have an unit cell larger than 8Å, *i.e.* $CoFe_2O_4$ ($a = 8.39$ Å).

The magnetic coupling between tetrahedral A and octahedral B sublattices is antiparallel. A net magnetic moment results when not all magnetic moments are compensated (twice as much B sites than A sites) [47]. The Curie temperature of *CFO* is with $T_C = 495$ °C well above room temperature, and the large magnetic moment of 377 emu/cm^3 (fully inverse), strong crystalline anisotropy, large magnetostrictive constants ($\lambda_{100} = -470 \cdot 10^{-6}$ $\lambda_{111} = 120 \cdot 10^{-6}$) [47] and high resistance make it a suitable candidate as magnetic phase in room temperature MF composites.

Epitaxial growth of spinels on typical substrates used for thin films (i.e. *STO*, *MgO* or $MgAl_2O_4$) is possible [48], but 2d growth is challenging due to formation of granular surfaces [49]. Lüders et al. have shown that growth of spinels $CoCr_2O_4$ [21] and $NiFe_2O_4$ [50] can be tuned to achieve nanometric (111)-faceted pyramids which are aligned along [110] directions of the (001) *MgO* or $MgAl_2O_4$substrate (figure 1.3(b)). Similar surface morphology is found for $CoFe_2O_4$ on $SrTiO_3$(001) and $MgAl_2O_4$(001) [51, 52]. In spinels the (111) surface energy is by a factor of 4-5 lower than the (100) [53], which favors the formation of (111)-faceted surfaces to minimize total energy in epitaxial thin films. If the substrate is (001) oriented pyramidal islands with (111) facets are the equilibrium

structure, their size and density can be controlled by the deposition conditions [21, 50]. The growth of flat epitaxial (001) thin films is challenging, but is favorable for growth of flat epitaxial thin films on (111) oriented substrates [51, 54]. Nevertheless, for the growth of vertical composite heterostructures, this tendency of 3d growth on (001) substrates may favor the formation of columnar spinel structures.

In this thesis we will show that proper deposition conditions permit fabricating either well shaped vertically composites or flat spinel films for integration in horizontal heterostructures.

CHAPTER 2

Experimental techniques

In this chapter an overview of the experimental techniques for sample preparation and characterization used in this thesis are described.

2.1 Sample preparation

The samples presented in this thesis have been prepared by physical vapor deposition techniques suitable for a wide range of functional oxide materials [1, 26, 55, 56]. Vertical composite heterostructures of $BaTiO_3$-$CoFe_2O_4$ have been grown with radio-frequency-magnetron sputtering located at the ICMAB. While $BiFeO_3$-$CoFe_2O_4$ vertical heterostructures and single phase $BiFeO_3$ were grown by pulsed laser deposition (PLD) setup located at department of Applied Physics and Optics at the University of Barcelona. $CoFe_2O_4$ and $BaTiO_3$ single phase films were grown by PLD at the ICMAB and selected depositions were done with in-situ reflection high energy electron diffraction (RHEED) monitoring.

2.1.1 Target preparation

The targets used in the PLD and sputtering processes have been prepared by solid state reaction, mixing the commercial powders (purity 99.9% or higher), these were thouroghly grinded by hand-mortar to obtain a homogeneous mixture. The powders were sintered in a tubular furnace and the quality of the product was probed by x-ray diffraction. The final powder is compacted into a pellet of $1\,inch$ diameter at a load of $40\,MPa$ and sintered in air. For targets containing volatile elements, like Bi, a lower process temperature (700-900 °C) is used to avoid loss of stoichiometry during the preparation of powder and target. Additionally, the Bi content in our $BiFeO_3$ target is enriched by 10% to prevent

the evaporation of the highly volatile Bi during target preparation For composite targets each constituent is synthesized individually and then the powders are mixed with the corresponding ratio, subsequently pressed and sintered in a pellet of 1 $inch$ for PLD and 1.3 $inch$ for sputter targets. A list of the target used for this thesis are presented in the Table 2.1.

Table 2.1: Prepared ceramic targets during this thesis, all commercial powders used for the synthesis were of 99.9% or better purity.

target	short name	chemicals	composition
$BaTiO_3$	*BTO*	commercial $BaTiO_3$ powder	100 mol% BTO
$BiFeO_3$	*BFO*	Fe_2O_3 and Bi_2O_3	10 mol% Bi-excess
$CoFe_2O_4$	*CFO*	CoO and Fe_2O_3	100 mol% CFO
$BaTiO_3$-$CoFe_2O_4$	*BTO-CFO*	pre-sintered BTO and CFO	65 : 35 mol% BTO:CFO
$BiFeO_3$-$CoFe_2O_4$	*BFO-CFO*	pre-sintered BFO and CFO	65 : 35 mol% BFO:CFO 10 mol% Bi-excess
$La_{2/3}Sr_{1/3}MnO_3$	*LSMO*	$SrCO_3$, La_2O_3 and MnO_2	100 mol% LSMO 66.7 : 33.3 mol% La:Sr ratio
$SrRuO_3$	*SRO*	$SrCO_3$ and RuO_2	100 mol% SRO

2.1.2 Radio-frequency sputtering

In the sputter process a target is bombarded by energetic ions, which cause the expulsion (sputtering) of surface atoms. The ions are generated in a plasma close to the target surface, typically the inert gas argon is used as it is easily ionized, has a considerable mass and is not reactive. A bias voltage accelerates the argon ions on the target and neutral atoms are ejected from its surface, some reach the substrate and nucleate there. To reduce electric charge building up on insulating dielectric targets, the applied potential is modulated by oscillating electric fields in the MHz range (radio frequency (rf) sputtering).

A higher yield is achieved by using magnetron cathodes, they consist of an assembly of strong permanent ring magnets and confine the electrons on a longer path close to the target and thus to increase the efficiency of argon ionization. A simplified scheme is shown in figure 2.1(a) and the actual set-up with picture during an sample deposition is in figure 2.1(b).

The substrate is glued with silver paint to the heater, which can achieve a maximal substrate temperature of around 850 °C. The target to heater distance is set to 6cm. For the deposition a dynamic pressure (0.266 $mbar$) with an argon and oxygen gas mixture (3:1 ratio) are used. Presputtering of 15 min before the actual deposition cleans the target surface and stabilizes the plasma, the thickness of the deposited film is calibrated by the

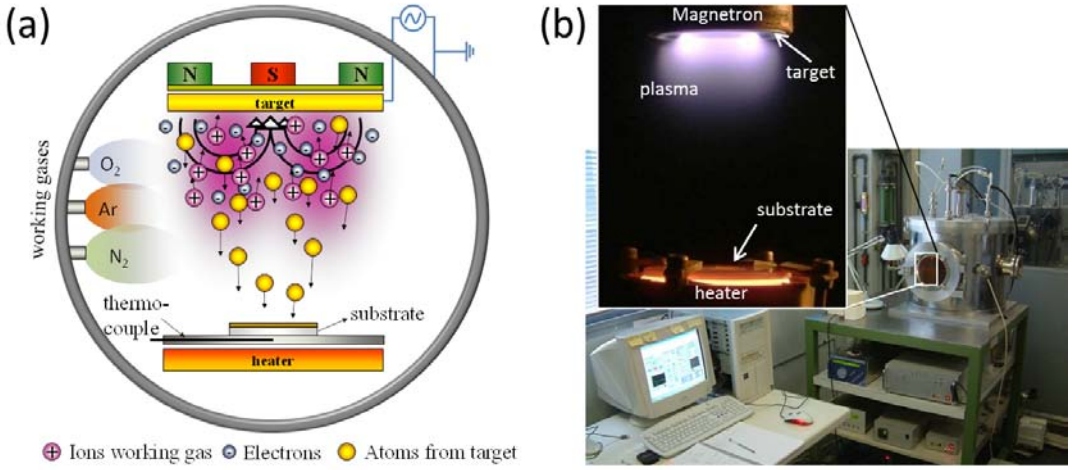

Figure 2.1: Sketches of the (a) radio-frequency magnetron sputter process and (b) the set-up used at ICMAB for the deposition of $BaTiO_3$-$CoFe_2O_4$ composites. The inset shows a photograph during a deposition. Features are labeled correspondingly.

deposition time. The sample is colled ($-5\,°C/min$) in a static oxygen pressure of $450\,mbar$. The samples are removed close to room temperature.

For this thesis we studied the growth and properties of vertical heteroestructures combining FM $CoFe_2O_4$ and $BaTiO_3$ as FE phase on (001) substrates. We have grown series of films investigating the effects of substrate temperature (T_S), growth rate (gr) and thickness (t). A temperature range from 500-850 °C and growth rates from 0.5-2.8 nm/min have been probed (the growth rate was changed by the applied rf-power from 15-45 W).

2.1.3 Pulsed laser deposition

Two pulsed laser deposition (PLD) set-ups were used. One chamber is located at the department of Applied Physics and Optics at the University of Barcelona (PLD-UB) and the second system is at the Institut de Ciència de Materials de Barcelona (PLD-ICMAB), see figure 2.2(c) and 2.2(d) respectively. PLD-UB is top-loaded and each time the sample is changed the deposition chamber is opened. While in the PLD-ICMAB the deposition chambers are accessed via load-locks to insert and remove the samples or targets from the main chamber, which allows to permanently maintain a high vacuum in the main chambers. One chamber is equipped with reflection high energy electron diffraction (RHEED) set-up to monitor the film growth *in-situ*.

A basic PLD set-up is sketched in figure 2.2(a). A KrF excimer laser with wavelength $\lambda = 248\,nm$ and a pulse-width of $34\,ns$ (PLD-UB) and $25\,ns$ (PLD-ICMAB) is focused on a stoichiometric target inside a high vacuum chamber the vaporized target material condenses on a substrate. An example picture of a plasma plume during the ablation of $La_{2/3}Sr_{1/3}MnO_3$ is shown in figure 2.2(b), the target is on the left and the plasma plume

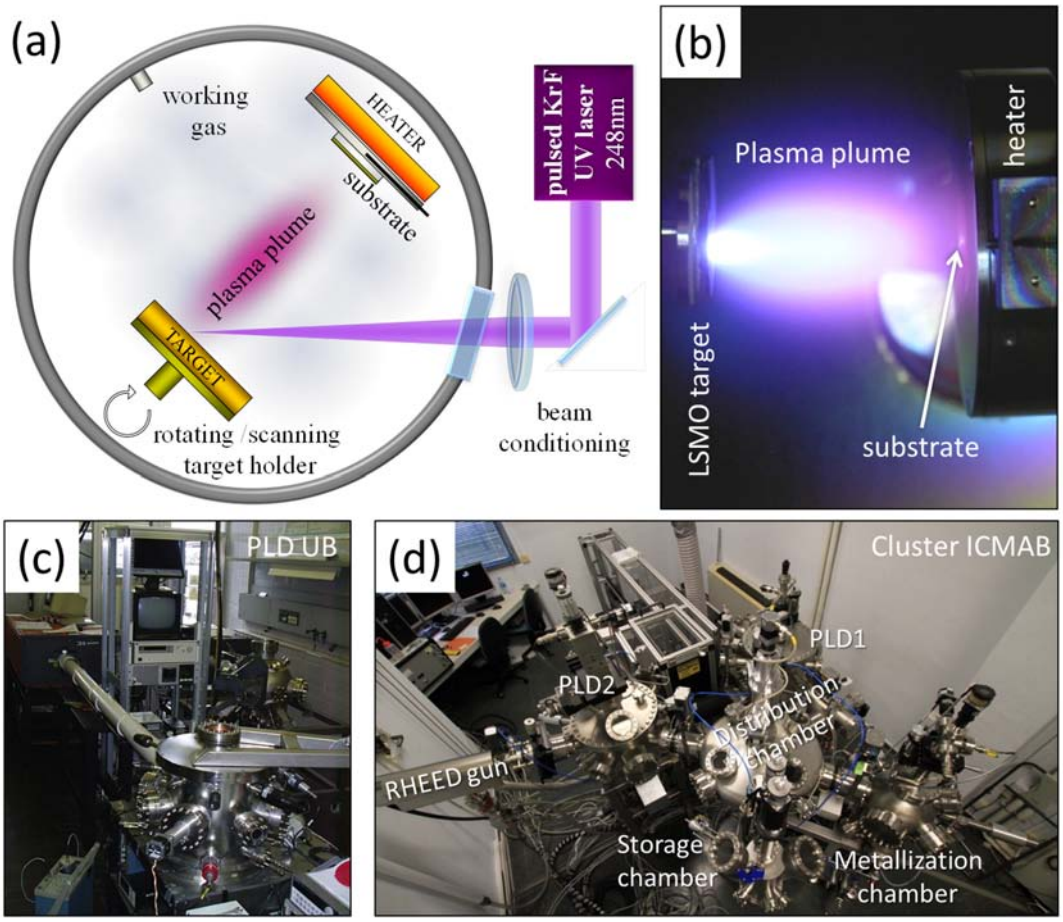

Figure 2.2: General sketch of the components of a (a) PLD set-up. (b) Typical plasma plume generated by the interaction of the laser pulse with the target material. The heater with clued substrate are on the right. Pictures of the PLD set-ups used at UB (c) and ICMAB (d).

propagates towards the substrate mounted on a heater.

The PLD process can be simplistically divided into three steps: *laser-target interaction – plasma plume expansion – thin film growth.* (A) *Laser-target interaction* Intense laser pulses ($\lambda = 248\,nm$) are focused on a ceramic target (area of the laser spot is a few mm^2), which for most materials has very high absorption rate and short optical penetration depth (in the range of a few tens of nm). The thermal diffusion length of oxides is typically low, thus the pulse energy is absorbed by a very small target volume (see sketch in figure 2.3(a)). A very thin surface layer of the target evaporates in a plasma, which expands vertically to the surface. It may contain neutral and ionized atoms and molecules, electrons and even clusters of the target material. (B) *Plasma plume expansion* is very fast and the plume typically reaches the substrate in less than $10\mu s$. Presence of background gas conditions the plasma dynamics. (C) *Thin film growth* occurs as the material in the plume arrives in a few μs on the surface (with a large instantaneous supersaturation). The system has time for nucleation, diffusion and growth processes until the next plasma pulse with $1/f$

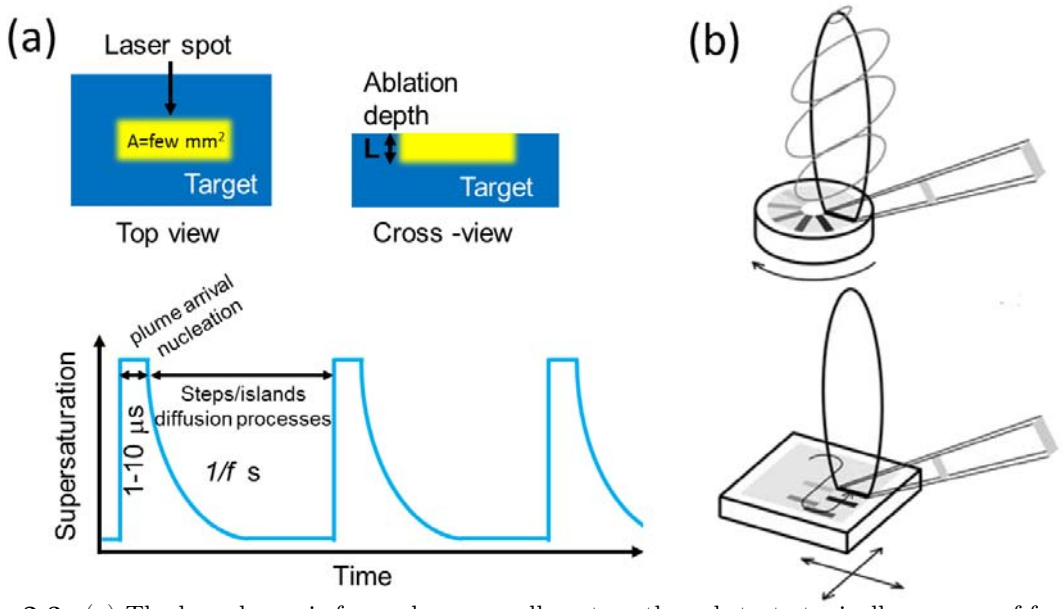

Figure 2.3: (a) The laser beam is focused on a small spot on the substrate typically an area of few mm^2. As the UV light ($248\,nm$) is strongly absorbed and thermal diffusion is slow only a thin layer of the target evaporates. The material in the plume arrives within μs and generates a large supersaturation on the substrate surface, which produces first quick nucleation of small islands and then slower diffusion and rippening processes within the time to the next pulse ($1/f$). (b) In PLD-UB the target is rotated during ablation, while in PLD-ICMAB the surface is scanned laterally as depicted in the sketch (adapted from [57]).

time interval arrives as indicated in figure 2.3(a) bottom panel.

Before the deposition the target surface is polished and dust is removed by dry nitrogen ex-situ. The vacuum chambers are pumped to the base pressure ($\leq 10^{-7}\,mbar$). In the PLD-UB the target is rotated while in the PLD-ICMAB the target is scanned as is illustrated in figure 2.3(b). To achieve same initial condition for all depositions a selected area is pre-ablated. A shutter is placed between substrate and target to avoid deposition on the substrate during pre-ablation. The working gas is oxygen with dynamic oxygen flux during deposition. The used heaters permit a maximal substrate temperature of $850\,°C$.

Reflection high energy electron diffraction

In case of horizontal heterostructures (*BTO* and *CFO* grown in PLD-ICMAB) some samples have been grown with *in-situ* observation by reflection high energy electron diffraction (RHEED), which allows to monitor the growth process *in-situ*. The RHEED set-up consists of an electron source ($30\,keV$) with the electron beam directed close to gracing incidence (0-5°) on the substrate/film surface and a diffraction pattern is observed on a phosphorescent screen. The RHEED system has a differentially pumped electron source [58] that allows to operate with high oxygen pressure as $0.4\,mbar$ in the deposition chamber. The image on the phosphorescent screen, the intensity of selected lines or regions

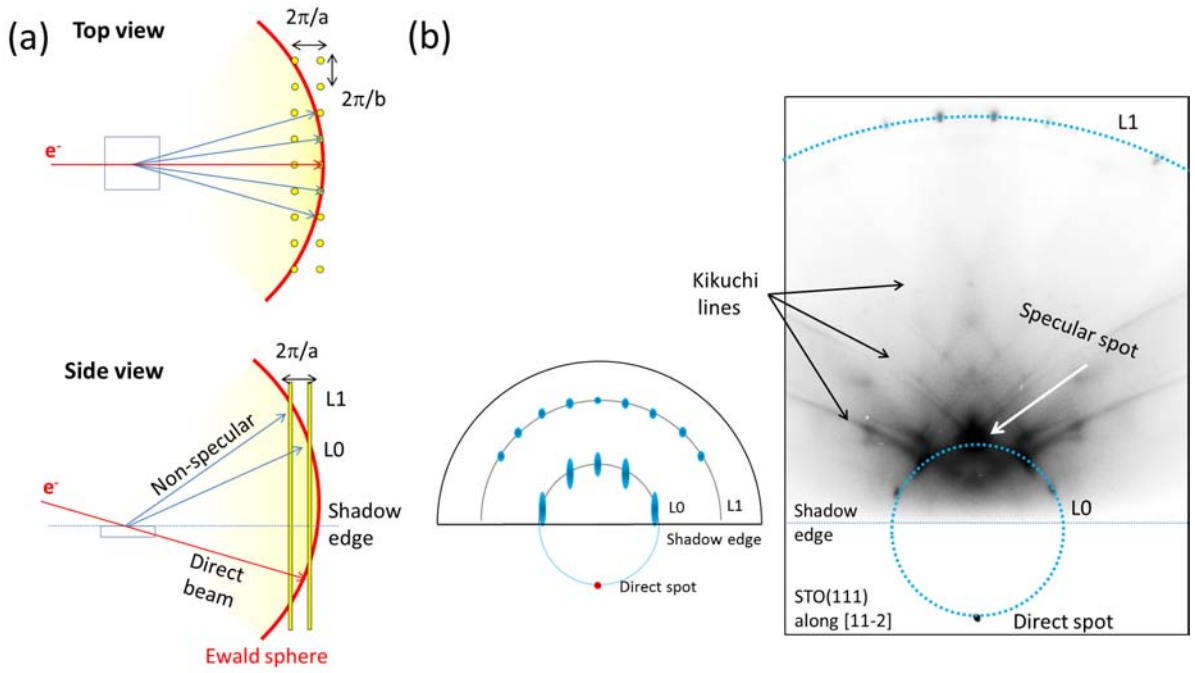

Figure 2.4: Phenomenological description of RHEED diffraction. A 2 dimensional atomic layer in real space transforms into a 2d set of lattice rods infinitely expanded in surface direction. (a) Ewald sphere construction is shown from top and as side view ($L0$ and $L1$ stand for 0^{th} and 1^{st} laue zone). (b) The left drawing illustrates a theoretically derived image on the RHEED screen and below an RHEED image obtained from a $SrTiO_3$(111) single crystal surface.

is digitized by a CCD camera and monitored over the time [59].

The strong interaction of electrons with matter limits the interaction only to the uppermost layers of the crystal, so that a simplistic description considering only the last layer of the film as perfectly 2 dimensional sheet of atoms [60]. This allows a qualitative understanding of the RHEED pattern considering only geometric aspects and under the condition of only elastic scattering of the electrons occurs (at $30\,keV$ the wavelength is $\lambda \approx 0.17\,\text{Å}$). The 2d sheet of surface atoms corresponds in reciprocal space to an arrangement of lattice rods in the direction normal to the surface, a schematic drawing is shown in figure 2.4(a) (for a complete description of RHEED see reference [61]). Similar to XRD the intersection of the rods with the Ewald's sphere fulfill the diffraction condition and lead to diffraction spots positioned on an arc, also named Laue zones. A schematic drawing of the observed pattern is in figure 2.4(b), an experimental image from a $SrTiO_3$(111) single crystal surface is shown next to it. In the experimental image a feature called Kikuchi-lines can be observed, and originate from inelastically scattered electrons diffracted by a set of lattice planes.

Usually the surfaces are not perfect and irregularities transform the ideal spots into streaks as the reciprocal rods broaden and thus the intersection with the Ewald sphere is increased [62]. The streaks can transform gradually to 3d spot pattern if the film roughness

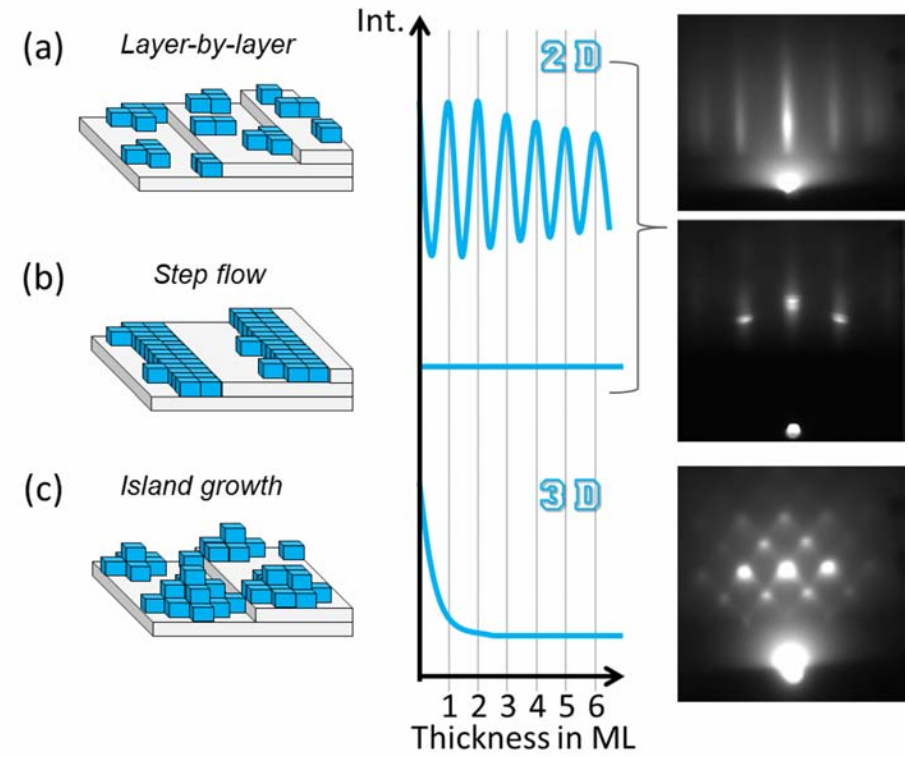

Figure 2.5: Three growth modes are commonly observed. (a) *layer by layer growth mode* a 2d growth mode were the new film layer is completed before the growth of the next. The RHEED intensity is oscillating; it is highest for low step density (fully terminated layer) and lowest for high step density (half filled layer). (b) In *step flow growth mode* the adsorbed atoms diffuse to the terrace step edge before 2d islands can nucleate on the terraces. The average RHEED intensity remains constant. (c) In *island growth modes* multilayered islands form 3d surfaces. The RHEED intensity can drop or increase in function of the evolving pattern, no oscillations are observed.

is increases furthermore (see some examples in the right panel of figure 2.5).

The intensity of the specular spot, which corresponds to the directly reflected beam, is very sensitive to the steps density on the surface. Steps originate at the edge of terraces, edges of 2d islands or holes, thus a perfect crystalline surface has a very low steps density and is considered to be close to an ideal 2d surface.

Consequently, the observation of the RHEED intensity can give hints on the growth mechanism and the roughness of the growing film. For ultra-flat films, ideally *layer by layer* or *step flow* growth mode are desired. In *layer by layer* or *Frank-van der Merve* growth mode the adatoms nucleate on the terrace surface where in the ideal case no new layer (multilevel islands) forms until the remaining 2d holes in the growing layer are filled.The RHEED intensity decreases until half layer is filled (highest step density), then consecutively the holes are filled until the new layer is complete and thus the RHEED intensity increases to its initial height. These oscillation (see figure 2.5(a)) allows to count *in-situ* the number of layers and terminate the growth process on a fully terminated layer. Despite a *perfect* layer by layer growth does not exist and a new layer starts to grow before

the previous is fully terminated, persistent oscillation can sometimes be observed over a large number of monolayers.

In case of high surface diffusivity and low flux, adsorbed atoms can diffuse a long distance and tend to reach a terrace step, *step flow* growth mode. As the surface does not change remarkably the average RHEED intensity remains constant during growth, see a simplified scheme in figure 2.5(b). Nevertheless, in real observations (not shown here) after each laser pulse a small intensity decrease followed by full recovery of the intensity is observed, reflecting the evolution of the step density. Even if this growth mode results in high quality surfaces it is not suitable to count the amount of MLs grown and thickness has to be calibrated ex-situ. The interruption of the growth process for a few minutes can allow the system to recover a more ordered state, due to coalescence or migration of islands to the edges, reduction of multilayered islands due to interlayer diffusion, and consequently reducing steps, kinks and ledges [63].

If the strength of the interaction between adatoms is larger than to the surface atoms, directly 3d islands form. Further growth of this 3d clusters in combination with coarsening will results in rough 3d surfaces. This growth mode is called *island* or *Volmer-Weber* growth mode. In some cases a few ML grows perfectly 2d and at a critical thickness a transition 3d growth mode takes place, this is called *layer plus island* or *Stranski-Krastanov* growth mode. The resulting RHEED pattern is a transmission pattern as shown in figure 2.5(c). The intensity of an selected initial diffraction spot can decrease or increase as function of the overall evolution of the diffraction pattern, no oscillations are be observed.

2.2 Sample characterization

2.2.1 Atomic force microscopy

Atomic Force Microscopy (AFM) has been used to obtain information about the surface morphology of composite and single phase thin films, a simplified scheme is shown in figure 2.6. A silicon cantilever with a nanometer sharp tip is used to sense the interaction between the surface and the tip, while it is scanned over the sample surface. Bending of the cantilever is sensed by a laser beam deflected on a 4-quadrant photodiode. The surface morpholgy can be investigated by means of contact or non-contact methods. In *contact* mode the tip of the cantilever stays in contact with the surface while rastering over the surface and the change in local sample height (z) is recorded. Generally we used *non-contact* tapping mode for the observation, the tip is oscillating at resonance frequency and barely touches the surface. A high vertical resolution of 1Å and lateral resolution in the nanometer range can be achieved. The lateral resolution (typically around 10-20 nm)

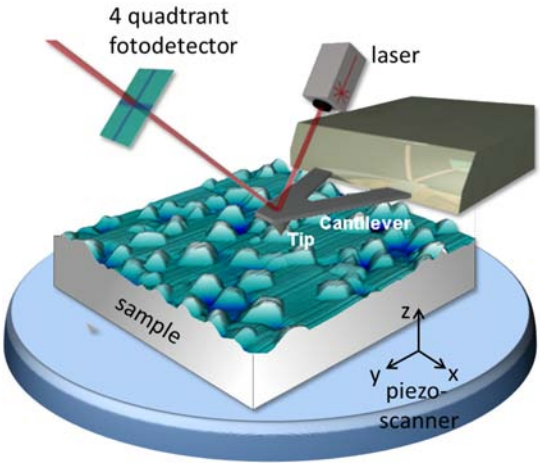

Figure 2.6: Illustration of a typical AFM set-up with the main components: the sample is placed on sample stage, which is rastered below the cantilever tip, where a laser beam is reflected on a 4-quadrant detector.

is limited by the tip size and shape, tip convolution takes place if the observed objects are of similar dimension. The measurements were performed with the microscopes located at the technical service at ICMAB handled by the technical staff.

Magnetic force microscopy (MFM) allows mapping of magnetic domains. First the morphology is acquired, then in a second scan the tip is lifted up a view tens of nm and the forces between magnetic tip and magnetic domains of the film are measured. Also, electric fields can be generated locally by using conducting tips and by rastering the tip over the surface (in contact mode) the FE phase can be polarized and the domains visualized. Zavaliche et al. [64] showed electro-magnetic coupling at the nanoscale of FE/FM nanocoposites by mapping the very same sample region in MFM mode before and after electric poling of the FE phase.

Further studies combining piezo-response force microscopy (PFM) in combination with MFM have been performed by collaborators at the University of Geneva.

2.2.2 Scanning electron microscopy

Scanning electron microscopy (SEM) has been used for the analysis of the composite topology (Fei Quanta 200EF located at ICMAB). A focused electron beam is scanned over the area of interest, see simplified sketch of the components of a SEM in figure 2.7(a). The electrons are generated by a cold-cathode field emission gun and the kinetic energy can be varied from 0.5-30 keV. Electrons have a strong interaction with the sample material and can reveal additional information beside the topography (see scheme in figure 2.7(b)). They can be *a*) *scattered elastically* maintaining the beam energy and some of them have scatter angles close to 180 degree, *back-scattered* electrons, and can be detected close to the surface normal of the sample. The scattering coefficient is strongly related to the atomic number of the specimen, regions of the sample containing elements with higher atomic number appear

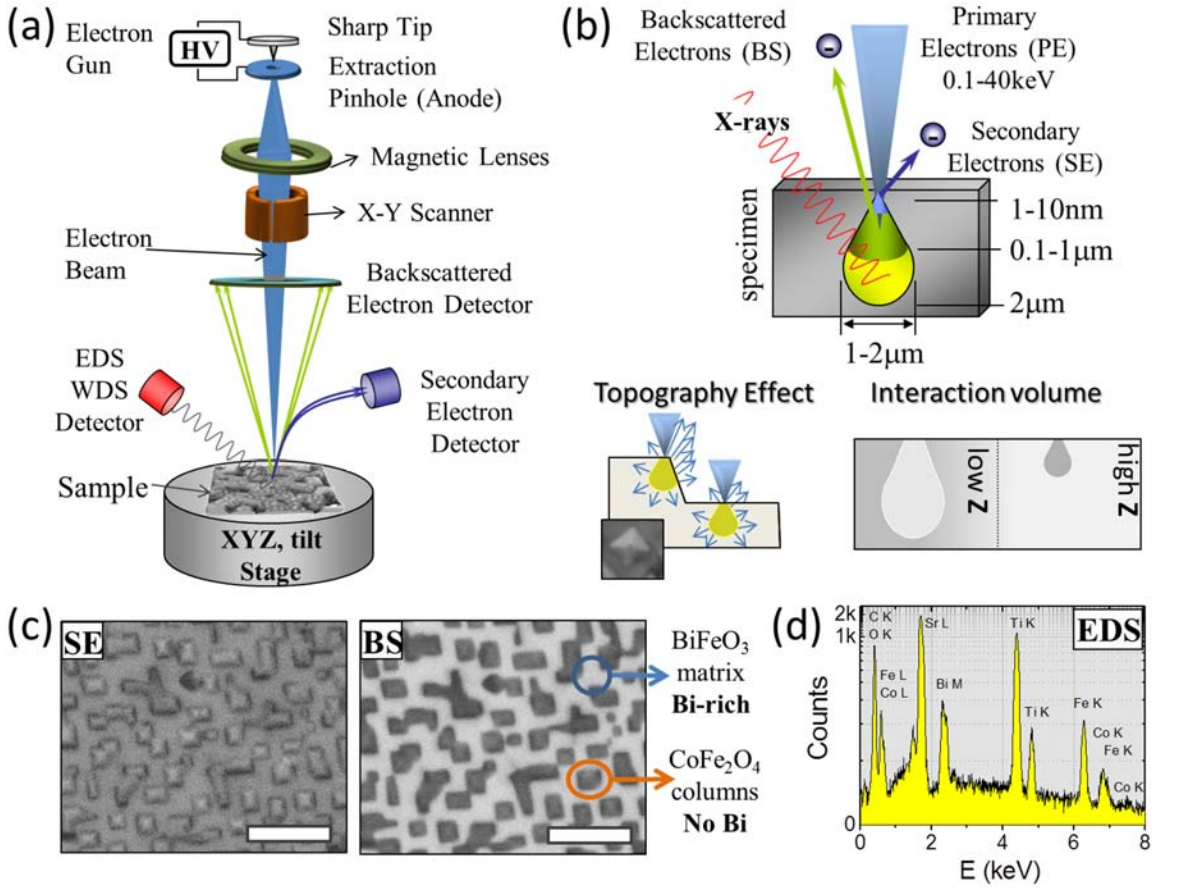

Figure 2.7: (a) Schematic drawing of the main components of a SEM microscope. (b) Interaction of the electron beam with the material. Two sketches below indicate the effect of topography on electron yield (corners have ha higher yield than flat regions or holes) and variation of the interaction volume due to atomic number (Z). (c) Example images of a $BiFeO_3$-$CoFe_2O_4$ film with matrix-column structure taken at $20\,keV$, secondary electrons image (SE) and backscattered electrons image (BS). Brighter regions in the BS image correspond to Bi-rich zones ($BiFeO_3$-matrix) where Bi has a much larger atomic number Z_{Bi}=83 compared to *CFO* columns with Fe and Co ($Z_{Fe} = 26$, $Z_{Co} = 27$). (d) Typical energy dispersive spectra (EDS) of the film. The transitions causing the peaks are marked. Highest intensity peaks Sr and Ti correspond to the substrate; Co, Fe and Bi to the film.

brighter than zones with lighter elements. For example the $CoFe_2O_4$ fraction contains relatively light elements ($Z_{Fe} = 26$, $Z_{Co} = 27$) while $BiFeO_3$ contains heavy Bi (Z_{Bi}=83). This measure mode allows obtaining a chemical map and thus the phase separation of the nanocomposite. While *b*) *inelastic scattering* causes the emission of *secondary* electrons (SE) with low energy. Only electrons created close to the surface (5-10 nm) have sufficient energy to leave the sample. Variations in the topography like edges, grains or small particles on the surface have influence on the yield of the secondary electrons and contribute to the contrast of the image (see inset in figure 2.7(b)). Furthermore, *c*) *inelastic scattering* can cause radiation like Bremmstrahlung and characteristic X-ray radiation. With the latter element specific electronic transitions can be analyzed and quantified using either energy or wavelength dispersive spectroscopy, EDS or WDS respectively. EDS has moderate

acquisition times and an energy resolution of about $130\,eV$. Overlapping peaks from elements with similar atomic number (i.e. Fe $Z_{Fe} = 26$ and Co $Z_{Co} = 27$, see a sample EDS spectrum of a 100nm thick *BFO-CFO* nanocomposite film) and huge peaks from substrate elements can hinder the quantification of the film composition. WDS has a much higher energy resolution about $5\,eV$, but the wavelength analysis is very time consuming. The quantitative analysis is performed by normalization to standard samples for all elements present in the sample.

2.2.3 Transmission electron microscopy

The micro-structure of $BiFeO_3$-$CoFe_2O_4$ vertical composite films was investigated by transmission electron microscopy (TEM). The manipulation of the microscopes was done by Dr. B. Warot-Fonrose at CEMES (Toulouse) using a FEI Tecnai F10 field emission microscope with aberration correction and by J.M. Reblet using a Jeol J2010 field emission microscope at the Universitat de Barcelona. TEM was operated with high electron energies ($300\,keV$). The electron beam is focused by electromagnetic lenses through a thin, electron-transparent, sample specimen (typically with a thickness of less than hundred nanometers) and an image is captured by a CCD camera. The extremely short electron wavelength allows a high local resolutions below 2Å. High resolution TEM (HRTEM) images can be achieved with an additional set of aberration correcting lenses.

While the electrons pass through the sample the interaction may cause some energy loss due to inelastic scattering processes. The primary electrons beam has a very well-defined energy and allows the analysis of the energy loss of the electrons, termed electron energy loss spectroscopy (EELS). It can be used to measure the chemical composition with a lateral resolution of around $2\,nm$ and chemical mapping of larger sample regions. The fine structure of the spectra may provide further information on the chemical bonding (*i.e.* different oxygen environment around an iron oxide has strong influence on the shape of the K-edge [65]).

The samples in cross-section geometry were prepared by cutting the substrate in the corresponding direction (close to the [110] zone axis), two crystals are glued by epoxy face-to-face and then the specimen was mechanically thinned from both sample sides down to a thickness of approximately 20-30 μm. The sample center was further thinned by ion milling to achieve an ultra thin electron transparent region.

2.2.4 X-ray diffraction

X-ray diffraction (XRD) is sued to measure lattice spacings, texture and epitaxial relationships [66, 67] by angular analysis of scattered X-ray intensity.

In a 4-circle diffractometer, four angles are used to explore the position of the samples diffraction spots. The equatorial plane of the diffractometer is fixed and contains two angles defining the direction of the incident ω (omega) and diffracted beam θ (theta) with respect to the sample surface. The rotation of the sample around its surface normal corresponds to φ, while ψ is the tilt of the sample plane normal to the $\omega/2\theta$ plane.

A crystal lattice consists of a very regular 3d distribution of atoms in repetitive units (the unit cell). Parallel planes are separated by a distance d. Each atom works as a scatterer of the incoming X-rays and interference takes place. Due to the very high number of scatterers, constructive interference is only observable in very specific directions. *Bragg's law* describes this phenomena for two adjacent planes: $2d_{hkl} \cdot sin\theta = n \cdot \lambda$, where d_{hkl} are the inter-plane distance of the atomic lattice with the Miller index hkl, θ is the incident angle with respect to the sample plane, λ is the wavelength of the incoming radiation, and n is the diffraction order. In a 3d crystal each family of lattice planes can be described by a reciprocal lattice vector $\mathbf{G}^*_{hkl}$ which is perpendicular to the family of lattice planes: $\mathbf{G}^*_{hkl} = h\mathbf{a}^* + k\mathbf{b}^* + l\mathbf{c}^*$ and $|\mathbf{G}^*_{hkl}| = 1/d_{hkl}$, where $\mathbf{a}^*$, $\mathbf{b}^*$, $\mathbf{c}^*$ are the reciprocal lattice basis vectors. The difference between the wavevector of the incident beam $\mathbf{k}_i$ and the diffracted beam $\mathbf{k}_d$ (both with magnitude $1/\lambda$) defines the scattering vector $\mathbf{\Delta k} = \mathbf{k}_d - \mathbf{k}_i$, in case $\mathbf{\Delta k}$ equals $\mathbf{G}^*_{hkl}$ constructive interference occurs.

In figure 2.8(a) the observable region (radius $2/\lambda$) in reciprocal space is sketched for a cubic sample along the [100]/[001] plane with center (000) being the origin of the limiting sphere. The points labeled with hkl present the reciprocal lattice points contained in the selected crystalographic plane. Using Ewald's construction one can geometrically visualize experimental conditions for diffraction experiments. The incident wavevector $\mathbf{k}_i$ (with $|\mathbf{k}_i|$=$1/\lambda$) finishes at the (000) origin and the incident angle ω, if one draws a sphere (red dotted circle in figure 2.8(a)) in reciprocal space with radius $1/\lambda$ (length of $\mathbf{k}_i$) around its origin one may find lattice points laying on the circumference, here (103). As in this case $\mathbf{\Delta k} = \mathbf{k}_d - \mathbf{k}_i = \mathbf{G}^*_{hkl}$ the condition for constructive interference is fulfilled. The angle between the wavevectors corresponds to the detector angle $2/\theta$. Two gray regions are in practice not accessible thus one incident or exit beam are below the surface.

To characterize epitaxial thin films texture, epitaxial relationship and lattice parameters different measure modi are available:
$\omega/2\theta$***-scan***: A *symmetric* $\omega - 2\theta$-scan is a direct measure of the spacing of d_{hkl} planes parallel to the surface (see figure 2.8(b)). It thus corresponds to a scan along the $(00l)$ family of planes in figure 2.8(a).
ω***-scan***: also called *rocking curve*, the ω angle is varied while the detector position is fixed to a Bragg reflection. The width of the obtained curve is a signature of the miss-orientation of the planes with respect to the normal of the plane. Typically the full width at half

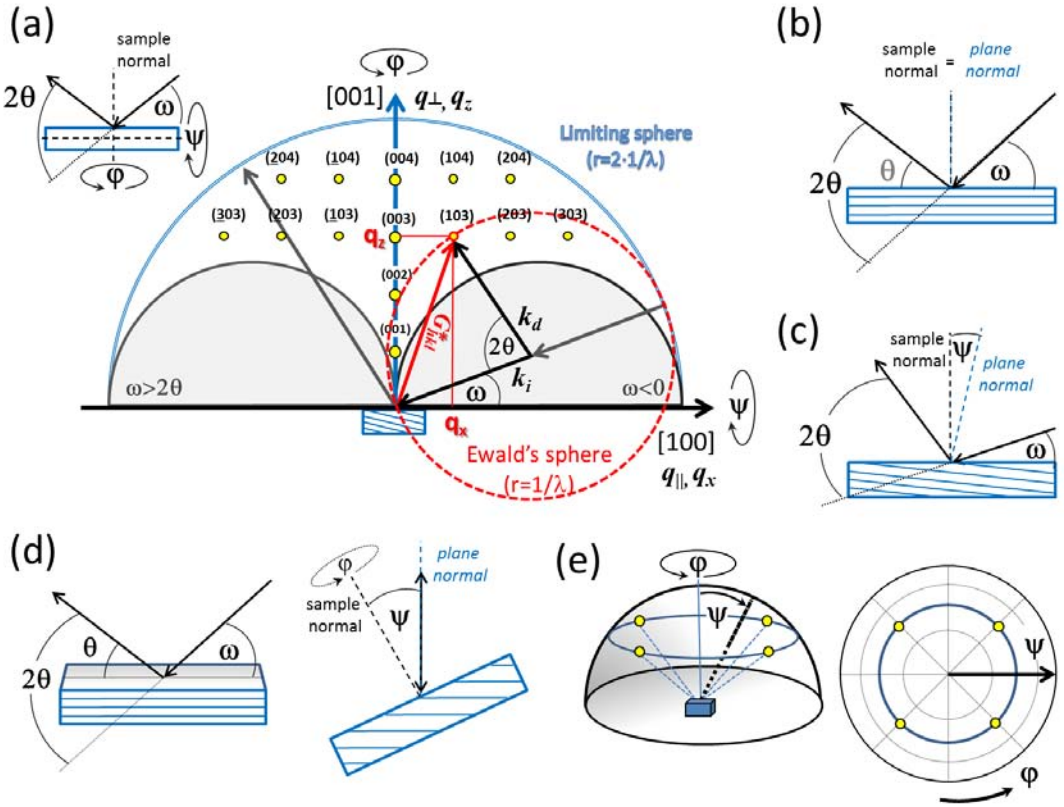

Figure 2.8: (a) Accessible reciprocal space for a cubic crystal, for the sample mounted with the [100] axis parallel to the plane of diffraction (ψ=0° and φ=0°). Construction of the Ewald's sphere being the (103) plane in diffraction condition. The inset on the upper left show the possible roations of the sample to rotate the sample with respect to the laboratory system. Sketches of geometry for (b) *symmetric* scan ω=θ, ψ=0°; for (c) *asymmetric* scan $\omega \neq \theta$, ψ=0°; and for (d) φ scans, the sample is tilted and (hkl) reflection is a symmetric scan ω=θ, $\psi \neq 0°$. (e) Sphere of the *pole figure* defined by spherical coordinates φ and ψ and projection of the pole sphere. If a single ψ value is selected, then the blue line corresponds to a φ-scan.

maxim (FWHM) is used for comparison ($\text{FWHM}_{substrate} \approx 0.005° << \text{FWHM}_{film}$).

Area scans - Reciprocal space maps: A region around symmetric and asymmetric reflections is measured by acquiring a series of $\omega/2\theta$-scans each off-set by $\Delta\omega$. Lattice plane can be accessed by a setting ω, 2θ and φ adequately. Asymmetric Bragg reflections can be accessed by $\omega = 2\theta - \psi$, where ψ is the plane tilt in direction of the diffraction plane ((c)). These area scans can be transformed to reciprocal space maps (RSM), and in- and out-of-plane parameters can be deduced for film and substrate reflections: $q_\parallel = |\mathbf{G^*_{hkl}}| \cdot sin(\theta - \omega)$ and $q_\perp = |\mathbf{G^*_{hkl}}| \cdot cos(\theta - \omega)$.

φ-scan: A specific family of $\{hkl\}$-planes is selected, by setting a symmetric $\omega/2\theta$ and a sample tilt ψ is perpendicular to plane of incidence (see figure 2.8(d)), and the sample is rotated around φ. Plotted intensity *vs.* φ angle for film and substrate is used to determined the epitaxial relationship. ***Pole figure***: The φ-scans are measured at different tilt angles $0\,° \leq \psi \leq 90\,°$ (for time optimization often only a specific region is measured).

A graphical representation is sketched in figure 2.8(e).

In the ICMAB XRD ω and $\omega - 2\theta$ scans were carried out, in 2-circle Bragg-Brentano diffractometers: Rigaku Rotaflex RU-200B and Siemens D5000 with point detectors. The in-plane texture and reciprocal space maps were measured by a Bruker D8 Advance 4-circle diffractometer with 2d detector. The instruments are located at the ICMAB, being the measurements performed by the staff of the XRD scientific service.

2.2.5 Magnetic characterization

The magnetization (M) of the samples was measured at ICMAB with a Quantum Design MPMS 7XL - SQUID magnetometer (MPMS - Magnetic Property Measurement System; SQUID - Superconducting QUantum Interference Device). The samples weremeasured at the low temperature and magnetometry scientific service at ICMAB. A maximal magnetic field $\mu_0 H$ of $7\,T$ was applied. The temperature during the measurements can be set from $2\,K$ to $400\,K$, anyhow if not noted differently the samples were measured at room temperature. Its sensibility allows to detect field changes down to $10^{-14}\,T$. Rests of silver paint from the deposition process is removes previous to the measurement and the negative slope caused by the diamagnetic substrates is subtracted from the M-H loop by fitting a linear slope for $\mu_0 H \geq 3.5\,T$.

2.2.6 Electric characterization

The electric characterization of some of the film prepared in this thesis has been performed in the framework of the PhD thesis of I. Fina. The obtained results will be mentioned only very briefly. For this purpose films have been deposited on $SrTiO_3$ substrate doped with 0.5% Nb films or on thin electrodes of $La_{2/3}Sr_{1/3}MnO_3$ or $SrRuO_3$. Platinum top electrodes ($A = 0.18mm^2$, $t = 200nm$) were deposited by I. Fina using a shadow mask. Two top electrodes were contacted with tungsten needles (top to top electrode method) thus the measurement consists of two thin film capacitors connected in series through the bottom electrode. To probe the ferroelectricity at room temperature an AixAcct TF2000 Analyzer was used to measure the polarization of the films.

To obtain an accurate measure of the spontaneous polarization; the following methods have been used: dynamic hysteresis mode (DHM), the dielectric leakage current compensation (DLCC) and positive up negative down (PUND). A thorough description of the methodology and results can be found in Ref. [68].

PART II
Results

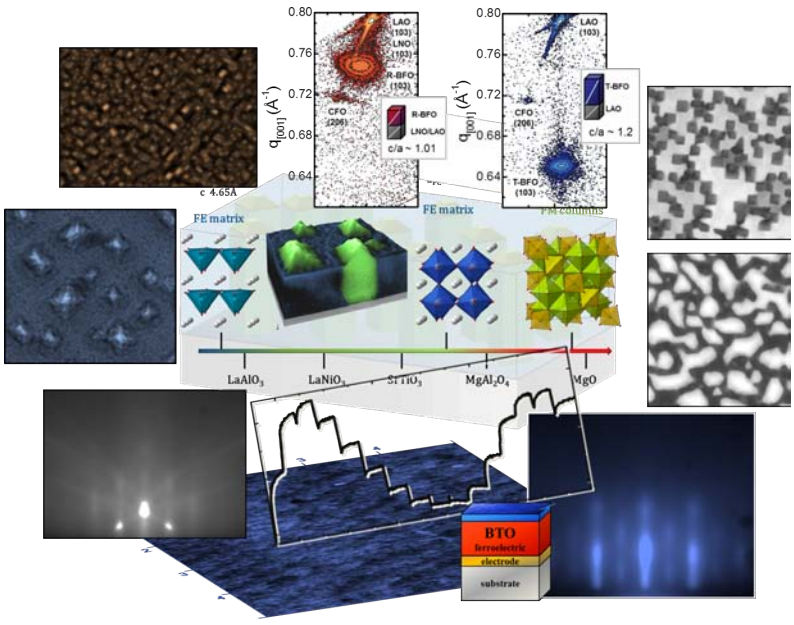

CHAPTER 3

$BaTiO_3$–$CoFe_2O_4$ horizontal heterostructures

Horizontal heterostructures are *a priori* a simple way to combine a FE and FM materials [69], and tuning the volume ratio of FE and FM material can be chosen by the layer thicknesses [69]. However, the growth of high-quality horizontal heterostructures combining perovskites and spinels has been elusive due to a strong tendency of 3d growth [70–75], caused by the structural dissimilarity, large lattice mismatch (typically 5..8%) and unfavorable surface energy anisotropy in the spinels ($CoFe_2O_4$, $NiFe_2O_4$, $CoCr_2O_4$) [21, 53]. The surface energy of spinel (001) planes is very high compared with the lowest energy surface (111) planes. Thus growth of flat CFO(001) is challenging because it tends to form (111)-faceted islands [21, 51].

We will show here that in spite of such structural dissimilarities high-quality heterostructures can be formed with the perovskite BTO as FE material and the spinel CFO as FM layer. First, we will detail the growth of single films of CFO and BTO. Then, the integration of BTO and CFO in bilayered biferroic heterostructures, which are grown on epitaxial metallic perovskite oxide electrodes, $SrRuO_3$ (SRO) or $La_{2/3}Sr_{1/3}MnO_3$ (LSMO) with atomically flat surfaces (see references [20, 63, 76]). Ultra flat surfaces are found for both stacking orders (CFO on BTO [BTO-bottom] and BTO on CFO [BTO-top]). We studied the effect of the strain state of the functional layers (FE, FM) in dependenceof thestacking order, as well as, on their physical properties.The CFO layer is found to be relaxed independently of its position in the stack, while the strain state of the BTO layer is very sensitive to the stacking order. The out of plane polarization of the BTO is affected accordingly, whereas P is bulk like in $substrate/CFO/BTO$, and is strongly enhanced to about $50\mu C/cm^2$ in the inverse $substrate/BTO/CFO$ structure.

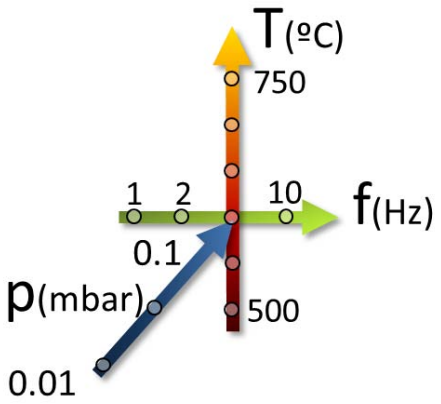

Figure 3.1: Schematic overview of the deposition conditions that have been varied for the $CoFe_2O_4$ film growth.

3.1 Optimization of $CoFe_2O_4$ growth conditions

Thin films with cubic spinel structure (typical lattice constants for spinel oxides are around 8.3-8.4Å) were prepared on large variety of substrates and buffer layers [49, 77, 78]. Flat, epitaxial (001)-oriented *CFO* films (a=8.392 Å) grow on substrates with similar lattice constants and consequently low misfmatch like the rocksalt *MgO* (a_{MgO}=4.21 Å $\approx a_{CFO}/2$, $f = -0.3\%$) or the spinel $MgAl_2O_4$ (*MAO*, a_{MAO}=8.08 Å, $f = 3.8\%$) are suitable. Nevertheless, *CFO* has a larger mismatch $F \approx$ 5-8 % with perovskite substrates or thin films ($a \approx$ 3.85 to 4Å). The large mismatch and the surface energy anisotropy of spinels results in a tendency to form rough surfaces [21, 50, 51], and can favor polycrystallinity - in particular (111) oriented grains [79]. Ma *et al.* [80] grew very flat *CFO* films by PLD on isostructural $MAO(001)$ substrates using growth temperatures as low as 250 °C and low oxygen/ozone pressure of 0.01 $mbar$. The structural quality is improved significantly for T_S higher then 400 °C , nevertheless at 690 °C 3d-like growth is appreciated. The work concentrates on *MAO* substrates, no structural or morphological details are given for films grown on *STO* at higher T_S.

Our strategy is to explore growth conditions minimizing the thermodynamic driving force, which favors 3d growth. Kinetic limitations may be imposed by an increased growth rate or a decreased deposition temperature, while at the same time degradation of the crystallinity is avoided[81]. In figure 3.1 a schematic overview of the probed parameters on the growth of *CFO* ($t = 45\,nm$) on bare $STO(001)$ substrates is shown. We explored the temperature range from 500 to 750 °C at 0.1 $mbar$ and 5 Hz, then at T_S of 600 °C the pulse rate was varied from 1 to 10 Hz (0.1 $mbar$), as well as, the oxygen background pressure from 0.01 to 0.1 $mbar$ at 5 Hz (see graphic overview in figure 3.1).

In figure 3.2(a)-(c) XRD $\omega/2\theta$-scans are shown, all films are (001) textured for the whole temperature range (500 to 750 °C, 5 Hz and 0.1 $mbar$), nevertheless at temperature above 700 °C an increasing intensity of (111) reflections is observed. The position of

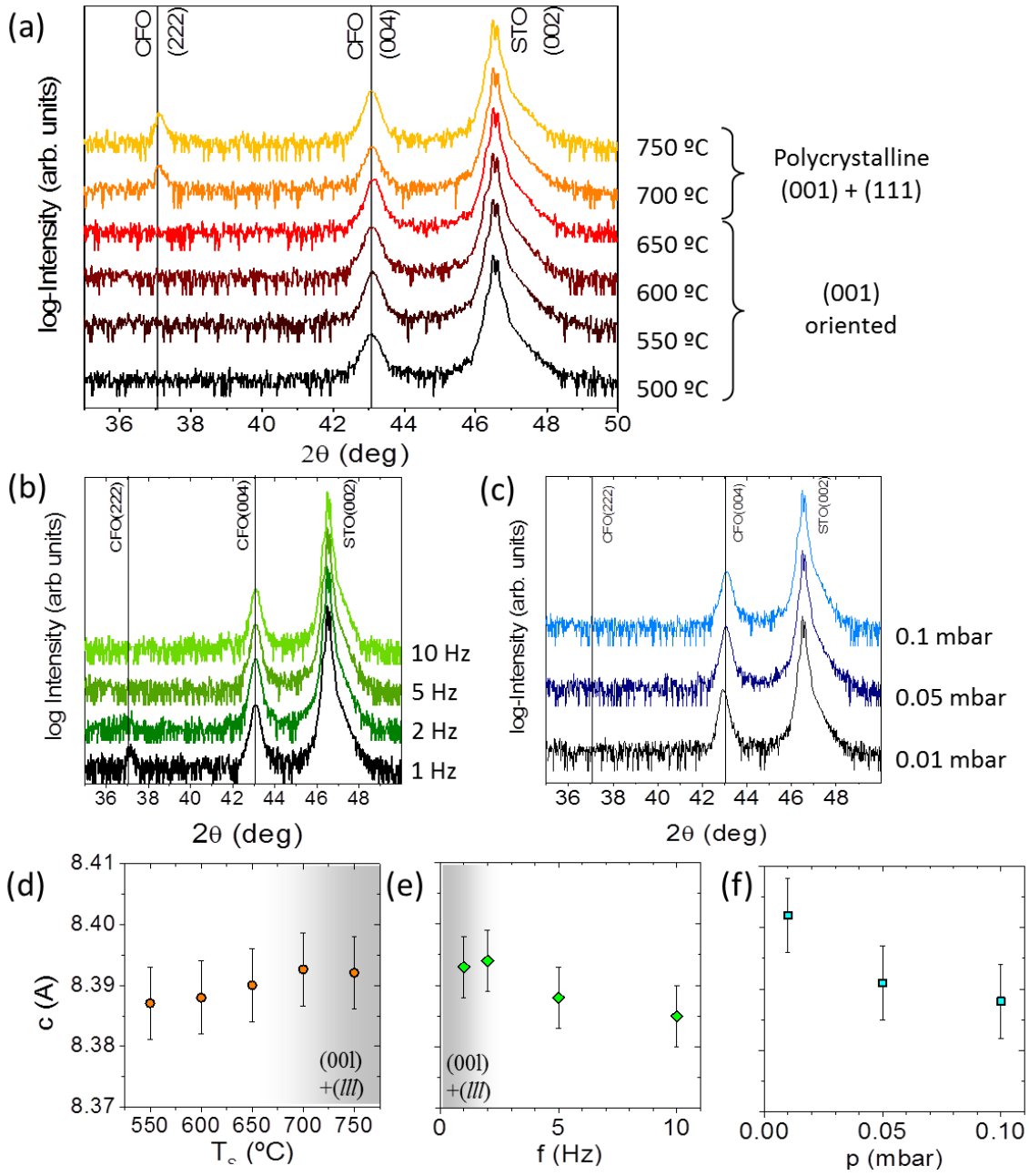

Figure 3.2: XRD $\omega/2\theta$ scans of *CFO* films on *STO*(001) prepared at different conditions of (a) growth temperature T_S=500-750 °C (5 Hz, 0.1 $mbar$), (b) laser frequency f=1-10 Hz (600 °C, 0.1 $mbar$) and (c) oxygen pressure p=0.01-0.1 $mbar$ (600 °C, 5 Hz). The corresponding out-of-plane lattice parameter as function of T_S, f and p are plotted in (d)-(f), respectively.

the (004) *CFO* peaks, close to its bulk value ($2\theta = 43.06\,°$), indicates that the films grow relaxed. Use of low laser repetition rate 1 Hz (T_S= 600 °C and 0.1 $mbar$) possibly favors the formation of (111) oriented grains, thus a small (lll) diffraction peak is visible in figure 3.2(b). The influence of the oxygen pressure is more evidenced at low pressure $p = 0.01\,mbar$, where the *CFO*(004) peak shifts to lower 2θ angles indicating an expanded cell in out-of-plane direction. The evolution with T_S, f and p of the out of plane cell

parameter, all close to bulk *CFO*, is shown in figure 3.2(d)-(f), respectively.

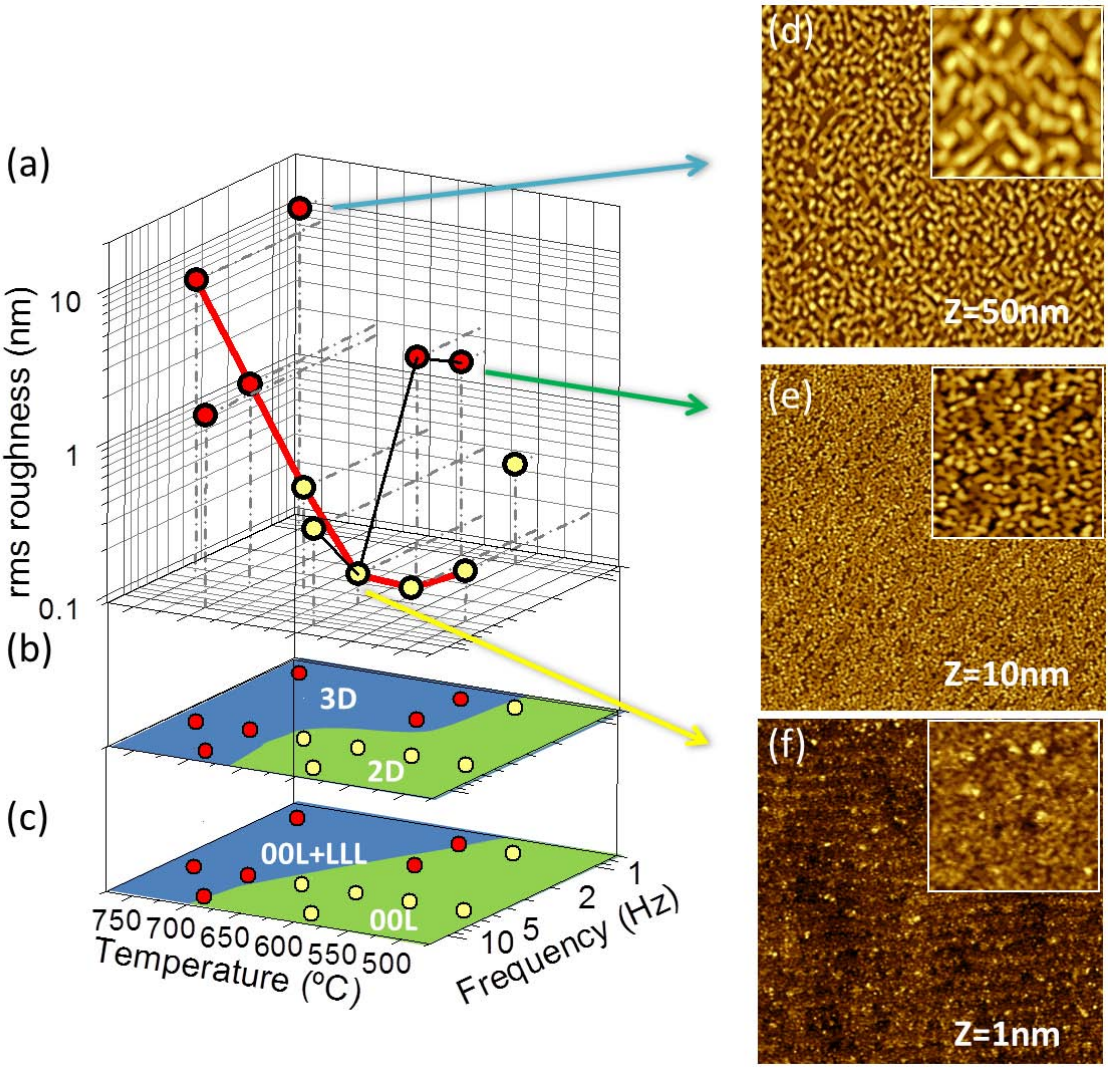

Figure 3.3: (a) *CFO* film roughness obtained by AFM at the different temperatures and laser repetition rates. Red line connects temperature series at $5\,Hz$ and black line frequency series at 600 °C. Films with rms roughness below $0.42\,nm$ are yellow. ((b),(c)) Schematic summary of surface roughness and film texture vs. growth parameters. (e-g) Selected topographic AFM images ($5\times5\,\mu m^2$, insets are $1\times1\,\mu m^2$) of films grown at different laser repetition rates and temperatures: (d) $5\,Hz$, 750 °C; (e) $5\,Hz$, 600 °C; and (f) $5\,Hz$, 750 °C.

The surface roughness of this sample set (T_S, p) was measured by AFM, and the resulting values are plotted in the 3d plot in figure 3.3(a), directly below the regions for 2d growth and pure (001) texture are highlighted in parameter maps, see figures 3.3(b) and (c) respectively. For selected data points illustrative AFM topographic images are shown in the right column (figures 3.3(d)-(f), scan size is $5\times5\,\mu m^2$, insets are $1\times1\,\mu m^2$). Films grown at relatively low temperature (600 $°C$) with a low deposition rate (laser frequency $1\,Hz$) present a rough surface with $rms > 1.5\,nm$ (figure 3.3(e)). While maintaining the growth temperature and increasing the laser frequency to $5\,Hz$, the AFM image shows

terraces and steps (figure 3.3(f)) with a low *rms* roughness $\approx 0.1\,nm$, indicating a flat 2d surface. At this point, T_S= 600 °C and $5\,Hz$ growth rate, a rough surface morphology is formed again if the growth temperature is increased to 750 $°C$ (figure 3.3(d)).

Summarizing, relatively high laser repetition rates (f) and low temperature ($T_S \leq$ 600 °C) lead to fully (001) textured films with smooth *CFO* surfaces . In the following the conditions (T_S= 500 °Cand $5\,Hz$ at $p = 0.1\,mbar$) were selected to deposit the *CFO* layer in the perovskite/spinel heterostructures described in Section 3.3.

3.2 Optimization of $BaTiO_3$ growth conditions

Reports on the preparation of *BTO* thin films by PLD usually focus on one growth parameter; the deposition temperature (T_S) [82–84], the oxygen pressure (p) [85–87], the growth rate (gr) [88] or thickness (t) [87, 89, 90]. Investigated ranges of substrate temperatures and laser repetition rates are 600..800 $°C$ and 1..5 Hz, respectively. *In-situ* RHEED assisted film growth typically lower repetition rates of 1 and $2\,Hz$ are used. The oxygen pressure, studied in a broad range from *HV* conditions to $0.2\,mbar$ proved to play an important role [85, 86]. Interestingly lower pressures (HV) favored c-axis orientation of *BTO* films grown on highly mismatched substrates like *MgO*.

Considering these studies we have chosen T_S= 700 °C, $p = 0.02\,mbar$ and $f = 5\,Hz$ as starting point and investigated the influence of pressure p, growth temperature T_S and growth rate gr (changing f) for films grown simultaneously on (001) oriented *STO* and *LSAT* substrates maintaining the film thickness constant around $150\,nm$.

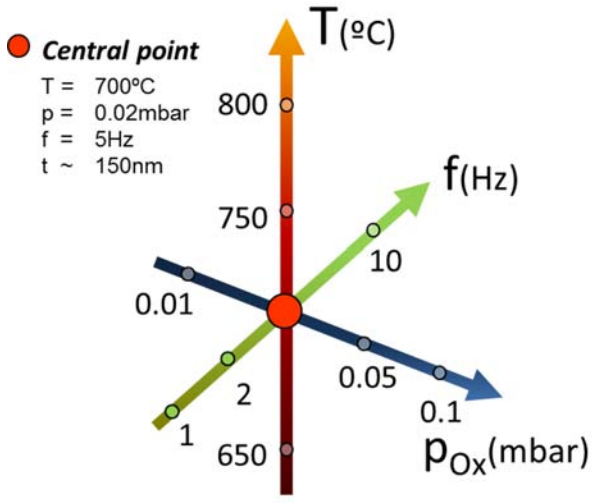

Figure 3.4: Schematic overview of the deposition conditions that have been varied for the $BaTiO_3$ film growth. The parameter for the central point are temperature T=700 $°C$, oxygen pressure p=0.02 $mbar$, laser pulse rate $f = 5\,Hz$. The thickness of the films is around t=150 nm.

figure 3.4 indicates graphically the parameter ranges: the temperature was probed in steps of 50 $°C$ from 650-800 $°C$, the oxygen pressure in the range of $p = 0.01$ to $0.1\,mbar$, and the laser repetition rate from $f = 1$ to $10\,Hz$.

3.2.1 Crystal orientation and strain dependency on growth parameters

The out-of-plane texture was determined by XRD $\omega/2\theta$-scans, measured between $2\theta = 10\,^\circ$ and $120\,^\circ$, in figure 3.5(a) is plotted the representative sample pair at the central point.

Despite the different mismatch of the substrate ($F_{BTO/STO} = 2.3$ % and $F_{BTO/LSAT} = 3.3$ % [1]), the $\omega/2\theta$-patterns are similar for both substrates. The $(00l)$ substrate reflections are marked with **S**, and $(00l)$ BTO reflection are labeled **B**. No spurious phases nor additional orientations are detected. The inset in figure 3.5(a) shows an amplified region around the (002) film reflection, for comparison the 2θ position of c and a oriented bulk BTO is indicated by vertical lines. The $\mathrm{FWHM}_{2\theta}$ is for $STO \approx 0.35\,^\circ$ and $LSAT \approx 0.2\,^\circ$, furthermore rocking curve with a $\mathrm{FWHM}_\omega \approx 0.5\,^\circ$ on both substrates indicating a high crystalline quality of the films. Pole figures around the (202) reflection indicate a cube-on-cube epitaxial relationship $[100]BTO(001)||[100]STO, LSAT(001)$. The out-of-plane lattice parameters are determined from the $\omega/2\theta$-scans and the in-plane parameters were derived from RSM around the (103) reflection. The RSM in figure 3.5(b) STO and 3.5(c) $LSAT$, respectively for BTO films grown on STO or $LSAT$ substrates, appear qualitatively identical with BTO lattice parameters: $c \approx 4.11(1)$ Å and $a \approx 4.01(1)$ Å .

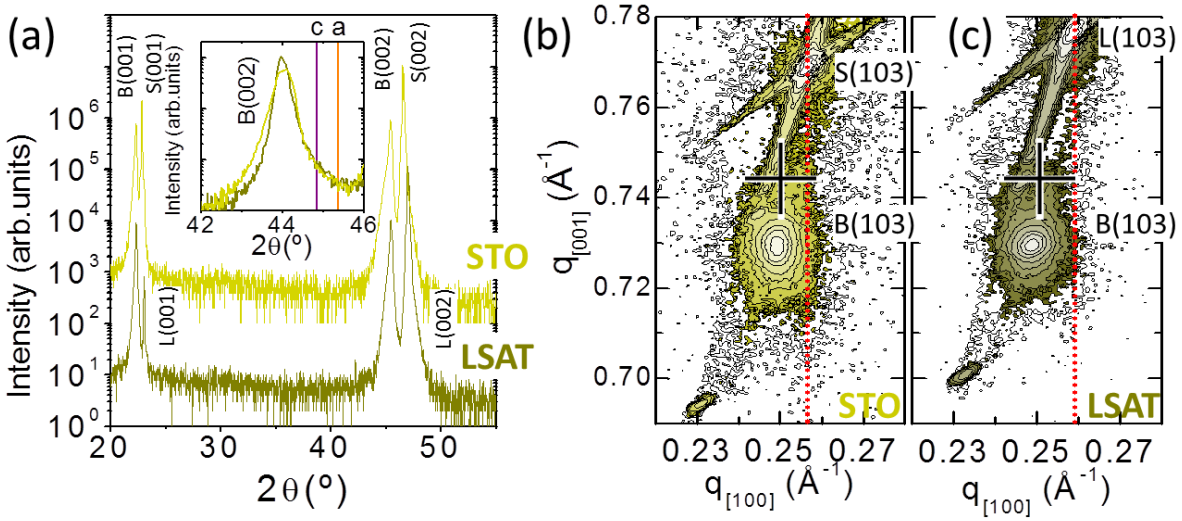

Figure 3.5: (a) XRD $\omega/2\theta$-scans for BTO films grown on STO and $LSAT$ at 700 °C , 0.02 $mbar$ and 5 Hz. Inset shows amplified region around (002), vertical lines indicate positions of bulk BTO a- and c-parameter. RSM around the (103) reflection on STO (b) and $LSAT$. The cross indicates c-oriented BTO(103) bulk position. The vertical dotted line indicates position of the in-plane substrate parameter.

To compare the lattice strain for the different growth conditions (T_S, p, f) amplified regions of the $\omega/2\theta$-scans around the (004) substrate reflection are shown in figure 3.6 for both substrates, STO (left column, 3.6(a)-(c)) and $LSAT$ (right column, 3.6(d)-(f)). As

[1] Lattice parameters: a_{BTO}=3.994 Å, a_{STO}=3.905 Å, a_{LSAT}=3.866 Å.

guide for the eye, the vertical lines in the scans correspond to bulk positions for *c*-oriented *BTO* ($2\theta = 99.4°$, marked as dotted purple line) and *a*-oriented *BTO* ($2\theta = 100.9°$, marked as dotted orange line).

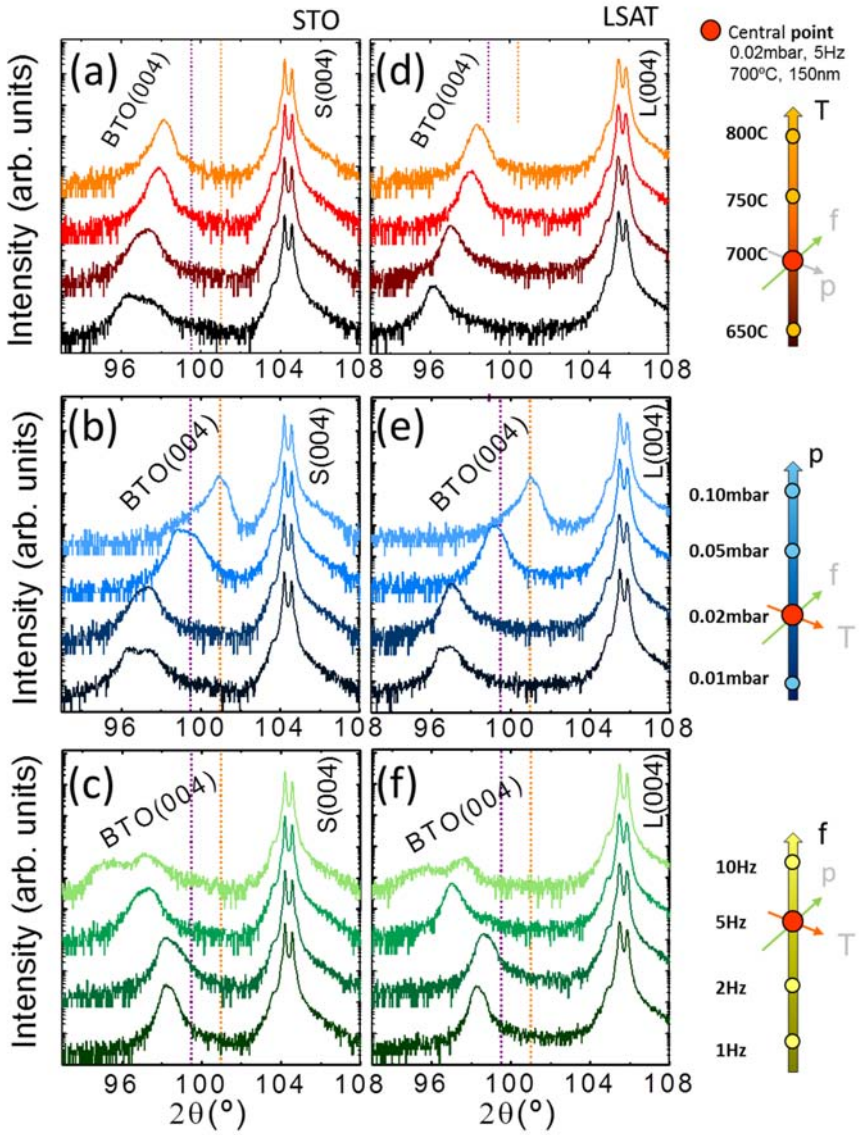

Figure 3.6: XRD $\omega/2\theta$-scans around the (004) substrate reflection (*STO*(S): (a)-(c) and *LSAT*(L): (d)-(f)). The evolution as function of growth temperature (a),(d), oxygen pressure (b),(e) and laser pulse rate (c),(f) are presented. The vertical lines indicate bulk positions *c-BTO* (purple) and *a-BTO* (orange). The sketches at the right indicate the changed deposition parameter.

Influence of growth temperature

The evolution of the $\omega/2\theta$-scans as function of T_S are shown in figure 3.6(a) for *STO* and 3.6(d) for *LSAT*. At all deposition temperatures the peaks are found below $2\theta_{peak} < 99.4°$, corresponding to a lattice parameter in out-of-plane direction larger than *c*-axis

of bulk *BTO*. A strong deformation at low deposition temperature (T_S=650°C) is found, with $\varepsilon_{650°C}$=2.27 % ($c_{650°C}$=4.13 Å), but reduces with increased substrate temperature to $\varepsilon_{800°C}$=1.04 % ($c_{800°C}$=4.08 Å). The observed lattice parameters are similar to values reported in literature [84, 85]. The film grown on *STO* at 650°C presents a double peak, which indicates the presence of two different out-of-plane lattice parameters, $c_{650°C}$=4.13 Å and $c^*_{650°C}$=4.10 Å, the later with lower intensity (factor 1/2), both peaks have a similar in-plane parameter of a=4.01 Å. On *LSAT* substrates a single *BTO* reflection is present. For 800° the in-plane parameter is a=4.00 Å very close to *BTO*'s bulk a-parameter $a_{BTO\ bulk}$=3.994 Å. The derived *BTO* lattice parameters are plotted in figure 3.7(b) for T_S, p and f. If a split diffraction peak is present the lower intensity peaks are shown as unfilled squares, while the reflections with higher intensity are shown as red filled squares. The c-parameter for *BTO* films on *LSAT* are integrated in the plot as half filled blue/white circles. The bottom panels show the c/a ratio as indicator for the tetragonality (bulk c/a = 1.01) and the cube root of the *BTO* cell volume compared to bulk (horizontal line $\sqrt[3]{V}_{bulk} \approx 4.01$ Å). While the c/a ratio is notably enlarged for most films, also the cell volume is increased, which is likely caused by oxygen vacancies due to low oxygen pressure (p_{Ox}=0.02 $mbar$) during the deposition. We find that the c-parameter are enlarged significantly compared to *BTO* bulk ($c_{BTO\ bulk} \approx 4.04$ Å). The in-plane a-parameter is also found to be somewhat larger than the corresponding bulk value ($a_{BTO\ bulk} \approx 3.99$ Å).

The epitaxial stress does not appear to influence significantly the lattice parameters considering the similar strain on both substrates. We note that these films are relatively thick ($\approx 150\,nm$), and thus absense of residual elastic strain could be expected considering the lattice mismatch, $F = 2.3\%$ and 3.2% for *STO* and *LSAT*, respectively. The expansion of the in-plane parameters is thus unexpected considering the compressive epitaxial mismatch. However, appart the possible formation of oxygen vacancies at low pressures, we may have to take into account that a phase transition occurs during the cool down (at 120 °C in bulk *BTO*), being the a-parameter of the cubic (high temperature) phase larger than the a-parameter of the tetragonal (low temperature) phase as our films are relatively thick (150nm) and should be fully relaxed at the end of growth. In addition the formation of oxygen vacancies or defects (point defects or stoichiometry) originated by the high energetic plasma particles typical for PLD at low deposition pressures could also contribute to the increased volume.

Influence of deposition pressure

A strong influence on the out-of-plane lattice parameters is found for the oxygen pressure present during the deposition. The $\omega/2\theta$-scans are shown in figure 3.6(b) and 3.6(e)

for *STO* and *LSAT*, respectively. At the lowest pressure (0.01 *mbar*) a double peak is observed for both substrates *STO* and *LSAT* although less pronounced for the latter. The (103) RSM of the film on *STO*(001) (central panel in figure 3.7(a)) shows two

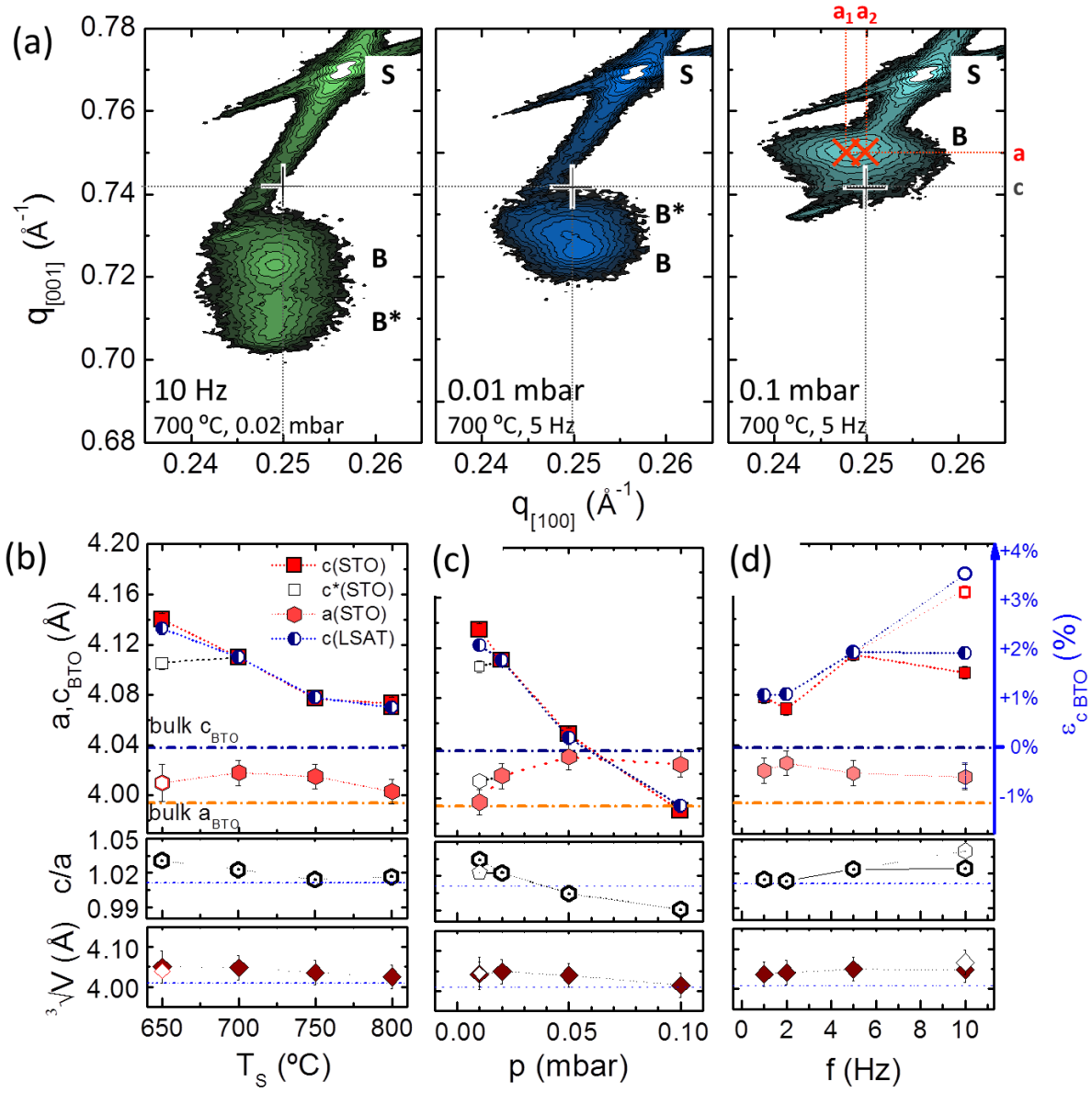

Figure 3.7: (a) XRD (103) RSM of selected *BTO* films on *STO*(001), growth conditions (T_S, p_{Ox} and f) are indicated in each panel. **S** and **B** mark substrate and film reflection, **B*** labels the lower intensity *BTO* reflection in case of double peak. The bulk position of *c* oriented *BTO* is marked by a black cross and dotted lines. The two possible *a* domains (a_1, a_2) are marked by red crossed and red dotted lines. (b), (c) and (d) show the derived film parameters as variation of the growth temperature (T_S), oxygen pressure (p) and pulse rate (f), respectively. The upper panel shows the measured *c* and *a* lattice parameters of *BTO* on *STO*(001) as filled symbols, open symbols correspond to lower intensity *BTO** peaks. *c*-parameter of films on *LSAT*(001) are plotted as half filled blue circles. The right caption indicates the epitaxial strain in out-of-plane direction. Horizontal lines mark the bulk parameters of *BTO*. The central panels show the c/a ratios and the bottom panels shows the pseudo-cubic parameter (a_{PC}) calculated from cube root of the cell volume $\sqrt[3]{V} = a_{PC}$, dotted horizontal lines mark bulk values.

peaks **B** and **B*** (the latter with lower intensity), with corresponding lattice parameters $c_{0.01\,mbar} \approx 4.13$ Å, $a_{0.01\,mbar} \approx 4.00$ Å and $c^*_{0.01\,mbar} \approx 4.10$ Å, $a^*_{0.01\,mbar} \approx 4.02$ Å. With increasing oxygen pressure the out-of-plane parameter decreases monotonically and at $0.1\,mbar$ it matches fully *a*-oriented $BTO \approx 3.99$ Å (see RSM right panel in figure 3.7(a), positions for bulk *a* domains are marked by red crosses and dotted lines with corresponding label; bulk *c*-domain are marked by black cross and corresponding dotted lines). The in-plane parameters vary correspondingly, occurring the transition from *c* to *a* oriented *BTO* films at oxygen pressures around $0.05\,mbar$. The *BTO* c/a ratio and cell volume are enlarged for lower pressures, while for $0.1\,mbar$ both are bulk-like value (with $c/a \approx 0.99$, expected for *a* oriented *BTO*). The relevance of the deposition pressure on the formation of *a*, *c* oriented *BTO* films has been reported [85, 86], with similar results to our study. The transition from *c*- to *a*-oriented *BTO* films occurs in spite of the compressive epitaxial stress caused by *STO* or *LSAT* (001), where *BTO*(100) should have, *a priori*, higher energy (film-substrate interface and domain boundaries) than *BTO*(001). Contributions from boundary conditions, like FE transition of *BTO*, might play a role. *BTO* undergoes a ferroelectric phase transitions from cubic to tetragonal phase while cooling, with larger cubic lattice parameter than the *a*-parameter of the tetragonal phase. Without bottom and top electrodes, oxygen vacancies and other point defects in low pressure films could provide compensating charges, whereas in high pressure films *a*-orientation could be more efficient reducing the overall energy of the film. Finally, we note that it is also reported that ultrathin (few *nm*) thick *c*-oriented films of *BTO* can be grown at 0.1 or $0.2\,mbar$ [91].

Influence of laser repetition rate

The growth rate was varied by the laser repetition rate (f) from 1 to $10\,Hz$ ($700°C$, $0.02\,mbar$), see corresponding XRD $\omega/2\theta$-scans in figures 3.6(c) *STO* and 3.6(f) *LSAT*. An increasing pulse rate has a similar effect as decreasing the temperature, a low repetition rate of $1\,Hz$ leads to more relaxed out-of-plane lattice parameters $c_{1Hz} \approx 4.07$ Å while increasing f to 5-10 Hz, $c_{5-10Hz} \geq 4.12$ Å. A double peak (intensity ratio 1:2.5, the lower intensity peak is labeled **B***) is found at high laser repetition rate of $10\,Hz$ on both substrates (see also the (103) RSM in the left panel of figure 3.7(a)). The out-of-plane parameter for the stronger expanded fraction (lower intensity) is $c^*_{10Hz} \approx 4.16$ Å indicating a deformation around $\boldsymbol{\varepsilon}^* \approx +3\%$ while the less c-expanded one (higher intensity) $c_{10Hz} \approx 4.12$ Å is in the order of $\boldsymbol{\varepsilon}$=+1.8%. The RSM shows that both reflections have the same in-plane parameter of $a_{10Hz} \approx 4.015$ Å. It is difficult to say which layer corresponds to the one in contact with the substrate, but the less tensed and more intense reflection may indicate

some relaxation with thickness. On the other hand at slow growth rate ($f = 1\,Hz$) very sharp (004) reflection are found ($\mathrm{FWHM}_{2\theta} = 0.5°$, see figures 3.6(c) and 3.6(f)), even a weak Kα-splitting can be appreciated. As a consequence the c/a ratio decreases from high to low growth rate, it is significantly enhanced ≥ 1.025 for high growth rates (5, 10 Hz) while at low rate it is closer to bulk. The cell volume appears to be slightly enhanced for all samples likely for the low deposition pressure (0.02 $mbar$).

Considering the probed growth parameters, the optimal growth conditions appear to match well with the chosen central point, T=700 °C, p=0.02 $mbar$ and f=5 Hz, the (004) reflection is sharp single peak and enhanced tetragonality (c/a=1.025, c/a BTO bulk is 1.01).

3.2.2 Dependency of the morphology on the growth parameters

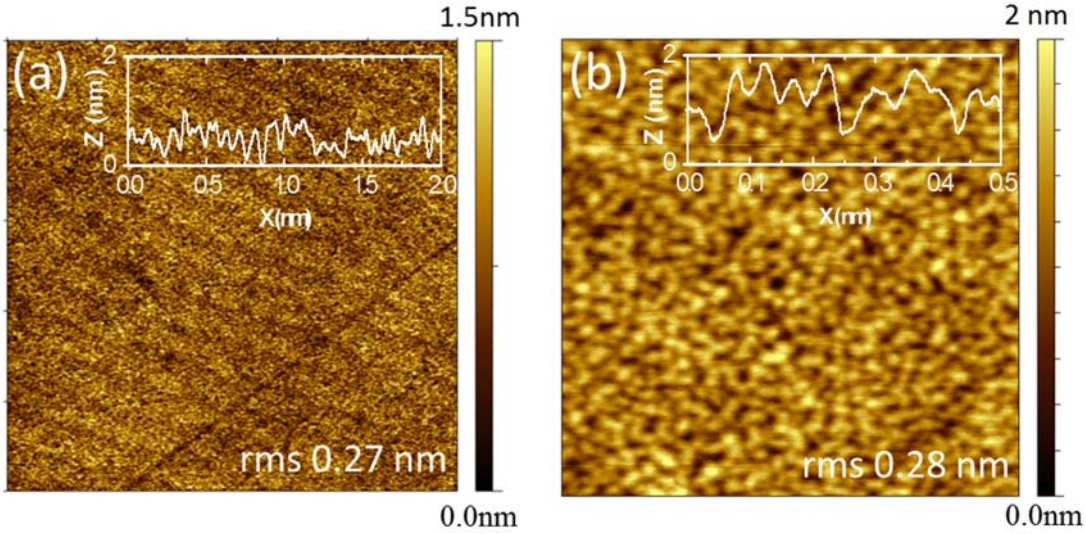

Figure 3.8: AFM images of BTO film of 150 nm thickness on STO (650 °C, 0.02 $mbar$ and 5 Hz) with scanned size (a) $5 \times 5\ \mu m^2$ and (b) $1 \times 1\ \mu m^2$. Insets show typical horizontal line profiles.

The morphology of the films on both substrates was analysed by AFM. As an example we show in figure 3.8 the AFM topography images obtained for a BTO/STO(001) sample grown at 650 °C for $5 \times 5\ \mu m^2$ and $1 \times 1\ \mu m^2$ scanned area, see figure 3.8(a) and 3.8(b) respectively. Typical height profiles are shown as insets. Despite the considerable film thickness ($\approx 150nm$) a 2d terrace-like morphology can be appreciated in the $5 \times 5\,\mu m^2$ image , nevertheless the $1 \times 1\,\mu m^2$ image indicates a more granular like surface. Thus the terraces are not atomically flat and hence present a dense structure of small islands. The surface roughness is very low $rms \approx 0.27\,nm$ and from the inset in figure 3.8(b) peak-valley heights are in the range 1 to $4\,uc_{BTO}$. Such a morphology of macroscopic terraces with high density of small islands was reported for a 13uc thin BTO film on Nb:STO(001) observed by *in situ* scanning tunnel microscopy (STM) [92]. The higher resolution in

their experiment revealed up to 4 open layers any of them atomically flat and terminated with flat islands about 10 nm in diameter. Other authors [84] have reported pseudo 2d structures on 125 nm thick films. In our samples the morphology is qualitatively similar (terraces with islands) for most of the explored growth parameters and for both substrates (figure 3.9). We note that the substrates used had terrace widths in the range of 120 to 350 nm, corresponding to a miscut in the range of 0.06 to 0.19°.

An overview of the observed morphologies is shown in figure 3.9(a). The AFM image of the central sample is presented in the center-top and those corresponding to the extremes of each growth parameter range are shown on the sides. In the bottom panel the dependence of the rms surface roughness with the growth parameters T_S, p and f are plotted in figure 3.9(b), 3.9(c) and 3.9(d), respectively. The surface roughness slightly increases for high substrate temperatures 800°C (rms_{STO}=0.75 nm, rms_{LSAT}=0.37 nm) as terraces are still insinuated despite the bigger multilayered islands with lateral dimensions 50 to 100 nm and heights between 2 and 5 uc.

An increased oxygen pressure strongly deteriorates the 2d like surface morphology. While films at low deposition pressures ($< 0.05 mbar$) are flat and 2d-like with $rms_{<0.05mbar} \approx 0.25\,nm$. For the deposition pressure of 0.1 $mbar$ the resulting surface (figure 3.9(a)) has an absence of terraces-like features, is more granular with homogeneously distributed outgrowths (around 60 to 80 nm wide and 4 to 10 nm high) and consequently an increased rms roughness of $rms_{0.1mbar} \approx 1.75\,nm$ (figure 3.9(c)).

No influence on the surface morphology can be appreciated varying the laser repetition rate, all films show rms surface roughness of rms=0.2 to 0.3 nm. Clear terrace-like features are only visible for 2 and 5 Hz, less pronounced for 10 Hz. For slow repetition rate of 1 Hz the surface appears more granular-like compared to the higher rate ones.

In summary, flat 2d-like BTO films with $rms \leq 0.3\,nm$ are achieved for a wide range of deposition conditions, a notable transition to 3d growth ($rms \approx 1.75\,nm$) is only evident for high oxygen deposition pressure of 0.1 $mbar$.

3.2.3 In-situ RHEED

The growth of BTO thin films was further investigated using *in situ* RHEED at the previously optimized growth conditions (700 °C, 0.02 $mbar$). We note an instrumental difference is the larger target substrate distance of 65 instead of 47 mm in the RHEED chamber and usually lower laser repetition rate of 1 or 2 Hz.

Here we present RHEED observation during the deposition of a BTO film grown on bare STO(001) substrate. In figure 3.10(a) the RHEED pattern for the substrate is shown. It has been acquired along the [100]STO azimuthal direction at an angle of incidence of

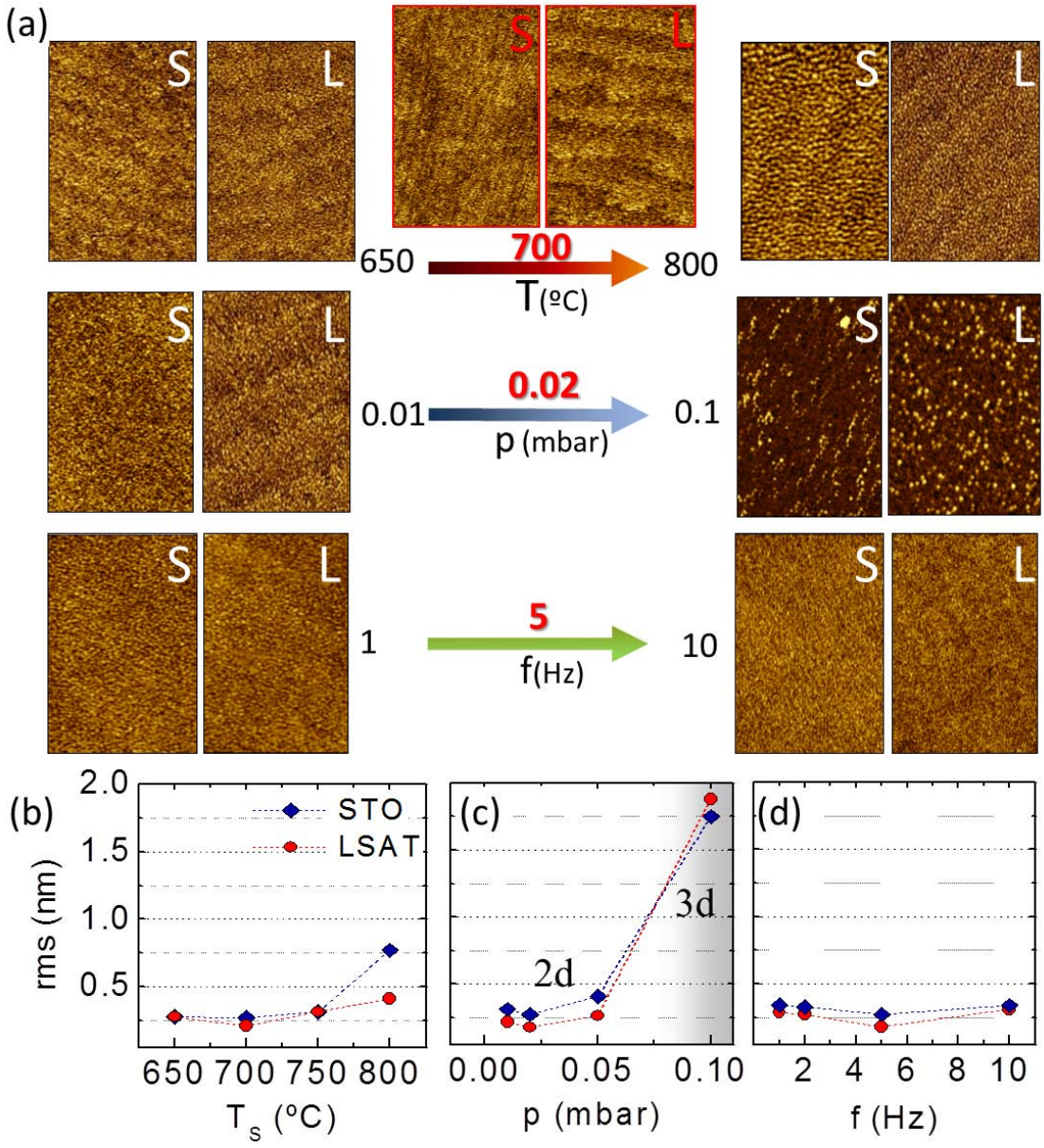

Figure 3.9: (a) AFM morphologic images ($2 \times 3\ \mu m^2$) around the central deposition conditions: $700°C$, $5\,Hz$, $0.02\,mbar$ for BTO films ($t = 150\,nm$) on STO (S) and $LSAT$ (L). For each series the images are corresponding to the extremes of the probed growth parameter. Rms roughness as function of temperature T_S (b), pressure p (c) and pulse rate f (d).

1.9°. The central specular (00) spot, first (01), (01) and second (02), (02) order Bragg spots and Kikuchi-lines are observed (labeled K in the figure). The presence of Kikuchi lines, formed by inelastic scattering processes, are common for highly crystalline flat substrate surfaces. During the experiment the specular spot intensity, within the rectangular area in figure 3.10(a) marked as red box, was monitored, as well as the intensity along the yellow line. Specular RHEED intensity is plotted in figure 3.10(c), where start and stop of the laser is marked with green and red arrows, respectively.

First, at the beginning of BTO growth, the intensity shows oscillation and thus

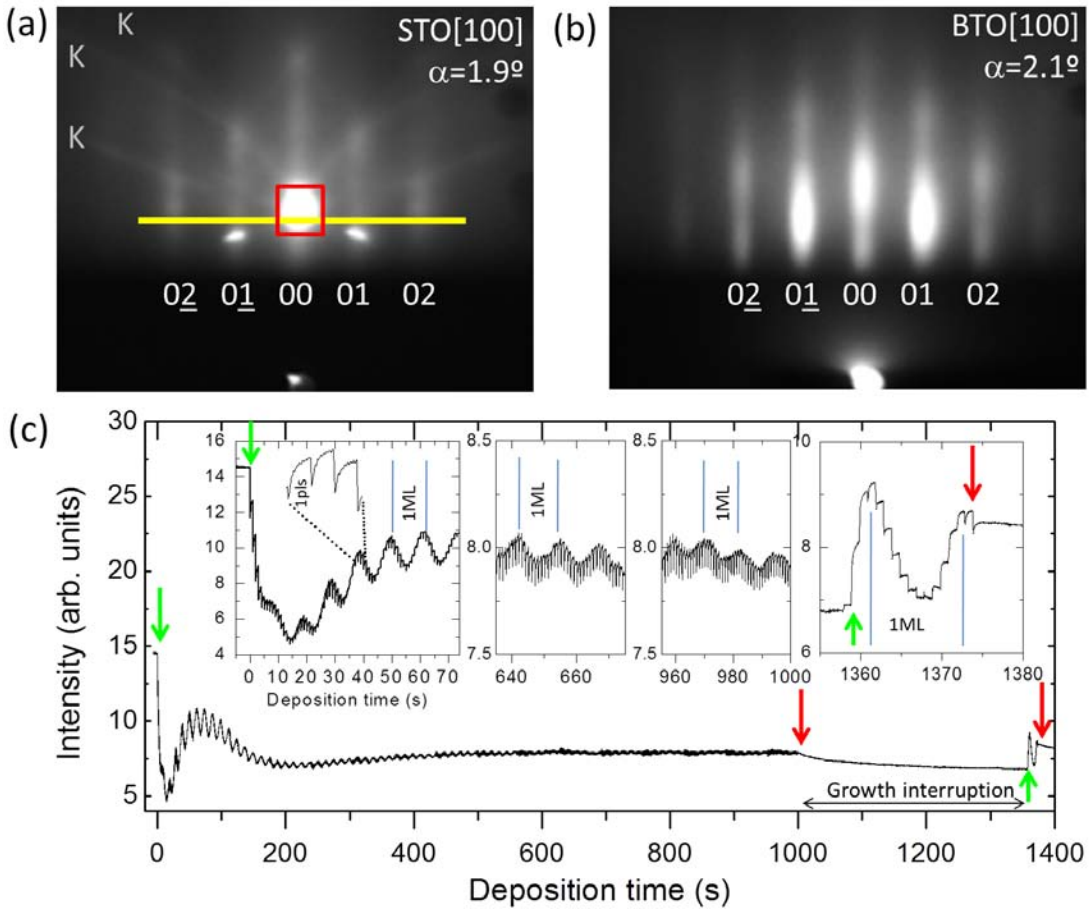

Figure 3.10: RHEED patterns obtained along [100] azimuthal direction for $STO(001)$ (a) and $BTO(001)$ (b). K indicates Kikuchi-lines, the red box corresponds to the region integrated for the specular spot intensity and the yellow horizontal line corresponds to a continuously saved intensity line-scan. (c) Specular spot intensity acquired during deposition of BTO at 700 °, 0.02 $mbar$ and 1 Hz, insets show amplified regions. Green and red arrows mark laser ON/OFF status, respectively.

indicates layer-by-layer growth mode. Each maximum corresponds to a fully terminated layer, which is in average every 13.5 pulses 1 ML , corresponding to a growth rate of $\approx 0.3\,\text{Å}/pls$. Due to high sampling rate of 56 ms the short term relaxation processes after each pulse are observable (in the leftmost inset of figure 3.10(c) 3 pulses are amplified, delay time between each pulse (pls) is 1 s). The steep drop after each laser pulse is caused by the instantaneous increase of island step density when the ablated material is deposited on the surface. Then an exponential increase in intensity takes place, thus the total island step density is reduced by: migration of small clusters to the terrace edges, or to bigger 2d islands, or migration from top of an island to the lower layer. During the growth of the first layers the specular intensity dropped and only weak oscillations occur in the very beginning, then specular intensity recovered and remains nearly constant (figure 3.10(c)). The origin of such behavior can be related to interference of the growing layer with the pattern originated from the substrate, also the change of the diffracting material itself can

result in changes in position and/or size of the measured diffraction spots and thus the integrated intensity.

The intensity oscillations are still present after ≈ 650 pulses (≈ 55 *ML*), see inset of figure 3.10(c), and even after around 1000 pulses oscillations are present. The amplitude damping is caused by an increased level of disorder at the surface due to formation of multilevel 2d islands. We interrupted the deposition (maintaining the actual growth conditions) for 360 *s*, expecting that the surface mobility of the atoms at the surface may lead to a flatter surface. A sharp intensity increase within 3 pulses is noted then the undulation starts, after 13 pulses we stopped the deposition reaching the intensity maximum and thus a terminated layer (figure 3.10(c) rightmost inset). The total thickness is 81 *ML*, corresponding to a thickness of around 33 *nm*. The RHEED pattern of the grown *BTO* layer was taken at the end of the deposition along the [100] direction at an incident angle of 2.1°, see figure 3.10(b). The streaky shape of the spots are indicative for a flat 2d-like surface.

Intensity profiles along the horizontal line profiles (yellow line in figure 3.10(a)), spanning the 1^{st} and 2^{nd} order Bragg spots of the substrate and the film, allow to determine the in-plane lattice spacing ($a_{||}$) during the growth. At the deposition temperature (700°*C*)

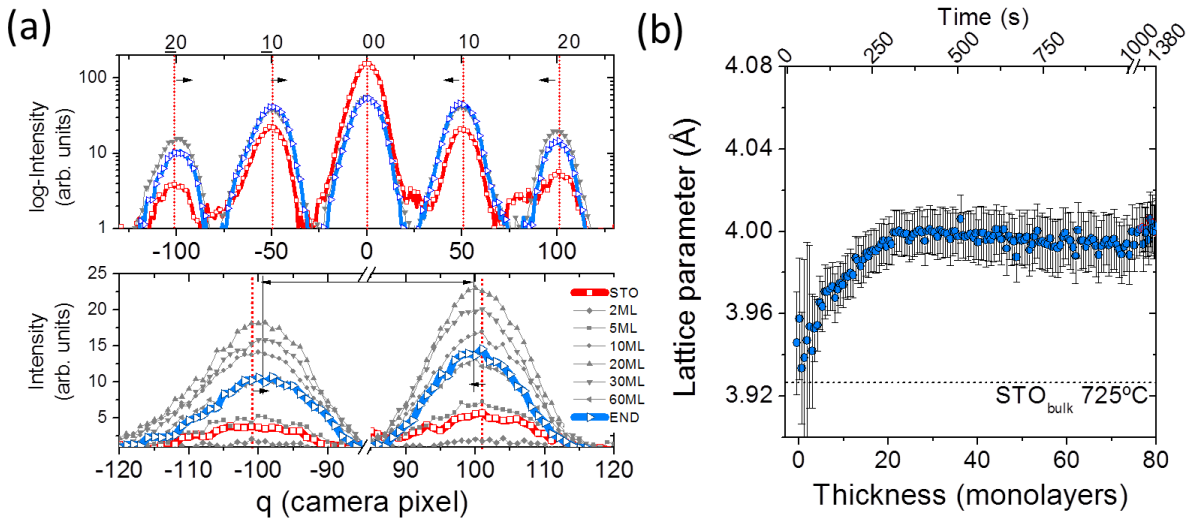

Figure 3.11: Rheed intensity line profiles acquired during deposition of *BTO* on *STO*(001), $T_S = 700°C$. (a) profiles for different thicknesses bottom panel shows amplified region of the (2̲0),(20) reflection. (b) Deduced in-plane spacing for the *BTO* layer as function of thickness.

the lattice parameter of *STO* is about $a_{STO\,700C} \approx 3.93$ Å, while that for bulk *BTO* is calculated to be $a_{BTO\,700C}$=4.03 Å (thermal expansion coefficient of *STO* is around $\approx 1 * 10^{-5}\,K^{-1}$ [93] and *BTO* $1 * 10^{-5}\,K^{-1}$ [83]). In figure 3.11(a) selected profiles are shown for different thickness's and an amplified region around the second order reflections is on the bottom. The first profiles correspond to *STO* (red curve) and the last one at the

end of the deposition after around 80 *ML* of *BTO* (blue curve); profiles with intermediate thicknesses are labeled correspondingly. The peak maxims were determined using Gaussian fits, and the substrate Bragg peaks were used as reference for the conversion of camera pixels to reciprocal spacing (q). A slight shift to smaller q-values (figure 3.11(a) shown in camera pixels) for the distance between the 2^{nd} order reflections is observed and indicates an increase of the in-plane parameter. To reduce the data volume for fitting (a line is acquired every 56 ms) and improve the noise ratio an average of 10 lines was used. The resulting in-plane parameter as a function of *BTO* thickness (in *ML*) is presented in figure 3.11(b). The continuous relaxation starts right from the beginning and after 18-20 *ML* ($\approx 8nm$) the in-plane parameter of the *BTO* film remains constant at around 4.00(1) Å which is close to the expected bulk *BTO* (4.03 Å) at 700 °C.

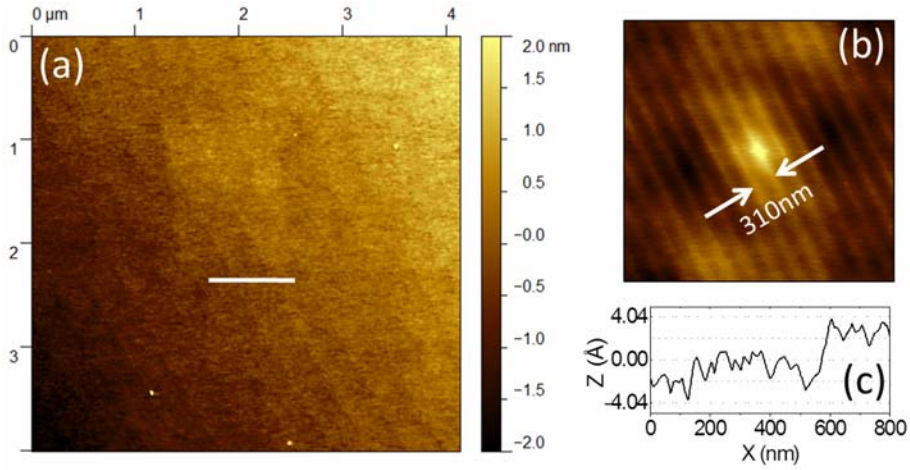

Figure 3.12: (a) Topographic AFM image of the sample whose RHEED data are presented in figures 3.10 and 3.11. (b) A 2d auto-correlation image of the surface. The corresponding terrace width is indicated, (c) a height profile along the white line marked in (a).

BTO lattice parameters of the film were *ex-situ* measured at room temperature by $\omega/2\theta$ and RSM are a=3.99 Å and c=4.13 Å, resulting in a enlarged c/a ratio of 1.03 but also the cell volume, which is similar to films grown in the standard PLD chamber (1 Hz, 700 °C, 0.02 $mbar$, 150 nm, c = 4.08 Å). Despite the RHEED observation suggests fully relaxed *BTO* at a film thickness of 30 nm, a further relaxation with increasing thickness can not be discarded, as well as, minor differences of the growth conditions in both chambers. The topographic AFM image (figure 3.12(a)) shows a very flat surface with terrace-like features, consistent with the observed layer-by-layer growth mode. The *rms* roughness is 0.2 nm and the terrace width is about 310 nm (determined from the 2d autocorrelation image, see figure 3.12(b)). A line profile (figure 3.12(c)) shows height variations of 1/2 or 1 unit cell of *BTO* (the grid in the figure corresponds to 1/2 unit cell, $a/2 \approx 2.02$ Å). The streaky RHEED pattern at the end of *BTO* growth (figure 3.10(b)) indicates a certain disorder (an atomically flat surface should be more similar to the *STO* surface before the

Table 3.1: Lattice mismatch in % between *LSMO*, *SRO*, *BTO* and *CFO*. Values are referred to room temperature for bulk crystals. Not used combinations are left blank. It has to be noted that *LSMO* and *SRO* grow fully strained, and thus the effective mismatch with top *BTO* and *CFO* is respect to *STO*.

Film / Substrate	*LSMO* (3.87Å)	*SRO* (3.93Å)	*BTO* (4.01Å)	*CFO* (8.39Å)
STO (3.91Å)	-1.02%	0.51%	2.56%	7.29%
LSMO (3.87Å)			3.62%	8.40%
SRO (3.93Å)			2.04%	6.74%
BTO (4.01Å)				4.61%
CFO (8.39Å)			-4.41%	

deposition), consequently the surface most likely is formed by a very dense array of 2d islands as described in Section 3.2.2.

3.3 Implementation in horizontal heterostructures

3.3.1 Overview of prepared samples

Here horizontal heterostructures, more exactly bi-layers, composed by alternating *CFO* and *BTO* layers will be discussed. As bottom electrodes $SrRuO_3$ (*SRO*) and $La_{2/3}Sr_{1/3}MnO_3$ (*LSMO*) have been chosen for its good compatibility to the *STO* substrate, all have a perovskite structure with low lattice mismatch about -1 and +0.5% (see Table 3.1). These electrode materials grow epitaxially for tens of *nm*, are fully strained to the substrate and present very high structural and surface quality. A moderate mismatch of *BTO* of around $\approx +2$ to 3.6% with respect to *STO* or electrodes permits epitaxial growth with plastic relaxation of the film. Also, the growth of high quality *CFO* films on top of the electrodes is expected despite the larger mismatch of about 5 to 7%, as they are structurally similar to bare *STO*. Nevertheless, the epitaxy of *BTO* on *CFO* appears *a priori* more challenging taking into account the large tensile mismatch of -4.4% and structural dissimilarity, which may reduce the formation of the polar *c*-axis in (001) substrate direction.

The bi-layered heterostructures where prepared using the previous optimized growth conditions (Section 3.1 *CFO* 500 °C, 0.1 *mbar*, 5 *Hz*; Section 3.2 *BTO* 700 °C, 0.02 *mbar*, 5 *Hz*). Two distinct types of stacking order are possible in bi-layers, we will referred to them as *BTO-bottom* and *BTO-top*, indicating that *BTO* is the 1^{st} or 2^{nd} layer in the stack. The samples were grown in a single process on *STO*(001) in the same chamber, in the further description we will note the layer thickness (in *nm*) of the *CFO* and *BTO* layers as subscripts; for example *STO*(001)//*SRO*/*BTO*/*CFO* (SB_nC_m, *BTO-bottom*) and *STO*(001)//*SRO*/*CFO*/*BTO* (SC_mB_n, *BTO-top*). The substrate plus

electrode are abbreviated as **S** for $STO(001)//SRO$ and **L** for $STO(001)//LSMO$. A set of heterostructures differing in the stacking order, film thickness and bottom electrode were prepared and observed in-situ by RHEED, see Table 3.2. RHEED results suggest that the growth of the bilayers does not depend significantly on the electrode.

3.3.2 Growth and structural characterization of Bi-layers

In the following, we will describe results derived from *in-situ* RHEED observation of samples with thick *BTO* layer ($\approx 80\,nm$) and ultrathin *CFO* layer $\approx 7\,nm$ (samples: *BTO-bottom* [$LB_{72}C_7$] and *BTO-top* [LC_7B_{85}]) using *LSMO* as electrode. figure 3.13(a) shows the time dependence of the intensity of the RHEED specular spot during the growth of the *LSMO* layer, while figure 3.13(b)-(d) show the consecutively grown bi-layers *BTO-bottom*/*CFO* and *CFO*/*BTO-top* (figure 3.13(e)-(g)). The corresponding RHEED patterns after each deposition step are shown . The *LSMO* bottom electrode grows 2d on $STO(001)$ in the used deposition conditions of substrate temperature and oxygen pressure [76, 94], in layer-by-layer growth mode as indicate the RHEED intensity oscillations (figure 3.13(a)). Damping of the intensity oscillations is evidenced, but the intensity recovery at the end of the growth (see the inset of figure 3.13(a)) with streaky patterns suggests

Table 3.2: Sample list of grown *BTO/CFO* bilayers and single *BTO* and *CFO* layers on *LSMO* or *SRO* buffered $STO(001)$, identified respectively with L or S. Thickness of *BTO* (B) and *CFO* (C) are indicated as subscripts. The c/a ratio refers to the *BTO* layers.

	Sample name	$\mathbf{t}_{BTO}$ (nm)	$\mathbf{t}_{CFO}$ (nm)	**c/a**	**c*/a***	
BTO - bottom	$SB_{25}C_{100}$	25	100	1.06	1.11	
	$SB_{35}C_{50}$	35	50	1.06	1.1	RHEED
	$SB_{80}C_{15}$	80	15	1.05	1.1	
	$LB_{25}C_{100}$	25	100	1.07	1.1	
	$LB_{72}C_7$	72	7	1.04	1.09	RHEED
BTO - top	$SC_{100}B_{25}$	25	100	0.98		
	$SC_{50}B_{35}$	35	50	1.00		RHEED
	$SC_{15}B_{80}$	80	15	1.00		
	$LC_{100}B_{25}$	25	100	0.99		
	LC_7B_{85}	85	7	1.00		RHEED
single	SB_{25}	25	–	1.06	1.11	
	LB_{25}	25	–	1.09	1.1	
	SC_{100}	–	100	–	–	

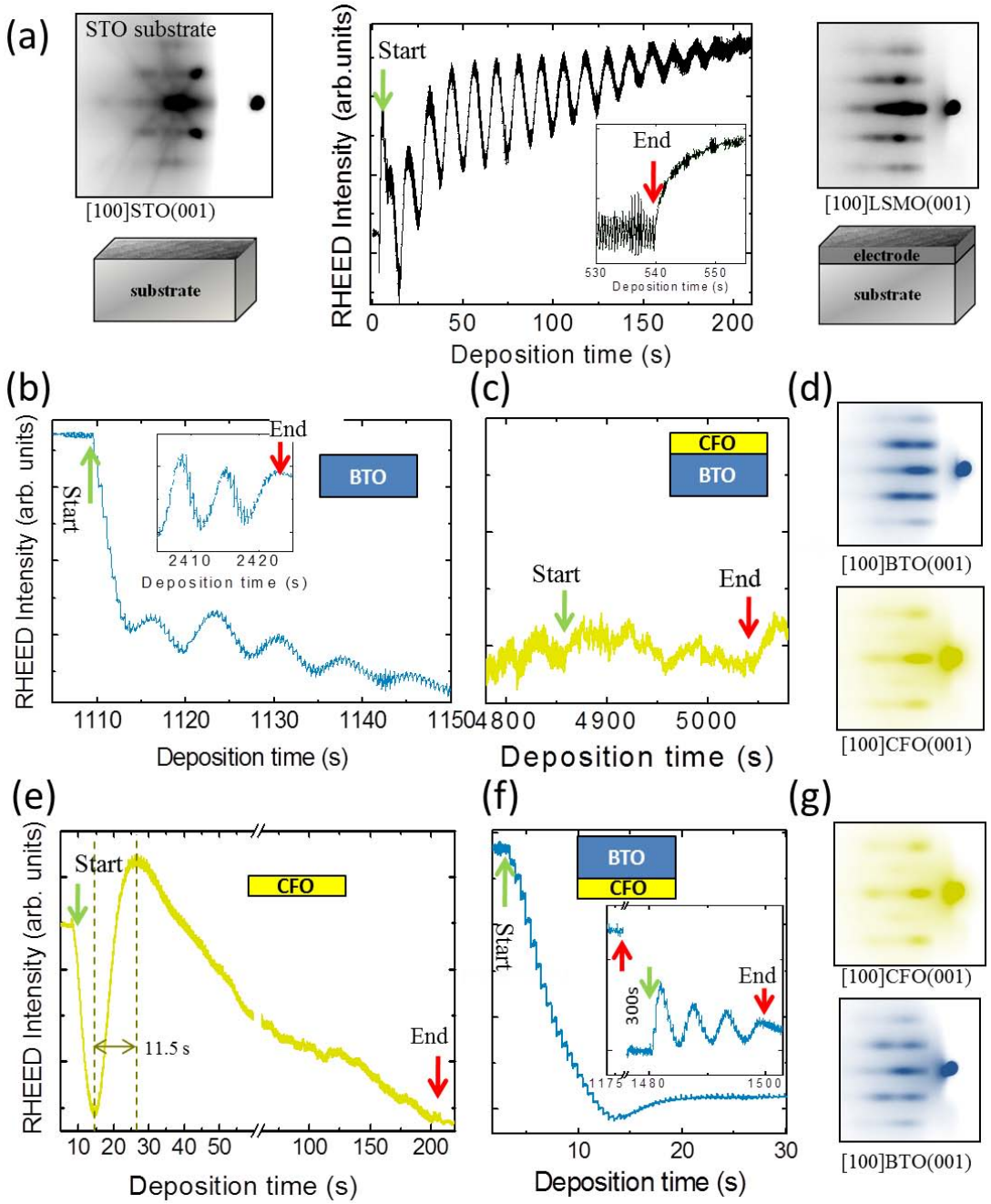

Figure 3.13: RHEED observation during the grown of $LB_{72}C_7$ and LC_7B_{85} samples; specular intensity and patterns for each layer. (a) The initial growth stage of *LSMO* (only for one sample), the inset shows the intensity recovery at the end of growth. (b), (c) *BTO* and *CFO* specular spot intensity during growth (sample $LB_{72}C_7$) and patterns at the end of each layer (d). (e)-(g) Specular intensity and patterns for the inverse heterostructure (sample LC_7B_{85}). Insets in (b) and (f) correspond to the final growth stage, after growth interruption. In both cases oscillations are found and the film is stopped at a terminated layer.

that *LSMO* grows flat. Intensity damping is observed in other deposited *LSMO* films, in agreement with other authors [94], and it could be due in part to mixed layer-by-layer and step flow mechanisms [63], thus ex-situ AFM showed terrace-and-steps morphology.

The growth of the *BTO-bottom* ($LB_{72}C_7$) heterostructure will be described first. *BTO*

grows in layer-by-layer mode as indicate the RHEED intensity oscillations (figure 3.13(b)). As on bare *STO* substrate the layer-by-layer mode can be maintained all along the *BTO* thickness by growth interruptions of a few minutes to smooth the surface, after growth interruption a strong recovery of RHEED intensity oscillations is observed and thus allows terminating the growth on a complete layer (see inset of figure 3.13(b), RHEED pattern at the end of growth is in figure 3.13(d)). The RHEED intensity for consecutive *CFO* growth (figure 3.13(c)) remains constant, suggesting conservation of the flat surface and an overall low step density. Neither intensity oscillations nor intensity recovery are observed, which is likely caused by low substrate temperature and high-rate deposition conditions used to kinetically suppress 3d growth. The streaky pattern at the end of the growth suggests a flat surface of the *CFO* layer (see figure 3.13(d)) and absence of additional diffraction spots indicate epitaxial growth following the orientation of the bottom layer .

In the *BTO-top* heterostructure, first the thin *CFO* layer and *BTO* is grown (LC_7B_{85}). This scenario should reduce the structural quality of the *BTO* layer as *CFO* is not isostructural in addition to a large tensile lattice mismatch (-4.4 %) compared to compressive mismatch to *STO* (+2.56 %) or *LSMO* (+3.62 %). The specular RHEED intensity for *CFO* exhibits an oscillation of one period at the beginning of the growth, and corresponds to one unit cell of *CFO* (the deposition rate was confirmed by XRR by single *CFO* films). Even there is a small decay in the intensity, a streaky RHEED pattern at the end of the growth (see figure 3.13(g)) attests a flat surface. Next, the *BTO* layer was grown. In the early growth stages there is intensity recovery after each laser pulse, but intensity oscillations are not observed (figure 3.13(f)). Nevertheless, layer-by-layer mode was evident after growth interruption for a few minutes and the clear intensity oscillations allowed to stop the growth at a complete layer (see inset of figure 3.13(f)). Despite the mentioned dissimilar crystalline structure and high lattice mismatch, epitaxial and 2d growth of *BTO* is qualitatively very similar to *BTO-bottom* considering the streaky RHEED pattern at the end of the deposition (see of figure 3.13(g) *BTO-top* and 3.13(d) *BTO-bottom*). The absence of additional Bragg spots in the RHEED pattern, also attests fully epitaxial growth of the *BTO* layer on top of *CFO*.

The evolution of the in-plane lattice parameter during the growth of each layer in both heterostructures was analyzed. Beginning with *BTO-top* sample (LC_7B_{85}) three corresponding profiles just before *CFO* deposition, after growth of 1 *uc* (corresponding to the first maximum in figure 3.13(e)), and at the end of the *CFO* growth (7 *nm*) are shown in figure 3.14(a). The reduced distance between the $(0\ -2)$ and $(0\,2)$ streaks in the reciprocal lattice corresponds to an increase of the in-plane *CFO* parameter. For the *BTO-top* layer streak distance widens see extracted profiles (3.14(b)) after 1.1, 6.6 and 86 *nm* and thus a reduction of the lattice parameter. Having in mind the *CFO*

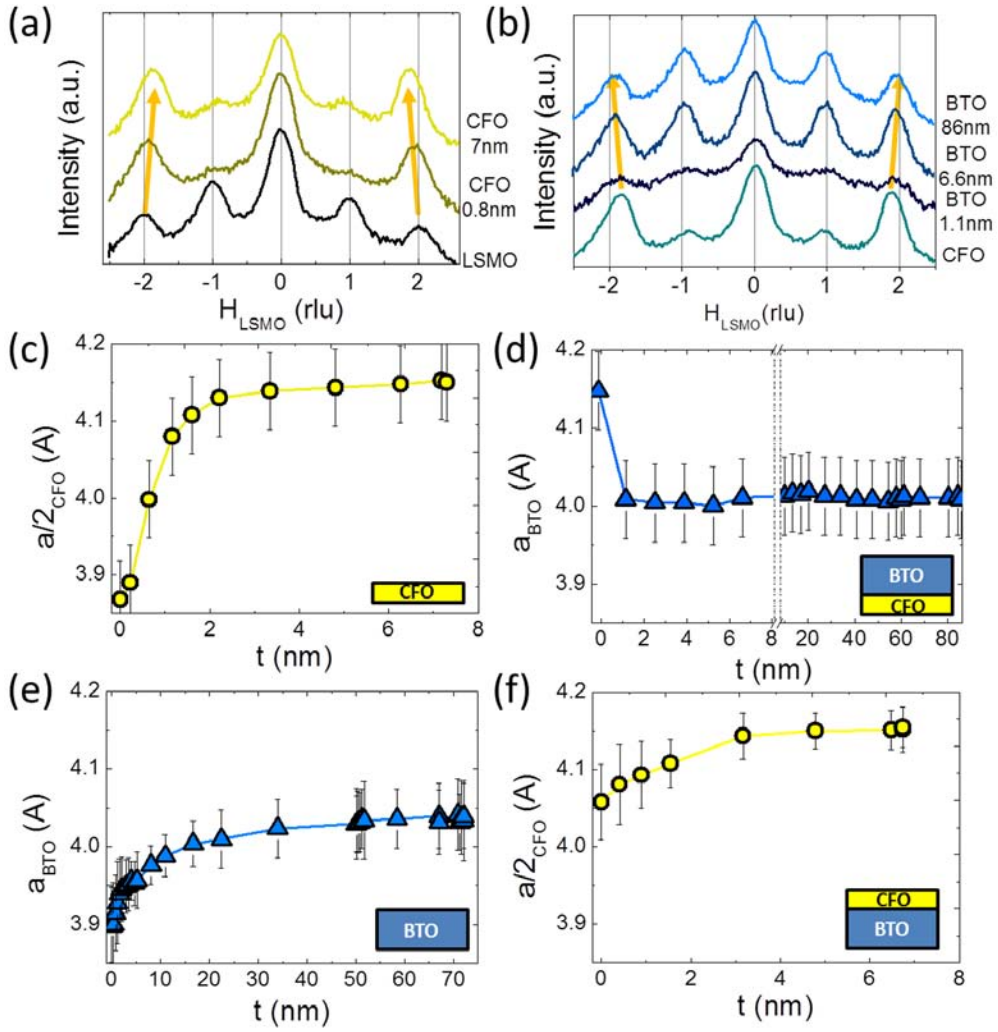

Figure 3.14: Analysis of the in-plane lattice parameters as function of the layer thickness during the growth of LC_7B_{85} sample: ((a),(c)) *CFO* on *LSMO* and ((b),(d)) *BTO* on *CFO*. The starting point is the RHEED pattern recorded after deposition of a $La_{2/3}Sr_{1/3}MnO_3$bottom electrode. ((a),(b)) show selected lines labeled with the corresponding layer thickness and in ((c),(d)) the derived in-plane lattice parameter of *CFO* (a) and *BTO* (b) are plotted. ((e),(f)) show the derived in-plane lattice parameter for BTO and CFO of the inverse stacking order ($LB_{72}C_7$).

lattice parameter, a large bulk mismatch $F > 7\,\%$ ($a/2_{CFO} \approx 4.2\,\text{Å}$, $a_{STO} = 3.91\,\text{Å}$) and $F > -4.4\,\%$ ($a_{BTO} \approx 3.994\,\text{Å}$, $a/2_{CFO} \approx 4.2\,\text{Å}$) the structural difference of *CFO* spinel to the perovskite layers a fast relaxation (a view *nm*) may be expected. The evolution of the *BTO* and *CFO* in-plane parameters during growth are in figure 3.14(c) and (d), respectively. Indeed, already during the first $2\,nm$ (about 3-4 unit cells) the relaxation R is $\approx 80\,\%$ to 4.15 Å (figure 3.14(c)). Note that for very thin films 1 to $2\,nm$ a contribution to $a_{||}$ caused by the smaller substrate can be present and thus can lead to an underestimation of R. The *BTO-top* layer grows on a bulk-like *CFO* lattice, and relaxes immediately (below $2\,nm$) thus R is around $100\,\%$ and the corresponding relaxed in-plane parameter measured was about 4.01 Å, close to*BTO* bulk value at 700 °C [35].

In the inverse stacking *BTO-bottom*, nevertheless the *BTO* layer is isostructural to *LSMO*, it starts to relax progressively (log shape) above a very low thickness of 1-2 *uc*, see figure 3.14(e). After the total deposited thickness of t=72 *nm*, the *BTO* lattice is relaxed to an in-plane parameter 4.03 Å close to fully-relaxed cubic *BTO* at 700 °C [35]. The relaxation R reaches 75% after the deposition of 20 *nm BTO* and is around 100% at the end of growth. The 7 *nm CFO* grown on top of *BTO* relaxes quickly during the first 4 *nm* by around 80% to an interplanar distance of 4.16 Å, with only small increase within the next 3 *nm*, suggesting it is already relaxed in-plane.

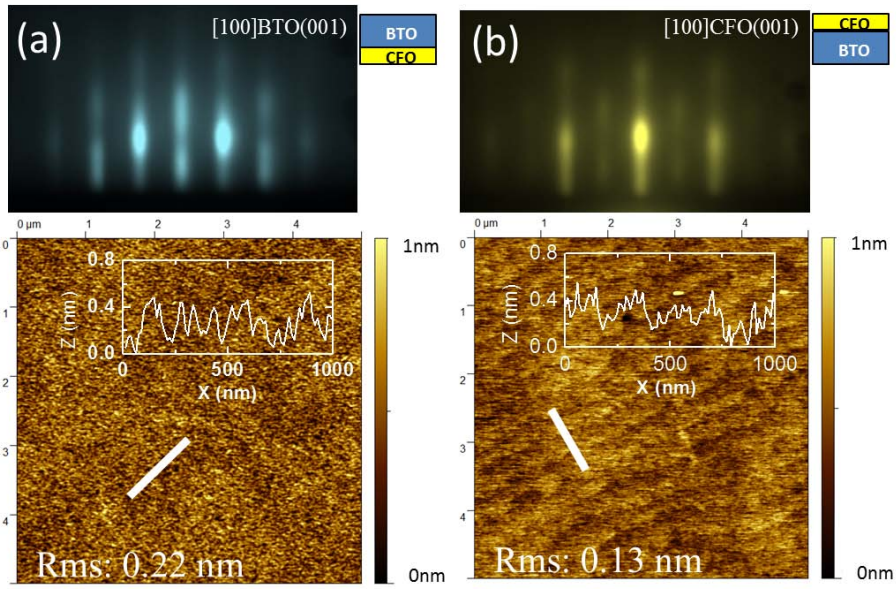

Figure 3.15: RHEED patterns at the end of deposition of the (a) *CFO/BTO* (LC_7B_{85}) and (b) *BTO/CFO* ($LB_{72}C_7$) heterostructures on *STO//LSMO*(001). The corresponding topographic AFM ($5 \times 5\,\mu m^2$) images are in the bottom panels, with insets showing height profiles along the marked lines.

AFM topographic images, figure 3.15 bottom panels, corroborate the surface flatness expected by the corresponding RHEED patterns, shown in the top panels. Both epitaxial heterostructures present very flat surfaces with step-and-terrace morphology and surface roughness below 0.13 *nm*. In the case of the $LB_{72}C_7$ sample (Fig. 3.15) terrace width and step height are around 350 *nm* and 4Å, respectively (miscut angle of 0.07 °). Step height corresponding to half spinel *uc* was recently reported in other spinels directly grown on *STO*(001) substrates [80]. In the LC_7B_{85} sample (figure 3.15) terrace width and step height are around 140 *nm* and 4Å, respectively (miscut angle is 0.16 °).

In-situ RHEED points to strongly varying lattice parameters of *BTO* depending on the stacking order. $\omega/2\theta$ scans and (103) RSMs were used to measure out-of-plane and in-plane parameters of the samples listed in Table 3.2. Here we want to compare two sample sets corresponding to thick *BTO* ($\approx 80nm$) and thin thin *CFO* ($\approx 7nm$), as well as, thin *BTO* ($\approx 25nm$) with thick *CFO* ($\approx 100nm$) in *BTO top* and *bottom* configuration.

Both sets are deposited on *LSMO* electrodes, nevertheless no differences were observes in samples with *SRO* electrodes. The strong overlap of *CFO* (004) reflections with the *BTO* (002) reflection (especially in the case of *BTO-bottom*, see figure 3.16(a) and (c), bulk positions are labeled) and low diffraction intensities, for both (004) and (206) diffraction spots, hamper an exact determination of the *CFO* parameters. No (206) diffraction spot is observed in the RSM for small *CFO* thickness, see figure 3.16(b). Referring to previously discussed RHEED observation and experiments on single *CFO* thin films, we can consider *CFO* basically relaxed in- and out-of-plane even for thin films. Here, the thick *CFO* films ($100nm$) show bulk-like parameters independent of their position in the stack, bulk (004) 2θ position is marked in the figure at $43.06\,^\circ$ (figure 3.16(c)) and in the RSM as white cross (figure 3.16(d)). For *BTO* layers a more complex scenario is present. First, we like to discuss the case of *BTO-bottom* (see figures 3.16(a)-(d)) sample. Two shoulders appear in the $\omega/2\theta$-scans (figure 3.16(a) and (c)), one is corresponding to a fraction of *BTO* which is strongly expanded in out-of-plane direction, labeled **B*** (directly in contact with the *LSMO* electrode), its in-plane parameter matches the substrate/electrode (a red dotted line in figure 3.16(a) and (c)) is a guide to the eye for the substrate in-plane parameter) and a partially relaxed fraction is labeled **B**. The calculated lattice parameters for *BTO-bottom* are summarized in figure 3.16(e). We find an highly strained *BTO* (B*) with out-of-plane and in-plane lattice parameters of $\approx 4.28(2)\,\text{Å}$ and $3.91(1)\,\text{Å}$ respectively, and thus an enlarged to tetragonality ratio $c/a \approx 1.10$. With increasing BTO thickness the partially relaxed B component becomes more prominent ($t \geq 35nm$) with op and ip parameters relaxing to around $4.14(1)\,\text{Å}$ and $3.98(1)\,\text{Å}$, respectively. Similar to single *BTO* films, that corresponds to a larger than bulk c/a ratio of ≈ 1.04 films, also the cell volume appears to be slightly larger than bulk (likely originated by the low oxygen pressure during deposition).

In the inverse structure, *BTO-top* we could observe by RHEED, sample LC_7B_{85}, an immediate in-plane relaxation of *BTO* on *CFO* and thus its strain state is very different. The $\omega/2\theta$ scan (figure 3.16(a)) shows a single $BTO(002)$ peak with larger than bulk *BTO* *c*-parameter (the peak is shifted to lower 2θ compared to the marked *BTO* bulk position), while for the thinner *BTO* film of sample $LC_{100}B_{25}$ it is close to the bulk position (figure 3.16(c)). In the RSMs (figure 3.16(b) and (d)), the $BTO(103)$ reflections, are broad, indicating an inhomogeneous distribution of the in-plane lattice parameter (which is also evidenced by an enhanced width of the (002) rocking curve, $\text{FWHM}_{bottom} \approx 0.6\,^\circ$ to $\text{FWHM}_{top} \approx 1.8\,^\circ$ an idicator for stronger mosaicity caused by the *CFO*). In the RSM a vertical red dotted line indicates the ip-paramter of bulk *CFO*, which can be considered the substrate for the *BTO-top* layer, also for comparison the op-position of *a*-oriented *BTO* are indicated as dotted orange horizontal lines in figure 3.16(b) and (d)). The center position

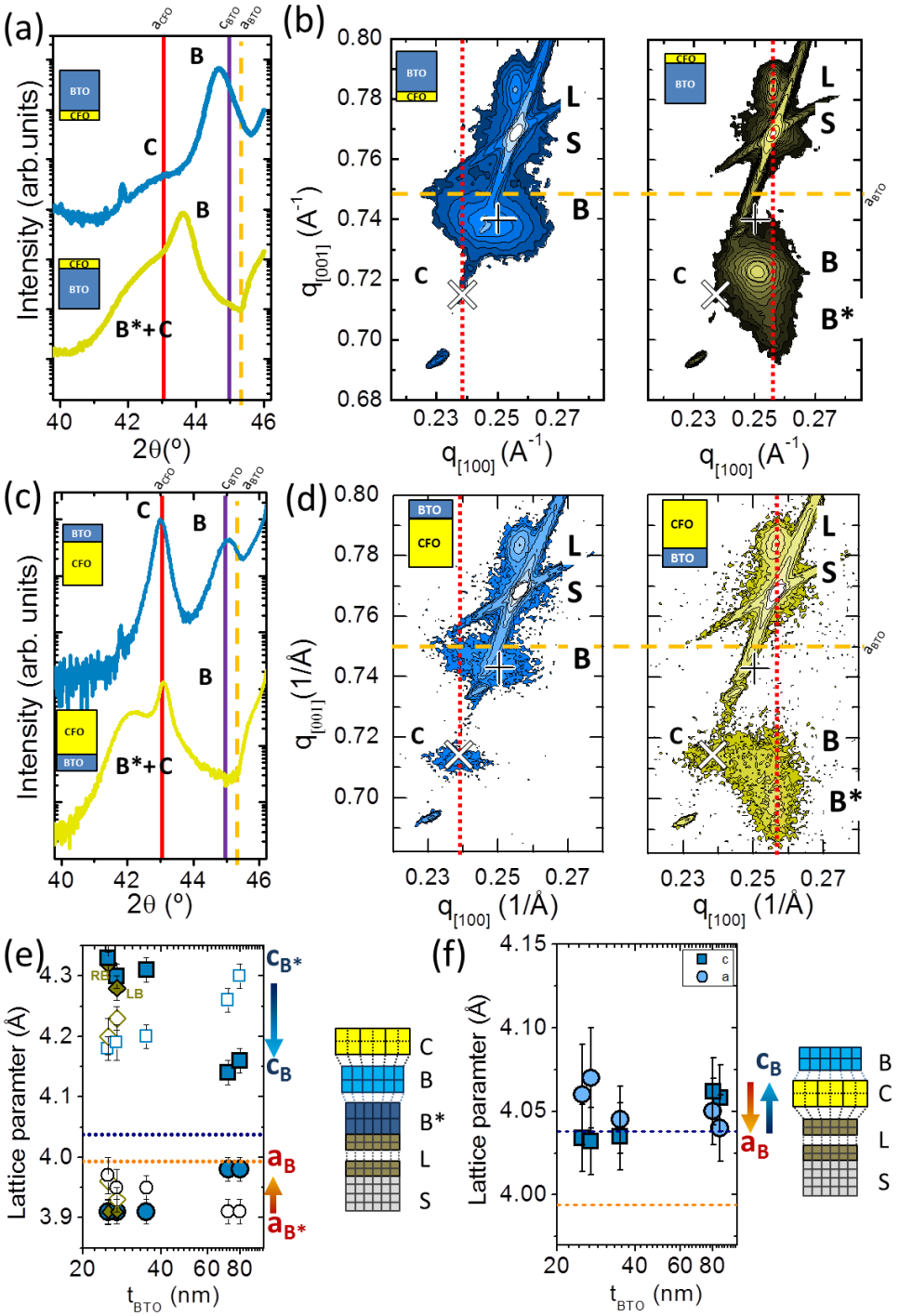

Figure 3.16: (a),(c) XRD $\omega/2\theta$ scan of a *BTO-top* (blue) and CBLS *BTO-bottom* (dark yellow) sample with thickness of (a) 80*nm BTO* and 7*nm CFO* and (c) 25*nm BTO* and 100*nm CFO*. Vertical lines mark the position of *CFO*(004) and *BTO*(002),(200) reflections in bulk. (b),(d) XRD RSM around (103) reflections of STO (S), LSMO (L) and BTO (B) and the (206) of CFO (C). The symbol + marks the position of BTO(103) reflection in bulk, and x CFO(206) bulk position. Red dotted vertical lines indicate in-plane parameter of the contact interface *BTO* is grown on (*LSMO* or *CFO*). An orange horizontal line marks the bulk position of the op-parameter for *a*-oriented *BTO*. Sketches indicate stacking order and approximate layer thickness. (e), (f) Calculated op and ip lattice parameter for *BTO*. Schemes on the side indicate relaxation depending on the stacking order.

of the 80 *nm* thick *BTO* layer correspond to a_{80}=4.04(4) Å and c_{80}=4.07(1) Å, while it is for the 25 *nm* thick layer a_{25}=4.06(4) Å and c_{25}=4.03(1) Å, for comparison the RSMs in figure 3.16(b) and (d) mark the bulk *BTO* position for *c*-oriented *BTO* (white cross) and the position of op-parameter corresponding to *a*-oriented *BTO* is marked as short dash horizontal line. The retrieved data points for all *BTO-top* samples are plotted in figure 3.16(f). Compared to room-temperature bulk *BTO* ($a = 3.994$ Å and $c = 4.038$ Å), the data indicates a nearly relaxed *BTO* is found for *BTO-top* with tetragonality ratios around 1.0 (*BTO-bulk* $c/a = 1.01$), whereas a strongly enhanced tetragonality in *BTO-bottom* ($c^*/a^* = 1.1$, relaxing with increasing thickness to $c/a = 1.04$).

In conclusion the strain state of *BTO* (bulk *BTO* c/a ratio is 1.01) is strongly dependent on its position in the heterostructure; in *BTO-bottom*, it grows compressively strained with a larger than bulk tetragonality (initially 1.1 and reducing with thickness to 1.04 in 80 *nm* thick samples), whereas in *BTO-top* it relaxes immediately resulting in a c/a-ratio $0.95 < c/a < 1.05$ (measured out-of-plane *c*-parameter close to bulk *BTO*).

3.3.3 Functional properties of bilayered heterostructures

A brief overview of the functional properties of the *BTO-CFO* bilayered heterostructures is now given (more details can be found in the PhD thesis of I. Fina [68] and [95]). The electric properties of the here discussed bilayers, were measured relative to their position of ferromagnetic *CFO* and ferroelectric *BTO* in the stack. We have shown that the stacking order strongly affects the strain state of *BTO* and thus it is expected that ferroelectric properties (polarization and critical temperature) are affected as well.

BTO-bottom bilayers show enhanced remanent (P_R) and saturation (P_S) polarization (up to P_R=54 $\mu C/cm^2$,P_S=64 $\mu C/cm^2$ – sample $SB_{25}C_{100}$) compared to the corresponding *BTO* bulk value ($P_{S\ bulk}$=26 $\mu C/cm^2$), when the *BTO* thickness is below around 35 *nm* see figure 3.17(a). Enlarged *P*-values for *BTO-bottom* have been reported previously [35], but the use of better lattice matched substrates (scandates) was necessary to avoid plastic relaxation. Nevertheless, it indicates that a strong enhancement of polarization is also possible with *STO* substrates. Also in *BTO-top* samples high polarization (P_R=15 $\mu C/cm^2$,P_S=33 $\mu C/cm^2$ – sample $SC_{100}B_{25}$) is found, see figure 3.17(b). This is remarkable, thus it suggests that the formation of *a*-oriented domains is minoritary in this heterostructure. Biferroicity is confirmed, the magnetic properties of the *CFO* in the heterostructures comparable to samples grown on bare *STO* substrates [96]; *i.e.* a slightly reduced saturation magnetization, respect to bulk, of around 250 emu/cm^3 and in-plane easy magnetization direction. Here example magnetization loops are shown for *BTO-bottom* ($SB_{25}C_{100}$) and *BTO-top* ($SC_{100}B_{25}$) grown on *SRO* electrodes (which are

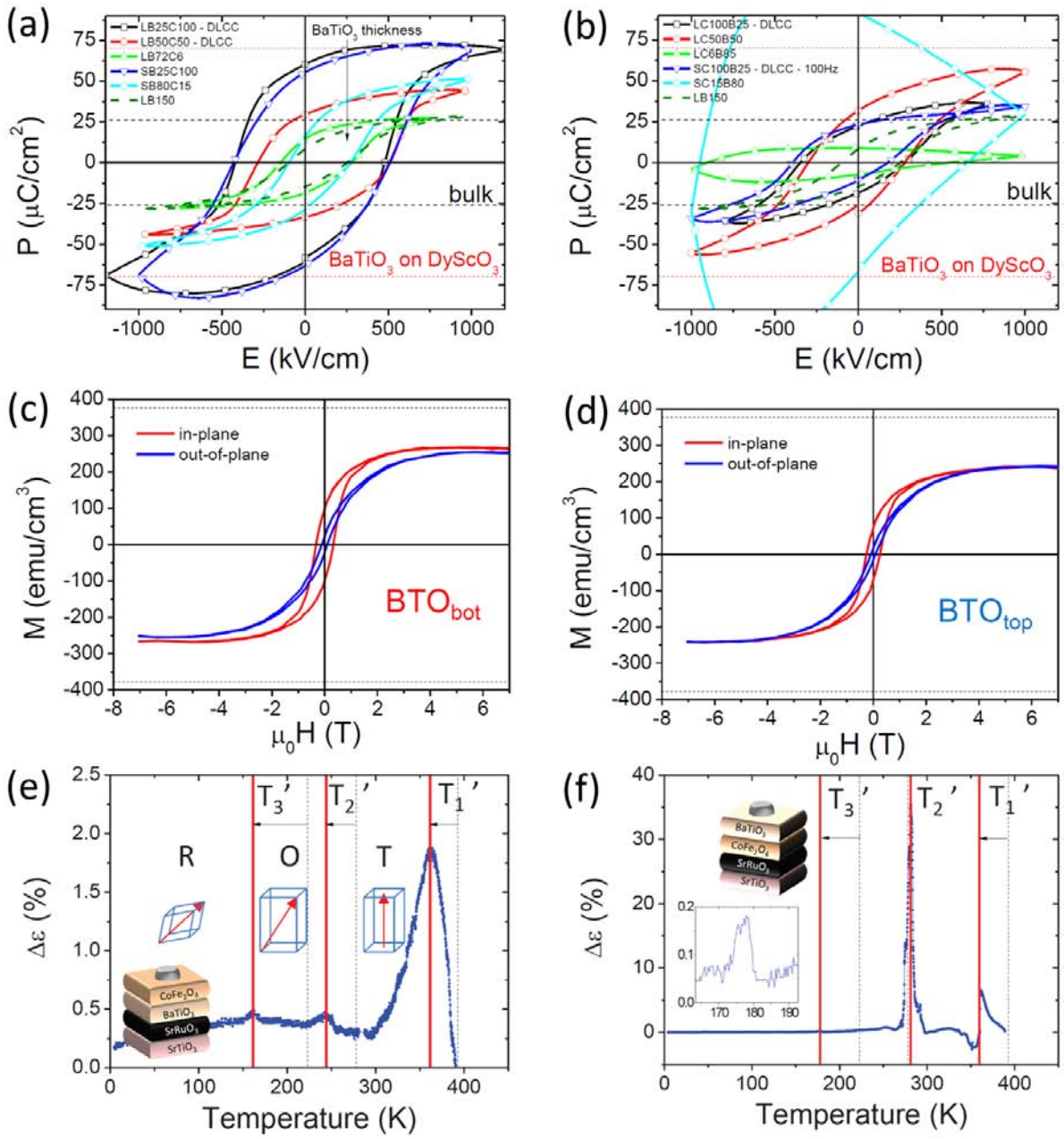

Figure 3.17: Polarization loops of obtained at $1kHz$ of BTO/CFO heterostructures. (a) for *BTO-bottom* (b) *BTO-top*. Horizontal lines (black dotted) bulk BTO polarization $26\,\mu C/cm^2$, (red dotted) strained BTO on $DyScO_3$ [35]. (c) and (d) Example M(H) magnetization loops for *BTO-bottom* and *BTO-top* samples on *SRO* electrode at room temperature. (a), (b), (e) and (f) are reproduced from [68]. (c) and (d) are reproduced from [95]

not ferromagnetic at RT) are shown in figure 3.17(c) and (d), respectively.

Furthermore, measurements of dielectric permitivity of BTO versus temperature reveal features at temperatures close to the characteristic structural bulk BTO transitions (BTO bulk transitions are at $T_1 \approx 120\,°C$ (cubic-tetragonal), $T_2 \approx 5\,°C$ (tetragonal-orthorombic) and $T_3 \approx$-90 °C (ortorhombic-rhombohedral); see also figure 1.5(c)). Inter-

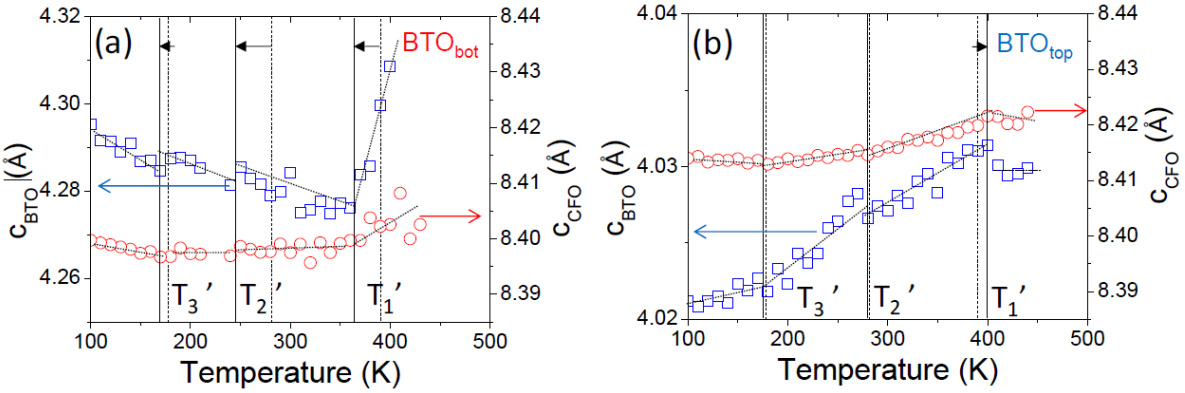

Figure 3.18: XRD $\omega/2\theta$ temperature dependence of bilayered heterostructures. Out-of-plane parameters for *BTO* (left axis, blue curve) and *CFO* (right axis, red curve) for (a) *BTO-bottom* ($LB_{25}C_{100}$) (b) *BTO-top* ($LC_{100}B_{25}$) heterostructures. Vertical dotted lines indicate bulk *BTO* transition temperatures and solid lines temperatures where a change in slope of *BTO* appear (indicated by lines behind the data points, as guide to the eye). figure is adapted from [95].

estingly, comparing these permittivity measurements vs. temperature, without and with applied high magnetic field ($\mu_0 H$=9 T), significant changes of the permittivity around the *BTO* transitions were observed. This can be interpreted as *direct magnetoelectric* response due to interface mediated coupling affecting structural phase transitions. A large variation around 36% was observed for *BTO-top* around 280 K, while the other transitions cause smaller changes. In *BTO-bottom* the changes are much weaker but still differences up to 2% are found. The data suggests, that clamping of the substrate does not fully suppress the structural transitions of *BTO* and it so does not impede magnetoelectric coupling. Additionally, magnetization versus temperature measurements of *CFO* grown on top of *BTO* (*BTO-bottom* sample $SB_{25}C_{100}$), a weak change of the magnetization at the *BTO* tetragonal to cubic phase transition around 360 K is observed [95], indicating that also a *converse magnetoelectric* effect occurs in this bilayered heterostructure. The tight binding at atomic level of the epitaxial grown thin film, and thus elastic clamping to the much thicker substrate, might hinder or slightly modify for structural transitions or mechanical responses of the film. In collaboration with colleagues from CNRS-Ecole Centrale (Paris) temperature dependent XRD $\omega/2\theta$-scans around the (002) substrate reflection was measured on this bi-layered structures. The data presented in figure 3.18 correspond to *BTO-bottom* ($LB_{25}C_{100}$) and *BTO-top* ($LB_{25}C_{100}$) heterostructures (similar to the heterostructures with the observed ME coupling, with the advantage that the reflection of the electrode layer is not interfering with the *BTO* reflection of the *BTO-top* layer). As expected linear temperature dependence of the *STO*(002) is found and served as control for the measurement. In figure 3.18(a) and (b) the temperature evolution of the out-of-plane parameters of *BTO* (left axis) and *CFO* (right axis), in the 90 K - 470 K temperature range, is shown for *BTO-bottom* and *BTO-top* respectively. *BTO-bulk*

transitions are indicated by dashed vertical lines (at temperatures T_1, T_2 and T_3) and the solid vertical lines (T_1', T_2' and T_3') indicate temperatures where changes of the slope of out-of-plane lattice parameter (of both *BTO* and *CFO*) are appreciated. Compared to *BTO-bulk* temperatures for *BTO-top* these changes appear about 30 °C below and *BTO-top* they coincide nearly with the bulk *BTO* transitions. Thus these measurements indicate that structural transition temperatures coincide with the temperatures where features in the permittivity were observed (see figures 3.17(e) and (f)). It is also remarkable that the out-of-plane parameters of *BTO* and *CFO* appear to change slope simultaneously, although much less pronounced for *CFO*, which may be interpreted as presence of a structural coupling between both layers. We can conclude that the elastic clamping to the substrate did not hamper the elastic interaction between *BTO* and *CFO* in these bilayer heterostructures, allowing observation of direct magnetoelectric coupling between *CFO* and *BTO* layers, which is a genuine indication of interface-mediated magnetoelastic response of *CFO* propagation in the thinner *BTO* layer.

3.4 Summary

We have optimized the conditions for the growth of *CFO* and *BTO* on *STO*(001) to achieve thin films with very smooth surfaces (*rms* roughness $< 0.2\,nm$). In the case of *CFO* kinetic limitation, using low growth temperature and high growth rate, was the key. In the case of *BTO*, moderately low growth temperature ($T_S \approx$ 700 °C) and pressure ($p \approx 0.02\,mbar$) are required for *c*-oriented films. The tendency to roughening is likely due to formation of multilayered islands. Using RHEED we demonstrate that growth interruptions permit smoothing of the surface, recovering conditions for layer-by-layer growth. The use of RHEED has also permitted monitoring *in-situ* the strain relaxation of *CFO* and *BTO*. *CFO* and *BTO* have been integrated in epitaxial heterostructures on *STO*(001) buffered with bottom electrodes, being *BTO* either bottom of top layer. *CFO* is ferromagnetic at room temperature with saturation magnetization values similar to the typically obtained in single films on *STO*(001) substrates. *BTO* is ferroelectric at RT. When *BTO* is bottom layer in the heterostructure, it is highly strained (c/a ratio is 1.1) and displays a highly enhanced polarization up to around $54\,\mu C/cm^2$. Such enhancement had been only achieved until now on more lattice matched scandate substrates. Epitaxy of *BTO* and *CFO* occurs with immediate lattice relaxation and the resulting *BTO* films presents bulk like ferroelectric properties. Temperature dependent measurements of electric permittivity and lattice parameters, show that anomalies in the electric permittivity coincides with structural transitions of the *BTO* layers. This suggests that at least partially the clamping to the rigid substrate is released and elastic coupling between the functional layers is possible.

Table 3.3: Sample list of grown *CFO* single layers grown by PLD.

Sample	T_S (°C)	**p** $(mbar)$	**f** (Hz)
A120217-02	500	0.1	5
CSTO-01	550	0.1	5
CSTO-02	600	0.1	5
CSTO-03	650	0.1	5
CSTO-04	700	0.1	5
CSTO-05	750	0.1	5
CSTO-12B	600	0.1	1
CSTO-23	600	0.1	2
CSTO-14	600	0.1	10
CSTO-17B	600	0.01	5
CSTO-16	600	0.05	5
A121120-01	550	0.1	1
A121122-01	750	0.1	1
A121120-02	700	0.1	10

Table 3.4: Sample list of grown *BTO* single layers grown by PLD.

Sample Name	Substrate	T_S (°C)	**p** $(mbar)$	**f** (Hz)
A091210-03	STO(001)	650	0.02	5
A091210-04	LSAT(001)	650	0.02	5
A091202-01	STO(001)	700	0.02	5
A091202-02	LSAT(001)	700	0.02	5
A091202-03	STO(001)	750	0.02	5
A091202-04	LSAT(001)	750	0.02	5
A091202-03	STO(001)	800	0.02	5
A091202-04	LSAT(001)	800	0.02	5
A091210-01	STO(001)	700	0.01	5
A091210-02	LSAT(001)	700	0.01	5
A091222-01	STO(001)	700	0.05	5
A091222-02	LSAT(001)	700	0.05	5
A091203-01	STO(001)	700	0.10	5
A091203-02	LSAT(001)	700	0.10	5
A100119-01	STO(001)	700	0.02	1
A100119-02	LSAT(001)	700	0.02	1
A100120-01	STO(001)	700	0.02	2
A100120-02	LSAT(001)	700	0.02	2
A100121-01	STO(001)	700	0.02	10
A100121-02	LSAT(001)	700	0.02	10
B100423	STO(001)	700	0.02	1 (RHEED)

Table 3.5: Sample list *BTO/CFO* bilayers and single *BTO* (700 °C, 0.02 *mbar*) and *CFO* (500 °C, 0.1 *mbar*) layers on *LSMO* (L) or *SRO* (S) buffered *STO*(001); in the text layer thickness is indicated by subindices for *BTO* (B) and *CFO* (C). The PLD cluster at ICMAB has two chambers with same geometry, although in the target–heater distance is $d_{T/H} = 47\,mm$ for PLD (no RHEED) and $d_{T/H} = 65\,mm$ for PLD (RHEED)

Sample Name	**Text Label**	**Substrate**	$\mathbf{f}_{BTO}$ (Hz)	$\mathbf{f}_{CFO}$ (Hz)	**PLD Chamber**
A100527-02	$SB_{25}C_{100}$	$SRO/STO(001)$	5	5	PLD (no RHEED)
B100720	$SB_{35}C_{50}$	$SRO/STO(001)$	2	5	PLD (RHEED)
A100528-01	$SB_{80}C_{15}$	$SRO/STO(001)$	5	5	PLD (no RHEED)
A101117-01	$LB_{25}C_{100}$	$LSMO/STO(001)$	5	5	PLD (no RHEED)
B100408	$LB_{72}C_{7}$	$LSMO/STO(001)$	2	5	PLD (RHEED)
A100727-01	$SC_{100}B_{25}$	$SRO/STO(001)$	5	5	PLD (no RHEED)
B100722	$SC_{50}B_{35}$	$SRO/STO(001)$	2	5	PLD (RHEED)
A100728-01	$SC_{15}B_{80}$	$SRO/STO(001)$	5	5	PLD (no RHEED)
A101116-01	$LC_{100}B_{25}$	$LSMO/STO(001)$	5	5	PLD (no RHEED)
B100426	$LC_{7}B_{85}$	$LSMO/STO(001)$	2	5	PLD (RHEED)
A100526-02	SB_{25}	$SRO/STO(001)$	5	–	PLD (no RHEED)
A101115-01	LB_{25}	$LSMO/STO(001)$	5	–	PLD (no RHEED)
A100527-01	SC_{100}	$SRO/STO(001)$	–	5	PLD (no RHEED)

CHAPTER 4

$BiFeO_3$–$CoFe_2O_4$ vertical heterostructures

It is known that preparation of single phase films presenting a volatile element requires precise optimization of growth conditions, i.e. $(Pb, Zr)TiO_3$, $BiMnO_3$ or $BiFeO_3$, which is basically due to volatility of Pb or Bi. Typically, an excess of the volatile element in the target is used, and the process conditions are optimized to loss this excess, in our case the *BFO* targets have an excess of 10% Bi (see Table 2.1). It was reported that for the growth of *BFO-CFO* nanocomposite thin films temperature and growth rate can be used to tune the pillar size without the authors concerning Bi-loss during growth [8, 28]. Nevertheless, a narrow window of suitable growth conditions is expected from previously studies of pure *BFO* [97, 98]. Which should strongly impact on crystal structure, stoichiometry and morphology. In thin films, epitaxial stress is another parameter that can strongly influence the crystallographic structure of the *BFO* phase [42, 46, 99, 100]. Thus epitaxial stabilization, facilitated by similar Gibbs energy of some *BFO*-phases [36], may allow the growth of other phases than the popular rhombohedral *R-BFO*. Indeed, a quasi tetragonal *T-BFO* phase with large c/a ratio has been stabilized in single phase thin films by several groups [41–43, 101–106]. A high ($150\,\mu C/cm^2$) polarization along the [001] axis, close-to-room-temperature phase transitions and huge piezoelectric effects caused by coexisting rhombohedral- and super tetragonal-like phases [43, 107, 108] are appealing for integration of *T-BFO* in nanocomposites.

Our aim is to gain knowledge on the growth parameters that allow to exploit the richness of this complex material without compromising stoichiometry. At first, we focus on the influence of the temperature and laser frequency (growth rate) during self-assembled growth of *BFO-CFO* columnar nanocomposites on (001) and (111) oriented *STO*

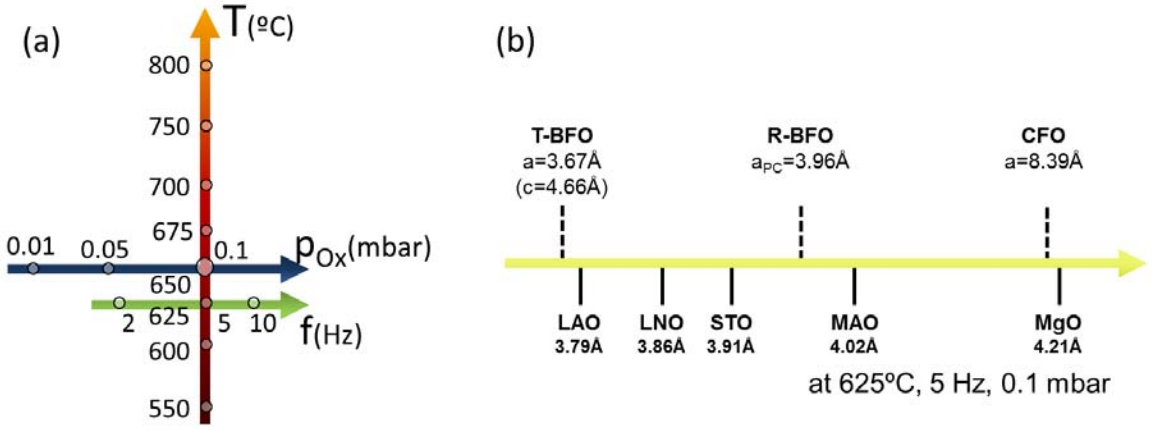

Figure 4.1: Schematic overview of the deposition conditions that have been varied for the *CFO-BFO* composite growth. The parameters used for optimization are growth temperature, pressure and laser frequency (a). At optimized growth parameters T_S=625 °C, 0.1 $mbar$ and 5 Hz the substrate were used to probe the influence on composite structure (b).

substrates, to investigate the impact on crystal structure, morphology, and stoichiometry and to elucidate the possibility to control pillar size and lateral ordering. Therefore, we optimized growth conditions to achieve nanocomposites with substrate texture and absence of additional oxide phases (Bi_2O_3 or Fe_xO_y reported for single *BFO* films [97, 98]). We considered oxygen pressure (0.01 to 0.1 $mbar$) and growth temperature (550 to 800 °C) at a fix fluency 1.8 J/cm^2 and 5 Hz laser repetition rate, see figure 4.1(a). A suitable region around 600 to 650 °C (0.1 $mbar$, 5 Hz) was identified. Hence a more detailed T_S series (600-675 °C) with smaller T_S-step was prepared and the influence of the overall growth rate, varied by the laser frequency (2 to 10 Hz), was investigated at T_S=625 °Cand $p = 0.1\,mbar$). Next, we were interested in stabilizing metastable supertetragonal *T-BFO* as matrix in nanocomposites as well as in single phase films on $LAO(001)$ substrates, exploring the influence of growth temperature in the range of 550 to 750 °C ($p = 0.1\,mbar$, $f = 5\,Hz$). Finally, we evaluate the effect of substrate induced stress on the composite structure and properties by growing on a variety of nanocomposite samples on lattice mismatched (001) substrates (see figure 4.1(b), all films were deposited at T_S=625 °C, $p = 0.1\,mbar$ and $f = 5\,Hz$).

A strong influence of the growth temperature and growth rate (laser repetition rate) is observed on the nanoobject morphology, basically due to reduction of the bismuth content as the deposition temperature increases or growth rate decreases. Consequently, deposition temperature and laser repetition rate are not suitable free parameters to control the nanoobjects morphology in *BFO* nanocomposites. We could stabilize metastabe tetragonal-like *T-BFO* as single phase films on $LAO(001)$ substrates – although in a very small growth temperature window (around 700 °C) – and as *T-BFO* matrix in columnar

composite films – in a much broader temperature range (550-675 °C). Nanocomposites with (00l) texture and column-matrix topology can be grown on substrates inducing compressive stress on *BFO*, while tensile stress favors its decomposition.

4.1 R-$BiFeO_3$–$CoFe_2O_4$ vertical heterostructures

4.1.1 Optimization of growth conditions

We have grown simultaneously *CFO-BFO* composites on *STO*(001) and (111). A moderate temperature of 650 °C, laser fluence of 1.8 J/cm^2 and laser repetition rate of 5 Hz might favor epitaxy and phase separation whereas avoiding deterioration of *BFO* due to *Bi* volatility. First, we explored the oxygen pressure p from 0.01 to 0.1 $mbar$, which is known to strongly influence the growth of single phase *BFO* [97]. Corresponding XRD $\omega/2\theta$ patterns are shown in figure 4.2(a) for (001) and 4.2(b) for (111) substrates (insets show an amplified region around a suitable substrate reflection and both film phases).

Vertical lines indicate the bulk positions for *CFO* and *BFO*. Clear phase separation is observed for 0.1 $mbar$, while at low pressure (0.01 $mbar$) only spinel oxide phase is visible on both substrates. Similar *BFO* decomposition at low deposition pressure was found for *BFO* single phase films [97]. We subsequently used 0.1 $mbar$ (5 Hz) when exploring the temperature range between 550 and 800 °C (temperature step 50 °C). The XRD $\omega/2\theta$ scans for samples grown on (001) and (111) substrate, are in figure 4.2(c) and 4.2(d), respectively. Data indicates that phase separated and epitaxial textured *BFO* and *CFO* with absence of other phases or orientations, only appears in a small range from around 600 °C to 650 °C. Samples prepared at 550 °C present minor presence of Bi_xO_y weak intensity of *CFO* and a broad *BFO* peak on (001) and nearly no reflection on (111) substrates are observed. Films grown above 650 °C present a strong decrease in *BFO* intensity, the appearance of Fe_xO_y reflections (labeled *FO*) or additional textures like spinel (110). To explore in more detail this narrow temperature window, we grew an additional series with smaller T_S step starting at 600 °C(0.1 $mbar$, 5 Hz).

The XRD $\omega/2\theta$ scans of these samples on *STO*(001) and (111) substrates are compared in figures 4.3(a) and 4.3(b), respectively. In all nanocomposite films, both the *BFO* (label B) and *CFO* (label C) phases are textured as the corresponding substrate, neither spurious phases nor other crystal textures are present (confirmed by full range scans, not shown here). The vertical lines mark the position of the reflections for bulk samples. Out-of-plane parameters $d_{CFO(hkl)}$ of *CFO* on *STO*(001) and (111), $d_{CFO(001)} \approx 8.37$ Å and $d_{CFO(111)} \approx 4.84$ Å, are measured for all growth temperatures. It corresponds to a compressive strain ε around -0.2 to -0.3% for both orientations. Concerning *BFO*

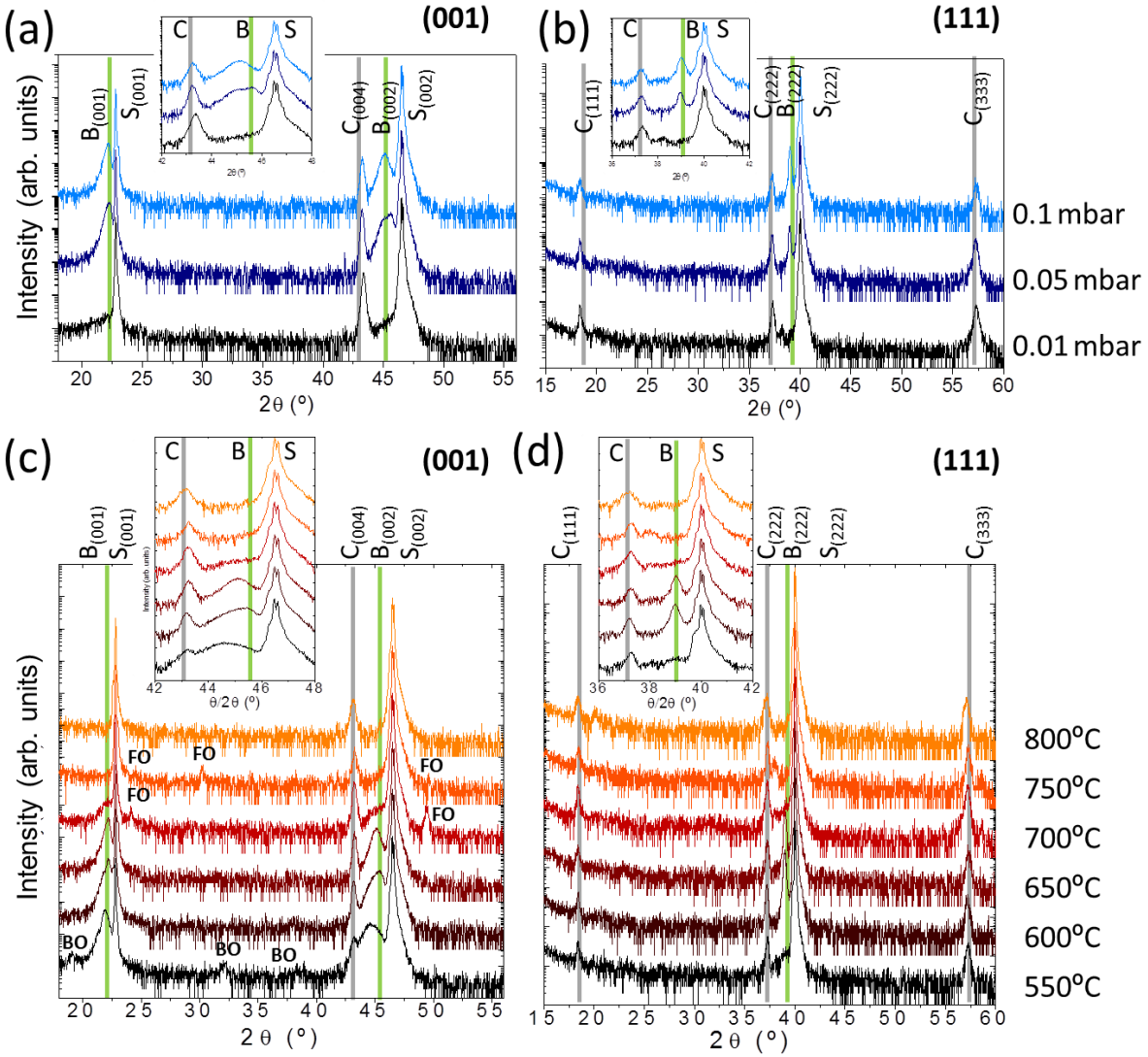

Figure 4.2: $\omega/2\theta$-scans for *CFO-BFO* composite samples with thickness around 100 nm grown at 650 °C and 5 Hz for different oxygen pressures (a) on $STO(001)$ and (b) STO(111). Composites grown at 0.1 $mbar$ and 5 Hz for a series of substrate temperatures on (c) STO(001) and (d) STO(111). Vertical lines indicate film reflections which are labeled C, B, S for *CFO*, *BFO* and *STO*. FO and BO refer to weak reflections of Fe_xO_y and Bi_xO_y, respectively.

reflections there is a double peak in the case of (001) films, corresponding to strained ($d_{BFO(001)} \approx 4.03$Å, $\varepsilon = 1.8\%$) and relaxed ($d_{BFO(001)} = 3.96$Å) *BFO*. The two peaks are labeled S for strained and R for relaxed *BFO*.

Appropriate deconvolution of the underlying R and S peaks (see figure 4.3(a)) allows determining the relative contribution to the diffraction pattern. The temperature dependencies of the $BFO(002)/CFO(004)$ peaks intensity ratio are shown as the inset of figure 4.3(a) for both R and S *BFO*. It turns out that the intensity ratio for the relaxed part decreases with the growth temperature, while the strained one remains constant (see inset in figure 4.3(a)). Thus, there is a reduction of the measured total diffracted intensity from *BFO* in the samples prepared at high temperature. In the case of films on $STO(111)$

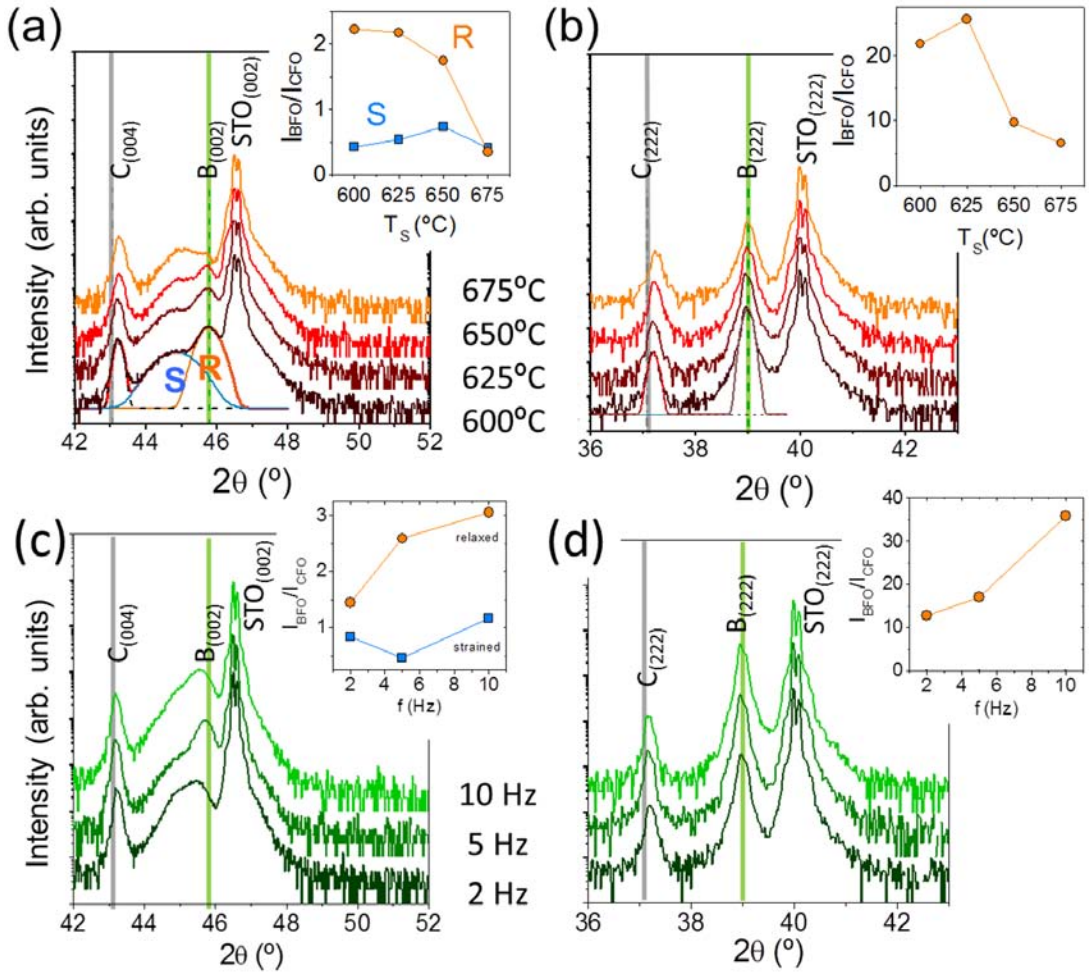

Figure 4.3: XRD $\omega/2\theta$ scans amplifications for samples grown at $0.1\,mbar$ and $5\,Hz$ for different temperatures on (a) STO(001) and (b) STO(111); and for films grown at 625 °C and $0.1\,mbar$ for different laser frequencies on (c) STO(001) and (d) STO(111). The vertical lines mark the position of bulk *CFO* (C) and *BFO* (B) reflections. Labels *S* and *R* correspond to strained and relaxed $BiFeO_3$, respectively. Insets: intensity ratio between *BFO* and *CFO* reflections as a function of the substrate temperature. Intensities were calculated from Gaussian fits (the corresponding ones to the 600 °C samples are shown in the main panels).

only fully relaxed *BFO* reflections ($d_{BFO(111)} = 2.29$Å) are observed (figure 4.3(b)). As well as for the films grown on $STO(001)$, a decrease of the BFO/CFO peaks intensity ratio with increasing growth temperature occurs (see the inset in figure 4.3(b)).

The laser repetition rate determines the average growth rate of the film and thus higher rate should favor the stabilization of *Bi* containing phase while lower rates favor its desorption. The XRD $\omega/2\theta$ scans of samples prepared at $f = 2$, 5 and $10\,Hz$ are presented in figure 4.3(c) and (d) for *STO* (001) and (111), respectively. Similar to the temperature series, we observe for both substrates phase pure textured films and as anticipated an decrease of the *Bi* content while lowering the laser repetition rate and the opposite tendency while increasing it. It will be shown below that the intensity reduction of the *BFO* peaks is due to the loss of *Bi* at high temperature.

Phase separation and epitaxial relationships

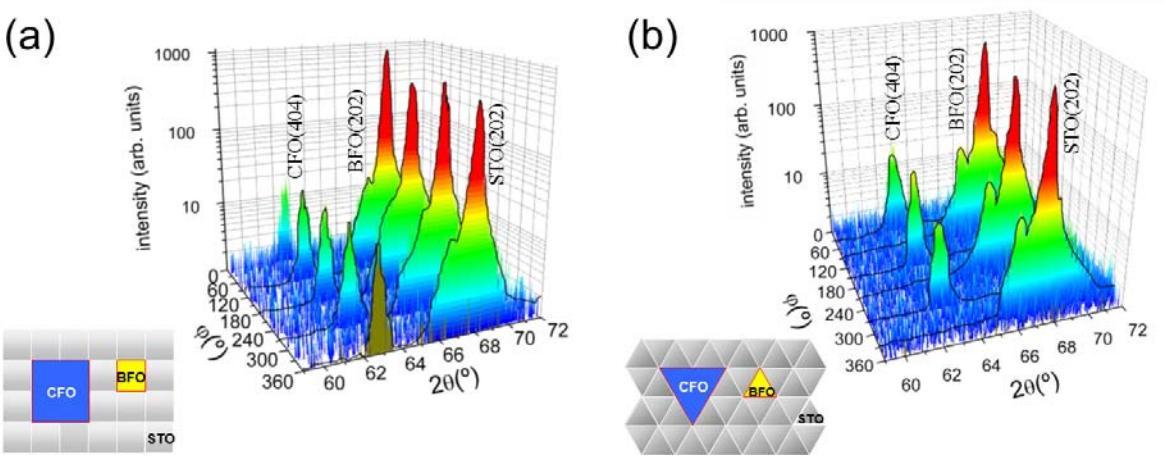

Figure 4.4: XRD $2\theta/\varphi$ maps for t=100 nm nanocomposite films grown at 650 °C on (a) STO(001) and (b) STO(111); sketches indicate the epitaxial relationship for each substrate.

$2\theta/\varphi$ area scans around asymmetrical reflections were collected to determine the in-plane texture, around the (202) substrate reflection. The scans show that spinel and perovskite phases grow epitaxially on both substrates. In the case of the (001) samples (figure 4.4(a)), there are four $BFO(202)$ and four $CFO(404)$ reflections occurring at the same φ angles of the $STO(202)$ ones. It indicates cube-on-cube epitaxial relationship of both phases with the substrate: $[100]BFO(001)||[100]STO(001)$ and $[100]CFO(001)||[100]STO(001)$. In the case of the (111) samples (figure 4.4(b)), there are three $BFO(202)$ reflections located at the same φ position that the $STO(202)$ ones, whereas the three $CFO(404)$ reflections are shifted by 60 °. The epitaxial relationships are $[1\text{-}10]BFO(111)||[1\text{-}10]STO(111)$ and $[11\text{-}2]CFO(111)||$ $[1\text{-}10]STO(111)$. Schematic drawings of the epitaxial relationships for (001) and (111) samples are plotted in figures 4.4(a) and 4.4(b), respectively.

Morphology

The dependence of the morphology on the deposition temperature and laser repetition rate is shown in the topographic AFM images in figure 4.5, for (001) films (T_S (a), and f (b)) and (111) films (T_S (c), and f (d)). Height profiles, along the lines marked, are presented below each image.

First, samples grown on (001) oriented substrates at different temperatures are discussed. Unless the sample deposited at 675 °C, the other (001) films present the expected [28] columnar growth of the *CFO* spinel with {111} faceted squared pyramidal objects, embedded in a flat *BFO* perovskite matrix, and oriented in-plane along [110] directions of the substrate. The morphology of both phases is illustrated with a 3d view

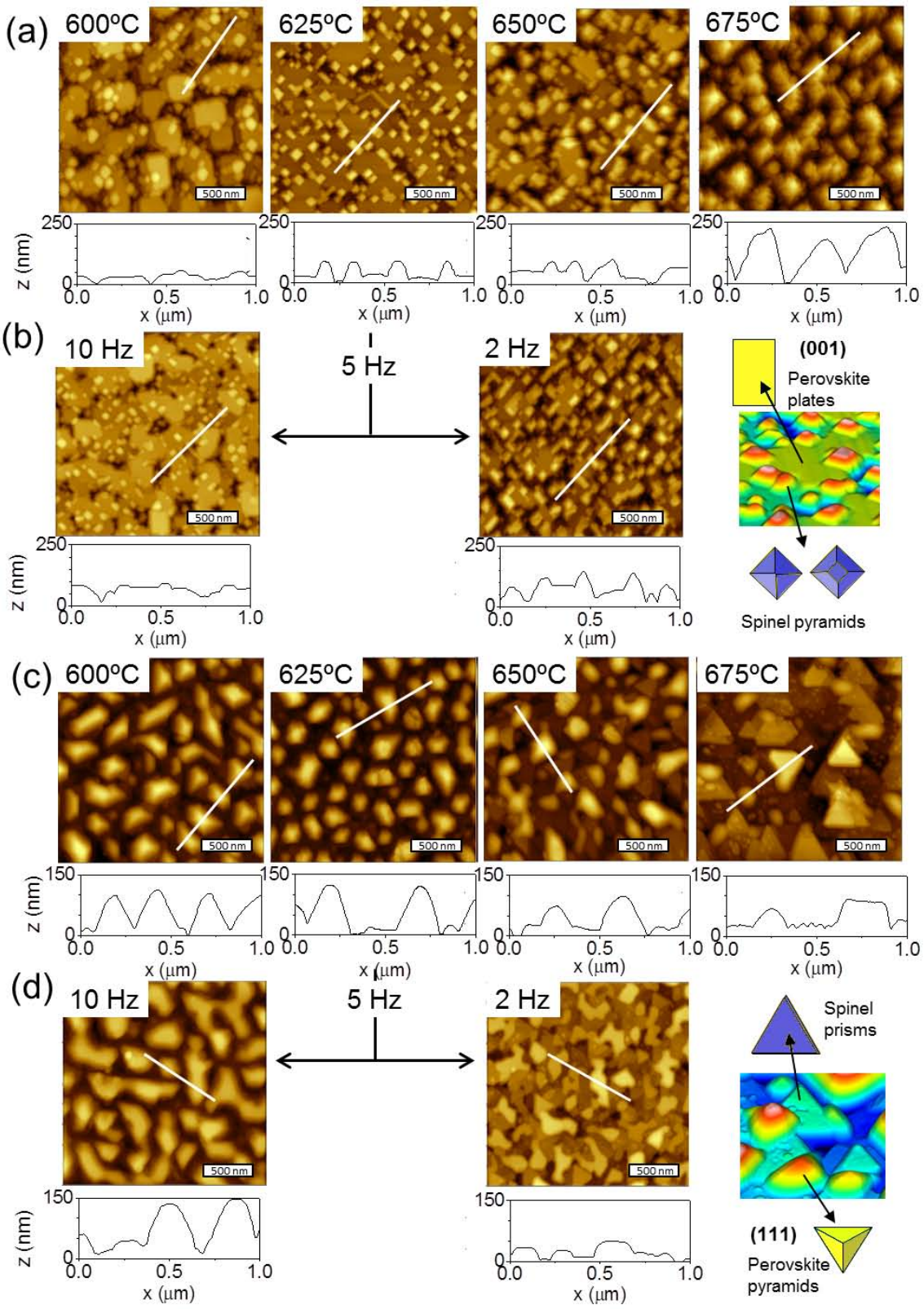

Figure 4.5: AFM topographic images of nanocomposite films on (a), (b) $STO(001)$ and (c), (d) $STO(111)$, grown at different substrate temperature and laser frequency, respectively. Line scan are indicated as white lines and plotted below each image. Panels on the right in (b) and (d) show a 3d view of an AFM image and sketches of the shape of the spinel and perovskite nanostructures for both orientations.

AFM image and sketches on the bottom right side of figure 4.5(b). The *CFO* pyramids protrude on *BFO* plates with varied height. Higher the deposition temperature, the pyramids stick out more on the *BFO* matrix (typical height in the 650 °C and the 625 °C are around $50\,nm$ and $20\,nm$, respectively). It causes the apparent lateral size of the pyramids to increase with the temperature. This is evident in the 675 °C sample, where the morphology is basically determined by {111} faceted pyramids. The laser repetition rate (figure 4.5(b)) and thus growth rate indicates a similar influence; while higher f corresponds to a reduction of T_S and reducing gr corresponds to an increased T_S. At high rate ($10\,Hz$) *BFO* plateaus with protruding pyramidal structures are present while for decreasing rate the *BFO* plateaus start to vanish and pyramid sizes are increasing (in average around $65 \pm 20\,nm$ at $10\,Hz$ and $100 \pm 35\,nm$ at $2\,Hz$).

In the case of (111) oriented samples, those deposited at 600 °C and 625 °C present a high density of 100 faceted triangular pyramidal *BFO* nanoobjects, as expected for this orientation and the dominant molar ratio of *BFO* respect to *CFO*. In the 650 °C sample there is a lower density of *BFO* pyramids, with lower height $60\,nm$, (much lower than the typical $110\,nm$ in height of the 625 °C sample). On the other hand some triangular prisms are observed, likely to be (111) oriented *CFO*. The change in morphology increasing temperature is dramatic in the 675 °C sample, where most of the islands are spinel prisms and only a small number of {100} faceted *BFO* pyramids are still visible. In the panel at the right the shape of the (111) oriented *BFO* and *CFO* nano-objects are sketched.

In the following the samples grown at optimal conditions (625 °C, $0.1\,mbar$, $5\,Hz$) on both substrates are described in more detail. Both SEM and AFM are used to complement the observations, see figure 4.6. First, in figure 4.6(a) a SE and a BS image of the (001) sample are shown in the top and bottom panel, respectively. The islands are formed with nearly square base and are clearly faceted, some appear to have a truncated top. The islands are oriented along [110] substrate directions and thus the pyramids facets can be expected to be {111}. Characteristic for the BS SEM image is that *BFO* phase corresponds to the bright regions. The contrast originates from the large the atomic number of Bi (Z=83) which is much higher than that of Fe (Z=26) and Co (Z=27). The topographic AFM image (figure 4.6(b)) gives additional information about the height of the objects and identification of the facets. As can be seen, *BFO* is a flat matrix surrounding the *CFO* islands, which have pyramidal shape and some show a flat top (truncated pyramids). The bottom panel in figure 4.6(b) shows the cosine filtered AFM image, light contrast corresponds to flat regions while dark contrast corresponds to tilted planes. The directional slope distribution (figure 4.6(c)) was calculated of the shown AFM image. In the center a large dark spot accounts for the large amount of flat region in the sample. Also four arms in [110] sample direction can be seen, they basically correspond to the tilted facets of the

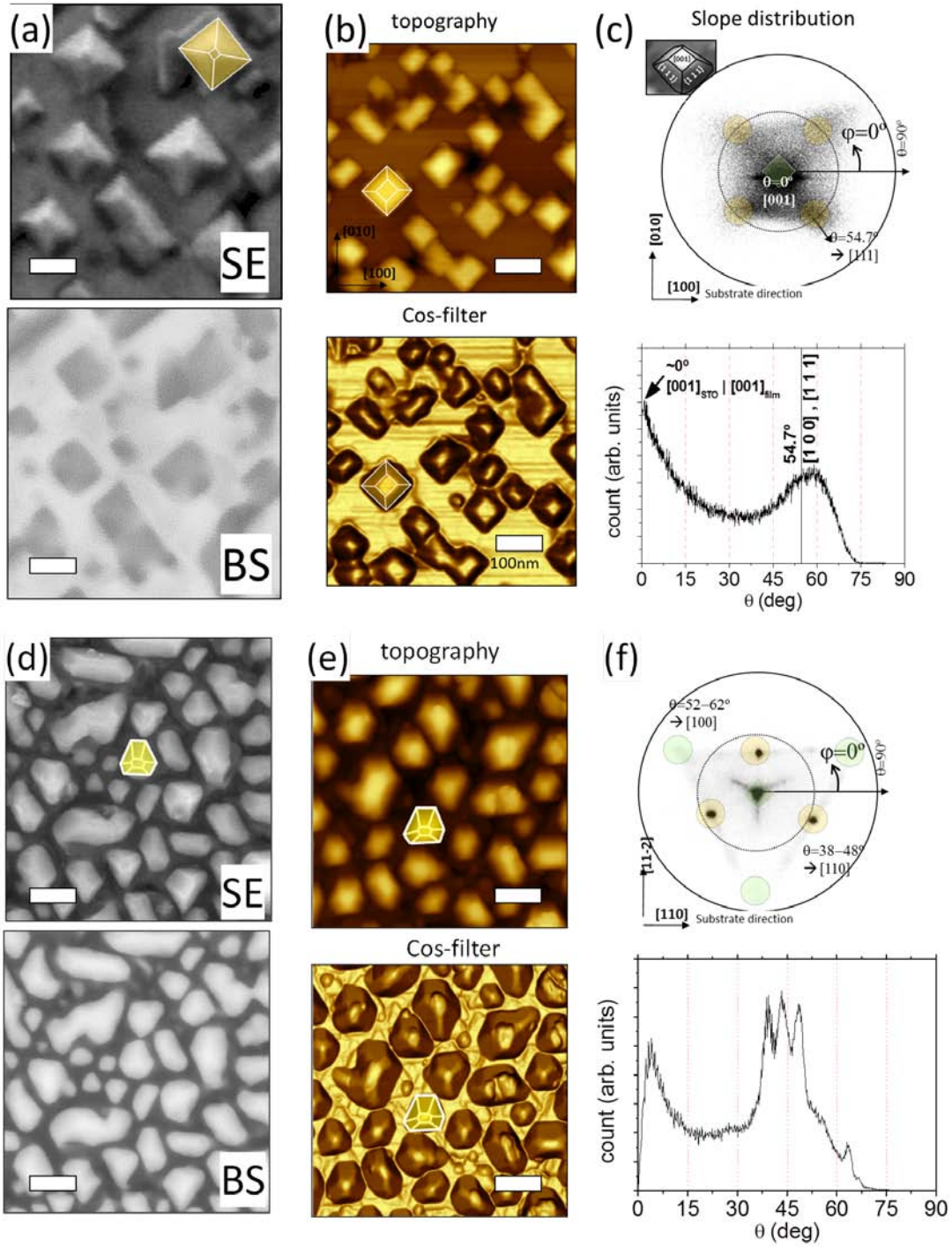

Figure 4.6: Morphology of *CFO-BFO* composites grown on *STO*(001) ((a)-(c)) and *STO*(111) ((d)-(f)) at optimal growth temperature (625 °C, 5 Hz and 0.1 mbar). (a), (d) Secondary electrons (SE) images (top) and backscattered electrons (BS) image bottom. *Bi*-rich phase appears bright, thus $Z_{Bi} = 83$ compared to $Z_{Fe} = 26$, $Z_{Co} = 27$ rich spinel phase. Note that in (001) films the matrix is *BFO*, while in (111) it forms the islands. (b), (e) AFM topography (top) and same image with cosine filter applied (bottom), bright and dark contrast correspond to local flat and inclined surface planes, respectively. (c), (f) Calculated slope distribution as slope angle θ/φ map (top) and as slope count vs. slope angle θ (bottom).

pyramids. Below the slope distribution a statistical count of the overall tilt angles reveals two peaks one around 0 ° (flat regions) and a second one around 60 °corresponds to the tilted planes of the pyramids and correlates well with the expected 54.7 ° of {111} spinel planes.

Similar measurements were performed for the (111) oriented samples. Here also islands and a flat matrix are identified, but being the *BFO* islands and the *CFO* matrix. The BS image in figure 4.6(d) shows islands with a strong bright contrast (*Bi* rich), while the *CFO* matrix remains dark. The surface area occupied by the islands reflects to the ratio of *BFO*/*CFO* is 65/35) having in mind the island strongly protrude from the surface. (111) oriented perovskite islands are expected to from {100} surface facets [8, 28] and triangular base. Though, islands in our samples show a higher number of facets. Most have a more hexagonal-like base and show six instead of three facets (see figure 4.6(e)). Also a slope distribution was calculated and reveals three mayor facets slopes (see three dark spots 120 ° rotated in the sample plane). The slope varies slightly around 45 °(one peak at 38 °, one at 44 ° and one at 50 °), see figure 4.6(f). Sixty degrees rotated to this spots one can observe much weaker spots corresponding to tilt of about 60 °. Considering a cubic structure with (111) plane facing up, it acounts for 0 ° while cutting {111} planes form facets with an angle of 70.5 ° with this plane. Also, {110} and {100} planes may form facets at 35.3 ° and 54.7 °, respectively. Considering the flat spinel prisms they basically contribute to 0 ° slopes. Facet analysis of most samples reveal peaks around 35-40 ° as well as 50-55 ° indicating that the surface of *BFO*(111) islands is composed of both {100} and {110} facets.

4.1.2 Limitations by Bi-volatility

The strong reduction of the intensity of the *BFO* reflections at the highest temperatures could signal *Bi* loss that would decrease the amount of *BFO* in the nanocomposite thin films. Although XRD measurements only revealed presence of Fe_xO_y phases in films deposited at temperatures above 700 °C, reflections from some of these phases could overlap with the $CoFe_2O_4$ spinel ones (Fe_3O_4 and γFe_2O_3 also spinel structure with similar lattice parameters: $a_{CFO} = 8.392$ Å, $a_{Fe_3O_4} = 8.394$ Å, and $a_{\gamma\, Fe_2O_3} = 8.352$ Å). We performed chemical analysis by EDS and WDS on $t = 100\,nm$ (001) samples to quantify the composition. The dependence of the $[Co]/[Fe]$ and $[Bi]/([Co]+[Fe])$ cationic ratios, obtained by WDS, on the deposition temperature is plotted in figure 4.7(a) and for the laser repetition rate in 4.7(b) (note T_S is fixed at 625 °Cfor the *f*-series). Previously measured morphology by AFM (figure 4.5(a) and (b)) is likely to show a correlation between morphology and the film composition. This can be directly observed in the

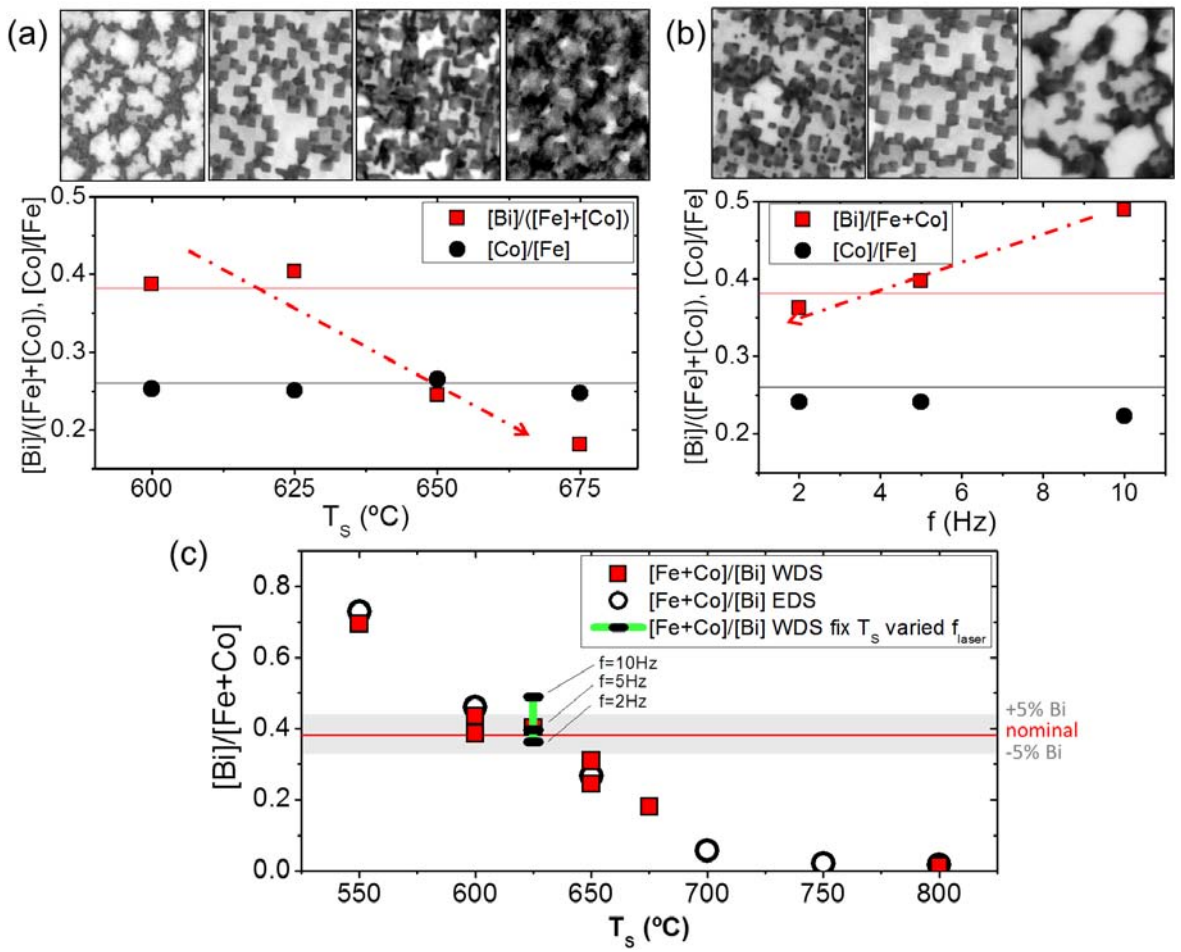

Figure 4.7: Cationic composition ratio, $[Co]/[Fe]$ and $[Bi]/([Co]+[Fe])$, as a function of the substrate temperature (a) and laser repetition rate (a). The upper panel show the backscattered electrons FSEM images for the corresponding parameter. Composition was measured by WDS for films with $t = 100\,nm$. (c) $[Bi]/([Co] + [Fe])$ composition over a larger temperature range 550-800 °C (open data points are measured with EDS, filled data points with WDS), the WDS data for fixed T_S but varied f are integrated as green vertical line with black bars as data points labeled correspondingly. A gray region of ±5% around the nominal $[Bi]/([Co] + [Fe])$ is indicated as well.

BS electron images, upper panels in figure 4.7(a) and (b). The $BiFeO_3$ phase (matrix) is identified as the bright regions, containing the heavy element Bi Z_{Bi}=83), while the darker regions are CFO columns (Z_{Fe}=26 and Z_{Co}=27). Inspection of these images shows a monotonic reduction of the surface fraction of the matrix vs. increased substrate temperature, it is less obvious for the f series, here the amount of matrix is reduced with reduced growth rate (lower f). Thus the BS electron images identify a direct correlation of Bi los as substrate temperature is increased or laser repetition rate is reduced.

The chemical analysis by WDS indicates, that the $[Co]/[Fe]$ ratio fits approximately the nominal value (0.26) for all films; Bi-content is mapped by the $[Bi]/([Co]+[Fe])$ ratio and varies significantly. Only in samples grown at 600 and 625 °Cand $2 - 5Hz$ the ratio is around the nominal one (0.38), a substantial reduction of the Bi amount

increasing the substrate temperature above 650 °C is appreciated. On the other hand, a rather strong increase of +10% Bi content is observed for faster laser repetition rate ($10Hz$). This tendency of the measured composition fits well with data from other growth series, with samples prepared in a broader temperature range (figure 4.7(c), measured by EDS and WDS, for completeness the series of varied laser repetition rate is integrated as vertical green line with labeled bars as datapoints). There is a strong and monotonic reduction of the $[Bi]$ compared with ($[Co]$+$[Fe]$) as temperature increases, and samples with $T_S \geq$ 700 °C are virtually Bi free. Nevertheless, before formation of Fe_xO_y phases occurring at higher Bi deficiency, some Bi deficiency in the BFO matrix could occur as a first option for stoichiometry accommodation, as recently suggested by the possibility of a significant Bi deficiency in BFO single layers [109, 110]. But also integration of excess Fe in existing CFO columns may accommodate a certain off-stoichiometry caused by Bi loss. This may indicate the absence of an optimal growth window with fully stoichiometric $BiFeO_3$-$CoFe_2O_4$, and thus T_S or f may not be considered free parameters to change the lateral dimensions or distribution. We also may conclude that stoichiometric samples can be grown at 625 °C considering the other growth parameters as constant (*i.e.* laser fluence, oxygen pressure, target substrate distance), which in real experimental conditions may slightly vary due to the instrumental errors. We may have to consider a band of ±5% around the nominal Bi content as our optimal growth conditions as indicated in figure 4.7(c).

The magnetic hysteresis loop of a nominally stoichiometric (001) sample (deposited at 625 °C) is displayed in figure 4.8(a), with the magnetization normalized to the CFO volume (39%). The loop is completely saturated above around 20 kOe, and the coercive field (see the inset) is around 1.5 kOe. The saturation magnetization of the samples is plotted in figure 4.8(b) against the substrate temperature. We note that CFO volume is considered to be constant in all samples since they were deposited sequentially and using the same number of laser pulses. The samples deposited at the lower temperatures, 600 °C and 625 °C, have magnetization saturation around 440 emu/cm^3, which closely fits the bulk magnetization (fully inverse CFO $M_S = 380$ emu/cm^3, partially inverted CFO experimental $M_S = 430$ emu/cm^3 [111]). With increasing Bi loss (increased T_S) there is an enhanced magnetization in the nanocomposites deposited at higher temperature, particularly in the 675 °C sample. It is noted that the 650 and the 675 °C samples were deficient in Bi in around 35 and 52%, respectively, whereas their saturation magnetization, compared with the value of the stoichiometric samples, is increasing by around 12 and 35%, respectively. Though formation of additional magnetic phases like γFe_2O_3 or Fe_3O_4, as well as off-stoichiometric $CoFe_2O_4$ ($[Co_xFe_{1-x}O] \cdot [Co_{1-x}Fe_{1+x}O_3]$) should increase the expected nominal film magnetization, where the saturation magnetisation of this phases

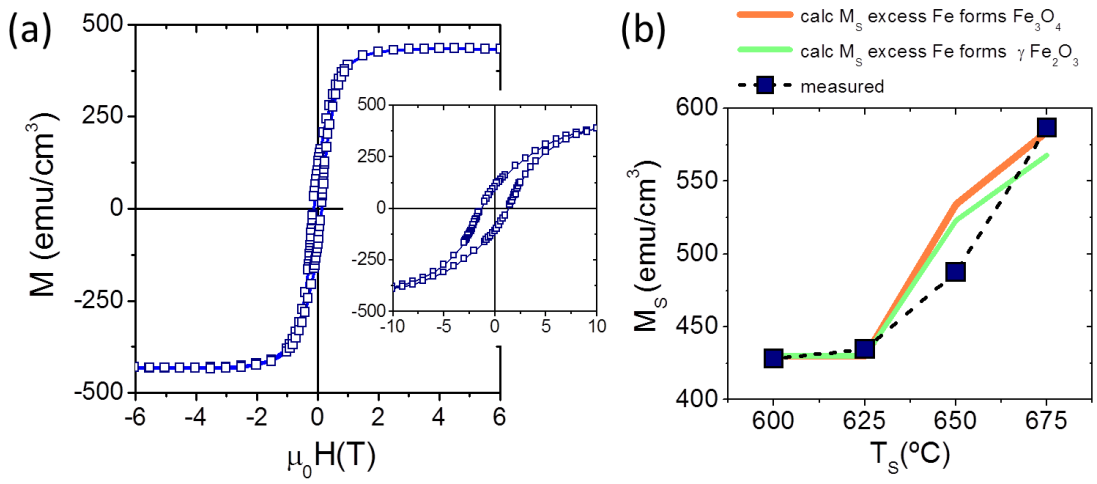

Figure 4.8: (a) Magnetization hysteresis loop (measured at room temperature, with the field applied in the plane) of a $t = 100\,nm$ sample deposited at 625 °C on $STO(001)$. A zoom of the low field region is in the inset. (b) Saturation magnetization normalized to $CoFe_2O_4$ volume plotted against the T_S. Red and green line show calculated M_S for the formation of γFe_2O_3 and Fe_3O_4 phases resulting from Fe excess after Bi loss in $BiFeO_3$.

are $M_{S\ [\gamma Fe2O3]} = 390\ emu/cm^3$ and $M_{S\ [Fe3O4]} = 480\ emu/cm^3$and off-stoichiometric CFO could be considered to have $390 < M_S < M_{S\ [Fe3O4]}$ (CFO considered Co remains on B-sites). If we simplistically assume that the excess Fe of $BiFeO_3$ after Bi loss is integrated in the film as γFe_2O_3 or Fe_3O_4, we can estimate the additional volume for this phase fraction at each temperature (here for simplicity we assume $M_S\,bulk = 430\ emu/cm^3$ which is about the value of stoichiometric samples (600 and 625 °C). The volume fraction of CFO remains constant (39%) the additional magnetic fractions for a Bi loss of 35% (650 °C) are $V_{\gamma Fe2O3} = 9.3vol\%$ ($+M_S = 93\ emu/cm^3$) and $V_{Fe3O4} = 8.5vol\%$ ($+M_S = 138\ emu/cm^3$), whereas for Bi loss of 52% (675 °C) one obtains $V_{\gamma Fe2O3} = 13.8vol\%$ ($+M_S = 104\ emu/cm^3$) and $V_{Fe3O4} = 12.5vol\%$ ($+M_S = 154\ emu/cm^3$). The resulting values of the saturation magnetization are plotted as lines in figure 4.8(b), and match relatively well with the measured data points. The measured magnetization increase at 650 °C is lower than the calculated one, which may suggests that part of the Bi deficit could be accommodated in a $Bi_{1-x}Fe_2O_3$ matrix [109, 110].

We notice that the presence of ferromagnetic $Fe-O$ phases in the case of single BFO films [97, 112] was only observed at pressures below $10^{-3} - 10^{-2}$mbar for similar growth temperatures. In XRD scans we do not observe diffraction peaks corresponding to α-Fe_2O_3 non FM phase in the nanocomposites deposited at 650-675 °C and an oxygen pressure of $0.1\,mbar$. Therefore we should conclude that the codeposition of BFO with CFO somehow favors the stabilization of magnetic $Fe-O$ oxides at relatively higher oxygen pressures. The microscopic mechanism for such reinforced stabilization remains unknown at present. However, the existing spinel structure CFO crystallites, may act

as template and promote, via epitaxial stabilization, the growth of isomorphous Fe-O magnetic oxides (i.e γFe_2O_3 or Fe_3O_4) on their surface. Due to the expected similar shape of crystallites of γFe_2O_3 or $Fe_3O_4$and $CoFe_2O_4$ morphological inspection using SEM and AFM did not allow distinction among them.

The instability of *BFO* during the growth of $BiFeO_3$-$CoFe_2O_4$ nanocomposites thin films (as well as single phase $BiFeO_3$ films) might be directly related to sublimation of Bi since its vapour pressure at 675 °Cis slightly lower than $10^{-2}\,mbar$ [113]. Moreover, the reported vapor pressure refers to equilibrium data of a condensed phase and its vapor, during heteroepitaxial growth of a two phases nanocomposite the process is more complex, with the probability of Bi adsorbtion on *CFO* islands expected to be low, due to the high structural dissimilarity.

4.1.3 Strain effect in $CoFe_2O_4$-$BiFeO_3$ composites on $SrTiO_3$(001)

Strain of *BFO* and *CFO* in *CFO-BFO* Composites

In previously discussed XRD $\omega/2\theta$-scans (figure 4.3) of samples on STO(001), strained (S) (c_S = 4.04Å) and relaxed (R, c_R = 3.96Å) fractions of *BFO* were identified. The peak around 45.78 °, labeled R, corresponds to the $BiFeO_3$(002); its position matches the position of bulk *BFO* (a_{BFO} = 3.96Å) thus signaling the presence of relaxed *BFO*. On the other hand the strained (S) fraction might have two different origins. First, the *BFO* layer (matrix) in contact with the *STO* substrate could be coherently strained to the substrate. As *BFO* has a larger lattice parameter than *STO*, with moderate lattice mismatch of +1.4%, it could be in-plane compressed and out-of-plane expanded (supposing a constant unit cell volume). A second origin for a larger out of plane parameter of the S-*BFO* might be a thin *BFO* layer forming at the vertical surface of *CFO* columns. The column surface area in contact with *BFO* matrix could be significant and as *CFO* lattice parameter is larger than *BFO* (mismatch -5.6%, considering *CFO* as substrate), thus *BFO* could be tensile strained in the out-of-plane direction and thus show enlarged c-paramter.

We have grown nanocomposite films with thickness from 10 to 200 nm. figure 4.9(a) shows corresponding XRD $\omega/2\theta$ scans around the STO(002) reflection. While the intensity of the strained (S) *BFO* fraction remains constant with thickness the intensity of the relaxed (R) *BFO* fraction increased steadily. This indicates that the origin of the strained *BFO* is likely caused by *BFO* epitaxially strained to the substrate, as an increased S intensity would be expected if it is caused by the *CFO-BFO* interface (increasing amount with thickness). The XRD RSM for a 200 nm thick film (figure 4.9(b)) indicates that the R fraction is in-plane and out-of-plane relaxed (a, c = 3.96Å), while S fraction has the

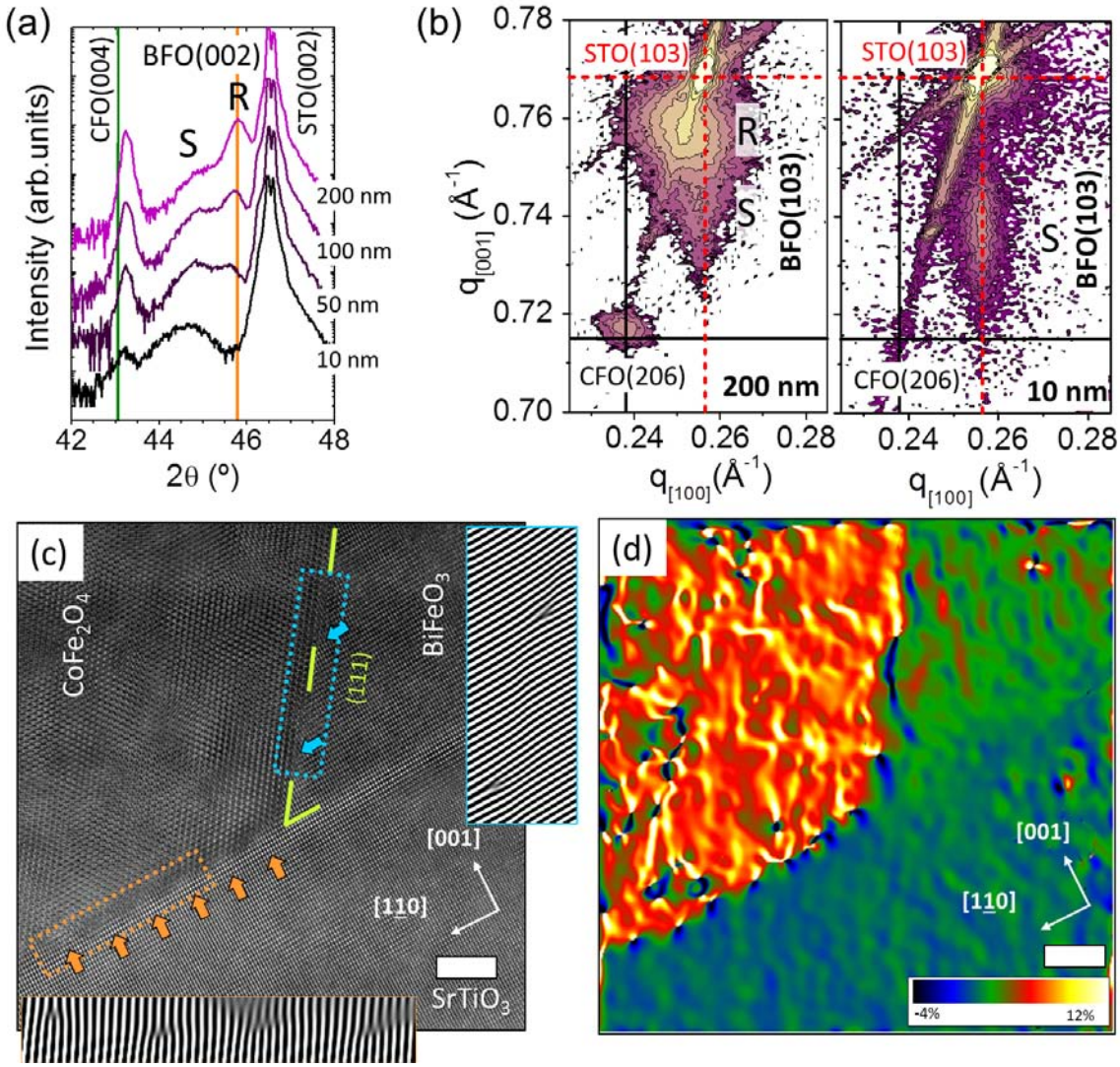

Figure 4.9: (a) XRD $\omega/2\theta$ scans around the $STO(002)$ reflection for a several thicknesses, the samples have been grown at 650 °C. Vertical lines indicate bulk film positions. R and S correspond to relaxed and strained $BFO(002)$ (b) reciprocal space maps for thicknesses $t = 200\,nm$ and $10\,nm$. Vertical and horizontal lines indicate positions for $CFO(206)$ and $STO(103)$ bulk reflection. (c) HRTEM image and (d) geometric phase analysis (GPA) deformation map along the [110] direction, the reference being taken in the STO substrate. Scale bars correspond to $5\,nm$.

same in-plane parameter as the substrate (main peak is elongated along the in-plane STO position, indicated by a vertical dotted red line). As the S fraction in the $200\,nm$ thick film is partially overlapped by the main R-peak, we compare the RSM of the $10\,nm$ film (figure 4.9(b)), here only S BFO fraction is present and its in-plane parameter ($a = 3.905$Å) clearly coincides with the substrate and elongation in out-of-plane direction is evident ($c = 4.04$Å). High resolution TEM images were used to investigate the interfaces at a local scale, in figure 4.9(c) a region with a triple interface including substrate and both CFO and BFO phases, which interface is formed by (111) plane (zone axis is $[1-10]$). Similar inverted CFO pyramids close to the substrate were reported for $BiFeO_3$-$CoFe_2O_4$ [8] and

$PbTiO_3$-$CoFe_2O_4$ [114] nanocomposites.

A deformation map (figure 4.9(d)) derived by geometric phase analysis (GPA, see reference [115] for more details) indicates that the interface of *BFO* respect to *STO* presents no in-plane misfit contrast and thus is fully epitaxial strained by the substrate (in the imaged area). Therefore, relaxed and strained *BFO* coexist, with S fraction originated at the substrate interface and R evolving by relaxation during film growth, compatible with XRD measurements. FFT filtered areas (insets in figure 4.9(c)) of the HRTEM image indicate dislocations (marked by arrows) formed in both *CFO*/*STO* and *CFO*/*BFO* interfaces, and thus signaling both interfaces are semicoherent. The in-plane deformation of *CFO* relative to the *STO* substrate in figure 4.9(d) leads to an in-plane misfit of about $7.4 \pm 0.9\%$ signaling a complete in-plane relaxation (mismatch *CFO*/*STO* = 7.45%), in agreement with XRD RSM (figure 4.9(b)). Nevertheless, the XRD results from $\omega/2\theta$ and RSM indicate that *CFO* is compressive strained along the *c*-axis ($\varepsilon \approx -0.2\%$) In the $\omega/2\theta$ scan (figure 4.9(a)) the *CFO*(004) peak is at 2θ=43.2° ($c_{CFO} \approx 8.37$ Å) with no significant variation for increasing thickness; and is smaller than bulk *CFO* (8.39 Å). Indeed, $a_{CFO,bulk}/2 = 4.196$ Å $a_{STO} = 3.905$ Å, an elongation of the *c*-axis of *CFO* rather than a compression should be observed. On the other hand the *CFO* out-of-plane compression could also be elastic residual strain caused by the ferroelectric phase, since *BFO* nanocomposite phase cause compressive stress on *CFO* along the growth direction ($a_{BFO\,bulk} = 3.96$Å, $c_{BTO\,bulk} = 4.038$ Å $< a_{CFO\,bulk}/2 = 4.195$ Å). This assumption is compatible with the experimental observation of the relaxed (bulk-like) in-plane *CFO* parameter, thus discarding substrate-induced *c*-axis deformation, and compression in the out-of-plane direction. Also, vertical deformation of *CFO* by *BFO* would be compatible with observations of vertical strain in columnar nanocomposite films of other complex oxides [24, 25].

Summarizing, *BFO* starts to grow fully strained to the substrate and then relaxes with thickness. On the other hand, *CFO* is fully in-plane relaxed (directly at the substrate interface) while an out-of-plane compression about -0.2% is observed. Despite semicoherent interfaces between *CFO* and *BFO* the compression may be caused by the *BFO* matrix surrounding the *CFO* columns.

Release of residual strain in *CFO* by selective etching of the *BFO* matrix

A simple way to definitively determine if the *CFO* residual strain is elastic and caused by the *BFO* phase, might be removing the *BFO* matrix by selectively by chemical etching, and measure the influence on the remaining *CFO*. The {111} faceted *CFO* planes present a high chemical stability and as also {111} nanofaceting along the *CFO* - *BFO* vertical

interfaces [114] should facilitate the removal of *BFO* leaving the *CFO*-columns standing free. We used 10% HCl solution for the etching process, and 180 s etching time was enough for the removal of the matrix (in a 100 nm thick film), as confirmed by SEM, thus longer etching times removed the film completely. For the experiments we chose a sample at optimal growth conditions with nominal thickness of 100 nm. The image in figure 4.10(a) is a secondary electrons SEM image (tilted about 45 °) of the sample before etching and the inset is the overlayed backscattered electron image showing the *BFO* matrix as bright contrast. After etching (figure 4.10(b)) the morphology changes dramatically, as the matrix is no longer observed. Only in some places one can observe a small bright contrast in the BS SEM image (inset figure 4.10(b)). The sketch in figure 4.10(c) roughly summarized the process and the corresponding morphologies. The removal of *BFO* is also evident from XRD and EDX measurements (figure 4.10(d) and (e)). The XRD $\omega/2\theta$-scan shows a total removal of the relaxed *BFO* reflection ($\approx 45.7\,°$) present in the as-grown diffraction pattern (black curve) in comparison with the etched film (red curve), note that the films are vertically offset by factor 10 to permit better visibility. A small peak corresponding to strained *BFO* still remains (about 1/3 the intensity of the unetched film). Also the EDX spectra (figure 4.10(e)) acquired before and after etching, show almost no presence of Bi and a reduced amount of Fe after the etching, which goes in hand with the observed backscattered images.

To determine the impact on the *CFO* out-of-plane residual strain XRD $\omega/2\theta$ scans (figure 4.10(d)) where the *CFO* peak does not change appreciably upon etching (a dotted vertical line indicated the position of the as-grown film). It is remarkable that no shift in the *CFO* peak after the removal of *BFO*, and therefore, contrary to previous assumptions, the *CFO* vertical strain is of non-elastic nature. The reason causing this strain remains unknown, but we would like to mention as a possible cause slight chemical modifications (oxygen/cation disorder or even chemical intermixing) occurring during growth to reduce interfacial stress by partially adapting its parameter to that of *BFO*, as has been reported to occur in heteroepitaxial growth of other complex oxides [116]. On the other hand, even if *BFO* had been completely removed after etching, it could be speculated that *CFO* remains strained in a metastable state due to an energy barrier. If this was the case an annealing of the sample would favor the relaxation of *CFO*. Therefore, we annealed the etched sample for 3 h in air at various temperatures up to 500 °C (step 100 °C) and measured the $\omega/2\theta$ of the same angular region. Anyhow, no relaxation of the *CFO* peak in direction to its bulk parameter nor a change in the *BFO* reflection are observed (see figure 4.10(d), the vertical gray line indicated bulk *CFO*(004) position and the dotted line the position measured in the as grown film). This observation points to an equilibrium state of *CFO* rather than a metastable one, with defects causing the strain remaining

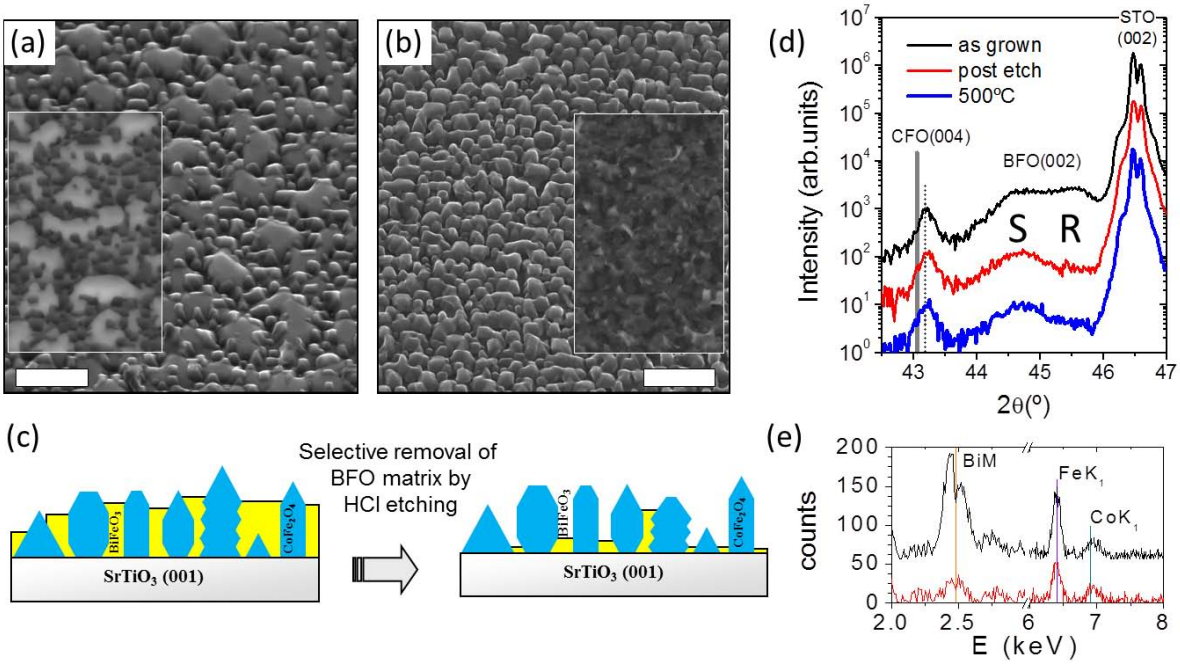

Figure 4.10: Composite sample with $t = 100\,nm$. SEM images secondary electrons, sample tilted 45 ° along [110] direction of the as grown film (a) and after HCl etching (b). Insets: backscattered electron images. Scale bars are 500 nm. (c) Sketches indicate the resulting morphologies. (d) XRD $\omega/2\theta$ scans before (black curve) and after (red curve) etching. $\omega/2\theta$-scans after additional annealing steps in air for 3 h are presented for 500 °C (blue line) and 700 °C (orange line). Vertical lines indicate position of *CFO* in the as-grown film (dotted line) and for bulk *CFO* (gray continuous line). (e) EDX spectra before (top curve) and after (bottom curve) etching.

unaltered. It is still to be elucidated to which extend the vertical strain found in other columnar nanocomposites [24, 25] is caused by the elastic interaction between the two phases or is of non elastic nature as found here for $BiFeO_3$-$CoFe_2O_4$.

Functional properties and magneto electric coupling

We characterized the switching behavior by combined magnetic force microscopy (MFM) and piezo response microscopy (PFM) at the nanoscale similar [64]. PFM measurements reveal that the *BFO* matrix can be stable polarized up and down applying electric fields ($\pm 12\,V$), in figure 4.11(a) three regions are visible (as-grown, then a square region was written at $+12\,V$ and in the center a square was written with $-12\,V$). The response was confirmed to occur only for matrix regions, no piezo response is observed for the *CFO* columns. Macroscopic magnetization measurements reveal a saturation magnetization (M_S) of 440 emu/cm^3, remanent magnetization in (001) direction is about 280 emu/cm^3 (65% of M_S). The in-plane (100) direction was also measured and shows a more S-shaped magnetization curve with considerable lower remanent magentization (170 emu/cm^3 38% M_S). This two measurements show that each phase maintains its corresponding ferroic

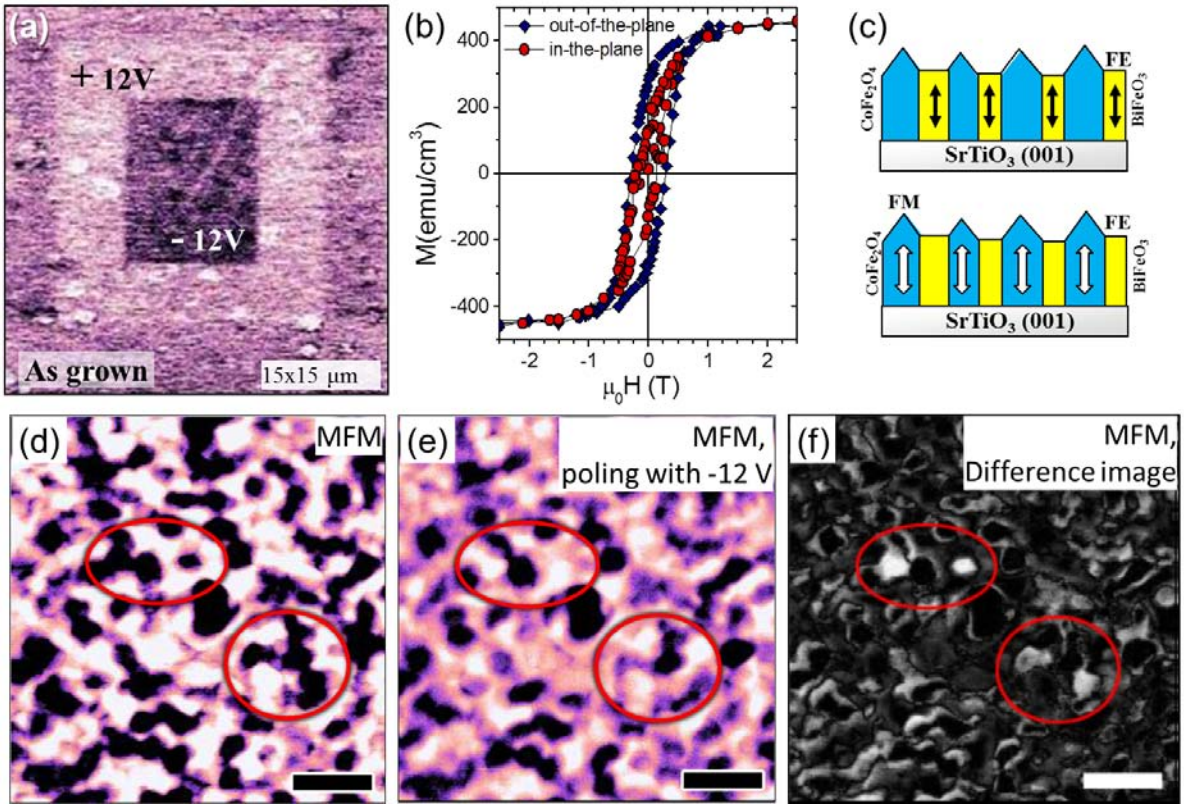

Figure 4.11: Composite with 100 nm thickness on $STO(001)$. (a) Piezo response microscopy image after writing two squared region with oposite electric field ($\pm 12\,V$), the other region corresponds to the as grown film. (b) Magnetization loop of a similar sample showing magnetization loops along (100) and (001) substrate directions. (c) Sketches indicate the biferroic response of the composite, each phase maintaining their corresponding ferroic properties. (d) and (e) The samples were premagnetized with a field of $2\,T$ consecutive MFM measurement show CFO pillars before and after electrically poling the region with $-12\,V$, respectively. (f) Difference image of (d) and (e): white areas (circled in red) indicate *CFO* pillars magnetically switched following a reversal of the polarization in *BFO*. (Bars are 300 nm)

properties, see sketch figure 4.11(c). MFM measurements after magnetizing in a $2\,T$ external field (figure 4.11(d)) showed about 80% of the CFO columns magnetized in the field direction, in agreement with SQUID measurements.

To investigate the eventual ME coupling in the sample, first defined regions were alternately poled with $+12\,V$ and -12 V. Polarization switching was confirmed by PFM images at each step, while MFM was used to probe its effects on the *CFO* magnetization (figures 4.11(d) and (e), before and after poling with $-12\,V$, respectively). In figure 4.11(f) we show the difference image obtained by subtraction of MFM images collected before and after $-12\,V$ poling. The difference image reveals a magnetization reversal in 12% of *CFO* pillars as a result of *BFO* polarization switching, with similar results when a $+12\,V$ poling was used. It indicates the presence of a magnetoelectric coupling: the electrical poling causes strain in *BFO* by converse piezoelectric effect, the strain propagates to *CFO* by mechanical coupling at the *BFO-CFO* interface, and finally the magnetization of *CFO*

columns is reversed by magnetostriction. We notice that previous studies on *BFO-CFO* composites showed 50% reversal under similar experimental conditions [64]. The lower switching percentage observed in our sample can be due to different ferromagnetic column size and distribution, or local leakage in the FE matrix.

4.2 T-$BiFeO_3$–$CoFe_2O_4$ vertical heterostructures

BFO single phase films have been successfully grown on a variety of substrates range from highly compressive to tensile in-the-plane [117]. Recent studies have shown that strongly deformed tetragonal-like *BFO* can be stabilized on $LAO(001)$ substrates implying a strong compressive stress around +4.5% (bulk *BFO* a=3.96 Å) [42, 43]. This phase promises large polarizations ($150\,\mu C/cm^2$) and a FE polarization direction close to [001] direction, which makes this phase appealing for integration in columnar nanocomposites.

In previously considered nanocomposites all phases are cubic, vertical interfaces between *CFO* and *BFO* have a moderate mismatch of about 5% and we have seen that they are semicoherent (see Section 4.1.3). In case of the super-tetragonal *T-BFO* phase which has highly different in- and out-of-plane parameters ($a = 3.67$ Å, $c = 4.66$ Å) the formation of the nanocomposite might be more complex. formation of *T-BFO* at the substrate interface might be expected, thus fully coherent interfaces of *R-BFO* with *STO* were observed previously. Anyhow, the stability of *T-BFO* matrix with film thickness may be more challenging, as a fast relaxation of the *R-BFO* matrix on *STO* substrates was observed and the stress caused by the mismatch to *CFO* appears unfavorable. The latter is of large magnitude and of opposite sign in both in- and out-of-plane film directions being the mismatch with*CFO* -12% in the *T-BFO* a_{T-BFO}-direction, while it is about +10% in the *T-BFO* c_{T-BFO}-direction. Promisingly, the growth of spontaneous long-range phase ordering of other complex oxide *BFO*:Sm_2O_3 composites was reported with $a_{Sm_2O_3} = 10.92$ Å [7, 25].

Here we present data on the stabilization of largely tetragonal distorted *T-BFO* as matrix in columnar composites.

4.2.1 Dependence of growth temperature on formation of T-BFO–CFO heterostructures

Aiming to explore the possible fabrication of *T-BFO–CFO* columnar composites, we have grown *CFO-BFO* on $LAO(001)$ substrates ($p = 0.1\,mbar$, $f = 5\,Hz$) studying the effect of the substrate temperature in the range from 550 to 750 °C.

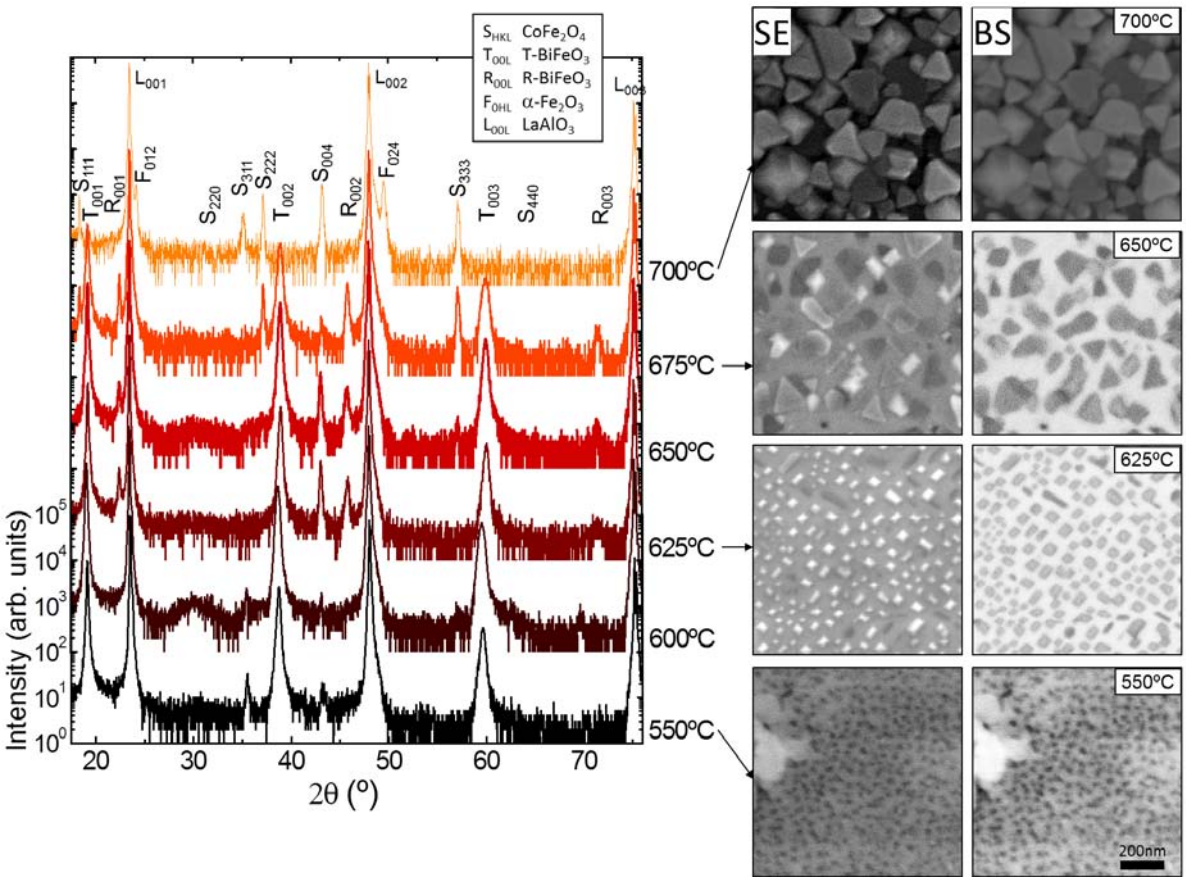

Figure 4.12: XRD $\omega/2\theta$ scans of *BFO-CFO* composite films on $LAO(001)$ substrates as function of the substrate temperature. The different phases in the diffraction patterns are indexed in the legend of the graph (upper right corner). In the optimal temperature range, $T_S \approx$ 625-650 °C, *BFO* and *CFO* grow $(00l)$ textured. Although a very small amount of *R-BFO* is present, the *T-BFO* phase is clearly dominating. With increasing temperature the *T-BFO* peak intensity decreases, thus for $T_S \geq$ 700 °C no *BFO* reflection can be observed. It suggests absence of Bi in the film and formation of Fe_xO_y phases. In previous studies we found similar tendencies, for *BFO-CFO* composites grown on *STO* substrates. The right panel shows SEM images (secondary (SE) and backscattered (BS) electrons) for selected samples.

Structural dependence on growth temperature

XRD $\omega/2\theta$-scans of *BFO-CFO* composite films on $LAO(001)$ substrates as function of the substrate temperature are shown in figure 4.12. Interestingly, for a broad range of growth temperatures the $(00l)$ reflections of largely tetragonally deformed *T-BFO* (labeled as $T_{(00l)}$) dominate the diffraction patterns. A much smaller fraction of $(00l)$ oriented *R-BFO* is present. Only in a small optimal temperature range, $T_S \approx$ 625-650 °C, *BFO* and *CFO* grow fully $(00l)$ textured. For lower and higher growth temperatures other spinel orientations like (111), (311) or (110) are observable (corresponding reflections are labeled in the figure). With increasing temperature the *T-BFO* peak intensity decreases, and vanishes for $T_S \geq 700$ °C. It suggests absence of Bi in the film and formation of Fe_xO_y phases, similar to previous study of *CFO–R-BFO* (figure 4.2).

figure 4.13(a) shows the XRD $\omega/2\theta$ scan of nanocomposite film grown at optimal temperature $LAO(001)$. *BFO* grows, *c*-axis textured, in the quasi-tetragonal (*T-BFO*) phase; only few weak reflections of the rhombohedral (*R-BFO*) phase are observed. *T-BFO* grows strained, with out-of-plane parameter of 4.63 Å(c parameter of bulk *T-BFO* is 4.66 Å), whereas *CFO* is relaxed (c = 8.39 Å).

XRD analysis of asymmetrical reflections confirmed epitaxial growth. Reciprocal space maps around $LAO(103)$ in figure 4.13(b) show that *T-BFO* on $LAO(001)$ is fully strained (a = 3.79 Å). The $CFO(206)$ reflection is barely observable due to its low intensity and the proximity of the Kβ component of the substrate reflection. The $CFO(115)$ asymmetrical reflection is presented in the side panels, resulting in a =8.38Å and c =8.40Å. In figure 4.13(c), the sum of the $\chi/2\theta$ frames in an interval $\Delta\varphi$=10 ° around the $LAO(202)$ substrate reflection is shown. In addition to the substrate peaks $CFO(404)$ and *T-BFO*(202) can be identified by their corresponding 2θ and χ positions, see also side panels in figure 4.13(c). The substrate $LAO(202)$ and the $CFO(404)$ film reflections are at χ =45 °, with $2\theta_{LAO}$ =70.28 ° and $2\theta_{CFO}$=62.55 °, respectively. Whereas, the *T-BFO*(202) reflections are found at $2\theta_{TBFO}$ =63.85 ° and χ of 50.9 ° resulting from a large distortion of the c/a axis of the *T-BFO* phase, being compatible with the RSM data. The φ-scans (figure 4.13(c)) around $LAO(202)$, $CFO(404)$ and *T-BFO*(202) acquired for $\Delta\varphi$ steps of 0.5 ° were integrated for the marked boxes. Each scan displays a set of four peaks (figure 4.13(d)), 90 ° apart, at the same φ angles, indicating $[100]CFO(001)||[100]LAO(001)$ and $[100]$*T-BFO*$(001)||[100]LAO(001)$, i.e. a cube-on-cube type epitaxial relationship.

Morphology as function of growth temperature

The morphology measured by SEM (SE and BS images) for selected samples is shown in the side panel of figure 4.12. For optimal substrate temperature (625-650 °C) pyramidal structures presenting {111} faceting and directional order of their bases along ⟨110⟩ substrate directions are found to be similar to composite films with *R-BFO* matrix, nevertheless the matrix appears to be much flatter and formation of *BFO* plateaus is less evident, see inset of figure 4.14(a) showing the superposed BS images that were acquired simultaneously. The BS signal is of higher intensity in the areas where *Bi* is present and confirm an homogeneous *T-BFO* matrix. The islands correspond to the *CFO* phase. The morphology in both cases is thus similar to that of nanocomposites on STO(001) substrates discussed previously. The cross sectional BS SEM image in figure 4.14(b) confirma the nanopillars topology of *CFO* (dark regions) in the *T-BFO* matrix (bright regions).

Increasing the temperature to 675 °C from XRD $\omega/2\theta$-scans leads to an increased intensity of (111) oriented *CFO*, and consequently in the SEM images (figure 4.12) appears

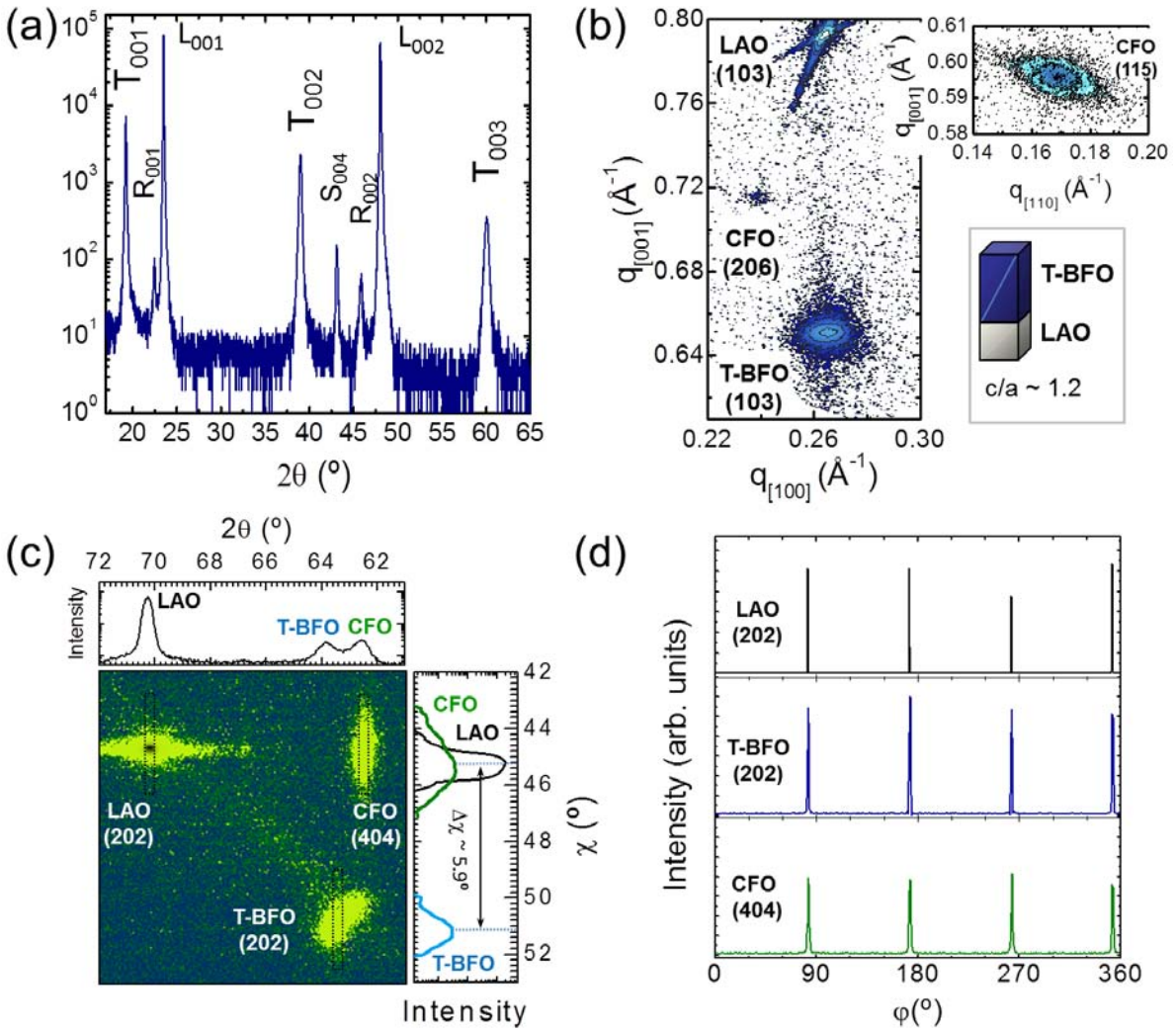

Figure 4.13: (a) XRD $\omega/2\theta$scans of *BFO-CFO* composite films on $LAO(001)$ grown at 625 °C. L, S, T, and R signal reflections from the substrate, spinel *CFO*, *T-BFO*, and *R-BFO*, respectively. (b) XRD reciprocal space map around $LAO(103)$. Inset panel shows the corresponding map around $CFO(115)$. (c) XRD amplified central region of the $\chi/2\theta$-frame around the (202) substrate reflection. Integrated intensity for 2θ and χ are presented in the top and lateral panels. The diffraction peaks are labeled correspondingly. The regions used for the integration of the φ scans (d), are indicated by dotted boxes.

a large amount of triangular based structures ($100 - 150\,nm$ lateral size, similar to *CFO* prisms observed previously on (111) oriented *STO* substrates), also the amount of pyramidal islands is reduced to about 10 per μm^2 (about 200 μm^2 are found in the 625 °C sample). Anyway the matrix appears still to be homogeneously distributed between the spinel structures. In the sample grown at highest temperature (≥700 °C) only granular surface morphology can be observed. The grains are similar to the 675 °C pyramidal and triangular faceted, but no *Bi* containing matrix is present and thus the contrast in the BS image results basically from the height of the grains.

The topology of the nanocomposite at optimal growth temperature 625 °C is summa-

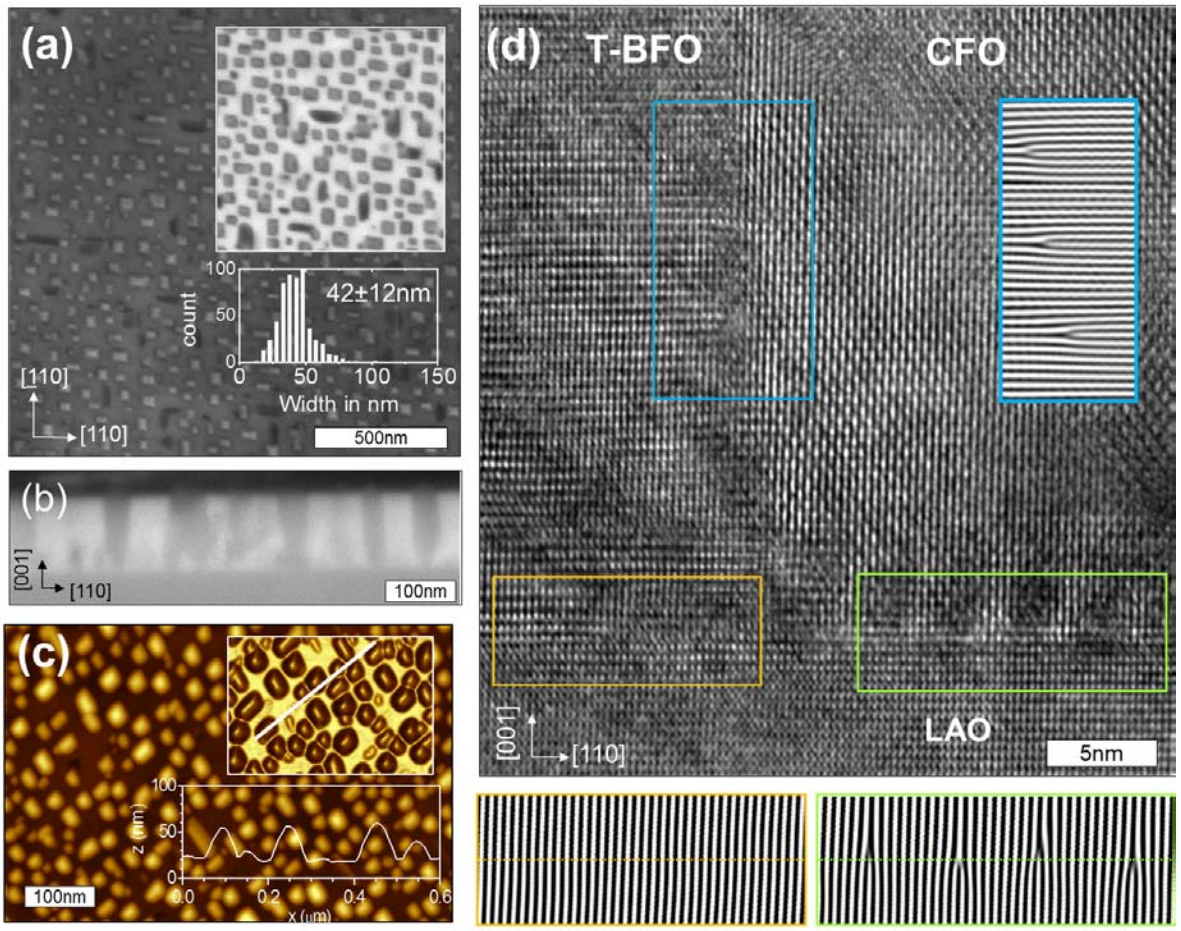

Figure 4.14: Morphology of *CFO-BFO* on *LAO*(001)grown at optimal growth conditions (625 °C). (a) SEM images (secondary electrons) and in the top right inset overlayed backscattered electrons image. Inset in the bottom right shows the histogram of the islands lateral size. (b) Cross-section view imaged with BS electrons. (c) Corresponding AFM topographic image, the inset corresponds to the cosine filtered image. A profile along the line marked in the main panel is shown in bottom panel. (d) Cross section HRTEM image of the triple interface between a *CFO* nanopillar, the *T-BFO* matrix, and the *LAO* substrate. The continuity of planes between the *T-BFO* and *LAO* and the presence of dislocations at the *CFO*/*LAO* substrate interface and at the *CFO*/*T-BFO* lateral interface are revealed by FFT filtered images corresponding to the marked regions in the graph.

rized in figure 4.14, showing SEM/AFM and TEM images of the surface morphology and *CFO–T-BFO–LAO* interfaces, respectively. The SE images (figure 4.14(a)) show faceted islands oriented along ⟨110⟩ in-plane directions; the majority of them have an square base and likely they have pyramidal shape; some few others islands are of hut-cluster type. The histogram of lateral size (inset) shows a quite narrow distribution with mean lateral size of approx 42 nm. The AFM topographic image (figure 4.14(c)) reveals a similar lateral size distribution ($\approx 53\,nm$, the larger value likely due to AFM tip convolution). The height of the objects protruding the matrix is in between 10 and 30 nm (a typical height profile, along the white line in the topographic image is shown in the bottom panel). Also slope distribution functions was calculated (not shown) revealing an average tilt about 48 °. This

is a slightly smaller slope for the {111} faceted *CFO* pyramids (54.7 °), and might be due to a convolution of the AFM tip with the surface morphology (not well resolved shape of the pyramids and rounded corners, which can be expected due to the height aspect ratio of the objects).

A more detailed view of the *T-BFO-matrix/CFO-nanopillar* interfaces was achieved by cross section HRTEM. figure 4.14(b) shows a cross section micrograph with a triple interface *CFO/LAO*, *T-BFO/LAO* and *CFO/T-BFO*. Fourier-filtered regions corresponding to the three interfaces are marked in figure 4.14(d) by boxes and are shown in the corresponding panels. The interface between *T-BFO* and the *LAO* substrate is fully coherent. *CFO* presents well-defined interfaces with both *LAO* substrate and *T-BFO* matrix, with misfit dislocations, approximately 5 nm apart. This is in good agreement with the geometric matching of each phase; *T-BFO/CFO* in [001] ($10\,TBFO$:$11\,CFO/2$, with residual misfit of 0.3%) and *CFO/LAO* in direction [110] ($9CFO/2\sqrt{2}$:$10LAO/\sqrt{2}$, with residual misfit of 0.4%). The interfaces are thus semicoherent, with extra atomic planes in *CFO* accommodating the high lattice mismatch with *T-BFO* matrix ($\approx 10\%$ tensile stressed, $a_{CFO} < c_{T-BFO}$) and to the substrate being the extra atomic planes in *LAO* ($\approx 10\%$ compressive stress, $a_{CFO} > a_{LAO}$).

Purely (00l) textured columnar nanocomposites with *CFO* columns and *T-BFO* matrix have been successfully prepared within a temperature range of 625 to 650 °C(5 Hz, 0.1 $mbar$). The interfaces between *CFO* and *T-BFO* are semicoherent and are not detrimental for stabilizing *T-BFO* phase for film thicknesses around 100 nm, only a minor fraction of *R-BFO* was observed by XRD.

4.2.2 Nearly tetragonal $BiFeO_3$ single films

In the previous Section, we have shown that *T-BFO* can be stabilized in nanocomposites with *CFO* as second phase on $LAO(001)$ substrates. Whereas, the phase-diagram for the growth of *R-BFO* single films was rather well known, this is not the case for *T-BFO* for which the process of growth by epitaxial stabilization has not been investigated in detail. To investigate this, a series of pure *T-BFO* samples was grown to probe the role of deposition temperature on the stabilization of $T\text{-}BiFeO_3$ on $LaAlO_3(001)$ substrates. The formation of epitaxial *T-BFO* was only obtained in a narrow temperature window, while competitive formation of rhombohedral *R-BFO* and thermal decomposition at lower and higher temperatures is observed, respectively.

T-$BiFeO_3$ dependency on growth temperature

In order to discern the effects of the substrate temperature (T_S) on the epitaxial stabilization of *T-BFO*, we have mapped its influence on the phases forming if deposited on compressive-straining $LAO(001)$ substrates. figure 4.15 shows the XRD $\omega/2\theta$-scans around symmetrical reflections of *BFO* films ($t = 100\,nm$ nominal thickness) grown at various temperatures T_S. For clarity, the patterns are vertically shifted. There are high intensity peaks corresponding

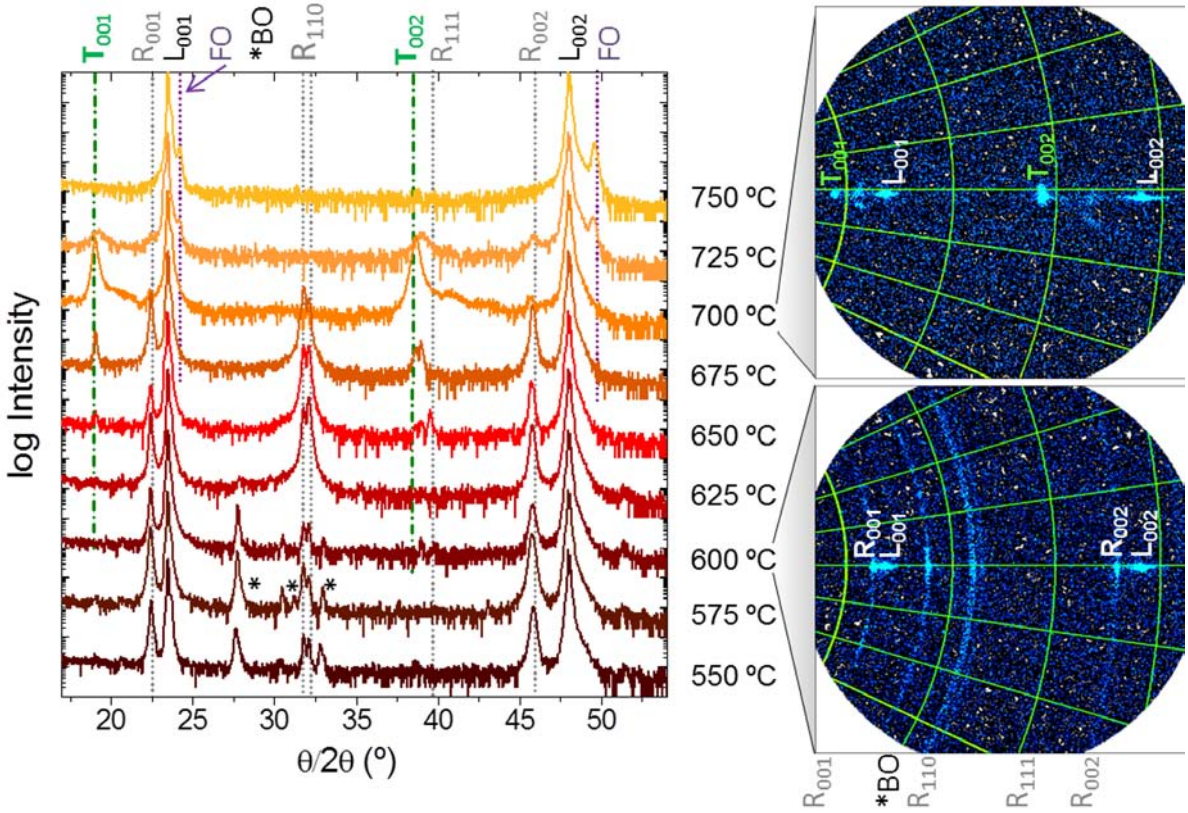

Figure 4.15: XRD $\omega/2\theta$ scans, labels at the right side indicate the deposition temperature T_S. The intensity is log scaled (starting at 1 *count*) and corresponds to the films grown at 550 °C; the other patterns are vertically shifted for clarity by factor 100. Labels at the top index the diffraction peaks. T and R correspond to the quasi-tetragonal and rhombohedral phases of *BFO*, respectively, L to LAO, and BO and FO to bismuth and iron oxides, respectively. The side panels show a $\chi/2\theta$-frame (similar $2\theta \approx 15 - 52°$ range, $\Delta\chi \pm 20°$) for low temperature (600 °C), arcs indicate a polycrystalline fraction of the thin film, while at high T_S =700 °C the films is fully $(00l)$ textured.

to *R-BFO* (indicated by green vertical lines and labels R) in the samples grown between 550 and 675 °C, with preferential $(00l)$ out-of-plane orientation at the lowest T_S and also with a large fraction of (110) oriented grains for growth temperatures between 625-675 °C.

Reflections indexed as bismuth oxide (BO, marked with asterisk) are also present in the samples grown at T_S =600 °C. For this sample a side bottom side panel in figure 4.15 shows a $\chi/2\theta$-frame acquired with a 2d detector ($2\theta \approx 15 - 52°$ range, $\Delta\chi \pm 20°$) apart of the $(00l)$ oriented *BFO*peaks close to the substrate reflections arcs indicate also a

significant fraction of polycrystalline grains. For higher deposition temperatures, *T-BFO*(00*l*) reflections (indicated by green vertical lines and labels *T* in the $\omega/2\theta$scans) is observed from 650 °C onwards, although *R-BFO* with *R*(110) and *R*(001) like orientations are dominant until 675 °C. The presence of *R-BFO*(110) orientation may be favored by the smaller lattice mismatch, -1.4% due to lattice coincidence of $3\,LAO(100) : 2\,BFO(110)_{PC}$ lattice spacings. Remarkably, only traces of *R-BFO* are found in the T_S =700 °C film, being *T-BFO*(001) totally dominant. The small shoulders on the right of the (001) and (002) *T-BFO* reflections signal the presence of a monoclinic R-like phase (M_R) that usually coexists with *T-BFO* [102, 106, 118]. This features can be observed also in the $\chi/2\theta$-frame in the top side panel of the 700 °C sample in figure 4.15. It is also appreciated that weak diffraction spots of this monoclinic *BFO* does not lay on the central line (χ=0 °) of the $\omega/2\theta$-scan and indicate a tilted fraction of this phase, that will be discussed later in more detail.

With further increase of T_S, *BFO* starts to decompose and the *T-BFO* peaks nearly vanish at T_S=725 °C. In parallel, reflections for responding to iron oxide (αFe_2O_3, marked with purple vertical lines) are observed on the right of the substrate peaks. Finally, in the T_S=750 °C sample only αFe_2O_3 is detected in the film.

The morphology of these samples was observed by SEM, While SE images are useful for moderately rough surfaces it was found that BS images present contrast in the flat *T-BFO* films related to the the formation of complex domain pattern. In figure 4.16(a), the BS image is shown, with an inset the corresponding of a SE image to show the contrast difference depending on the detected electrons. Domains in [100] and [010] direction (black arrows) show very strong contrast and have been found by other researcherS to be corresponding to T- and R- mixed phase regions [43, 102]. While other regions of the film indicate contrast [110] and [−110] direction (white arrows), possibly caused by twinned *T-BFO* domains. As the different domains are known to grow slightly tilted with respect to each other, this can influence the amount of back scattered electrons leaving the surface in direction of certain crystallographic directions in direction of the detector (electron channeling).

Similar complex domain patterns have been shown by other authors using AFM and actually more visible in piezoresponse force microscopy (PFM) [102, 103]. The topographic AFM image of this sample (figure 4.16(b)) shows flat morphology with lamellae-like inclusions in [100] direction (see the height profile along the marked line, direction [100]). They have a horizontal spacing of 60-70 *nm*, width of 200-250 *nm* and step heights of about 1-2 *nm* [43, 102].

At low T_S =550 °C the BS image (figure 4.16(c)), large islands with lateral dimension of 200-500 *nm* can be seen, on a structured background between the islands possibly

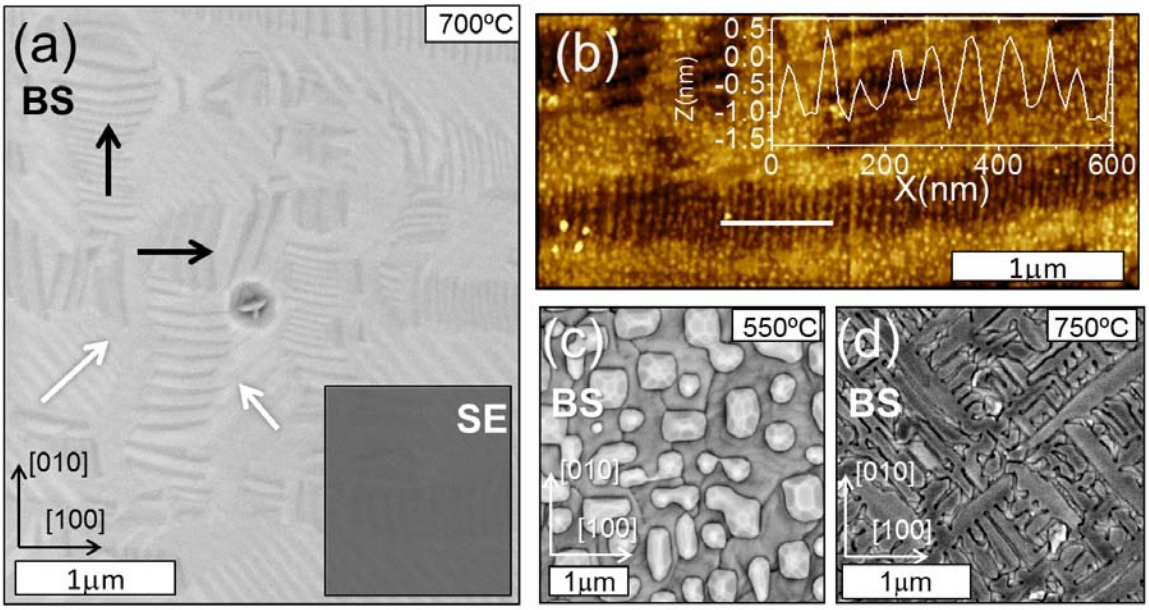

Figure 4.16: Morphology of selected samples grown at different temperatures. (a) SEM images of the sample grown at 700 °C. A barely observable contrast can be seen by secondary electrons (SE) which is shown as inset, much stronger contrast is in the backscattered electron (BS) image indicates a formation of a complex domain pattern. The black and white arrows indicate the principal domain features. AFM topographic image (b) of this *T-BFO* film, the inset shows a height profile along the drawn line with periodic height variations in the lamellae like areas. BS SEM images of a sample grown at low T_S=550 °C (c). Islands with lateral dimension of 200-500 nm, lighter contrast might indicate higher Bi content, but probably are due to thickness effect. (d) The film at highest T_S=750 °C is fully Fe_2O_3 textured, a maze like surface is present. No indication of Bi rich regions (light contrast) is observed.

formed by polycrystalline *BFO*. The islands show a lighter contrast which might indicate higher Bi content or even Bi_xO_y (in XRD $\omega/2\theta$ scans the films presented traces of Bi_xO_y). Nevertheless, this contrast is most likely due to a thickness effect, thus the islands are protruding much more from the surface than the thinner layer between them. The film at highest T_S=750 °C is fully Fe_3O_4 textured, on the surface a maze like surface is present as can be seen in figure 4.16(d). No indication of Bi rich regions are observed in the BS image.

T-BFO at optimal growth temperature

For a closer analysis we show separately the $\omega/2\theta$ scan *BFO* film grown at 700 °C in figure 4.17(a). A series of well-defined and high-intensity peaks correspond to (00l) *T-BFO* reflections (labeled T_{00l}), the corresponding $c_{T-BFO} \approx 4.66(1)$ Å paramter matches well the theoretical *T-BFO* out-of-plane parameter ($c_{theo} \approx 4.66$ Å [119]). Additional weak reflections are observed following the main *T-BFO* reflection at higher 2θ-angles, and can be attributed to a minor fractions of monoclinic *R*-like *BFO* (labeled M_R) and relaxed

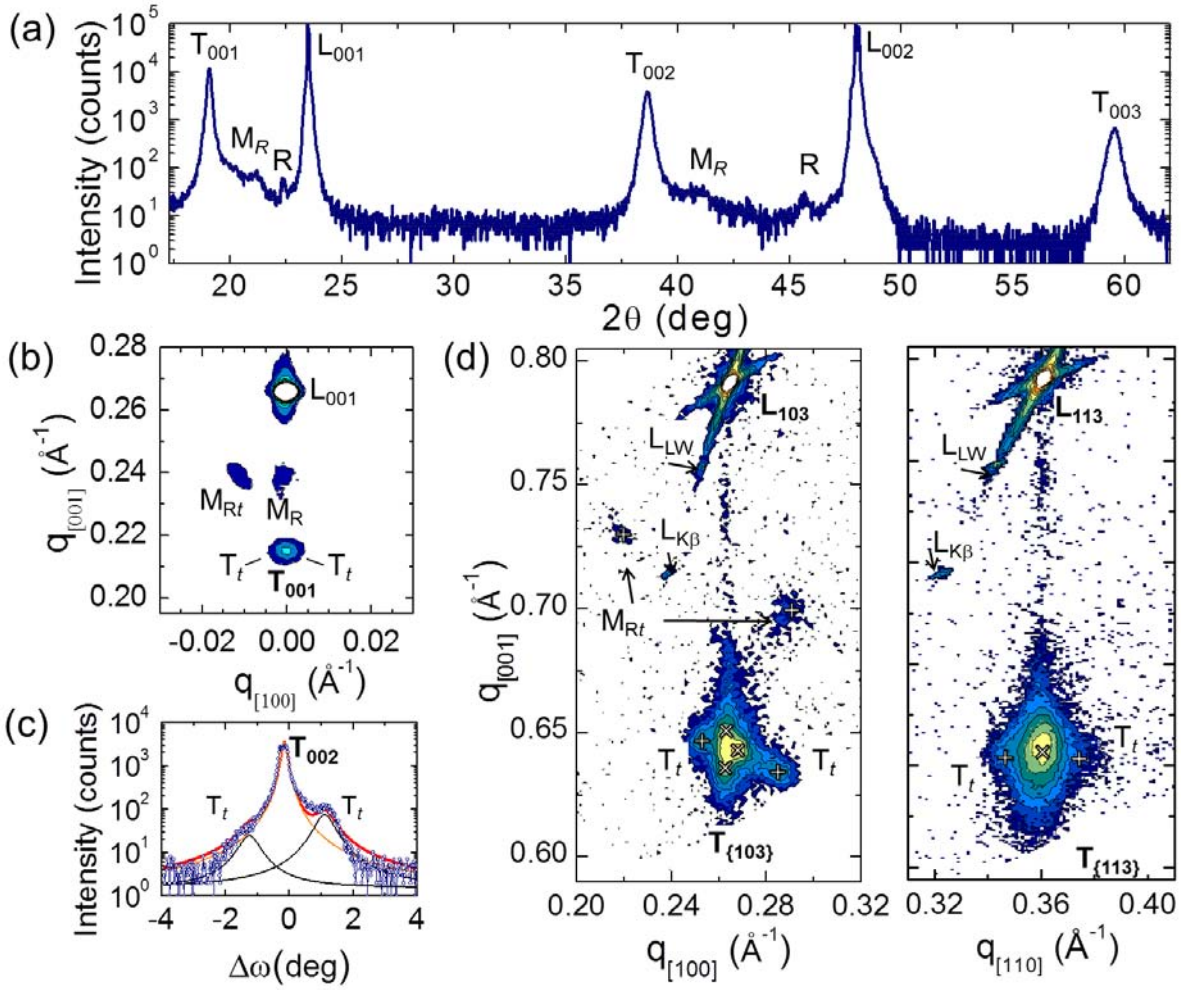

Figure 4.17: (a) XRD $\omega/2\theta$ scan of the *BFO* film gron at 700 °C. $(00l)$ peaks of T-like $BiFeO_3$, monoclinic R-like *BFO* and relaxed *R-BFO* are labeled T_{00l}, M_R and R, respectively. $L(00l)$ are substrate reflections. (b) Reciprocal space map around the (001) substrate reflection showing the presence of tilted M_R (M_{Rt}) domains. (c) rocking curve for the T_{002}-*BFO* reflection; the two shoulders at $\Delta\omega \approx 1.1\,^\circ$ indicate tilted T-like domains (T_t); (d) Reciprocal space maps around the (103) $LaAlO_3$ substrate reflection (labeled $L_{(103)}$); peaks caused by spurious $Cu_{K\beta}$ and W_L wavelengths are labeled $L_{K\beta}$, L_{LW}, respectively. The positions of the (103) reflections of tetragonal-like T-BFO, marked with $T_{\{103\}}$, are indicated by (x) symbols. The approximate peak positions of minor fraction of tilted T_t and M_{Rt} domains are also indicated (+).

bulk-like *R-BFO* (labeled *R*) domains. We used reciprocal space maps, shown in figures 4.17(b) around the (001) substrate reflection and 4.17(d) around the (103) and (113) substrate reflection.

Besides the prevalent principal *T-BFO* peak, minor traces of M_R, tilted M_R (labeled M_{Rt}) and tilted *T-BFO* (T_t) peaks indicate the formation of a complex domain structure in this highly deformed *BFO* layers. Nevertheless, relaxed *R*-like *BFO* diffraction spots are barely observed. The rocking curve around the *T-BFO*(002) reflection (figure 4.17(c)) reveals the presence of two shoulders caused by tilted *T*-like domains (with $\Delta\omega \approx \pm 1.1$-$1.2$).

Also a small splitting ($\Delta\omega = 0.15\,^{\circ}$) in the T_{002}-reflection can also be observed; it likely originates from twinning induced by the LAO substrate. The shape of the (103) *T-BFO* spots in the rsm (figure 4.17(d)) is compatible with monoclinic M_C structure reported in ref. [43, 120] using high-resolution diffractometers. Nevertheless, the (113) peak should split in two vertically displace spots, but here only one broad and in [001] enlarged peak can be observed. Other have resolved this peak splitting (three peaks in (103) and two peaks in (113)) with HR-XRD for similar sample thickness [104], while in [102] it is more like in our case. The lattice parameters of the T-like phase (M_C) are evaluated: $a \approx 3.75(1)$Å, $b \approx 3.80(1)$Å, $c \approx 4.66(1)$Å and $\gamma \approx 88.6(3)^{\circ}$. From data in figure 4.17, the out-of-plane lattice parameter of the M_R and *R-BFO* phases are $c_{MR-BFO} = 4.19(2)$Å, $c_{R-BFO} = 3.97(1)$Å in good agreement with previous reports [102–104].

In summary the data from XRD and morphology described above confirm that our *BFO/LAO* single films grown at 700 °C ($0.1\,mbar$, $5\,Hz$) are consistent with nearly tetragonal *T*-like *BFO* and are comparable reported films in literature.

4.2.3 Comparison of single and composite films with *T-BFO*

In this section single *BFO* films and *CFO-BFO* nanocomposites grown on $LAO(001)$ substrates are compared. Both series nominally have identical growth conditions (T_S = 550-750 °C, $0.1\,mbar$, $5\,Hz$). An intensity map of the XRD $\omega/2\theta$-scans for the different *BFO* single films (figure 4.18(a)) visualizes the formed phases as a function of the deposition temperature, with the white dotted box overlayed to the diagram marking the narrow optimal window to grow *T-BFO* (a green border on the bottom of the box indicates region of *T-BFO* formation). The dependence, in logarithmic scale, of the ratio of the $I_{T-BFO(002)}/I_{R-BFO(002)}$ peak intensities with T_S signals (figure 4.18(c)) quantitatively its critical influence. For single *BFO* films (red circles) the *T-BFO* phase is dominant in the T_S =700 °C film, but films grown at the closest T_S (675 °C) and *R-BFO*$(00l)$ diffraction peaks of similar intensity. At slightly higher T_S (725 °C), *T*- and *R-BFO* peak intensities are much reduced and an appearing αFe_2O_3 peak (labeled FO in figure 4.15) is indicative for bismuth loss and *BFO* decomposition. Thus the optimal window is much narrower than the reported for pure *R-BFO* films and nanostructures grown on $STO(001)$ substrates.

The above results indicate that the substrate-induced stress, necessary to stabilize the *T-BFO* phase, makes narrower the formation window of the *T-BFO* when compared to the *R-BFO* phase. Remarkably, in the case of *BFO-CFO* columnar nanostructures on $LAO(001)$, the *T-BFO* phase is obtained in a broader temperature range (550 °C to 675 °C) as indicates the XRD $\omega/2\theta$-intensity map in figure 4.18(b). The vertical interface between *T-BFO* and *CFO* was found to be semicoherent, in spite of the huge lattice

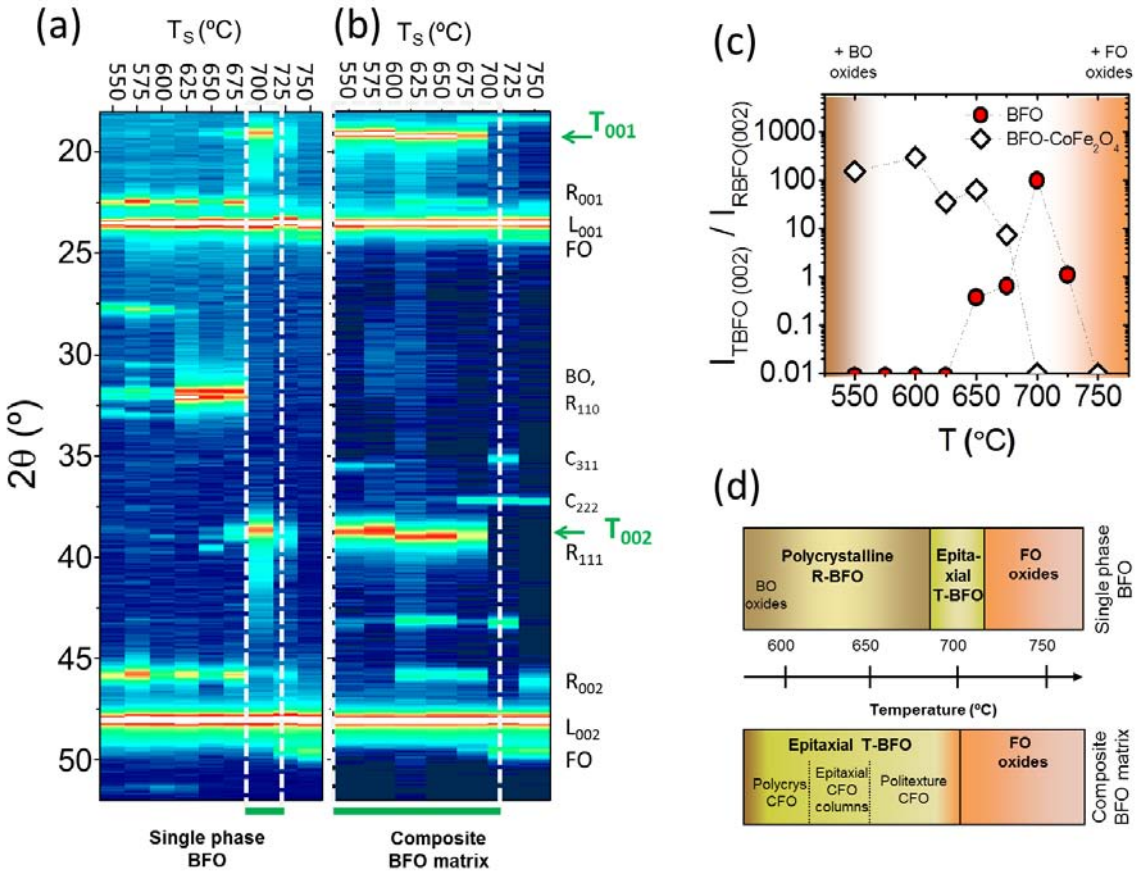

Figure 4.18: (a) Map of intensity of the diffraction peaks in the 15-52 ° range for *BFO* single films deposited from 550 to 750 °C and (b) for *CFO-BFO* nanostructures, reflections corresponding to *CFO* are labelled with C. (c) Ratio of intensity of *T-BFO*(002) and *R-BFO*(002) peaks as a function of the deposition temperature. (d) Sketch represents the distinct temperature regions considering formed phases in single films (top panel) and nanostructures (bottom panel).

mismatch (Section 4.2), and thus these interfaces likely favor the stabilization of *T-BFO*. The corresponding intensity ratios between (002) reflections of *T*- and *R-BFO* are plotted in figure 4.18(c) (diamonds), permitting a direct comparison with *BFO* single films data. The sketch in figure 4.18(d) overviews the dominant phases at T_S regions for single films and epitaxial nanostructures.

The presence of the nanocolumns has an impact on the crystal structure of the *T-BFO* matrix. In figure 4.19 we compare XRD measurements of this composite sample with a single *T-BFO* layer. As mentioned previously, in *T-BFO* single films on *LAO*(001) substrates the rocking curves around the (002) *T-BFO* reflection revealed two tilted domains (T_t), figure 4.17(c). The monoclinic (M_C) nature of the *T-BFO* was evidenced by RSM around the (103) reflection presenting a characteristic splitting of the Bragg spot. Such splitting was also observed by ϕ-scans around the (303) reflection, figure 4.19(c) being the *T-BFO*(303) peak formed by a major T_I and two minorT_{II} contributions. The

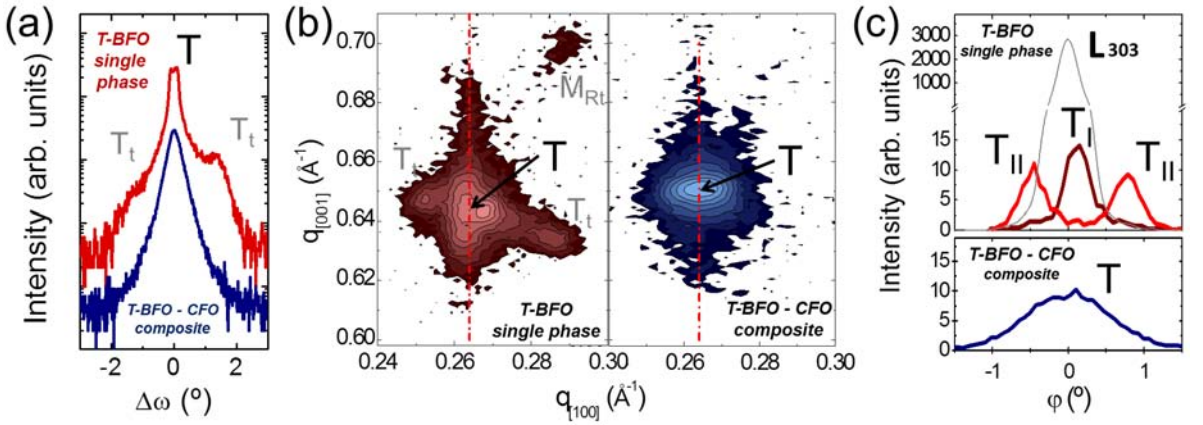

Figure 4.19: Comparison of XRD results of T-BFO phase in 100 nm thick in single phase and composite films; grown at their optimal temperature 700 and 625 °C, respectively. (a) Rocking curve around the (002) T-BFO reflection. While in single phase addional peaks (T_t) evidence tilted domains, no such feature is present in the composite sample. (b) RSM around T-BFO(103) reflection for the single phase film, showing multiple diffraction spots due to monoclinique splitting of the main peak (T), and presence of tilted domains T_t and M_{Rt}, and composite (right), the (c) ϕ-scans around the (303) reflection also show splitting of the film peaks in single phase T-BFO (originated by its monoclinic tilt and $a \neq b$) and a only one broad peak for the composite.

T_I peak, at a tilt angle χ of 50.2 °, is centered at the same ϕ as the $LAO(303)$ reflection (tilt angle 45 °), whereas the T_{II} reflections are shifted about 0.6 ° in ϕ and are tilted to a higher χ angle of 51.5 °. Also fractions of tilted domains are present (T_t and M_{Rt}) in this sample, figure 4.17.

In contrast, the composite samples only one broad peak is found in the φ-scan (figure 4.19(c)). Also, in the rocking curve (figure 4.19(a)) no satellite peaks are present and also in the RSM around the (103) reflections only one broad peak centered with respect to the substrate (position is marked by red line, in figure 4.19(b)). This evidences that the presence of rigid CFO columns with high area density favors the formation of more supertetragonal-like *BFO*. Nevertheless, there might be still a monoclinic distortion present, but is posibly shielded by the broad diffraction peaks observed for the composite film.

4.3 $BiFeO_3$–$CoFe_2O_4$ composites grown on a broad range of substrates

We have shown that in spite of the large structural mismatch, both *CFO* and *BFO* phases grow epitaxially forming nanocomposites with well-defined *CFO-nanopillar / T-BFO-matrix* morphology on highly compressive substrates, like $LAO(001)$, in addition to the *CFO-nanopillar / R-BFO-matrix* topology on $STO(001)$ substrates.

Here we aim to explore the viability of influencing the composite properties via substrate induced strain by growing nanocomposites on different (001) substrates LAO,

STO, $MgAl_2O_4$ (*MAO*) and *MgO* with $a_{LAO} < a_{STO} < a_{MAO} < a_{MgO}$. A couple of composite sample were grown with a thin (10 *nm*) buffer layer of $LaNiO_3$ (*LNO*) on *LAO* and $La_{0.67}Ca_{0.33}MnO_3$ (*LCMO*) on *STO* substrates. Both buffers have a pseudocubic bulk lattice parameter about $a = 3.86$ Å which if fully relaxed lays between a_{LAO} and a_{STO}. This results in a broad range of lattice mismatches on the film constituents (see overview in Table 4.1), ranging from compressive to tensile. Previously optimized growth conditions (625 °C, 0.1 *mbar* and 5 *Hz*) were used for this study.

We will show that appropriate substrate or buffer-layer selection for the growth of $BiFeO_3$-$CoFe_2O_4$ vertical composite, holds the key to tune functional properties of the composite samples. Stress of the matrix on the *CFO* columns may influence the magnetic anisotropy of *CFO* as it critically depends on its lattice strain [48, 121], which can influence the orientation of *CFO* easy axis favoring in- or out-of-plane directions. The polar direction of *BFO* can be rotated from [111] to nearly [001] depending on which structural variant grows as matrix. Thus the relative angle among the two polar axes can be varied.

Table 4.1: Lattice mismatch in % between $CoFe_2O_4$, *R*-$BiFeO_3$, and *T*-$BiFeO_3$ as layer and $LaAlO_3$(001), $La_{2/3}Ca_{1/3}MnO_3$(001), $LaNiO_3$(001), and $SrTiO_3$(001) as substrate. The mismatch of *R*-$BiFeO_3$ and *T*-$BiFeO_3$ with $CoFe_2O_4$ (latter considered as substrate) is also indicated.

Film Substrate	$CoFe_2O_4$ $a/2 = 4.196$Å	*R*-$BiFeO_3$ $a_{PC} = 3.96$Å	*T*-$BiFeO_3$ $a = 3.67$Å ($c = 4.67$Å)
$LaAlO_3$ $a_{PC} = 3.79$Å	+10.7%	+4.5%	-3.3% (+22.9%)
$La_{0.67}Ca_{0.33}MnO_3$, $LaNiO_3$ $a_{PC} = 3.86$Å	+8.7%	+2.6%	-5.1% (+20.6%)
$SrTiO_3$ $a = 3.905$Å	+7.4%	+1.4%	-6.1% (+19.2%)
$MgAl_2O_4$ $a/2 = 4.04$Å	+3.8%	-1.3%	-8.7% (+15.9%)
MgO $a = 4.21$Å	-0.3%	-5.5%	-12.6% (+11.1%)
$CoFe_2O_4$ $a/2 = 4.196$Å	–	-5.6%	-12.7% (+10.1%)

Morphology of composites in different substrates

The impact of the substrate on the growth of *BFO-CFO* nanocomposites was studied by SEM (figure 4.20), the images are ordered from smallest to largest substrate lattice parameter (indicated in the bottom panel if the figure). Secondary electron images (figure

4.20(SE)) reflect the topography, while the composition on the same region is measured by backscattered electron images (figure 4.20(BS) - bright contrast corresponds to *Bi*-rich phase). Composites with columnar topology (*CFO-columns* in *BFO-matrix*) were obtained on all compressive substrate or compressive substrate with buffer layer. *T-BFO* phase is only found on bare *LAO*(001) substrate, while it forms as *R-BFO* like phase on buffered substrate and bare *STO*. Theoretical studies suggest a sharp onset for the formation of single phase T-BFO just close to the mismatch with LAO [43, 119], so that even a thin *LNO* buffer layer (10 *nm* thickness) on *LAO* may reduces the substrate induced stress and thus hinders the stabilization of the *T-BFO* phase. In contrast, on tensile substrates (*MAO* $a_{MAO} = 8.08$Å, *BFO* mismatch -1.3% and *MgO* $a_{MgO} = 4.212$Å, *BFO* mismatch -5.5%) we find that *BFO* decomposes during growth, resulting in formation of *Bi*-rich dendritic structures on the surface while the rest is covered by pyramidal objects typical for spinel phases (see SEM images in figure 4.20 (top panels)).[21] Probably, the better matching of the Fe_xO_y oxides with these substrates provides a driving force favoring the decomposition of *BFO*.

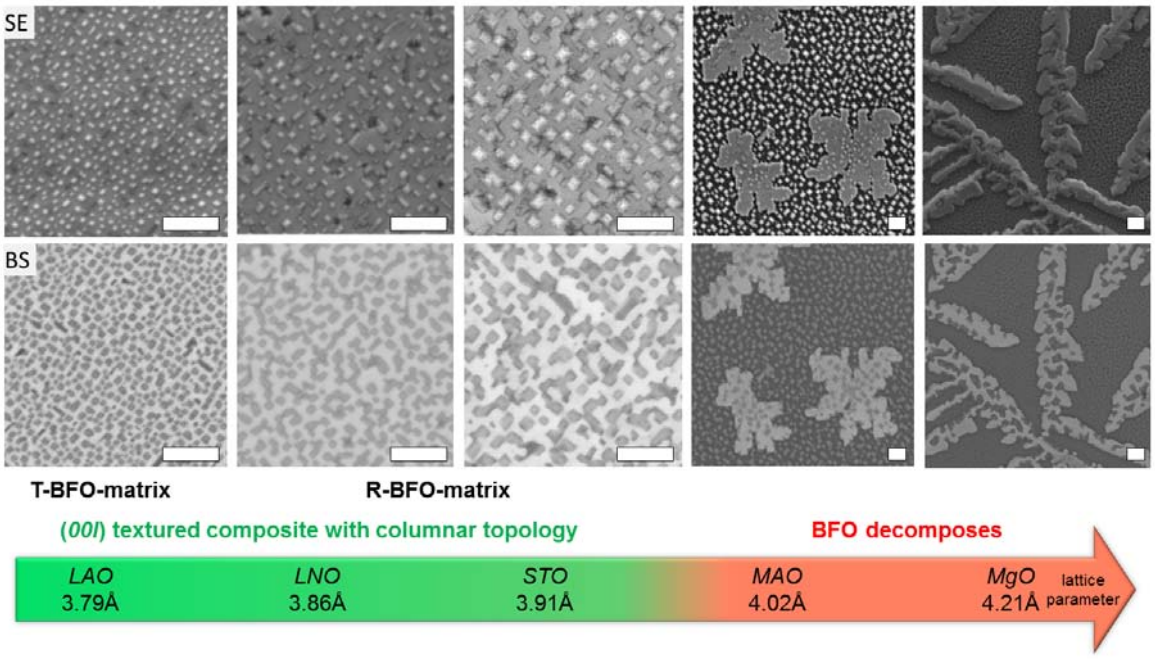

Figure 4.20: (top) Scanning secondary electrons images (SE) and backscattered electron images (BS) are shown for samples of 100 *nm* thickness grown on (001) substrates with increasing lattice parameter: *LAO*, $LaNiO_3/LAO$, *STO*, $MgAl_2O_4$, and *MgO* ($LaNiO_3$ (*LNO*)). Films grown on *LAO*, *LNO*/*LAO*, and *STO* have a closed *BFO* matrix with surrounded *CFO* columns. In contrast, *BFO* decomposes on substrates causing tensile stress on *R-BFO* ($MgAl_2O_4$ and *MgO*), forming *Bi*-rich dentritic structures and pyramidal spinel islands. (Scale bars are 500 *nm*). (bottom) Substrates and indication of formed phases.

Magnetic properties

Room-temperature magnetization loops of films with columnar topology on different substrates (and buffered substrates) are shown in figures 4.21(a) to (e). Measurements were performed with the magnetic field applied perpendicular (blue rhombi) and parallel (red diamonds) to the substrate surface, i.e along the [001] and [100] *LAO* directions. The magnetization has been calculated using the volume fraction of the *CFO* (38 vol-%) and yields a saturation value of $M_S \approx 400$ emu/cm^3 for films grown either on *LNO/LAO*(001) (figure 4.21(b)), *STO*(001) (figure 4.21(c)), *LCMO/STO*(001) (figure 4.21(d)) and *LAO*(001) (figure 4.21(e)). This saturation magnetization matches very well with the reported bulk value. For completeness, we include here (figure 4.21(a)) the magnetization loops of a $BaTiO_3$-$CoFe_2O_4$- nanocomposite deposited on the usual *STO*(001) substrates, having a little lower similar M_S value (see Section 5.3.1 for further details).

Although all films display a similar saturation, their magnetic anisotropy is markedly different. figure 4.21(a)-(e) show magnetization loops ordered with respect to the *CFO* out-of-plane strain, obtained by XRD $\omega/2\theta$-scans. The magnetization loops "'blue rhombi"' and "'red diamonds"' correspond to the out- and in-plane loops respectively. The progressive change of the loops with strain indicates in parallel with a released compressive out-of-plane strain the direction of the easy magnetization direction changes from out-of-plane to in-plane. The distinct magnetic anisotropy is better quantified by the different magnetization remanence/saturation (M_R/M_S) ratios or more simply by the $M_R[001]/M_R[100]$ which gives 4.06, 1.82, 0.74 and 0.43 respectively for the $BiFeO_3$-$CoFe_2O_4$ composites on *LNO/LAO*, *STO*, *LCMO/STO* and *LAO*, respectively. The $M_R[001]/M_R[100]$ ratio has a clear correspondence with the strain state of the film as reflected by the value, determined from the measured *c*-axis lengths and included in each panel. These data show that the in-plane magnetic easy axis is obtained for the film grown on *LAO*, which has the smaller strain ($\epsilon \approx -0.01\%$) whereas out-of-plane magnetization develops when increasing strain from films on *STO* to films on *LNO/LAO* ($\epsilon \approx -0.19\%$ and -0.33% respectively).

Due to its large magnetostriction of *CFO*, strain plays an important role on the magnetic anisotropy of films. Indeed, in pure *CFO* films under tensile strain, that is compressed out-of-plane cell parameter, the [001] direction is an easy axis, whereas (001) is an easy-plane in case of opposite or negligible strain [48, 121]. Our results for *CFO* in *BFO-CFO* nanocomposites follow exactly the same trend. The agreement extends beyond the results presented here. Indeed, in figure 4.21 we collect the $M_R[001]/M_R[100]$ ratio for the films described here and we also include the results we have obtained on a number of other (001)-oriented epitaxial nanocomposites having distinct strain state. Data correspond to *BFO-CFO* nanocomposites 4.21(b)-4.21(c) deposited in similar conditions on bare *STO*(001) or *LCMO* buffered *STO*(001) substrates, and also from

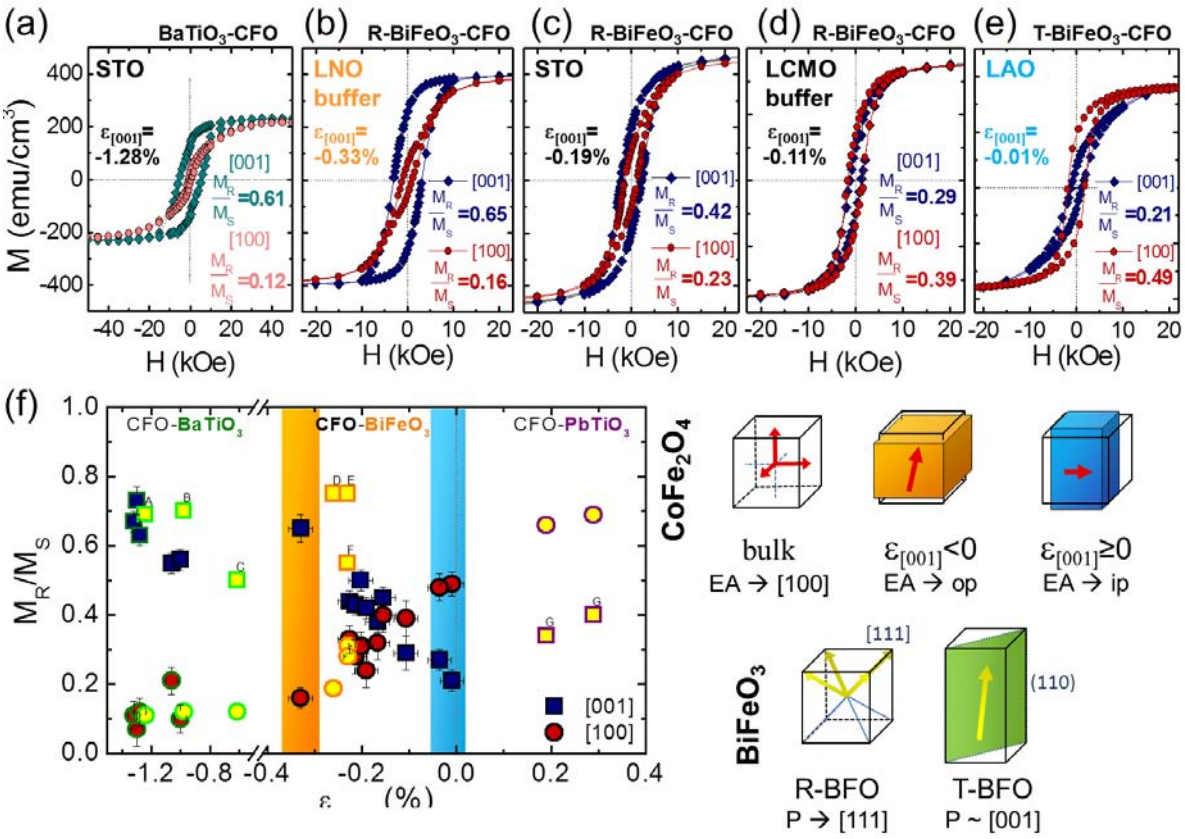

Figure 4.21: (a)-(e) Magnetization hysteresis loops measured at room temperature with the field applied in the plane (circles) and out-of-plane (rhombi) for *BaTiO*$_3$-*CFO*/*STO* samples (a), and *BiFeO*$_3$-*CFO*-composites on (b) LNO/LAO(001), (c) STO(001), (d) LCMO/STO(001) and (e) LAO(001). Magnetization is normalized to the *CFO* volume fraction. Labels in each panel indicate remanence/saturation magnetization ratio for parallel and perpendicular applied field. (f) $M_R[001]/M_R[100]$ remanence plotted vs. *CFO* out-of-plane strain. Solid symbols correspond to composite samples grown in our laboratory substrates are indicated. Capital letter labeled empty symbols correspond to values retrieved from literature: **A** ref [24], **B** ref [5], **C** ref [70], **D** ref [122], **E** ref [28], **F** ref [123] and **G** [124]. Simplified sketches indicating the dependencies of the *CFO* strain and the *BFO* phase on the directions of the magnetic easy axis and the spontaneous polarization, respectively, are plotted in the side panel.

BaTiO$_3$-*CFO* nanocomposites on *STO*(001) (see Chapter 5). We also include in figure 4.21(f) data from literature corresponding to *BFO*-*CFO*, *BaTiO*$_3$-*CFO*, and *PbTiO*$_3$-*CFO* nanocomposites.[5, 24, 28, 54, 70, 122, 123] (see Table 4.2 for information on these films and references). Data in figure 4.21(f) display a clear trend. It evidences the dominating influence of the strain on the magnetic anisotropy of *CFO* in nanocomposites: highly *c*-axis compressed *CFO* in *BTO* matrix shows highest perpendicular anisotropy, *c*-axis expanded *CFO* in *PbTiO*$_3$ matrix shows in-plane easy-axis and *CFO* in *BFO* matrix is situated in between these extremes. Thus, the magnetic anisotropy is tuneable from perpendicular to in-plane by the combined action of epitaxial strain induced by the substrate and the accompanying FE phase (see the sketch in figure 4.21(f)). On the other hand, we have demonstrated here that the substrate selection determines which *BFO* phase (*T* or *R*) forms in the nanocomposite, thus critically affecting the corresponding FE properties.

More precisely: the [001] crystal axes of both *BFO* phases in the nanocomposites are parallel to the [001] substrate direction and the direction of the spontaneous polarization depends on the specific phase of *BFO* (see the sketch in figure 4.21(f)), being almost parallel to the [001] *LAO* direction or at about 55° away from it for *T-BFO* [119] and *R-BFO*, respectively.

4.4 Summary

We have explored heteroepitaxy of biferroic $BiFeO_3$-$CoFe_2O_4$ composites with a dual selectivity on the orientation of both ferroic orders, by substrate selection, here STO(001) and (111). We have determined optimized growth parameter for the stoichiometric *CFO-BFO* nanocomposite within a small temperature window around 625 °C(0.1 $mbar$ and 5 Hz) and is similar for both substrates.

A small variation in the growth temperature results in dramatic effects in morphology and stoichiometry. Bi content decreases monotonically as temperature increases, and it appears that there is not an optimal window, significantly broad, where Bi stoichiometry is fully preserved. However, *BFO* could allow a certain Bi deficit before formation of Fe_xO_y spurious phases. Therefore, the deposition temperature and laser frequency can not be used as a free parameter to tune the pillar size.

BFO-CFO composites have been deposited on different substrates with broad range of lattice parameters: on compressive substrates we find heteroepitaxial growth of both composite phases maintaining substrate texture, and that substrates imposing strong tensile stress on *BFO* favor its decomposition. The structural differences in composites with *T*- and *R-BFO* like matrix allow to modify the functional properties: (1) by tuning of the magnetic anisotropy of the *CFO* pillars, and (2) by selection of structural phase of *BFO*, *R* and *T*, which permits the selection of the polar axis direction.

In (00l) textured *CFO–R-BFO* nanostructures the *CFO* nanopillars present compressive out-of-plane strain while the in-plane lattice parameter was relaxed. This compressive strain may be of elastic nature originated by the large amount of interfaces with the compressive *BFO* matrix that surrounds the nanopillars. Selective removal of the *BFO* matrix and post annealing at 500 °C did not release the this compressive strain and thus indicates that it is of nonelastic nature. Magnetoelectric coupling at the nanoscale, using scanning probe microscopies, showed local magnetization switching of 12% of the columns in the observed area. (00l) *CFO-perovskite* columnar nanocomposites investigated here and by other groups show a clear tendency of the measured out-of-plane strain in the *CFO* columns with the easy magnetization direction being favored to out-of-plane if the strain is compressive and to in-plane for tensile strain.

The mapping of the epitaxial stabilization of *T-BFO* in single films as a function of the deposition temperature has evidenced *T-BFO* phase formation in a very narrow T_S window, with chemical decomposition above and inefficient epitaxial stabilization below. While embedding *CFO* spinel columnar nanostructures within a *T-BFO* matrix allows to broaden the range of deposition temperatures for single *T-BFO* films grown on LAO(001) substrates. The difference is likely explained considering that in single films the epitaxial stabilization of the metastable *T-BFO* is driven by the film-substrate interface, whereas in the nanostructures the extra interfaces between the two phases can play a role. Furthermore, the formation of tilted M_R- and tilted $T_{I,II}$- domains in single layer films has not been observed in nanocomposite films.

Table 4.2: Remanence magnetization ratios at room temperature, out-of-plane lattice parameter and strain of $CoFe_2O_4$-$BiFeO_3$ (*CFO-BFO*), $CoFe_2O_4$-$BaTiO_3$ (*CFO-BTO*) and $CoFe_2O_4$-$PbTiO_3$ (*CFO-PTO*) nanocomposite films of varied thickness have been retrieved from literature. Values of $M_R[001]/M_R[100]$ were determined from the magnetization loops of the corresponding publication. Values for samples grown in this work are summarized as well.

Label	c (Å)	Composition	Substrate	t (nm)	$M_R[001]/M_R[100]$	Ref.
A	8.29	$1/3CFO$ - $2/3BTO$	$STO(001)$	400	6.27	[24]
B	8.31	$1/3CFO$ - $2/3BTO$	$STO(001)$	400	5.88	[5]
C	8.34	$1/3CFO$ - $2/3BTO$	$MgO(001)$	320	4.17	[70]
D	8.37	$1/3CFO$ - $2/3BFO$	$SRO/STO(001)$	300	2.68	[122]
E	8.37	$1/3CFO$ - $2/3BFO$	$SRO/STO(001)$	300	1.77	[28]
F	8.42	$1/3CFO$ - $2/3PTO$	$STO(001)$	≈230	0.58	[123]
F	8.41	$2/3CFO$ - $1/3PTO$	$STO(001)$	≈230	0.51	[123]
G	8.36	$2/3CFO$ - $1/3PTO$	$MgO(001)$	–	2.5	[124]
CBT825gr28t090	8.283	$0.35CFO$ - $0.65BTO$	$STO(001)$	90	10.3	*this work*, rf-sputtering
CBT825gr28t160	8.285	$0.35CFO$ - $0.65BTO$	$STO(001)$	160	5.26	*this work*, rf-sputtering
CBT825gr28t330	8.302	$0.35CFO$ - $0.65BTO$	$STO(001)$	330	4.58	*this work*, rf-sputtering
CBT850gr28t160	8.308	$0.35CFO$ - $0.65BTO$	$STO(001)$	160	4.83	*this work*, rf-sputtering
CBT825gr14t130	8.295	$0.35CFO$ - $0.65BTO$	$STO(001)$	130	4.25	*this work*, rf-sputtering
8LNCBFLAO	8.365	$0.35CFO$ - $0.65BFO$	$LNO/LAO(001)$	100	4.06	*this work*, PLD
19CBFSTO	8.375	$0.35CFO$ - $0.65BFO$	$STO(001)$	100	1.53	*this work*, PLD
18CBFSTO	8.376	$0.35CFO$ - $0.65BFO$	$STO(001)$	100	1.82	*this work*, PLD
88CBFSTO	8.376	$0.35CFO$ - $0.65BFO$	$STO(001)$	100	1.33	*this work*, PLD
17CBFSTO	8.378	$0.35CFO$ - $0.65BFO$	$STO(001)$	100	1.54	*this work*, PLD
24CBFSTO	8.379	$0.35CFO$ - $0.65BFO$	$STO(001)$	100	1.13	*this work*, PLD
7LCMOCBFSTO	8.382	$0.35CFO$ - $0.65BFO$	$LCMO/STO(001)$	100	0.74	*this work*, PLD
38CBFLAO	8.389	$0.35CFO$ - $0.65BFO$	$LAO(001)$	100	0.56	*this work*, PLD
42CBFLAO	8.391	$0.35CFO$ - $0.65BFO$	$LAO(001)$	100	0.43	*this work*, PLD

Table 4.3: Sample list $BiFeO_3$-$CoFe_2O_4$.

	Sample name	substrate	$\mathbf{T}_S$ (°C)	**f** (Hz)	**p** (mbar)	**t** (nm)	Target (mm)	Phase separation (PS)
Series: Growth Conditions	7CBFSTO	STO(100),(111)	550	5	0.1	100	13	traces Bi_XO_Y
	3CBFSTO	STO(100),(111)	600	5	0.1	100	13	PS, textured
	4CBFSTO	STO(100),(111)	650	5	0.1	100	13	PS, textured
	8CBFSTO	STO(100),(111)	700	5	0.1	100	13	*Bi* deficient
	2CBFSTO	STO(100),(111)	750	5	0.1	100	13	no $BiFeO_3$, traces other Fe_XO_Y
	5CBFSTO	STO(100),(111)	800	5	0.1	100	13	no $BiFeO_3$, traces Fe_XO_Y
	10CBFSTO	STO(100),(111)	650	5	0.05	100	13	PS, textured
	11CBFSTO	STO(100),(111)	650	5	0.01	100	13	no $BiFeO_3$
	17CBFSTO	STO(100),(111)	600	5	0.1	100	25.4	PS, textured
	18CBFSTO	STO(100),(111)	625	5	0.1	100	25.4	PS, textured
	19CBFSTO	STO(100),(111)	650	5	0.1	100	25.4	PS, textured
	20CBFSTO	STO(100),(111)	675	5	0.1	100	25.4	PS, textured, *Bi* deficient
	30CBFSTO	STO(100),(111)	625	2	0.1	100	25.4	PS, textured, *Bi* deficient
	33CBFSTO	STO(100),(111)	625	10	0.1	100	25.4	PS, textured
	15CBFSTO	STO(100),(111)	650	5	0.1	200	25.4	PS, textured
	45CBFSTO	STO(100)	625	5	0.1	200	25.4	PS, textured
TBFO matrix	35CBFLAO	LAO(001)	550	5	0.1	100	25.4	*T-BFO*, polycrys. *CFO*
	36CBFLAO	LAO(001)	600	5	0.1	100	25.4	*T-BFO*, polycrys. *CFO*
	42CBFLAO	LAO(001)	625	5	0.1	100	25.4	*T-BFO*+weak *R-BFO*, *CFO*(00*l*)
	38CBFLAO	LAO(001)	650	5	0.1	100	25.4	*T-BFO*+weak *R-BFO*, *CFO*(00*l*)
	39CBFLAO	LAO(001)	675	5	0.1	100	25.4	PS, *T-BFO*+textitR-BFO, *CFO* polycry.
	40CBFSTO	LAO(001)	700	5	0.1	100	25.4	*CFO* + *FO* polycrystal, no *BFO* observed
Substrates	8LNCBFLAO	LNO/LAO(001)	625	5	0.1	100	25.4	PS, textured
	37CBFMgO	MgO(001)	625	5	0.1	100	25.4	*BFO* desintegrate
	7LCMCBFSTO	LCMO/STO(001)	625	5	0.1	100	25.4	PS, textured
	86CBFMAO	MAO(001)	625	5	0.1	100	25.4	*BFO* desintagrate
	24CBFSTO	STO(001)	625	5	0.1	100	25.4	PS, textured
	88CBFSTO	STO(001)	625	5	0.1	100	25.4	PS, textured

Table 4.4: Sample list of grown T-$BiFeO_3$ layers on $LAO(001)$.

Sample	T_S (°C)	**p** ($mbar$)	**f** (Hz)	**Phases**
6BFOLAO	550	0.1	5	polycrystalline *R-BFO*, traces *BO*
7BFOLAO	575	0.1	5	polycrystalline *R-BFO*, traces *BO*
8BFOLAO	600	0.1	5	polycrystalline *R-BFO*
9BFOLAO	625	0.1	5	mainly *R-BFO* (00l) and (hh0)
10BFOLAO	650	0.1	5	mainly *R-BFO* (00l) and (hh0)
11BFOLAO	675	0.1	5	mainly *R-BFO* (00l) and (hh0), traces *T-BFO*(00l)
12BFOLAO	700	0.1	5	*T-BFO*(00l)
13BFOLAO	725	0.1	5	very low intensity *T*- and *R-BFO*, traces αFO
14BFOLAO	750	0.1	5	No BFO, αFO
17BFOLAO	700	0.1	5	*T-BFO*(00l)

CHAPTER 5

$BaTiO_3$–$CoFe_2O_4$ vertical heterostructures

Columnar biferroic $BaTiO_3$-$CoFe_2O_4$ nanostructures were reported by Zheng *et al.* [5] in 2004 using PLD as depositions technique (molar ratio was 2/3:1/3 and substrates (001)).

Here we study $BaTiO_3$-$CoFe_2O_4$ thin films grown by *rf*-magnetron sputtering from a single mixed target. Anyhow, differences with respect to PLD could be detrimental to fabricate self-assembled multifunctional composites: (i) typical for pulsed laser deposition is a huge instantaneous adatom supersaturation, while in sputtering a continuous deposition with low supersaturation takes place (ii) in PLD the growth rate is high (0.05 to 5 Å/s, depending on rate per pulse and laser repetition rate), but it is low for sputtered oxide films, around 0.08 to 0.47 Å/s in our case. Moreover, the maximal temperature of the heater in our experimental set-up is restricted to T_S=825 °C (for singular experiments it was increased to T_S=850 °C) which is significantly lower than the used by Zheng et. al [5, 70], using up to 1050 °C. The target has a molar ratio of 0.65 $BaTiO_3$ - 0.35 $CoFe_2O_4$ (volume ratio of 0.62*vol* BTO - 0.38*vol* CFO). A dynamic chamber pressure of 0.266 *mbar* with argon-oxygen 3:1 mixture, samples were cooled to RT in an oxygen atmosphere of 466 *mbar*. We aim to investigate the effects of substrate temperature, growth rate and thickness on phase separation, morphology and physical properties. First, a view samples were prepared with low growth rate (0.5 nm/min, 15 W) varying temperature (500-800 °C) and thickness (60 and 250 nm). At high temperature of 800 °C (250 nm) phase separation and principal (00l) texture is observed, but with polycrystalline traces were present. Therefor, we explored in detail growth conditions using higher growth rate (2.8 nm/min, 45 W) and higher growth temperatures (750-850 °C, centered around 825 °C). A schematic overview is in figure 5.1 for the series .

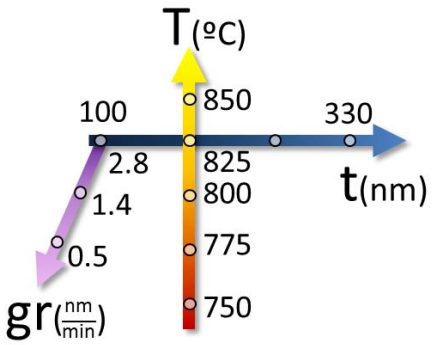

Figure 5.1: Schematic overview of the deposition conditions that used for the $BaTiO_3$-$CoFe_2O_4$ film growth.

In the following a detailed analysis of the crystalline structure, the surface morphology and the magnetic properties is presented. We also describe briefly the dielectric properties.

5.1 Preliminary study of growth conditions for *CFO-BTO* composites

We preliminary studied the effects of substrate temperature T_S (500 °C to 800 °C, with a T_S step of 100 °C, see XRD $\omega/2\theta$-scans in figure 5.2(a)) on the micro structure of films grown using a rf-power of 15 W (low grow rate, $gr \approx 0.5\,nm/min$) and film thickness about 60 nm, in addition 250 nm thick samples were prepared at 700 and 800 °C. Only a brief summary is presented in this section, based on this preliminary we explored other growth conditions in Section 5.2. Below $T_S \leq 600$ °C we observe an absence of crystallinity, for temperatures T_S=600-700 °C the films present (00l) texture ($c \approx 4.11$Å), but diffraction peaks corresponding to either *CFO* or *BTO*(00l) could not be discerned (see amplified regions in figure 5.2(b)). At high T_S=800 °C the film shows separated *CFO* (00l) and *BTO* (00l) peaks, resulting in $c_{CFO} \approx 8.29$Å and $c_{BTO} \approx 4.045$Å. Additionally, polycrystalline fractions of *BTO* are evidenced by (110), (111) and (112) peaks. The lattice spacing for the (00l) reflections are calculated from Gaussian deconvolution of the peaks. Thick films were prepared (700 and 800 °C) were prepared to check for minor fractions of *CFO* and *BTO* phase separation especially at the lower T_S=700 °C.

Thick films (t=250 nm) were grown at T_S=700 °C and T_S=800 °C and corresponding XRD $\omega/2\theta$-scans are shown in figure 5.2(c). Similar to the thinner samples a pure (00l) texture is found at T_S=700 °C, while additional *BTO* (110),(111) and (112) reflections appear at T_S=800 °C. An amplified region around the (004)*CFO*/(002)*BTO* reflections is in figure 5.2(d), at T_S=800 °C two contributions to the diffraction intensity are observed ($2\theta_{CFO(004)} = 43.6°$ and $2\theta_{BTO(002)}$=44.3 °). Therefore, the out-plane lattice parameters of *CFO* ($c_{CFO} = 8.3$Å) and *BTO* ($c_{BTO} = 4.09$Å) and so *CFO* is compressed about -1% while

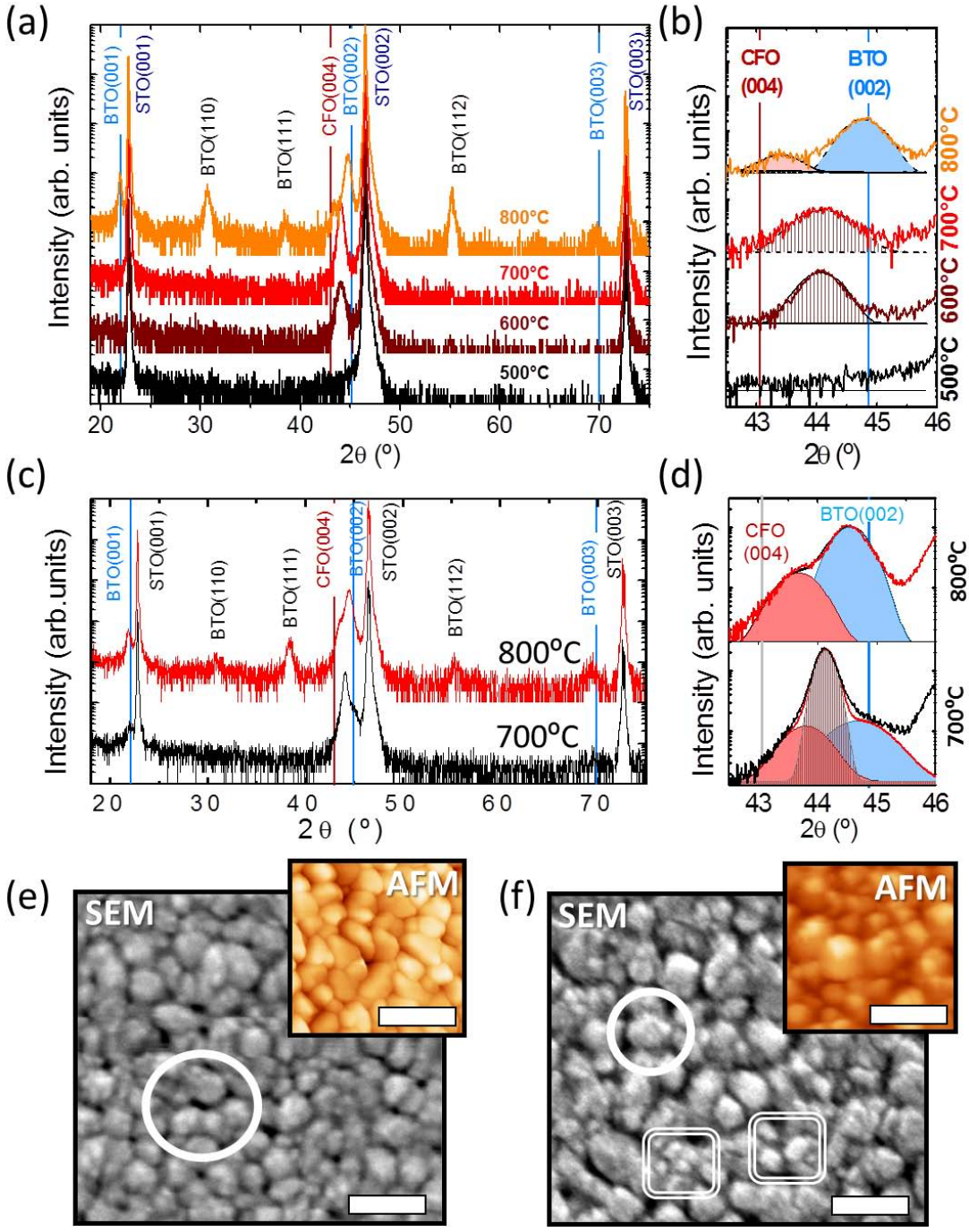

Figure 5.2: $\omega/2\theta$ scans of (a) 60 nm thick films at various T_S and (c) two 250 nm thick films at 700 and 800 °C, all grown at a growth rate of 0.5 nm/min. (b) and (d) Amplified regions around the $CFO(004)$ and $BTO(002)$ reflection. Fitted Gaussian profiles of $BTO(002)$ (light blue) and $CFO(004)$ (light red) reflection are below each curve; two at 800 °C, but three at 700 °C here also a large central peak (shaded brown) is present with 10 times the intensity of the two minor peaks. Vertical lines are bulk parameters for CFO (gray) and BTO (green). Morphology of 250 nm thick composite films obtained by SEM and AFM (inset) grown at (e) 700 °C and, (f) 800 °C. In FESEM images two grain types are marked: (circle) irregular and large ($> 100\,nm$) grains, (double lined squares) may correspond to CFO pyramid based column tops. Bars are 200 nm.

BTO is enlarged +1.3% compared to their bulk values (similar values were observed for 60 nm samples). At 700 °C three peak contributions can be discerned, a main diffraction peak at 44.1 ° is (shaded brown in figure 5.2(d)). Two small fractions ($< 1/10^{th}$ main peak intensity) corresponding to $BTO(002)$ ($2\theta = 44.1°$) and $CFO(004)$ ($2\theta = 44.1°$). The lower growth temperature limits the mobility of the adatoms, consequently the main peak might result from the formation of a solid solution of the composite phases, i.e. formation of $Ba(Ti_{1-x}[Fe, Co]_x)O_3$ where Ti^{4+} is substituted by $Fe, Co^{3+/4+}$. One may assume a linearly changing lattice parameter for the mixture of $BaTiO_3$ ($c = 4.04$Å) with $CoFe_2O_4$ ($a/2 = 4.196$Å) at a composition of $0.65mol\%BTO$-$0.35mol\%CFO$ it would be around $a_{mix} = 4.14$Å and thus $2\theta \approx 43.7°$ close to the measured 44.1 ° at 700 °C. Partial relaxation of the two constituents with increasing thickness might be a reason for the broad background and might be caused by additional fractions of BTO and CFO (as indicated by the fit in figure 5.2(d)).

Compared to previously reported BFO-CFO composites the column-matrix morphology can not be clearly evidenced by SEM and AFM in this 250 nm thick samples. The surfaces are granular with a surface roughness around $rms \approx 10\,nm$, peak to valley heights are around 50 nm and grain sizes are in the range of 90 to 110 nm, see AFM topographic images inset in figure 5.2(e) and 5.2(f) for 700 and 800 °C sample, respectively. Nevertheless, in the 800 °C sample two surface features can be differentiated (figure 5.2(f)): large grains diameter is about 90 to 120 nm (some examples are marked with circles) and smaller square based ones d is around 30 to 50 nm they are marked with double lined squares. The smaller objects may sugest the formation of CFO nanocolumns with pyramidal top protruding the sample surface, which could be expected from XRD results showing phase separation and dominant $(00l)$ texture. Nevertheless, neither AFM and SEM observations allowed to visually confirm a clear phase separation.

Comparing our results with observations of Zheng et al.[24, 125] we find a similar onset for phase separation around 750-800 °C (400 nm thick films). The diameter of columnar CFO embedded in BTO matrix varied from 10-12 nm at low T_S=750 °C to around 30-40 nm at high T_S=950 °C (high grwoth rates of around 8 nm/min [70]) without presence of polycrystalline phases. In our experimental set-up a limited T_S of 850 °C and growth rates up to 3 nm/min can be achieved. In the following we will explore if this growth conditions allow the growth of nanocomposites with an improved phase separation and absence of polycrystalline fractions.

5.2 Influence of deposition temperature and thickness (high growth rate)

By increasing the rf-power from 15 to 45 W the growth rate (gr) increased from 0.5 nm/min to 2.8 nm/min, respectively. In the following we present the effect of the increase in gr, and for the higher gr (2.8 nm/min) a study on two series changing T_S and t (Schematic overview is in figure 5.1).

5.2.1 Structural dependence on growth conditions

Influence of growth rate (T_S=825 °C, t=90 nm)

As first step we increase the rf-power from 15 to 45 W in steps of 15 W maintaining constant temperature at 825 °C, the deposition time was adjusted to obtain films with thickness around 100 nm. The XRD $\omega/2\theta$ scans of composites grown at 0.5, 1.5 and 2.8 nm/min are shown in figure 5.3(b). Here only amplified $\omega/2\theta$ scans around the (002) and (004) substrate reflections are shown. $BTO(00l)$ and $CFO(00l)$ reflections are appreciated in all samples, but $CFO(00l)$ reflections being weak in the $gr = 0.5\,nm/min$ sample (see zoom around $STO(004)$). It is noted also that reducing gr, there is an increased amount of polycrystallinity, with presence of (110), (111) and (112) BTO reflections (full range $\omega/2\theta$ scan is in figure 5.3(a), while only (111) reflections is within the zoomed region) The fraction of polycrystalline grains is reduced with increasing growth rate and at the highest rate of 2.8 nm/min the $BTO(111)$ peak height is comparable to the noise level of the measurement. In the case of the main $(00l)$ reflections, despite of the partial overlap of the reflections, the $BTO(004)$ and $CFO(008)$ peaks are well separated and permit fitting to respective Gaussian curves which allows determination of the out of plane parameter of both phases. Both BTO and CFO have the tendency to relax towards bulk lattice parameters lowering the deposition rate (figure 5.3(c)). In the case of BTO at 0.5 nm/min it is nearly c-bulk c_{BTO}=4.037 Å while at highest rate gr=2.8 nm/min it is notably expanded to c_{BTO}=4.067 Å, corresponding to an out-of-plane strain of $\varepsilon \approx 0.7\%$. But on the other hand CFO always shows a strained state with smaller out-of-plane parameter, relaxing slightly with decreasing growth rate from $\varepsilon_{2.8nm/min} \approx -1.4\%$ to $\varepsilon_{0.5\,nm/min} \approx -1.1\%$.

Influence of Growth Temperature ($gr = 2.8\,nm/min$, $t = 160\,nm$)

The growth temperature, was probed at high deposition rate with a narrow step of 25 °C from T_S=750 to 850 °C. The films are $(00l)$ textured and for increasing substrate

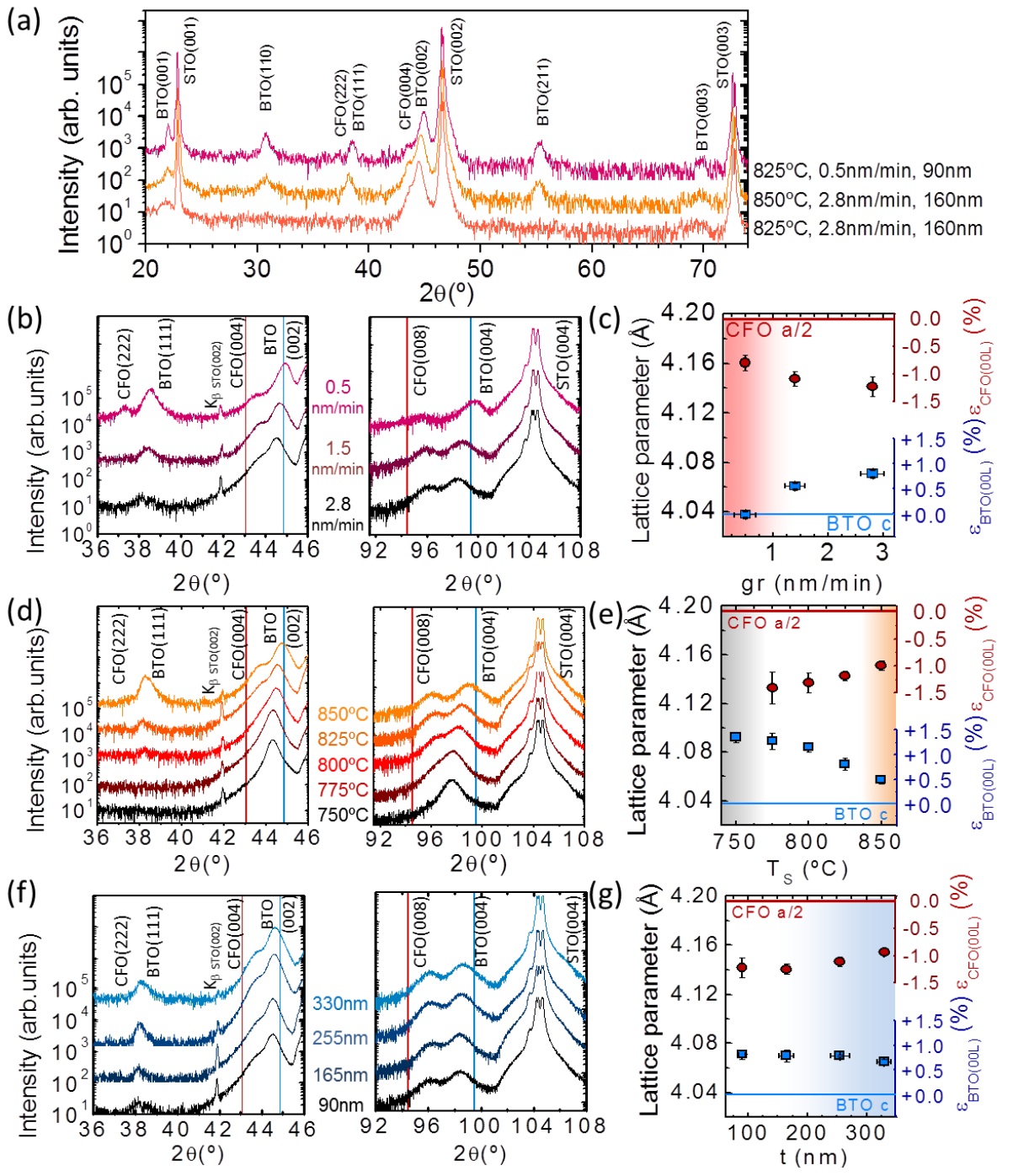

Figure 5.3: (a) $\omega/2\theta$ scans of selected samples, peaks are labeled and growth conditions are on the right. Evolution of (00l) texture for growth rate (T_S=825 °C, $t \approx 100\,nm$) (b), growth temperature at $gr = 2.8\,nm/min$ (d), and film thickness (T_S=825 °C, $gr = 2.8\,nm/min$) (f), with amplified regions of $\omega/2\theta$ scans around the STO(002) and STO(004) reflection. The diffraction peaks in the graphs are labeled and lines indicate the position of the reflections of bulk BTO (blue) and CFO (red). The calculated out-of-plane lattice parameters from the corresponding (00l) reflections are plotted in (c), (e) and (g). The color shade indicates polycrystalline films and at T_S=750 °C the gray shade the not observable phase separation of BTO and CFO.

temperature T_S both *BTO* and *CFO* tend to relax towards its bulk values (see figure 5.3(d) and 5.3(e), respectively). For the lowest T_S=750 °C there are single (00l) reflections, without separation of *BTO* and *CFO* peaks. Above 775 °C the reflections can be separated clearly, and in the sample grown at highest T_S=850 °C other *BTO* orientations are also clearly appreciated (full range $\omega/2\theta$ scans for 825 and 850 °C are in figure 5.3(a)). This observation is similar to the low growth rate but with onset of polycrystalline growth shifted to higher T_S by about 50 °C.

Influence of film thickness ($gr = 2.8\,nm/min$, T_S= 825 °C)

Well separated *BTO* and *CFO* phase and low amount of polycrystalline traces are found for T_S=825 °C and growth rate of $2.8\,nm/min$. These conditions were selected to prepare samples changing the thickness. The X-ray diffraction patterns and the dependence of the lattice parameters are shown in figure 5.3(f) and 5.3(g), respectively. With thickness the intensity of the diffraction peaks increases, whereas the lattice parameters remain nearly constant for increasing thickness ranging from 90 to 330 nm, only a slight relaxation is found. It is also noted that even for the thickest film the intensity for the *BTO* (111) reflection is very low compared to the dominating (00l) reflections of *BTO* and *CFO*.

Epitaxial relationship

Pole figure measurements around the (202) substrate reflection were used to probe the epitaxial relationship. Both phases of the composite (t=260 nm, T_S=825 °C, gr=2.8 nm/min) grows cube on cube as shown by a $2\theta/\varphi$ plot around the (202) substrate reflection (figure 5.4(a)), where *CFO*(404) and *BTO*(202) can be well distinguished and each showing four peaks separated 90 ° matching the the substrate positions. RSMs around the (103) substrate reflection were measured to determine the in-plane parameters. An example the RSM is shown in figure 5.4(b), with the corresponding reflections indicated. The center of the diffraction peak of *BTO*(103), marked with + symbol, has been used to calculate the in- and out-of-plane lattice parameters a and c, it is found that the latter is matching well with the determined from the $\omega/2\theta$ scan. Anyhow, the intensity of the *CFO*(206) reflection is very weak, and no sharp peak can be identified, the × cross indicates its approximate center position. As the *CFO* reflections do not allow accurate deduction of the in-plane lattice spacings, only *BTO* peaks have been calculated and are plotted in figure 5.4(c). Purely (00l) textured films show only a slight variation of the in- and out-of-plane parameter, $a = 4.01 \pm 0.01$ Å and $c = 4.07 \pm 0.02$ Å, and in fact both are larger than bulk *BTO* (a = 3.998 Å, c = 4.038 Å). We can observe that the *BTO* elongated along the c axis, which reduces while the deposition temperature increases. A similar

trend is displayed while the growth rate decreases; increasing thickness leads to slightly more relaxed parameters.

The variation of BTO strain with deposition temperature differs from that observed in nanocomposite films grown in a range of higher temperatures by pulsed laser deposition [24], where the BTO out-of-plane parameter did not show dependence on T_S but was relaxed for all films. We observe that films with higher polycrystalline fraction like (111) or (110) tend to have a more bulk like a and c lattice parameters. It is also found that at lower temperature T_S=750-775 °C (samples in which phase separation is not evident) the in-plane parameter a is strongly increased.

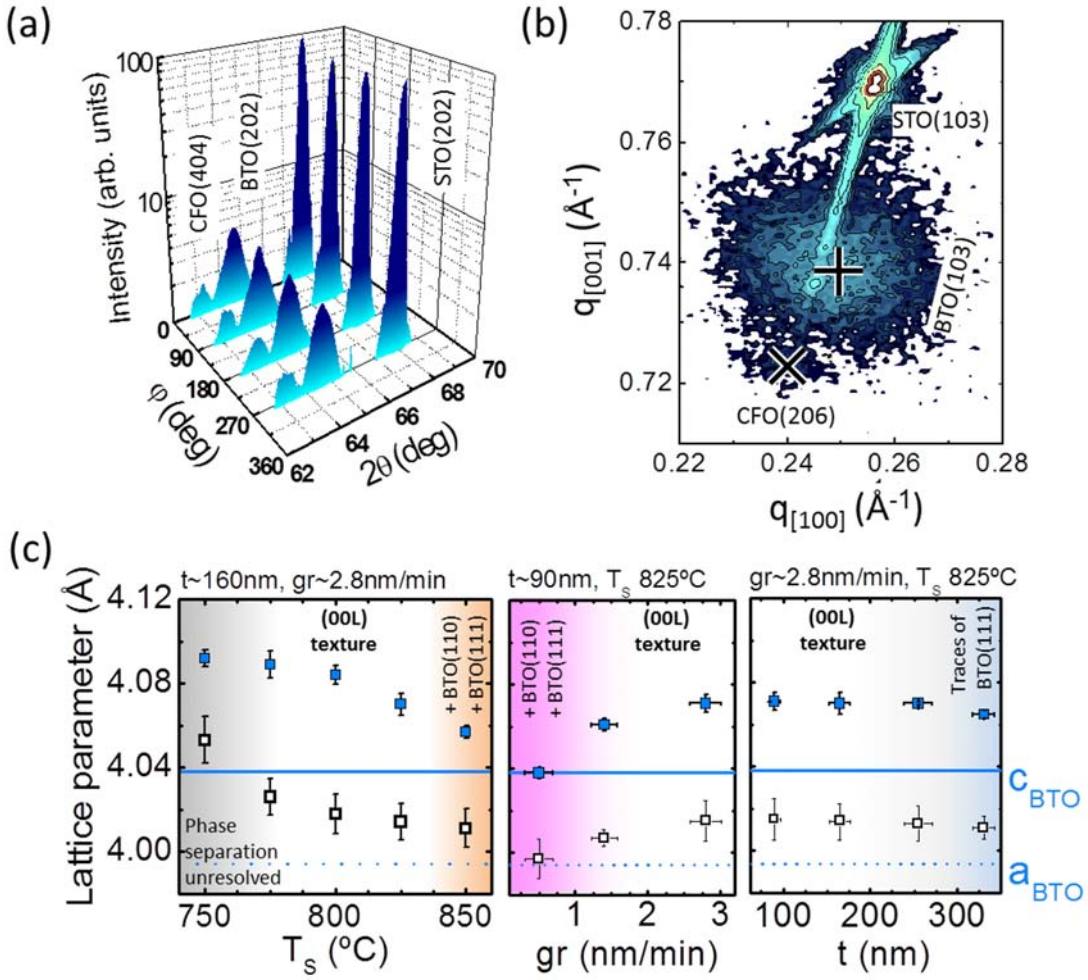

Figure 5.4: (a) XRD $2\theta/\varphi$ plot for a 265 nm thick sample grown at 825 °C and 2.8 nm/min; around the (202) $SrTiO_3$ reflection indicating cube on cube growth of the to constituent phases. (b) RSM around the STO(103) reflection, the center positions of the CFO(206) and BTO(103) film reflection are marked and labeled correspondingly. (c) the extracted a and c BTO parameters are plotted $vs.$ T_S, gr and t. Horizontal lines indicate bulk a and c BTO lattice parameters (the intensity for CFO is weak and does not allow a proper calculation of the lattice spacing). Growth conditions with additional features are present are indicated.

5.2.2 Morphology: evolution of surface features at high growth rate

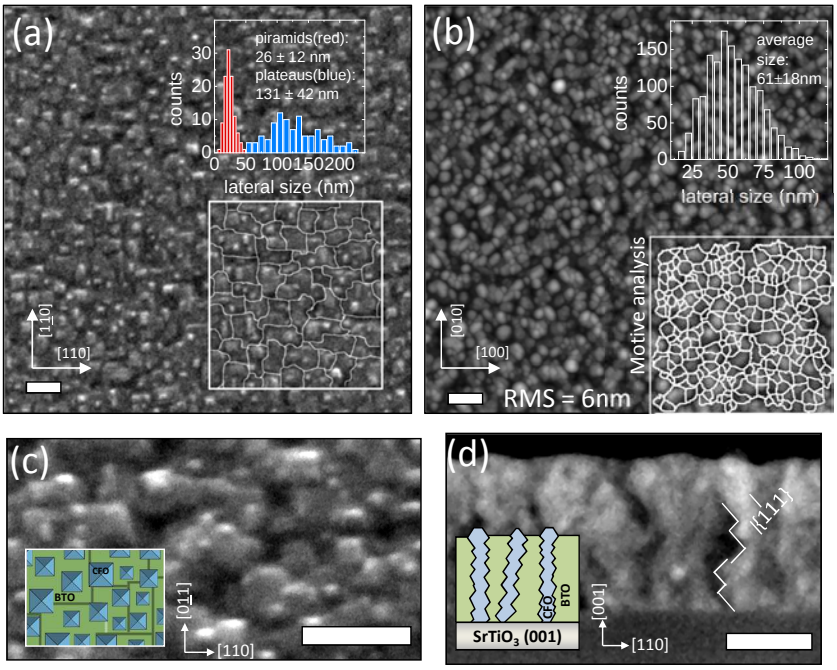

Figure 5.5: Surface morphology of the sample grown at 825 °C with $gr = 2.8\,nm/min$ and a thickness of 160 nm measured by (a) scanning electron microscopy and (b) atomic force microscopy. In the SEM image (a) two distinct features are observed: flat plateaus and small squared pyramidal objects emerge from the plateaus. AFM images (b) do not allow to differentiate this feature. The grain size distribution was obtained by motive analysis. The size distribution is shown in the upper right corner of each image. 45° tilted SEM image is presented in (c) with corresponding sketch and cleaved cross-section (d) suggest a columnar microstructure, the columns being faceted along (111) crystal planes, as indicated by sketch and white marks. Bars correspond to 100 nm.

The morphology of the samples was observed by SEM and AFM. The samples were not covered with carbon for the observation, and the field emission scanning electron microscope (Fei Quanta 200E) installed at the ICMAB allowing to obtain high lateral image resolution was used. The SEM image (figure 5.5) of a composite film (T_S=825 °C, $t = 255\,nm$, $rate = 2.8\,nm/min$) shows morphology of two distinctive phases. There are squared plateaus (marked in white in the inset of figure 5.5(a)), which can be ascribed to low energy (001) $BaTiO_3$ planes [28]; inside the plateaus small pyramidal objects may be seen, which can be ascribed to (111) faceted $CoFe_2O_4$ islands [8, 21, 28, 126, 127]. To quantify the sizes, around 100 objects were measured, the error bars plotted correspond to the mean standard deviation of the values.

The surface also was analyzed by AFM, an image of the same sample is presented in figure 5.5(b). It is noted that the convolution of the AFM tip is strong, due to the small lateral size ($l < 20\,nm$) of the objects. Apart of standard parameters like the *rms* roughness of 6 nm giving a basic idea of the smoothness of the surface, motive analysis allows to measure with good statistics the average grain size over the whole image excluding cut

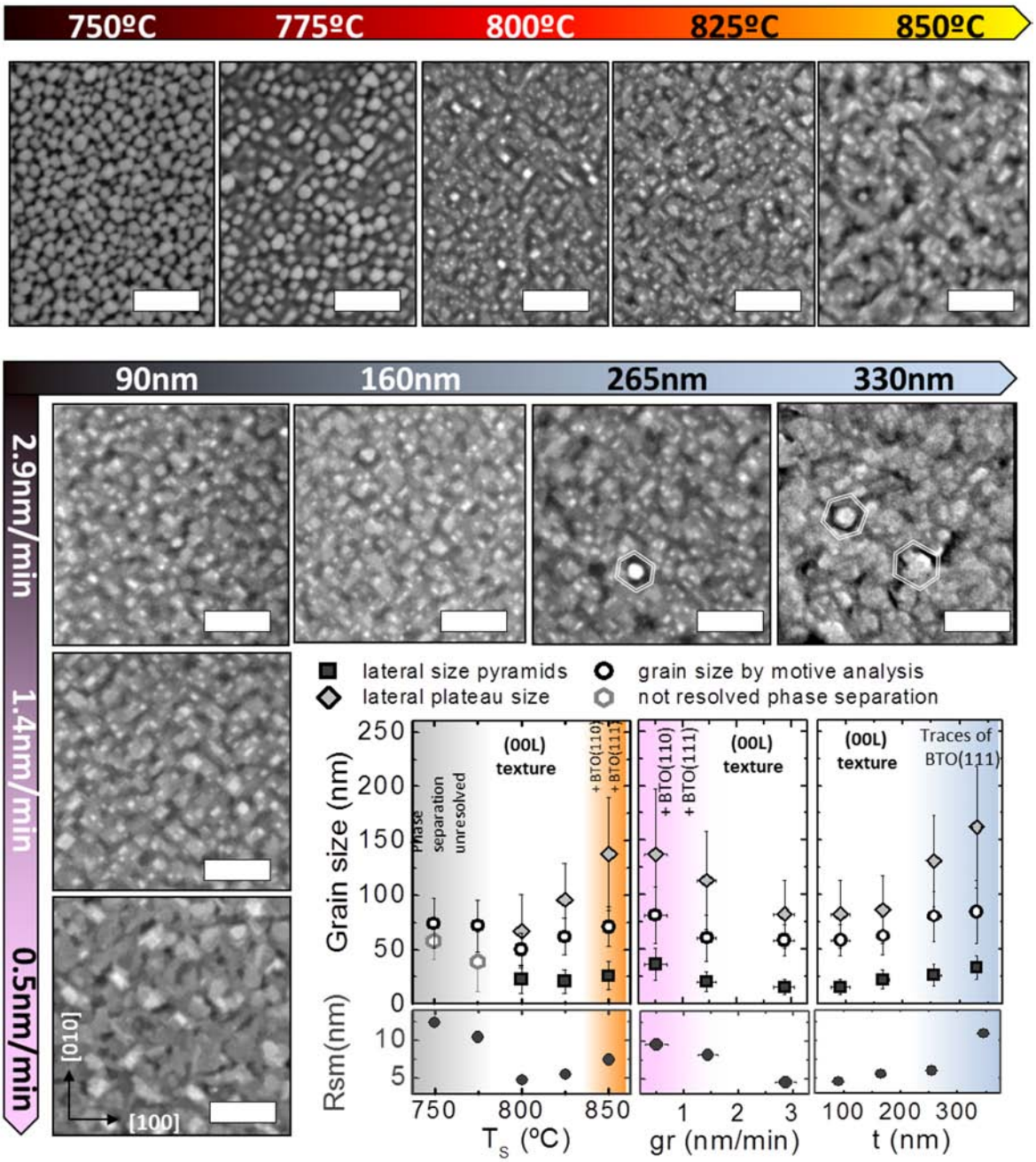

Figure 5.6: Top: SEM images showing the evolution of the morphology for composite films grown in the range of 750-850 °C ($gr = 2.8\,nm/min$, t= 160 nm.) **Bottom:** SEM images show the morphology as function of film thickness and growth rate (T_S= 825 °C). For increased thickness and reduced growth rate hexagonal-like objects (probably corresponding to (111) oriented BTO grains) are indicated by double lined white marks. Bars correspond to 100 nm. The data plots show the tendencies of grain size and surface roughness for all series: temperature, growth rate and thickness.

grains at the image limits. An inset is superposed in the bottom right and the corresponding size distribution can be seen above it. The scanning electron images allow a better lateral resolution for this composite samples. Although, they do not have the capability to obtain

the absolute heights from planar observations, a better understanding of the microstructure using SEM images can be obtained by tilting the sample, approximately 45° in figure 5.5(c), and a vertical cross section of the film (figure 5.5(d)) suggesting columnar structure of the *CFO* objects (sketched in the insets). The measurements of the film thickness by X-ray reflectivity is not suitable for such rough samples so that vertical sections have been used for this purpose. Indications of a (111) nanofaceting is observed in figure 5.5(d) this is in agreement with observation of Tan et al. in $PbTiO_3$-$CoFe_2O_4$ composites [114].

Rather strong changes in the topology as function of the growth conditions can be observed. Corresponding SEM images are presented for varying growth temperature in figure 5.6. A decreasing deposition temperature (T_S=750 and 775 °C) causes plateaus and islands to reduce in size, until they are barely distinguishable, and thus becoming a rough surface where the possible coexistence of both phases cannot be resolved. Characteristic for the surface of these two samples is a high roughness $rms \geq 12\,nm$ with peak-to-valley heights around 30 to 40 nm and lateral size around 75 nm. A kind of growth transition takes place for $T_S \geq$ 800 °C first a drop of the roughness by a factor of two to $rms = 5\,nm$ and the peak-to-valley height drops to 10 nm and additionally a clear phase separation in plateau-pyramid topology can be observed. In the T_S=800 °C sample plateaus have lateral dimensions around $70 \pm 20\,nm$ and the pyramids $17 \pm 8\,nm$. Further increased T_S up to 850 °C causes raise in roughness $rms = 7.8\,nm$ and object size (plateaus $143 \pm 45\,nm$, pyramids $27 \pm 11\,nm$). From x-ray diffraction we know that for this growth temperature emerging BTO(111), (112) and (110) diffraction peaks are observed, nevertheless topographic features could not be related to this phases.

figure 5.6 also shows (bottom panel) the influence of the thickness and growth rate on the morphology. With increasing thickness the lateral size of the plateaus and pyramidal island increases, also larger rms roughness is measured by AFM in the thicker samples ($\geq > 265nm$). Moreover, hexagonal-like grains are observed in the two thick samples, they may be related to the increasing polycrystalline fraction, *i.e.* (111) oriented BTO grains. The growth rate has a strong influence on the surface morphology (see figure 5.6 upper panel) and with decreasing rate the plateaus and pyramids increase in size. While for gr=1.4 nm/min the morphology is very similar to the higher rate. At lowest growth rate of 0.5 nm/min, the matrix appears more irregular and lesser but larger pyramids are observed, also hexagonal or triangular shaped objects have been observed, the increased amount of this morphological features probably is to to the much larger contribution of polycrystalline fraction of BTO and CFO. Indeed, for this sample a significantly higher intensity of (111) (112) and (110) reflections are present in the XRD spectra (figure 5.3(a)). An overview of the lateral dimensions and roughness of the films as function of the growth parameters is shown in the graphs of figure 5.6.

5.3 Functional Properties

5.3.1 Magnetic properties

The magnetic properties of the films have been investigated by SQUID magnetometry. The samples were measured at RT applying field up to $\mu_0 H = 5\,T$. The magnetization loops for in-plane ($H||[100]$) and out-of-plane ($H||[001]$) measurements are presented for the series studying temperature (figure 5.7(a)), growth rate (figure 5.7(b)) and thickness (figure 5.7(c)). The saturation magnetization is calibrated to the volume content of *CFO* in the composite which is 38 vol% and the diamagnetic signal of the substrate was removed by fitting the linear contribution at high magnetic fields. The saturation magnetization, strongly dependent on deposition conditions (temperature and growth rate), ranges from less than 100 emu/cm^3 to around 270 emu/cm^3, with little dependence on the thickness. The values of saturation magnetization, as well as coercive field and anisotropy, as a function of deposition temperature, growth rate and thickness are summarized in figure 5.8. Increasing deposition temperature leads to higher saturation magnetization, an increase from around 93 emu/cm^3 at 750 °C to around 230 emu/cm^3 at 825-850 °C. A maximal saturation around 270 emu/cm^3 is found for low growth rate and high temperature (0.5 nm/min, 825 °C). Anyhow, all samples present lower magnetization than bulk *CFO*, which is around 380 emu/cm^3. Reduction of magnetization is recurrently observed in single *CFO* films on *STO* substrates [77], whereas bulk like magnetization is obtained on isostructural $MgAl_2O_4$ substrates [80]. In our case the highest magnetization values correspond to samples prepared with high temperature and low growth rate; *i.e.* conditions favoring adatom mobility. Lower magnetization might be caused by formation of $BaTi_{1-x}(Co,Fe)_xO_\delta$ as well as intermixing of Ti^{x+} in the spinel phase $[Co_xTi_{1-x}]\,[Fe_yTi_{1-y}]_2\,O_4$ [47, 128–130]. Moreover it could favor defects as antiphase boundaries, causing too a reduction in magnetization.

The samples present also strong anisotropy. *CFO* is epitaxial and thus crystalline anisotropy has to be considered. In tensile stressed single phase *CFO* films, compressed out-of-plane cell parameter, the [001] direction is an easy axis, whereas (001) is an easy-plane in the case of opposite or negligible strain [48, 121], here out-of-plane compression of about 1% was measured and easy direction formed is also [001]. The shape anisotropy, relevant considering the particular columnar shape of the *CFO* nanostructures with high aspect ratio (r) ($d \approx 20\,nm$, $h = 160\,nm$ roughly leading to a high aspect ratio of 8), will also favor magnetization along the [001] direction. All samples (figure 5.7) have easy magnetization direction the out-of-plane [001] showing basically squared magnetization loops, while for the [100] direction S-like loops typical of hard axis are measured. We have quantified

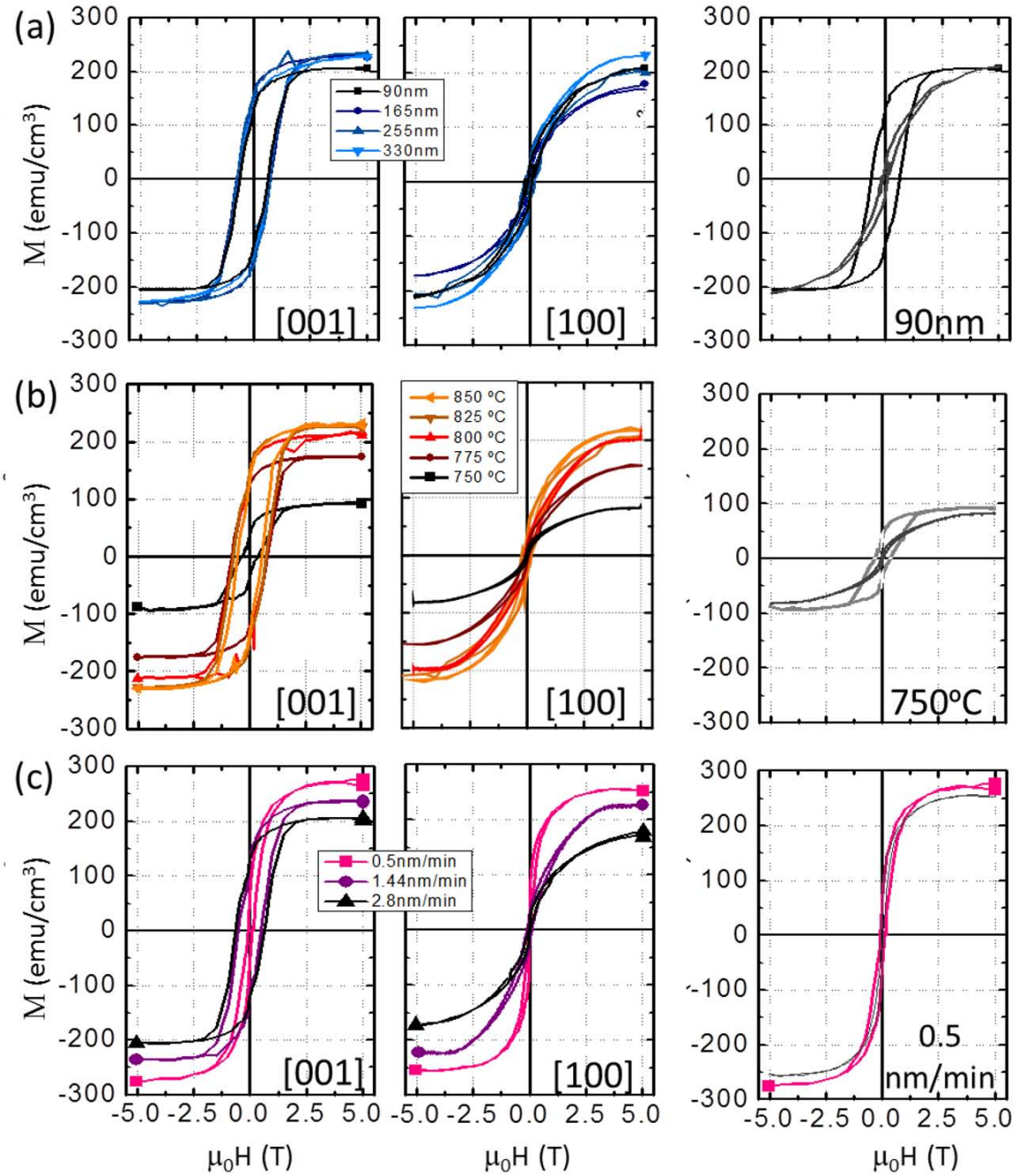

Figure 5.7: Magnetization loops measured at room temperature as function of sample thickness (a), growth temperature and (b) growth rate (c). The films ere measured along [001] and [100] substrate direction as indicated in the figures. The side panels compare the in and out-of-plane loops for films discussed in the text.

the anisotropy by means of the remanent magnetization ratio $r = M_R[001]/M_R[100]$, and the values of r for the three samples series (temperature, rate and thickness) are plotted in figure 5.8. In most of the samples r is very high, between 5 and 10. Analyzing the T_S dependence it can be appreciated that the lower r value, below 5, corresponds to the T_S=750 °C sample in which phase separation was not resolved. In the rest of the series

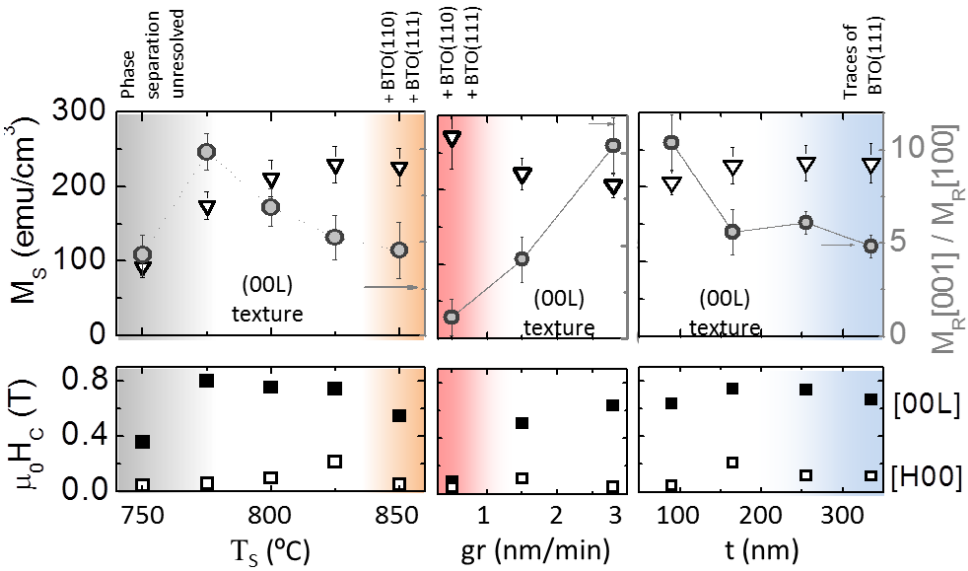

Figure 5.8: Saturation magnetization M_S and remanent magnetization ratio $M_R[001]/M_R[100]$ are shown in the upper panels as function of growth temperature, rate and film thickness. The bottom panels present the coercive fields for the [001] and [100] directions.

r decreases from around 8 to 5 as T_S increases from 775 to 850 °C. Growth rate has stronger influence, with monotonous increase of r from 1 (for $gr = 0.5\,nm/min$) to 10 (for $gr = 2.8\,nm/min$). Finally, r is found to reduce with increasing thickness, signaling that in the explored thickness range differences in the shape factor are not relevant. We also note that there is a correlation between the decrease of r and the presence of other *CFO* orientations observed by X-ray diffraction and indicated in figure 5.8.

Magnetic hysteresis loops along [001] present high coercive fields around $\mu_0 H \approx 0.6$ to $0.8T$ and square shape, while in [100] direction they are S-shaped with very small $\mu_0 H_C \approx 0.1\,T$. The sample grown at the lowest rate (gr=$0.5nm/min$, $90\,nm$ thick) presents low $\mu_0 H_C \approx 0.15\,T$ and S-like shape in both [001] and [100] directions. Polycrystallinity of *CFO*, as observed by XRD, may contribute to the similar hysteresis shape.

The deformation of the $CoFe_2O_4$ lattice, mainly caused by the $BaTiO_3$ matrix, can be a relevant factor in the magnetic anisotropy. The compression of the *CFO* in [001] direction is strong $\varepsilon_{[001]}$=−1.3% while in-the-plane parameter is nearly bulk. In bulk *CFO* the [100] and [001] crystal directions are equal considering magneto-crystalline anisotropy. *CFO* has a large negative constant for magnetostriction λ around $-350 \cdot 10^{-6}$ along these directions.[47] It is thus very sensible to lattice deformation, with the compressive strain along [001] favoring the easy axis in out-of-plane direction.[48, 121, 131] The compressive strain in [001] direction decreases with increasing growth temperature, decreasing growth rate and increasing thickness. figure 5.9 shows the saturation magnetization M_S, the M_R/M_S ratio for loops measured along [001] and [100] and the remnant magnetization

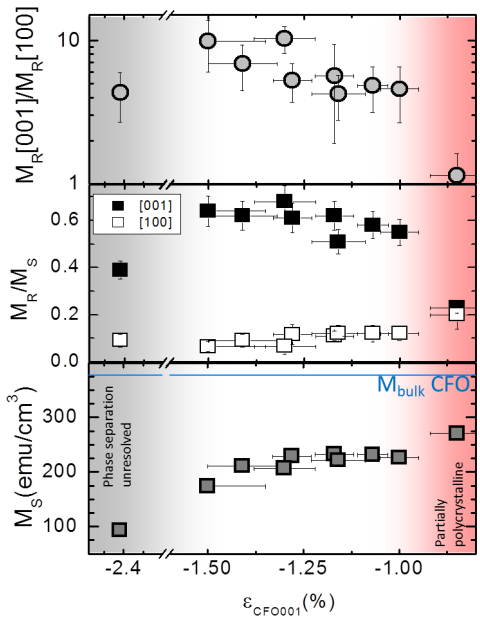

Figure 5.9: Saturation magnetization M_S, the relative magentization M_R/M_S and $M_R[001]/M_R[100]$ are shown as a function of *CFO* out-of-plane strain.

ratio r=$M_R[001]/M_R[100]$ plotted against *CFO* out-of-plane strain. It can be appreciated that the remanent magnetization ratio r decreases in the samples with less strained *CFO*. While M_S is lowest for the composite with unresolved phase separation, then increases significantly, remains constant from -1.4% to -1% and is highest for the more relaxed sample (with traces polycrystalline fraction). These results are comparable with the findings of Zheng [24]. Finally, it is noted that the parallel to the reduction of anisotropy when out-of-plane strain is lowered there is reduction of the coercive field (Fig. 5.8).

5.3.2 Electric properties

To allow electrical measurements, selected $BaTiO_3$-$CoFe_2O_4$ composite films were grown on 0.5% Nb doped STO(001) conductive substrates suitable as bottom electrode and crystallographically identical to undoped *STO*. No changed growth behavior was observed. After *ex-situ* deposition of *Pt* electrodes with different areas on top of the film, the films were analyzed by impedance spectroscopy (HP 4192A) as well as by FE analyzer (Aixacct 2000) by I. Fina at ICMAB. Here we only briefly summarize the results; a more detailed analysis is presented in the references [132, 133] and Chapter 5 of the PHD thesis by I. Fina [68]. Permittivity, losses and FE loops are presented there and correlated with structural data presented in this thesis.

$BaTiO_3$ maintains its FE character as polarization loops were measured for all tested samples. DLCC and PUND techniques were used to correct effects due to high leakage, but unfortunately no correlation with the growth parameters could be established, probably because most samples could not be saturated (only samples with thickness around 90 nm

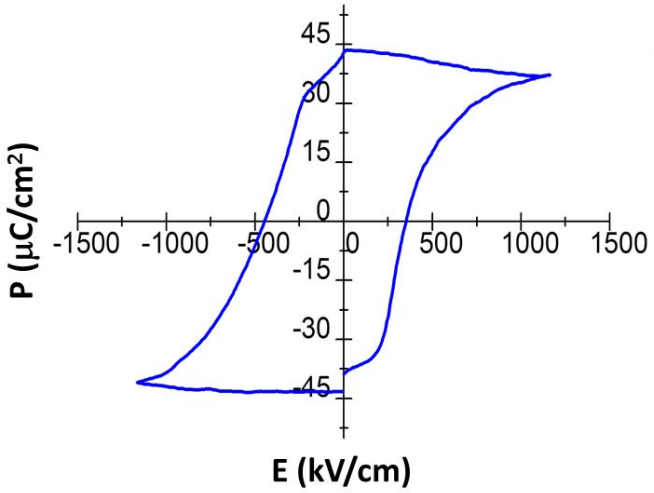

Figure 5.10: Example FE hysteresis loop measured with PUND for a composite grown at 825 °C with t=90 nm and gr = 2.8nm/min. Polarization is normalized to 2/3 BTO fraction, figure is adapted from [132].

could be saturated). The FE hysteresis loop for this sample (825 °C, gr=2.8 nm/min) is presented in figure 5.10. The sample was measured at 250 Hz, considering the BTO fraction is 65% (and that CFO is not contributing), a remanent polarization of $P_R \approx 40\,\mu C/cm^2$ is observed. This value is larger than for bulk BTO ($P_R \approx 26\,\mu C/cm^2$), which suggests that the experimental value is possibly overestimated due to leakage or the complex morphology may alter slightly a surface fraction of BTO:CFO [68].

The dielectric permittivity has been compared at 100 kHz ($tan\delta \approx 0.15$ for all samples) and revealed variations of the dielectric permittivity from 20 to 80 depending on the growth parameters. Similar to magnetic properties the system presents an increasingly larger dielectric permittivity if the films are grown at temperatures above 800 °C (as shown previously samples deposited at lower temperature lack phase separation and possibly strong intermixing). For composites with well defined phase separation ε_r is found to be about 40 to 60. Films with partially polycrystalline BTO show the highest values of $\varepsilon_r \approx 80$. Dielectric permittivity increases if BTO unit cell volume is closer to bulk, which goes in hand with the formation of larger BTO plateaus and lead to a higher dielectric response of the composite system.

5.4 Summary

The fabrication of $BaTiO_3$-$CoFe_2O_4$ nanocomposites by rf-sputtering was explored. We studied the effect of substrate temperature, growth rate and film thickness to obtain nanocomposites with well defined phase separation, crystal structure and morphology.

We find that BTO out-of-plain strain can be tuned between +0.5 to 1.3%, while CFO is compressivly strained between −0.9 to −1.4%. Increasing temperature and lowering the growth rate leads to larger lateral size of CFO columns (10-20 nm) and BTO plateaus

(80-160 nm) being both phases are less strained.

The compressive strain in out-of-plane direction of the CFO columns, (00l) texture, results in a strong magnetic anisotropy pushing the easy magnetization direction in out-of-plane direction. Anyhow, we find that the saturation magnetization of the composites is reduced by about 40%with respect to bulk $CoFe_2O_4$. It cannot be excluded that chemical mixing is a main factor for this reduction.

The samples suffer large current leakage due high amount of defects in the vertical nanostructures. The dielectric response of the composite system is improved when the BTO matrix has cell volume closer to bulk and larger BTO plateaus have grown. FE loops confirmed ferroelectricity, thus biferroic nanocomposite films have been achieved using rf-sputtering.

Table 5.1: Sample list *BTO-CFO* vertical nanocomposites grown by rf sputtering.

	Sample name	**T$_S$** (°C)	**gr** (nm/min)	**t** (nm)	Phase separation (PS)
Series I	CB-T500gr05t060	500	0.5	60	not crystalline
	CB-T600gr05t060	600	0.5	60	no PS
	CB-T700gr05t060	700	0.5	60	no PS
	CB-T800gr05t060	800	0.5	60	yes PS, (00l)+polycrystal
	CB-T700gr05t250	700	0.5	250	partial PS, (00l)
	CB-T800gr05t250	800	0.5	250	yes PS, (00l)+polycrystal
Series II	CB-T750gr28t160	750	2.8	160	no PS, (00l)
	CB-T775gr28t160	775	2.8	160	weak PS, (00l)
	CB-T800gr28t160	800	2.8	160	yes PS, (00l)
	CB-T825gr28t160	825	2.8	160	yes PS, (00l)
	CB-T850gr28t160	850	2.8	160	yes PS, (00l)+polycrystal
	CB-T825gr05t090	825	0.5	90	yes PS, (00l)+polycrystal
	CB-T825gr14t130	825	1.4	130	yes PS, (00l)
	CB-T825gr28t090	825	2.8	90	yes PS, (00l)
	CB-T825gr28t265	825	2.8	265	yes PS, (00l)+traces (lll)
	CB-T825gr28t330	825	2.8	330	yes PS, (00l)+traces (lll)

CHAPTER 6

Summary and General Conclusions

In this thesis we have studied two phase heterostructures with nanometric dimensions exploring the correlation of growth conditions on structural and functional properties. We investigated *horizontal 2d heterostructures (A)* and *self-organized complex vertical 3d heterostructures (B)*, both suitable model systems for sizable room temperature multiferroicity and magnetoelectric coupling.
(A) We have grown fully epitaxial *BTO-CFO horizontal heterostructures* with very sharp interfaces despite the structural dissimilarity between *BTO* and *CFO*.

• The stacking order strongly impacts the structural and dielectric properties of *BTO*. When used as bottom layer *BTO* has enhanced c/a ratio and ferroelectric polarization compared to bulk *BTO*, while as top layer (grown onto *CFO*) it has bulk-like c/a-ratio and ferroelectric polarization.

• The temperature dependence of the dielectric permitivity of the bilayers showed features at temperatures identified as structural transitions of *BTO*. An enhanced response at such transitions was observed by application of external magnetic fields and is thus due to elastic interaction of *CFO* and *BTO* facilitated by reduced clamping to the substrate.

(B) We found suitable growth conditions for self-organized *vertical heterostructures* for *BFO-CFO* and *BTO-CFO* nanocomposites with molar ratio 65%-35%.

• On (001) oriented substrates formation of ferromagnetic *CFO* columns embedded in a ferroelectric *BFO* or *BTO* matrix was achieved. In *BFO-CFO* nanocomposite using (111) oriented substrates the topology is inverted *CFO* forms the matrix and *BFO* the

embedded columns.

• The volatility of *Bi* in *BFO* limits the window of suitable growth conditions as *Bi* content decreases dramatically at higher growth temperatures, together with the stoichiometry the morphology of the nanocomposites is strongly affected. We varied growth temperature and laser repetition rate and conclude that neither can be used as independent growth parameter to tune pillar size and distribution.

• We have found that on (001) oriented substrates with different mismatch different *BFO* phases can be stabilized in nanocomposites with column-matrix topology. On highly in-plane compressive *LAO* substrates tetragonal like *T-BFO* matrix was stabilized, on less compressive substrates it favors rhombohedral like *R-BFO* matrix, while on tensile substrates decomposition of *BFO* was evidenced. Comparing the growth of *T-BFO* single and composite films, we found that in the nanocomposite system the temperature range for stabilizing the tetragonal *BFO* phase is much broader than for single phase films.

• We found a general trend of the out-of-plane compression/expansion of the *CFO* columns with the magnetization easy axis, favoring out-of-plane easy direction for compressive strain and in-plane for tensile strain. The polarization of *BFO* is strongly influenced by the formed phase and the easy polarization axis can be selected to be close to [001] direction in *T-BFO* and [111] in *R-BFO*. Magneto-electric coupling was evidenced for selected samples with *R-BFO–CFO* composition by scanning probe techniques which showed a magnetization reversal of 12% of the columns after electric poling.

In conclusion, both heterostructure geometries: columnar morphology, as well as, horizontal heterostructures show sizable magneto-electric coupling mediated by elastic interaction of the functional phases was observed close to and above room temperature. The functional properties can be tuned by adequate selection of substrate in vertical heterostructures or stacking order in horizontally layered heterostructures.

Outlook

We have shown that adequate selection of stacking order in horizontal heterostructures has a potential to reduce clamping of the rigid substrate and obtain magneto-electric coupling, but effectively is restricted to the region around the *BTO* transition temperatures. I believe that high coupling constants like in bulk laminated composites [19] are difficult to

achieve in thin film architecture. Nevertheless, full suppression of the substrate clamping could improve the response of epitaxial thin films. This could be achieved by:

• Patterning or deposition through stencils could release further the substrate clamping [134] and thus facilitate direct magneto-electric coupling by application of electric or magnetic fields.

• Anyhow, full absence of substrate clamping may only be achieved by growing the horizontal heterostructures on flexible substrates. Fabrication of silicon membranes is already a standard procedure and thus may be a suitable model system to proof that approach.

Self-organized spinel-perovskite nanocomposites with column-matrix topology were grown successfully. Nevertheless, the lack to easily control the nanocomposites spacial distribution, column size or composition (especially using a single target approach) remains a mayor challenge in their development. Strategies to overcome this limitations could include:

• Growing self-organized vertical heterostructures using a two-target approach, exploiting easier composition selection and tuneability of the feature sizes and distribution [135–137].

• Also local nanostructuring of the substrate or buffer layers this may help to produce nanocomposites with perfect spacial order and a narrower size distribution of the columns [138, 139].

• Recently, vertically self-organized $SrTiO_3$-MgOcomposites were used to create large surface area, mesoporous $SrTiO_3$ thin films by selective etching of the embedded MgO columns with promising application in photoelectrochemical water splitting [140].

PART III
Appendix

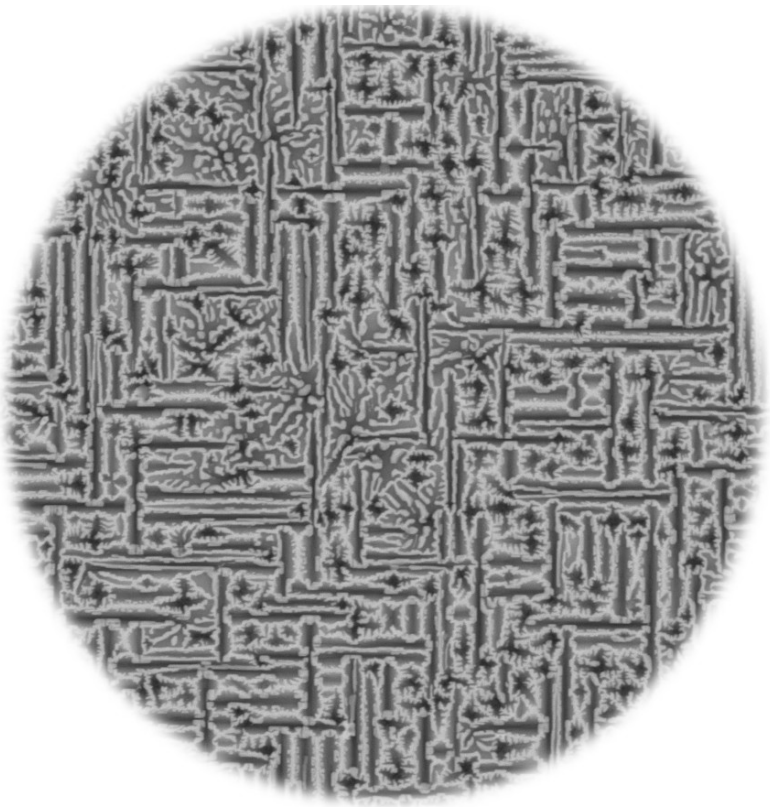

Abbreviations

f	laser repetition rate
gr	growth rate
p	oxygen pressure
t	thickness
T_S	substrate temperature
Å	Ångstrom
a, b, c	lattice parameters
ε	epitaxial strain
ϵ	dielectric constant
E, E_C	electric field, coercive electric field
F	lattice mismatch
FE	ferroelectric
FM	ferromagentic (here also *ferri*magentic materials are referred as such)
FWHM	full width half maximum
H, H_C	magnetic field, coercive magnetic field
ip, op	in-plane and out-of-plane lattice parameters in RSM
ME	magnetoelectric
MF	multiferroic
M, M_S, M_R	magnetization, saturation and remnant magnetization
ω	incident diffractometer angle
P, P_S, P_R	polarization, saturation and remnant polarization
ϕ	angle of in-plane sample rotation
ψ	tilt angle of diffraction plane to surface normal
$q_{[hkl]}$	reciprocal lattice spacing
R	lattice relaxation
rms	root mean square
RT	room temperature
θ	exit diffractometer angle
T_C, T_N	Curie temperature, Neel temperature
AFM	atomic force microscopy
BS	backscattered electrons

EDS,EDAX	energy dispersive X-ray spectroscopy
EELS	energy electron loss spectroscopy
MFM	magnetic force microscopy
RHEED	reflection high energy electron diffraction
RSM	reciprocal space map
rf-sputtering	radio frequency sputtering
PFM	piezoresponse force microscopy
PLD	pulsed laser deposition
SE	secondary electrons
SEM	scanning electrons microscopy
TEM	transmission electrons microscopy
XRD	X-ray diffraction
WDS	wavelength dispersive spectroscopy

BTO	$BaTiO_3$
BO	Bi_2O_3
BFO	$BiFeO_3$
R-BFO	$R-BiFeO_3$ (rhombohdral $BiFeO_3$)
T-BFO	$T-BiFeO_3$ (tetragonal-like $BiFeO_3$)
CFO	$CoFe_2O_4$
FO	Fe_3O_4 (Magnetite)
aFO	$\alpha-Fe_2O_3$ (Hematite)
gFO	$\gamma-Fe_2O_3$ (Maghemite)
NFO	$NiFe_2O_4$
PTO	$PbTiO_3$

BFO–CFO	$BiFeO_3$–$CoFe_2O_4$
BFO–NFO	$BiFeO_3$–$NiFe_2O_4$
R-BFO–CFO	*R-*$BiFeO_3$–$CoFe_2O_4$
T-BFO–CFO	*T-*$BiFeO_3$–$CoFe_2O_4$
BTO–CFO	$BaTiO_3$–$CoFe_2O_4$
PTO–CFO	$PbTiO_3$–$CoFe_2O_4$
BTO–NFO	$BaTiO_3$–$NiFe_2O_4$

LAO	$LaAlO_3$
LSAT	$(LaAlO_3)(SrAl_{0.5}Ta_{0.5})O_3$
LCMO	$La_{2/3}Ca_{1/3}MnO_3$
LNO	$LaNiO_3$
LSMO	$La_{2/3}Sr_{1/3}MnO_3$
MAO	$MgAl_2O_4$
MgO	MgO
SRO	$SrRuO_3$
STO	$SrTiO_3$

Scientific Communications

Publication List - Main Contributions

1 *Large out-of-plane ferroelectric polarization in flat epitaxial $BaTiO_3$ on $CoFe_2O_4$ heterostructures*,
N. Dix, I. Fina, R. Bachelet, L. Fàbrega, C. Kanamadi, J. Fontcuberta and F. Sánchez,
Applied Physics Letters 102, 172907 (2013)

2 *Mapping of the epitaxial stabilization of quasi-tetragonal $BiFeO_3$ with deposition temperature*,
N. Dix, R. Muralidharan, M. Varela, J. Fontcuberta and F. Sánchez,
Applied Physics Letters 100, 122905 (2012)

3 *Selectable spontaneous polarization direction and magnetic anisotropy in $BiFeO_3$-$CoFe_2O_4$ epitaxial nanostructures*,
N. Dix, R. Muralidharan, J.M. Rebled, S. Estradé, F. Peiro, M. Varela and J. Fontcuberta, J. and F. Sánchez,
ACSnano 4, 4955-4961 (2010)

4 *Response to "Comment on 'On the strain coupling across vertical interfaces of switchable $BiFeO_3$-$CoFe_2O_4$ multiferroic nanostructures' " [Appl. Phys. Lett. 96, 076101 (2010)]*,
N. Dix, R. Muralidharan, J. Guyonnet, B. Warot-Fonrose, M. Varela, P. Paruch, F. Sánchez and J. Fontcuberta,
Applied Physics Letters 96, 076102 (2010)

5 *Effects of morphology and strain on the dielectric response of multiferroic $CoFe_2O_4$-$BaTiO_3$ nanocomposite thin films*,
I. Fina, N. Dix, L. Fàbrega, F. Sánchez and J. Fontcuberta,
Journal of Applied Physics 108, 034108 (2010)

6 *On the strain coupling across vertical interfaces of switchable $BiFeO_3$-$CoFe_2O_4$ multiferroic nanostructures*,
N. Dix, R. Muralidharan, J. Guyonnet, B. Warot-Fonrose, M. Varela, P. Paruch, F. Sánchez and J. Fontcuberta,
Applied Physics Letters 95, 062907 (2009)

7 *Critical Limitations in the Fabrication of Biferroic $BiFeO_3$-$CoFe_2O_4$ Columnar Nanocomposites Due to Bismuth Loss*,
N. Dix, R. Muralidharan, B. Warot-Fonrose, M. Varela, F. Sánchez and J. Fontcuberta,
Chemistry of Materials 21, 1375-1380 (2009)

8 *Influence of substrate temperature in $BiFeO_3$-$CoFe_2O_4$ nanocomposites deposited on $SrTiO_3(001)$*,
N.Dix, R. Muralidharan, J.M. Caicedo, D. Hrabovsky, I. Fina, L. Fàbrega, V. Skumryev, M. Varela, J. Guyonnet, P. Paruch, J.M. Triscone, F. Sánchez and J. Fontcuberta,
Journal of Magnetism and Magnetic Materials 321, 1790-1794 (2009)

9 *Synthesis, structure and magnetic studies on self-assembled $BiFeO_3$-$CoFe_2O_4$ nanocomposite thin films*,
R. Muralidharan, N. Dix, V. Skumryev, M. Varela, F. Sánchez and J. Fontcuberta,
Journal of Applied Physics 103, 07E301 (2008)

10 *Sputtering growth and characterization of $CoFe_2O_4$-$BaTiO_3$ nanostructures*,
N. Dix, V. Skumryev, V. Laukhin, L. Fàbrega, F. Sánchez and J. Fontcuberta,
Material Science and Engineering B 144, 127 (2007)

Publication List - Collaborations

1 *Untangling Electrostatic and Strain Effects on the Polarization of Ferroelectric Superlattices*,
E. Khestanova, N. Dix, I. Fina, M. Scigaj, J. Rebled, C. Magén, S. Estradé, F. Peiró, G. Herranz, J. Fontcuberta and F. Sánchez
Advanced Functional Materials 26, 6446–6453 (2016)

2 *Monolithic integration of room-temperature multifunctional $BaTiO_3$-$CoFe_2O_4$ epitaxial heterostructures on Si(001)*,
M. Scigaj, N. Dix, J. Gázquez, M. Varela, I. Fina, N. Domingo, G. Herranz, V. Skumryev, J. Fontcuberta and F. Sánchez
Scientific Reports 6, 31870 (2016)

3 *Multiple strain-induced phase transitions in* $LaNiO_3$ *thin films*,
M. C. Weber, M. Guennou, N. Dix, D. Pesquera, F. Sánchez, G. Herranz, J. Fontcuberta, L. López-Conesa, S. Estradé, F. Peiró, J. Iñiguez and J. Kreisel
Physical Review B 014118 (2016)

4 *Absence of magnetic proximity effects in magnetoresistive* $Pt/CoFe_2O_4$ *hybrid interfaces*,
M. Valvidares, N. Dix, M. Isasa, K. Ollefs, F. Wilhelm, A. Rogalev, F. Sánchez, E. Pellegrin, A. Bedoya-Pinto, P. Gargiani, L. E. Hueso, F. Casanova and J. Fontcuberta
Physical Review B 93, 214415 (2016)

5 *Spin Hall Magnetoresistance as a Probe for Surface Magnetization in* $Pt/CoFe_2O_4$ *Bilayers*,
M. Isasa, S. Vélez, E. Sagasta, A. Bedoya-Pinto, N. Dix, F. Sánchez, L. E. Hueso, J. Fontcuberta and F. Casanova
Physical Review Applied 6, 034007 (2016)

6 *Engineering two-dimensional superconductivity and Rashba spin-orbit coupling in* $LaAlO_3/SrTiO_3$ *quantum wells by selective orbital occupancy*,
G. Herranz, G. Singh, N. Bergeal, A. Jouan, J. Lesueur, J. Gázquez, M. Varela, M. Scigaj, N. Dix, F. Sánchez, and J. Fontcuberta
Nature Communication 6:6028 (2015)

7 *Two-Dimensional Electron Gases at* $LaAlO_3/SrTiO_3$ *Interfaces: Orbital Symmetry and Hierarchy Engineered by Crystal Orientation*,
D. Pesquera, M. Scigaj, P. Gargiani, A. Barla, J. Herrero-Martín, E. Pellegrin, S. M. Valvidares, J. Gázquez, M. Varela, N. Dix, J. Fontcuberta, F. Sánchez and G. Herranz
Physical Review Letters 113, 156802 (2014)

8 *Interface and Bulk Charge Localization in Manganite Thin Films*,
D. Pesquera, M. Wojcik, E. Jedryka, V. Laukhin, N. Dix F. Sánchez, G. Herranz and J. Fontcuberta,
Advanced Materials Interfaces 2196-7350 (2014)

9 *EELS tomography in multiferroic nanocomposites: from spectrum images to the spectrum volume*,
L. Yedra, A. Eljarrat, J.M. Rebled, L.López-Conesa, N. Dix, F. Sánchez, S. Estradé and J. Fontcuberta,
Nanoscale 6646-6650 (2014)

10 *Yttria-stabilized zirconia/*$SrTiO_3$ *oxide heteroepitaxial interface with symmetry discontinuity*,
M. Scigaj, N. Dix, M. Cabero, A. Rivera-Calzada, J. Santamaria, J. Fontcuberta, G. Herranz and F. Sánchez,
Applied Physics Letters 104, 251602 (2014)

11 *The direct magnetoelectric effect in ferroelectric-ferromagnetic epitaxial heterostructures*,
I. Fina, N. Dix, J.M. Rebled, P. Gemeiner, X. Martí, F. Peiró, B. Dkhil, F. Sánchez and J. Fontcuberta,
Nanoscale 5, 8037-8044 (2013)

12 *Ultra-flat* $BaTiO_3$ *epitaxial films on Si(001) with large out-of-plane polarization*,
M. Scigaj, N. Dix, I. Fina, R. Bachelet, B. Warot-Fonrose, J. Fontcuberta and F. Sánchez,
Applied Physics Letters 102, 112905 (2013)

13 *Interface structure governed by plastic and structural dissimilarity in perovskite* $La_{0.7}Sr_{0.3}MnO_3$ *nanodots on rock-salt MgO substrates*,
P. Abellan, J. Zabaleta, J. Santiso, M.-J. Casanove, N. Dix, J. Aguiar, N. Browning, N. Mestres, T. Puig, X. Obradors and F. Sandiumenge,
Applied Physics Letters 100, 083104 (2012)

14 *The poisson ratio in $CoFe_2O_4$ spinel thin films*,
M. Förster, M. Iliev, N. Dix, X. Martì, M. Barchuk, F. Sánchez and Fontcuberta,
Advanced Functional Materials 22, 4344-4351 (2012)

15 *High mobility conduction at (110) and (111) $LaAlO_3/SrTiO_3$ interfaces*,
G. Herranz, F. Sánchez, N. Dix, M. Scigaj, and J. Fontcuberta,
Scientific Reports 2, 758 (2012)

16 *Probing individual layers in functional oxide multilayers by wavelength-dependent raman scattering*,
J. Kreisel, M. Weber , N. Dix, F. Sánchez, P. Thomas and J. Fontcuberta,
Advanced Functional Materials 22, 5044-5049 (2012)

17 *Strain analysis of multiferroic $BiFeO_3$-$CoFe_2O_4$ nanostructures by Raman scattering*,
O. Chaix-Pluchery, C. Cochard, P. Jadhav, J. Kreisel, N. Dix, F. Sánchez and J. Fontcuberta,
Applied Physics Letters 99, 072901 (2011)

18 *A phase transition close to room temperature in $BiFeO_3$ thin films*,
J. Kreisel, P. Jadhav, O. Chaix-Pluchery, M. Varela, N. Dix, F. Sánchez and J. Fontcuberta,
Journal of Physics Condensed Matter 23, 342202 (2011)

19 *Magnetocapacitance in $BaTiO_3$-$CoFe_2O_4$ nanocomposites*,
I. Fina, N. Dix, L. Fàbrega, F. Sánchez and J. Fontcuberta,
Thin Solid Films 518, 4634-4636 (2010)

20 *Enhanced thermal stability of Pt electrodes for flat epitaxial biferroic-$YMnO_3$/Pt heterostructures*,
R. Bachelet, R. Muralidharan, F. Rigato, N. Dix, X. Martì, J. Santiso, F. Sánchez and J. Fontcuberta,
Applied Physics Letters 95, 18190 (2009)

21 *Magneto-optic material selectivity in self-assembled $BiFeO_3$-$CoFe_2O_4$ biferroic nanostructures*,
K. Postava, D. Hrabovsky, O. Zivotsky, J. Pistora, N. Dix, R. Muralidharan, J.M. Caicedo; F. Sánchez and J. Fontcuberta,
Journal of Applied Physics 105, 07C124 (2009)

22 *Dielectric properties of $BaTiO_3$-$CoFe_2O_4$ nanocomposite thin films*,
I. Fina, N. Dix, V. Laukhin, L. Fàbrega, F. Sánchez and J. Fontcuberta,
Journal of Magnetism and Magnetic Materials 321, 1795-1798 (2008)

23 *Controlled magnetic anisotropy of $SrRuO_3$ thin films grown on nominally exact $SrTiO_3$(001) substrates*,
G. Herranz, F. Sánchez, N. Dix, D. Hrabrovsky I. C. Infante and J. Fontcuberta, M.V. García-Cuenca, C. Ferrater and M. Varela,
Applied Physics Letters 89, 152501 (2006)

24 *Kerr measurements on single-domain $SrRuO_3$ thin films*,
G. Herranz, N. Dix, F. Sánchez, B. Martínez and J. Fontcuberta,
Journal of Applied Physics 97, 10M321 (2005)

Contribution to Conferences

2013 (oral)	RHEED: A tool for surface characterization and in-situ growth control. and The ICMAB thin films laboratory. , N. Dix, I. Meeting on pulsed laser deposition and sputtering, ICMAB, Bellaterra (Spain)
2012 (oral)	RHEED; How it works. What can be learned ?, N. Dix, R. Bachelet and F. Sánchez, Nanoselect Meeting, St. Feliu (Spain)
2010 (poster)	Selectable spontaneous polarization and magnetic anisotropy in $BiFeO_3$-$CoFe_2O_4$ epitaxial heterostructures, N. Dix, R. Muralidharan, J.M. Reblet, S. Estrade, F. Peiro, M. Varela, J. Fontcuberta and F. Sánchez , Nanoselect Meeting, St. Feliu (Spain)
2009 (oral)	What drives magnetoelectric coupling in substrate unclamped biferroic nanocomposites, N. Dix, R. Muralidharan, B. Warot-Fonrose, M. Varela, J. Guyonnet, P. Paruch, F. Sánchez and J. Fontcuberta, Nanoselect Meeting, St. Feliu (Spain)
2009 (poster)	Interfacial strains in biferroic $BiFeO_3$-$CoFe_2O_4$ epitaxial columnar nanostructures, N. Dix, R. Muralidharan, B. Warot-Fonrose, M. Varela, F. Sánchez and J. Fontcuberta, 16th WOE Tarragona (Spain)
2009 (oral)	Lattice strain at interfaces in $BiFeO_3$-$CoFe_2O_4$ epitaxial nanostructures, N. Dix, R. Muralidharan, B. Warot-Fonrose, E. Snoeck, M. Varela, F. Sánchez and J. Fontcuberta, eMRS Spring Meeting, Strasbourg (France)
2008 (oral)	Controlling synthesis of epitaxial nanostructures with $CoFe_2O_4$ and highly volatile $BiFeO_3$., N. Dix, R. Muralidharan, M. Varela, F. Sánchez, J. Fontcuberta, Nanoselect meeting, St. Feliu (Spain)
2007 (oral)	Self-assembled growth and characterization of multiferroic nanostructures, N. Dix, V. Skumryev, V. Laukhin, L. Fàbrega, F. Sánchez, J. Fontcuberta, eMRS Spring Meeting, Strassbourg (France)
2007 (poster)	Self-assembled growth and characterization of multiferroic nanostructures, N. Dix, V. Skumryev, V. Laukhin, L. Fàbrega, F. Sánchez, J. Fontcuberta, THIOX, St. Feliu (Spain)

Acknowledgements

I would like to express my gratitude to the people that made this work possible, supporting me with advise and cheers through the passed years. Foremost, I would like to thank my supervisor Dr. Florencio Sánchez for his patience, encouragement and guidance to solve the growth paramter puzzles along the way. Thanks to the admirable sharp mind of my co-supervisor Prof. Josep Fontcuberta his suggestions and data reducing sketches helped a lot to get a clear view on which direction to go and to tackle the next steps. I also appreciate the availability of my tutor Prof. Javier Rodrigues.

I thank Dr. Muralidharan Rajaram for fruitful discussions and helpful advice in solving the riddles of the composite samples, Dr. Chidanand Kanamadi for his work on CFO thin films and Dr. Romain Bachelet for his assistance with the samples grown with in-situ RHEED. Also I'd like to thank Prof. Manuel Varela for using the PLD system at the Universitat de Barcelona, and for training on the systems by Dr. Eric Langenberg and Dr. Joffre Ventura. Dr. Carles Corbella and Macià Romeu for their efforts and assistance in the sample preparation. Dr. Ingrid Cañero, Dr. Llibetat Abad and Dr. Ulrike Lüders and Dr. Lluis Balcells for the introduction into use and maintenance of the rf-sputtering system.

Special regards are for Dr. Ignasi Fina who dedicated a huge amount of time and patience analyzing the electric properties of these complex sample systems. Thanks also Dr. Franco Rigato and Dr. Xavi Martì who shared share the office with me and for the enlightening discussions about sample growth, measurments and defining the *good* ones. In addition I would like to acknowledge everybody giving hints and planting questions at the group meetings or a coffee break; especially Dr. Gervasi Herranz, Prof. Vassil Skumreyev, Prof. Volodia and Dr. Llourdes Fabrega.

I'd like to acknowledge the support from various collaborations that helped to extract and understand many useful details. Thanks to Dr. Benedicte Warot-Fonrose I could get a deeper insight in TEM sample preparation, observation and analysis at CEMES (Toulouse). Also Josep Rebled, Dr. Lluis Yedra, Dr. Sonia Estrade and Prof. Francesca Peiro from Universitat de Barcelona for their help and discussions of the columnar composites. I appreciate the dedication of Dr. Jill Guyonet and Prof. Patrycia Paruch at University of Geneva for their PFM/MFM measurements. Temperature dependent XRD measurements on bilayered samples performed by Prof. Brahim Dhkil at Ecole Centrale Paris. Dr. Odette Chaix-Pluchery, Charlote Cochard and Prof. Jens Kreisel for their Raman measurements on nanocomposites and tetragonal-like BFO.

Essential for the daily work, I would also like to take the opportunity to state how much I appreciated the support and help of the technical services staff. Their expertise

enabled me to get a better understanding of each measure technique and improved the reliability of the measurements, also the sometime huge efforts maintaining the equipments. Thanks to Joan Esquius, Xavi Campos and Anna Crespi for measuring all my urgent samples and for your open ear on how to improve the XRD measurements. Dr. Bernat Bozzo and Jose-Manuel for their assistance with the SQUID measurements. Also a big thank you to the technical staff of the AFM service Maite Simón, Noemi Alonso and Andrés Gomez and Dr. Angel Perez. A very special thanks is going to the people that keep the institution technically sound and are always available when a disaster happened: Toni, Oriol, Carles, Jose and Floro. I have deep admiration for all hard working ants of the institutes administration for their assistance with paper work, namely Trini, Vicente, Pietat, Mariona, Rebeca and Maria and informatic services solving connectivity issues Javier, Marc and Angel.

I appreciated very much that I had the chance to meet so many people sharing vivid discussions about science and nons(ci)ence usually with a ant-free cup of coffee. Liber, Aitor, Puigma, Oriol, Patricia, Markos, Floren, Mariano, Ingrid, David H., Andrea, Emi, Mateusz, David P., Jone, Francisco, Joan, Xavi, Blai, Roque, Eric, Joffre, Emmerson, Omar, Simo, Pablo, Marc, Reza, Carlos and so many more ... a big thanks and always have the force of coffee on your side !

Finally, I would like to express my gratitude for the constant and unconditional support of my family.

Financial Support

I also like to acknowledge the financial support by the Spanish Government (Project numbers: MAT2008-06761, MAT2011-29269-C03, CSD2007-00041 and Grup de Recerca Consolidat Generalitat de Catalunya SGR 376).

To conduct this research work have benefited from an I3P-CSIC contract. After its completion, I was contracted (3 years) as "Technical Support" to contribute to establish the Thin Film Laboratories as Services at ICMAB.

Bibliography

[1] D. G. Schlom, L. Q. Chen, X. Pan, A. Schmehl, and M. A. Zurbuchen, Journal of the American Ceramic Society **91**, 2429 (2008).

[2] Y. Tokura and N. Nagaosa, Science **288**, 462 (2000).

[3] N. A. Hill, The Journal of Physical Chemistry B **104**, 6694 (2000).

[4] J. van Suchtelen, Philips Research Report **27**, 28 (1972).

[5] H. Zheng, J. Wang, S. E. Lofland, Z. Ma, L. Mohaddes-Ardabili, T. Zhao, L. Salamanca-Riba, S. R. Shinde, S. Ogale, F. Bai, D. Viehland, Y. Jia, D. G. Schlom, M. Wuttig, A. Roytburd, and R. Ramesh, Science **303**, 661 (2004).

[6] O. Lebedev, G. Van Tendeloo, S. Amelinckx, H. Ju, and K. Krishnan, Philosophical Magazine A **80**, 673 (2000).

[7] J. L. MacManus-Driscoll, Advanced Functional Materials **20**, 2035 (2010).

[8] H. M. Zheng, F. Straub, Q. Zhan, P. L. Yang, W. K. Hsieh, F. Zavaliche, Y. H. Chu, U. Dahmen, and R. Ramesh, Advanced Materials **18**, 2747 (2006).

[9] I. Levin, J. b. Li, J. Slutsker, and A. Roytburd, Advanced Materials **18**, 2044 (2006).

[10] Y. Wang, J. Hu, Y. Lin, and C.-W. Nan, NPG Asia Materials **2**, 61 (2010).

[11] D. Khomskii, Physics **2**, 20 (2009).

[12] H. Schmid, Ferroelectrics **162**, 317 (1994).

[13] W. Eerenstein, N. Mathur, and J. Scott, Nature **442**, 759 (2006).

[14] B. B. Van Aken, J.-P. Rivera, H. Schmid, and M. Fiebig, Nature **449**, 702 (2007).

[15] N. A. Spaldin, M. Fiebig, and M. Mostovoy, Journal of Physics: Condensed Matter **20**, 434203 (2008).

[16] T. Kimura, T. Goto, H. Shintani, K. Ishizaka, T. Arima, and Y. Tokura, Nature **426**, 55 (2003).

[17] C.-W. Nan, M. I. Bichurin, S. Dong, D. Viehland, and G. Srinivasan, Journal of Applied Physics **103**, 031101 (2008).

[18] C. A. F. Vaz, J. Hoffman, C. H. Ahn, and R. Ramesh, Advanced Materials **22**, 2900 (2010).

[19] G. Srinivasan, Annual Review of Materials Research **40**, 153 (2010).

[20] R. Bachelet, F. Sánchez, J. Santiso, C. Munuera, C. Ocal, and J. Fontcuberta, Chemistry of Materials **21**, 2494 (2009).

[21] U. Lüders, F. Sánchez, and J. Fontcuberta, Phys. Rev. B **70**, 045403 (2004).

[22] H. N. Lee, H. M. Christen, M. F. Chisholm, C. M. Rouleau, and D. H. Lowndes, Nature **433**, 395 (2005).

[23] V. A. Shchukin and D. Bimberg, Rev. Mod. Phys. **71**, 1125 (1999).

[24] H. Zheng, J. Kreisel, Y.-H. Chu, R. Ramesh, and L. Salamanca-Riba, Applied Physics Letters **90**, 113113 (2007).

[25] J. L. MacManus-Driscoll, P. Zerrer, H. Wang, H. Yang, J. Yoon, A. Fouchet, R. Yu, M. G. Blamire, and Q. Jia, Nat Mater **7**, 314 (2008).

[26] R. Ramesh and N. A. Spaldin, Nature Materials **6**, 21 (2007).

[27] Y. L. Li and L. Q. Chen, Applied Physics Letters **88**, 072905 (2006).

[28] H. Zheng, Q. Zhan, F. Zavaliche, M. Sherburne, F. Straub, M. P. Cruz, L. Q. Chen, U. Dahmen, and R. Ramesh, Nano Letters **6**, 1401 (2006).

[29] L. Yan, F. Bai, J. Li, and D. Viehland, Journal of the American Ceramic Society **92**, 17 (2009).

[30] E. Aksel and J. L. Jones, Sensors **10**, 1935 (2010).

[31] W. J. Merz, Phys. Rev. **76**, 1221 (1949).

[32] J. Shieh, J. H. Yeh, Y. C. Shu, and J. H. Yen, Applied Physics Letters **91**, 062901 (2007).

[33] R. Tazaki, D. Fu, M. Itoh, M. Daimon, and S. ya Koshihara, Journal of Physics: Condensed Matter **21**, 215903 (2009).

[34] W. Mason, J. Acoust. Soc. Am. **50**, 1281 (1971).

[35] K. J. Choi, M. Biegalski, Y. L. Li, a. Sharan, J. Schubert, R. Uecker, P. Reiche, Y. B. Chen, X. Q. Pan, V. Gopalan, L.-Q. Chen, D. G. Schlom, and C. B. Eom, Science **306**, 1005 (2004).

[36] O. Diéguez, O. E. González-Vázquez, J. C. Wojdeł, and J. Íñiguez, Phys. Rev. B **83**, 094105 (2011).

[37] D. Lebeugle, D. Colson, A. Forget, and M. Viret, Applied Physics Letters **91**, 022907 (2007).

[38] J. Wang, J. Neaton, H. Zheng, V. Nagarajan, S. Ogale, B. Liu, D. Viehland, V. Vaithyanathan, D. Schlom, U. Waghmare, N. Spaldin, K. Rabe, M. Wuttig, and R. Ramesh, Science **299**, 1719 (2003).

[39] F. Zavaliche, P. Shafer, R. Ramesh, M. P. Cruz, R. R. Das, D. M. Kim, and C. B. Eom, Applied Physics Letters **87**, 252902 (2005).

[40] G. b. Catalan and J. Scott, Advanced Materials **21**, 2463 (2009).

[41] D. Ricinschi, K.-Y. Yun, and M. Okuyama, Journal of Physics Condensed Matter **18**, L97 (2006).

[42] H. Béa, B. Dupé, S. Fusil, R. Mattana, E. Jacquet, B. Warot-Fonrose, F. Wilhelm, A. Rogalev, S. Petit, V. Cros, A. Anane, F. Petroff, K. Bouzehouane, G. Geneste, B. Dkhil, S. Lisenkov, I. Ponomareva, L. Bellaiche, M. Bibes, and A. Barthélémy, Phys. Rev. Lett. **102**, 217603 (2009).

[43] R. Zeches, M. Rossell, J. Zhang, A. Hatt, Q. He, C.-H. Yang, A. Kumar, C. Wang, A. f. Melville, C. f. Adamo, G. Sheng, Y.-H. Chu, J. f. Ihlefeld, R. Erni, C. Ederer, V. Gopalan, L. Chen, D. Schldin, N. Spaldin, L. j. Martin, and R. d. i. Ramesh, Science **326**, 977 (2009).

[44] C. Ederer and N. A. Spaldin, Phys. Rev. Lett. **95**, 257601 (2005).

[45] J. C. Wojdeł and J. Íñiguez, Phys. Rev. Lett. **105**, 037208 (2010).

[46] H. W. Jang, S. H. Baek, D. Ortiz, C. M. Folkman, R. R. Das, Y. H. Chu, P. Shafer, J. X. Zhang, S. Choudhury, V. Vaithyanathan, Y. B. Chen, D. A. Felker, M. D. Biegalski, M. S.

Rzchowski, X. Q. Pan, D. G. Schlom, L. Q. Chen, R. Ramesh, and C. B. Eom, Phys. Rev. Lett. **101**, 107602 (2008).

[47] S. Krupicka and P. Novak, *Handbook of Magnetic Materials, Volume 3*, edited by E. Wohlfarth (North-Holland Publishing Company, 1982).

[48] Y. Suzuki, G. Hu, R. van Dover, and R. Cava, Journal of Magnetism and Magnetic Materials **191**, 1 (1999).

[49] Y. Suzuki, Annual Review of Materials Research **31**, 265 (2001).

[50] U. Lüders, *Development and integration of oxide spinel thin films into heterostructuresfor spintronics*, Ph.D. thesis, Universitat Autonoma de Barcelona (2005).

[51] F. Rigato, *Epitaxial spinel ferrite films for spin-polarized tunnel transport*, Ph.D. thesis, ICMAB-CSIC, Universitat Autonoma de Barcelona (2010).

[52] N. Dix, *Construction of a Low Temperature Magneto-optical Kerr Effect Set-up and Application on Ferromagnetic Oxide Thin Films*, Master's thesis, Technische Universität Ilmenau (2006).

[53] R. K. Mishra and G. Thomas, Journal of Applied Physics **48**, 4576 (1977).

[54] L. Yan, Z. Wang, Z. Xing, J. Li, and D. Viehland, Journal of Applied Physics **107**, 064106 (2010).

[55] L. W. Martin, Y.-H. Chu, and R. Ramesh, Materials Science and Engineering: R-Reports **68**, 111 (2010).

[56] H. M. Christen and G. Eres, Journal of Physics: Condensed Matter **20**, 264005 (2008).

[57] A.-B. Posadas, M. Lippmaa, F. Walker, M. Dawber, C. Ahn, and J.-M. Triscone, in *Physics of Ferroelectrics*, Topics in Applied Physics, Vol. 105 (Springer Berlin / Heidelberg, 2007) pp. 219–304.

[58] G. J. H. M. Rijnders, G. Koster, D. H. A. Blank, and H. Rogalla, Applied Physics Letters **70**, 1888 (1997).

[59] D. Barlett, C. W. Snyder, B. G. Orr, and R. Clarke, Review of Scientific Instruments **62**, 1263 (1991).

[60] J. E. Mahan, K. M. Geib, G. Y. Robinson, and R. G. Long, Journal of Vacuum Science & Technology A **8**, 3692 (1990).

[61] A. Ichimiya and P. I. Cohen, *Reflection High-Energy Electron Diffraction* (Cambridge University Press, 2004) cambridge Books Online.

[62] G. Koster, in *In Situ Characterization of Thin Film Growth*, Woodhead Publishing Series in Electronic and Optical Materials, edited by G. Koster and G. Rijnders (Woodhead Publishing, 2011) pp. 3 – 28.

[63] R. Bachelet, F. Sánchez, J. Santiso, and J. Fontcuberta, Applied Physics Letters **93**, 151916 (2008).

[64] F. Zavaliche, H. Zheng, L. Mohaddes-Ardabili, S. Y. Yang, Q. Zhan, P. Shafer, E. Reilly, R. Chopdekar, Y. Jia, P. Wright, D. G. Schlom, Y. Suzuki, and R. Ramesh, Nano Letters **5**, 1793 (2005).

[65] M. T. Otten, B. Miner, J. H. Rask, and P. R. Buseck, Ultramicroscopy **18**, 285 (1985).

[66] B. D. Cullity and S. R. Stock, *Elements of X-Ray Diffraction* (Prentice Hall, 2001).

[67] M. Birkholz and P. F. Fewster, *Thin Film Analysis by X-Ray Scattering* (Wiley, 2006).

[68] I. Fina, *Ferroelectricity and magnetoelectric coupling in magnetic ferroelectrics and artificial multiferroic heterostructures*, Ph.D. thesis, Universitat de Barcelona (2012).

[69] I. Vrejoiu, M. Ziese, A. Setzer, P. D. Esquinazi, B. I. Birajdar, A. Lotnyk, M. Alexe, and D. Hesse, Applied Physics Letters **92**, 152506 (2008).

[70] H. Zheng, *Growth and characteriztion of multiferroic $BaTiO_3$-$CoFe_2O_4$ thin film nanostructures*, Ph.D. thesis, University of Maryland (2004).

[71] D. Mukherjee, T. Dhakal, R. Hyde, P. Mukherjee, H. Srikanth, and S. Witanachchi, Journal of Physics D **43**, 485001 (2010).

[72] H.-C. He, J. Wang, J.-P. Zhou, and C.-W. Nan, Advanced Functional Materials **17**, 1333 (2007).

[73] C. Deng, Y. Zhang, J. Ma, Y. Lin, and C.-W. Nan, Acta Materialia **56**, 405 (2008).

[74] J. Zhu, L. Zhou, W. Huang, Y. Li, and Y. Li, Journal of Crystal Growth **311**, 3300 (2009).

[75] Y. Zhang, C. Deng, J. Ma, Y. Lin, and C.-W. Nan, Applied Physics Letters **92**, 062911 (2008).

[76] R. Bachelet, D. Pesquera, G. Herranz, F. Sánchez, and J. Fontcuberta, Applied Physics Letters **97** (2010), 10.1063/1.3490713.

[77] M. Foerster, J. M. Rebled, S. Estradé, F. Sánchez, F. Peiró, and J. Fontcuberta, Phys. Rev. B **84**, 144422 (2011).

[78] J.-B. Moussy, Journal of Physics D **46**, 143001 (2013).

[79] R. Takahashi, H. Misumi, and M. Lippmaa, Crystal Growth & Design **12**, 2679 (2012).

[80] J. Ma, D. Mazumdar, G. Kim, H. Sato, N. Bao, and A. Gupta, Journal of Applied Physics **108**, 063917 (2010).

[81] J. Barth, G. Costantini, and K. Kern, Nature **437**, 671 (2005).

[82] H. Wang, Journal of Crystal Growth **177**, 67 (1997).

[83] J. Schubert, O. Trithaveesak, a. Petraru, C. L. Jia, R. Uecker, P. Reiche, and D. G. Schlom, Applied Physics Letters **82**, 3460 (2003).

[84] J. Shin, S. V. Kalinin, A. Y. Borisevich, E. W. Plummer, and A. P. Baddorf, Applied Physics Letters **91**, 202901 (2007).

[85] S. Mi, C. Jia, T. Heeg, O. Trithaveesak, J. Schubert, and K. Urban, Journal of Crystal Growth **283**, 425 (2005).

[86] J. b. Hiltunen, D. Seneviratne, H. Tuller, J. Lappalainen, and V. Lantto, Journal of Electroceramics **22**, 395 (2009).

[87] T. Zhao, F. Chen, H. Lu, G. Yang, and Z. Chen, Journal of Applied Physics **87**, 7442 (2000).

[88] M. Kawai, D. Kan, S. Isojima, H. Kurata, S. Isoda, Y. Shimakawa, S. Kimura, and O. Sakata, Journal of Applied Physics **102**, 114311 (2007).

[89] M. Jimi, T. Ohnishi, K. Terai, M. Kawasaki, and M. Lippmaa, Thin Solid Films **486**, 158 (2005).

[90] A. Petraru, N. Pertsev, H. Kohlstedt, U. Poppe, R. Waser, A. Solbach, and U. Klemradt, Journal of Applied Physics **101**, 114106 (2007).

[91] S. Valencia, A. Crassous, L. Bocher, V. Garcia, X. Moya, R. O. Cherifi, C. Deranlot, K. Bouzehouane, S. Fusil, A. Zobelli, A. Gloter, N. D. Mathur, A. Gaupp, R. Abrudan, F. Radu, A. Barthélémy, and M. Bibes, Natur Materials **10**, 753 (2011).

[92] X. Chen, S. Yang, J.-H. Kim, H.-D. Kim, J.-S. Kim, G. Rojas, R. Skomski, H. Lu, A. Bhattacharya, T. Santos, N. Guisinger, M. Bode, A. Gruverman, and A. Enders, New Journal of Physics **13**, 083037 (2011).

[93] D. de Ligny and P. Richet, Phys. Rev. B **53**, 3013 (1996).

[94] M. Huijben, L. W. Martin, Y.-H. Chu, M. B. Holcomb, P. Yu, G. Rijnders, D. H. A. Blank, and R. Ramesh, Phys. Rev. B **78**, 094413 (2008).

[95] I. Fina, N. Dix, J. M. Rebled, P. Gemeiner, X. Marti, F. Peiro, B. Dkhil, F. Sanchez, L. Fabrega, and J. Fontcuberta, Nanoscale **5**, 8037 (2013).

[96] F. Rigato, J. Geshev, V. Skumryev, and J. Fontcuberta, Journal of Applied Physics **106**, 113924 (2009).

[97] H. Béa, M. Bibes, A. Barthélémy, K. Bouzehouane, E. Jacquet, A. Khodan, J.-P. Contour, S. Fusil, F. Wyczisk, A. Forget, D. Lebeugle, D. Colson, and M. Viret, Applied Physics Letters **87**, 072508 (2005).

[98] H. Bea, M. Bibes, S. Fusil, K. Bouzehouane, E. Jacquet, K. Rode, P. Bencok, and A. Barthélémy, Physical Review B **74**, 020101(R) (2006).

[99] C. J. M. Daumont, S. Farokhipoor, A. Ferri, J. C. Wojdeł, J. Íñiguez, B. J. Kooi, and B. Noheda, Phys. Rev. B **81**, 144115 (2010).

[100] Y. Yang, C. M. Schlepütz, C. Adamo, D. G. Schlom, and R. Clarke, APL Materials **1**, 052102 (2013).

[101] D. Mazumdar, V. Shelke, M. Iliev, S. Jesse, A. Kumar, S. Kalinin, A. Baddorf, and A. Gupta, Nano Letters **10**, 2555 (2010).

[102] A. Damodaran, C.-W. Liang, Q. He, C.-Y. Peng, L. Chang, Y.-H. Chu, and L. Martin, Advanced Materials **23**, 3170 (2011).

[103] Z. Chen, Z. Luo, C. Huang, Y. Qi, P. Yang, L. You, C. Hu, T. Wu, J. Wang, C. Gao, T. Sritharan, and L. Chen, Advanced Functional Materials **21**, 133 (2011).

[104] H. Christen, J. Nam, H. Kim, A. Hatt, and N. Spaldin, Physical Review B **83** (2011), 10.1103/PhysRevB.83.144107.

[105] I. C. Infante, J. Juraszek, S. Fusil, B. Dupé, P. Gemeiner, O. Diéguez, F. Pailloux, S. Jouen, E. Jacquet, G. Geneste, J. Pacaud, J. Íñiguez, L. Bellaiche, A. Barthélémy, B. Dkhil, and M. Bibes, Phys. Rev. Lett. **107**, 237601 (2011).

[106] W. Siemons, M. D. Biegalski, J. H. Nam, and H. M. Christen, Applied Physics Express **4**, 095801 (2011).

[107] J. Scott, ChemPhysChem **11**, 341 (2010).

[108] J. Zhang, B. Xiang, Q. He, J. Seidel, R. Zeches, P. Yu, S. Yang, C. Wang, Y.-H. Chu, L. Martin, A. Minor, and R. Ramesh, Nature Nanotechnology **6**, 98 (2011).

[109] J. Ihlefeld, A. Kumar, V. Gopalan, D. Schlom, Y. Chen, X. Pan, T. Heeg, J. Schubert, X. Ke, P. Schiffer, J. Orenstein, L. Martin, Y. Chu, and R. Ramesh, Applied Physics Letters **91**, 071922 (2007).

[110] J. F. Ihlefeld, N. J. Podraza, Z. K. Liu, R. C. Rai, X. Xu, T. Heeg, Y. B. Chen, J. Li, R. W. Collins, J. L. Musfeldt, X. Q. Pan, J. Schubert, R. Ramesh, and D. G. Schlom, Applied Physics Letters **92**, 142908 (2008).

[111] V. Brabers, *Handbook of Magnetic Materials, Volume 8*, edited by K. H. J. Buschow (Elsevier, 1995).

[112] M. Murakami, S. Fujino, S.-H. Lim, L. Salamanca-Riba, M. Wuttig, I. Takeuchi, B. Varughese, H. Sugaya, T. Hasegawa, and S. Lofland, Applied Physics Letters **88**, (2006).

[113] A. Milch, Thin Solid Films **17**, 231 (1973).

[114] Z. Tan, J. Slutsker, and A. L. Roytburd, Journal of Applied Physics **105**, 061615 (2009).

[115] M. Hÿtch, E. Snoeck, and R. Kilaas, Ultramicroscopy **74**, 131 (1998).

[116] S. Estrade, J. Arbiol, F. Peiro, I. C. Infante, F. Sánchez, J. Fontcuberta, F. de la Peña, M. Walls, and C. Colliex, Applied Physics Letters **93**, 112505 (2008).

[117] I. C. Infante, S. Lisenkov, B. Dupé, M. Bibes, S. Fusil, E. Jacquet, G. Geneste, S. Petit, A. Courtial, J. Juraszek, L. Bellaiche, A. Barthélémy, and B. Dkhil, Phys. Rev. Lett. **105**, 079901 (2010).

[118] J. Kreisel, P. Jadhav, O. Chaix-Pluchery, M. Varela, N. Dix, F. Sánchez, and J. Fontcuberta, Journal of Physics Condensed Matter **23**, 4 (2011).

[119] A. J. Hatt, N. A. Spaldin, and C. Ederer, Phys. Rev. B **81**, 054109 (2010).

[120] R. Haumont, J. Kreisel, and P. Bouvier, Phase Transitions **79**, 1043 (2006).

[121] X. S. Gao, D. H. Bao, B. Birajdar, T. Habisreuther, R. Mattheis, M. A. Schubert, M. Alexe, and D. Hesse, Journal of Physics D **42**, 175006 (2009).

[122] F. Zavaliche, T. Zhao, H. Zheng, F. Straub, M. P. Cruz, P.-L. Yang, D. Hao, and R. Ramesh, Nano Letters **7**, 1586 (2007).

[123] j. Li, *Engineering of Self-Assembled Multiferroic Nanostructures in $PbTiO_3$-$CoFe_2O_4$ Thin Films*, Ph.D. thesis, Graduate School of the University of Maryland (2006).

[124] C. Y. Tsai, H. R. Chen, F. C. Chang, W. C. Tsai, H. M. Cheng, Y. H. Chu, C. H. Lai, and W. F. Hsieh, Applied Physics Letters **102**, 132905 (2013).

[125] H. Zheng, J. Wang, L. Mohaddes-Ardabili, M. Wuttig, L. Salamanca-Riba, D. G. Schlom, and R. Ramesh, Applied Physics Letters **85**, 2035 (2004).

[126] U. Lüders, F. Sánchez, and J. Fontcuberta, Applied Physics A **79**, 93 (2004).

[127] F. Sánchez, U. Lüders, G. Herranz, I. C. Infante, J. Fontcuberta, M. V. García-Cuenca, C. Ferrater, and M. Varela, Nanotechnology **16**, S190 (2005).

[128] R. Maier, J. L. Cohn, J. J. Neumeier, and L. A. Bendersky, Applied Physics Letters **78**, 2536 (2001).

[129] X. Wei, Q. Zhang, F. Li, C. Jin, and R. Yu, Journal of Alloys and Compounds **508**, 486 (2010).

[130] J. Van den Boomgaard, D. Terrell, R. Born, and H. Giller, Journal of Materials Science **9**, 1705 (1974).

[131] Y. Suzuki, R. B. van Dover, E. M. Gyorgy, J. M. Phillips, V. Korenivski, D. J. Werder, C. H. Chen, R. J. Cava, J. J. Krajewski, W. F. Peck, and K. B. Do, Applied Physics Letters **68**, 714 (1996).

[132] I. Fina, N. Dix, L. Fabrega, F. Sánchez, and J. Fontcuberta, Thin Solid Films **518**, 4634 (2010).

[133] I. Fina, N. Dix, L. Fabrega, F. Sánchez, and J. Fontcuberta, Journal of Applied Physics **108**, 034108 (2010).

[134] X. Lu, Y. Kim, S. Goetze, X. Li, S. Dong, P. Werner, M. Alexe, and D. Hesse, Nano Letters **11**, 3202 (2011).

[135] H.-J. Liu, L.-Y. Chen, Q. He, C.-W. Liang, Y.-Z. Chen, Y.-S. Chien, Y.-H. Hsieh, S.-J. Lin, E. Arenholz, C.-W. Luo, Y.-L. Chueh, Y.-C. Chen, and Y.-H. Chu, ACS Nano **6**, 6952 (2012).

[136] N. M. Aimon, D. Hun Kim, H. Kyoon Choi, and C. A. Ross, Applied Physics Letters **100**, 092901 (2012).

[137] A. N, K. D. H., S. XY, and R. C. A., ACS Applied Materials and Interfaces **7**, 2263 (2015).

[138] T. Sakamoto, K. Okada, A. N. Hattori, T. Kanki, and H. Tanaka, Nanotechnology **23**, 335302 (2012).

[139] R. Comes, H. Liu, M. Khokhlov, R. Kasica, J. Lu, and S. A. Wolf, Nano Letters **12**, 2367 (2012).

[140] A. L. Sangle, S. Singh, J. Jian, S. R. Bajpe, H. Wang, N. Khare, and J. L. MacManus-Driscoll, Nano Letters **16**, 7338 (2016).